

RWTH AACHEN UNIVERSITY

INTEGRITY ASPECTS FOR DUAL-FREQUENCY DUAL-CONSTELLATION GROUND BASED AUGMENTATION SYSTEM (GBAS)

Von der Fakultät für Elektrotechnik und Informationstechnik der Rheinisch-Westfälischen Technischen Hochschule Aachen zur Erlangung des akademischen Grades einer

Doktorin der Ingenieurwissenschaften

genehmigte Dissertation

vorgelegt von

Mihaela-Simona Cîrciu, M.Sc.

aus Rădăuți, Rumänien

Berichter:

1. Univ.-Prof. Dr.-Ing. habil. Michael Meurer
2. Ass. Prof. Fabio Dovis, Ph.D.

Tag der mündlichen Prüfung 27.03.2020

Diese Dissertation ist auf den Internetseiten der Universitätsbibliothek online verfügbar.

Abstract

For navigation in aviation, high performance requirements in terms of integrity, accuracy, continuity, availability, and robustness against interference need to be achieved. The Global Navigation Satellite System (GNSS) alone is not sufficiently accurate and cannot provide precision approach with the required integrity. The Ground Based Augmentation System (GBAS), a development of local-area differential GNSS aims at providing precision approach guidance meeting all of these requirements under low-visibility conditions. GBAS provides differential corrections and integrity monitoring of GNSS, which are broadcast via a Very High Frequency (VHF) radio data link, termed as Very High Frequency Data Broadcast (VDB). The system is currently under development with single-frequency single-constellation Global Positioning System (GPS) L1 stations being already in use. Several studies have shown that ionospheric anomalies that cause large spatial gradients pose a significant threat to this system [1, 2, 3]. With the increasing number of satellites broadcasting signals on a second Aeronautical Radio Navigation Service (ARNS) frequency (L5/E5a) available, the dual-frequency processing becomes a promising option for the next generation aviation users. The use of the signals in a second frequency band can remove the effect of the ionosphere which is one of the dominant sources of errors for the single frequencies user. However, it also yields many different options for processing. Until today there is no clear concept defined on how to use the new signals in a future Dual-Frequency Dual-Constellation (DFDC) GBAS to provide better performance compared to the existing system.

This thesis provides essential contributions to the development, standardization and implementation of a future DFDC GBAS. The new service type shall be able to provide sufficient availability, integrity and continuity to be usable globally. Relevant contributors to the error budget are reviewed, characterized and modeled in an appropriate way.

The thesis is structured as follows. First, it provides a detailed overview of the existing integrity concept for the single frequency GBAS. The goal of this review is to set the framework and identify the aspects needed in the development of the DFDC GBAS. Next, the thesis discusses the modifications needed when evolving to a DFDC system. The use of the signals from a second frequency band and second constellation enable many different processing modes. In this thesis, the proposal and the selection of the processing modes for a DFDC GBAS is based on upgrading the existing GBAS, but maintaining the main characteristics (e.g. maintaining the existing VDB link). This concept adds several constraints, such as backwards compatibility to the existing single frequency system and the limited remaining VDB capacity. Taking into account

all the constraints, the most promising processing modes are presented and discussed. Based on the selected modes, the thesis discusses the modifications to the integrity concept and identifies the different aspects that need to be taken into account for each of the processing modes, which is the main contribution on this part. This includes the need for the new ground multipath error models, new airborne multipath models and consideration of the satellite code biases in the integrity concept. Each of these aspects are discussed in the thesis and summarized next including the main contributions.

The first error source considered is the multipath and noise errors in the ground reference receivers. Until now, performance analysis of the ground multipath errors using the GPS L1 Coarse/Aquisition (C/A) signal has been studied. In this thesis, the performance analysis of the new signals from the Galileo satellites in the E1 and E5a frequency bands and GPS L5 signals as measured by the experimental GBAS test bed available at Deutsches Zentrum für Luft- und Raumfahrt e.V. (DLR) is presented. The results show that the raw noise and multipath level of Galileo signals and of the GPS L5 signals are smaller than that of GPS L1. The new signals are also less sensitive to the choice of carrier-smoothing time constant. As the Galileo constellation has different ground track repeatability from GPS, the applicability of the existing methods for the derivation of the ground multipath models is investigated in the thesis. The impact of different effects factor influencing the multipath models such as the smoothing time constant and the receiver parameters are studied. Furthermore, dual-frequency ground multipath error models are derived that differ from the combination of single frequency models.

Another important source of error to be considered in a future DFDC GBAS is the airborne multipath. With the removal of the ionospheric error, the airborne multipath error becomes a dominant source of error. The current models are defined only for GPS L1 100 seconds smoothing time constant and no models are available for the new signals broadcast by GPS satellites on L5 band and Galileo satellites. This thesis contributes to the development of the airborne multipath models for the new signals. The work proposes an improved methodology for the derivation of the multipath models for aviation using measurements from flight tests. The improvements include a proposal of a new method for the estimation of the carrier phase ambiguities, the separation of the receiver antenna errors from the multipath errors and an overbounding for the non-Gaussian distribution of the data. The removal of the antenna errors constitutes one of the main changes from the existing models. Until now, the receiver antenna errors were modeled together with the multipath errors. However, the results from this thesis show that these errors have different behavior than the multipath errors and thus a decomposition of these two errors is suggested. Different factor of influence on the airborne multipath, including airframe structure and antenna performance, the receiver bandwidth and correlator spacing and the smoothing time constant are investigated and discussed in this thesis.

A third aspect relevant for DFDC GBAS that is discussed in the thesis is the satellite code biases. These biases differ between satellites and depend mainly on

the GNSS receiver hardware (e.g. bandwidth and correlator spacing). If the ground reference stations and airborne receiver use different configurations, a residual error remains affecting the GBAS user. These biases can be calculated based on measurements from a high gain antenna. Initial estimates of the satellites code biases are used in this thesis to investigate the impact of the differential satellite code bias on a GBAS user. The results show that the residual errors are not negligible and vary from few centimeters to decimeters. The errors are especially important for the dual-frequency processing modes that combine the errors from different frequencies. Thus, they will affect the GBAS user and need to be taken into account in the integrity budget. The thesis proposes different concepts to include them in the integrity budget of the DFDC GBAS.

Finally, the thesis presents an assessment of the expected nominal performance of different processing modes for future DFDC GBAS. The evaluations are based on measurements from flight trials conducted on DLR's Airbus A320 aircraft. The error models developed in the thesis are used as input for the study. This work contributes to the tradeoff studies needed for a selection of an optimal processing mode for DFDC GBAS.

Acknowledgments

This PhD has been an important experience in my career and there are many people I would like to thank for supporting me during these years. First, I would like to express my deepest appreciation to my PhD advisor, Prof. Michael Meurer, who guided me during these years and gave me the opportunity to pursue my studies in RWTH Aachen and my work in the Navigation department of DLR. I appreciate all his involvement, contributions, technical discussions and new ideas that helped in my research and in improving and finalizing this work. I am also extremely grateful to my co-supervisor Prof. Fabio Dovis, who was one of the first mentors that introduced me in the satellite navigation and augmentation systems world during my studies at Politecnico di Torino. I will always remember one of his lectures when he gave me the first chance to work with a GNSS receiver. His continuous feedback and guidance helped me improve this work and I am very grateful to have had him as my co-supervisor.

My colleagues from the Navigation department of the Institute of Communications and Navigation of DLR had a very big contribution to my professional and personal development. I cannot begin to express my gratitude and thank to Dr. Michael Felux, who was my mentor, my office-mate and my friend during these years. He developed my passion for GBAS from my first days at DLR and mentored me over all the years both technically and personally. His support, guidance and encouragement had a strong contribution on the rough road of finishing this thesis. I am also very grateful to my colleagues Maria Caamano Albuerne and Daniel Gerbeth from the DLR's GBAS team. Working in this team has been an honor and I always appreciated their support, motivation, our meetings with interesting discussions and the team spirit. Special thanks for their contribution and support on the GBAS review chapter, it was very helpful to work and iterate together on this. Next, I would like to extend my sincere thanks to Dr. Stefano Caizzone, who introduced me in the antenna world and from whom I learnt a lot over these years. His motivation and expertise inspired me. Many thanks also to Steffen Thoelert who helped me understand and contributed to the satellite biases work and Christoph Enneking who helped me with the analysis of the errors through the ideal software receiver and always answered my receiver questions. I also had a great pleasure of working with Markus Rippl, whom I appreciate very much and always gave me valuable advice. Many thanks for managing the Dual Frequency Multipath Models for Aviation (DUFMAN) project to which this work contributed, it was a great experience to work together. I am also extremely grateful to my fellow PhD colleague and friend, Dr. Santiago Perea Diaz who always encouraged me and made the entire PhD administrative process much simpler by explaining me every step. Many thanks also to all my other colleagues with

whom I worked together or shared encouraging discussions: Anja Grosch, Alexandra Filip-Dhaubhadel, Friederike Fohlmeister, Veenu Kamra, Omar Garcia Crespillo and Dr. Okuary Osechas. I was very lucky to be surrounded by experts and wonderful people, I have learned a lot and these years defined a big part of who I am today.

Going through this process did not require only technical support and I would like to extend my sincere thanks to my friends for being next to me over these years, for motivating and coaching me.

I would also like to express my profound gratitude to my family, for all their unconditional love, encouragement and support through this process. They gave me strength and were always next to me despite the distance between us.

Above all, I would like to thank my husband-to-be, Javier. He stood by me all these years and supported me at each step. He always believed in me and gave me the courage and motivation to go on. This achievement would not have been possible without you and I am deeply grateful to have had you by my side on this journey. For all this and much more, I dedicate this thesis to you.

Contents

List of Figures **xi**

List of Tables **xvii**

1 Introduction **1**
1.1 Background . . . 1
1.2 State of the art . . . 2
1.3 Objectives and research questions . . . 3
1.4 Outline of work and associated contributions . . . 4

2 Current single frequency GBAS **7**
2.1 Fundamentals of GBAS and Approach Service Types . . . 7
2.2 Short discussion on the available documents . . . 9
2.3 GBAS Positioning . . . 10
2.4 GBAS Threat Space . . . 20
2.5 Integrity in GBAS . . . 21
2.6 Integrity in GAST-C . . . 34
2.7 Integrity in GAST-D . . . 48

3 DFDC GBAS and considerations **71**
3.1 Candidate options for DFDC GBAS . . . 72
3.2 Discussion on service types and current status . . . 76
3.3 Ground processing for DFDC GBAS . . . 83
3.4 Airborne processing for DFDC GBAS . . . 85
3.5 Threat space for DFDC GBAS . . . 87
3.6 Integrity in DFDC GBAS . . . 87

4 Ground multipath in DFDC GBAS **97**
4.1 Objectives and contributions . . . 97
4.2 Methodology, metrics and assumptions . . . 98
4.3 Facilities . . . 107
4.4 Results and discussion . . . 109
4.5 Publications . . . 135

5 Airborne multipath models **137**
5.1 Objectives and contributions . . . 137
5.2 Airborne multipath error . . . 138
5.3 State of the art: current airborne multipath models . . . 139

5.4 Overview of proposed methodology for new models . . . 141
5.5 Methodology for definition of multipath models from flight data . . . 144
5.6 Additional errors affecting the multipath estimation . . . 160
5.7 Separation of multipath error and antenna induced error . . . 166
5.8 Data collection for new models . . . 168
5.9 Impact of the processing on the multipath and noise error models . . . 171
5.10 Multipath error models for DLR's A320 . . . 180
5.11 Factors of influence on the airborne multipath models . . . 184
5.12 Initial multipath models derived within DUFMAN . . . 193
5.13 Publications . . . 194

6 Satellite code biases in DFDC GBAS 197
6.1 Objectives and contributions . . . 197
6.2 Overview of the satellite-induced code biases . . . 198
6.3 Considerations and metrics used for the satellite code biases . . . 200
6.4 Receiver design space considered . . . 202
6.5 Initial results for the differential satellite code biases . . . 204
6.6 Inclusion of satellite-biases in GBAS . . . 206

7 Assessment of different processing modes 213
7.1 Evaluation of position errors in flight test . . . 213
7.2 Assessment of nominal protection levels . . . 216
7.3 Discussion . . . 223

8 Conclusion 225
8.1 Summary and main contributions . . . 225
8.2 Recommendation and further research . . . 229

A Smoothing Filter 233
A.1 Single frequency smoothed pseudoranges . . . 233
A.2 Ifree smoothed pseudoranges . . . 234

B Smooth Multipath Derivation 237
B.1 Single frequency . . . 237
B.2 Dual frequency Ionosphere-free (Ifree) multipath estimation . . . 238

Bibliography 241

List of Figures

2.1 Broadcast GPS L1 PRC^n_{TX} from DLR GBAS test bed 16
2.2 B^n_m-values versus satellite elevation from one reference receiver (m) from the DLR's GBAS test bed 16
2.3 Lateral deviation definition 19
2.4 Vertical deviation definition 20
2.5 Relationship between performance parameters 23
2.6 Error handling in GNSS 24
2.7 Ground accuracy models versus elevation angle 29
2.8 Multipath and airborne accuracy models versus elevation angle 30
2.9 Monitoring used in GBAS integrity concept 33
2.10 Errors and threats as part of integrity concept in GAST-C 35
2.11 Ionospheric threat model 44
2.12 Steps for ionosphere mitigation in GAST-C 45
2.13 Tropospheric wall model 48
2.14 GAST-D requirements allocation 49
2.15 Box defining the touchdown requirements (from [64]) 50
2.16 P_{md} in range domain for the limit case 54
2.17 Limit on the P_{md} in range domain for the malfunction case 56
2.18 Limit on the P_{md} in range domain for the malfunction case 57
2.19 Errors and threats as part of integrity concept in GAST-D 58
2.20 Ionospheric gradient orientations constituting a threat to GAST-D from [13] 64

3.1 Example of distribution of VDB messages for a DFDC GBAS 78
3.2 Limit on the P_{md} in range domain for limit and malfunction case for DFDC 90

4.1 DLR GBAS Ground Facility close to Braunschweig Airport 108
4.2 Number of hours collected over one month in March 2018 for each PRN from Block IIF GPS 109
4.3 Number of hours collected over one month in March 2018 for each PRN from Galileo constellation 109
4.4 Raw code multipath and noise as a function of elevation of the GPS L1 and GPS L5 signals 111
4.5 Raw code multipath and noise as a function of elevation for GPS and Galileo signals 111
4.6 Mean C/N_0 over March 2018 for GPS L1 and L5 and Galileo E1 and E5a 112

4.7 Mean C/N_0 from August 2015 for GPS L1, GPS L5, Galileo E1 and E5a 113
4.8 Standard deviation for theoretical noise for GPS and Galileo signals . 114
4.9 Standard deviation for raw multipath for GPS and Galileo signals . . 115
4.10 $\sigma_{\text{pr_gnd}}$ results for 100 seconds smoothing time constant based on B-values (a) and CMC method (b) 117
4.11 Raw and smoothed multipath function of elevation for Galileo PRN 9 on E1 and GPS PRN 27 on L5 118
4.12 Multipath error envelope 119
4.13 Track orbiting skyplot projection of Galileo PRN 1 satellite for 10 days. Each color refers to a complete orbit revolution of 14 hours and 7 minutes 121
4.14 $\sigma_{\text{pr_gnd}}$ for GPS L5 signal for different smoothing time constants . . . 123
4.15 $\sigma_{\text{pr_gnd}}$ for Galileo E1 signal for different smoothing time constants . . 124
4.16 $\sigma_{\text{pr_gnd}}$ for Galileo E5a signal for different smoothing time constants . 124
4.17 Impact of the correlator spacing on ground multipath and noise error . 126
4.18 Ratio $\sigma_{\text{pr_gnd}_{\text{Ifree}}}$ GPS 100s smoothed- $\sigma_{\text{pr_gnd}_{L1}}$ GPS 100s smoothed function of elevation 127
4.19 Correlation between the 100 seconds smoothed B-values on GPS L1 and GPS L5 128
4.20 $\sigma_{\text{pr_gnd}_{\text{Ifree}}}$ for GPS L1/L5 and Galileo E1/E5a 129
4.21 Comparison B-values - CMC method using measurements from DLR GBAS test bed 131
4.22 Multipath autocorrelation function for reference receivers of the DLR's GBAS test bed 132
4.23 Comparison B-values - CMC method for using measurements from GBAS station in Malaga 133
4.24 Multipath autocorrelation function for the measurements from the reference receivers of the GBAS station in Malaga 133
4.25 100 seconds smoothed $\sigma_{\text{pr_gnd}}$ obtained from CMC method 135

5.1 Example of airborne multipath 139
5.2 $\sigma_{\text{pr_air}}$ curves derived from measurements collected with two different antennas 143
5.3 $CMC_{\text{Dfree,bias}}$ for L1 over time for GPS Pseudorandom noise (PRN) 8 148
5.4 $CMC_{\text{Dfree,bias}}$ versus elevation (plot (a)) and histogram of the $CMC_{\text{Dfree,bias}}$ (plot (b)) on GPS L1 for one satellite (PRN 10) in a ground scenario with low multipath 149
5.5 $CMC_{\text{Dfree,bias}}$ versus elevation (plot (a)) and histogram of the $CMC_{\text{Dfree,bias}}$ (plot (b)) on GPS L1 for one satellite (PRN 3) using measurements from flight tests 150
5.6 C/N_0 values from level segments of flights for GPS L1 (graph (a)), GPS L5 (graph (b)), Galileo E1 (graph (c)) and Galileo E5a (graph (d)) 152
5.7 Improved method for carrier phase ambiguities removal 153
5.8 Comparison of different methods used for estimating the bias due to carrier phase ambiguities 154

5.9 Code error due to the absolute antenna group delay for GPS L1 signal (a), Galileo E1 signal (b) and GPS L5/Galileo E5a signals (c) 163
5.10 Estimated code error due to antenna group delay for different scenarios 165
5.11 Position errors due to antenna biases for single frequency positioning (red curve) and dual frequency Ifree position solution (red curve) . . . 166
5.12 Calibration of antenna errors in a static ground scenario 167
5.13 Calibration of antenna errors on measurements from flight 168
5.14 Ground tracks of the flights conducted on DLR's A320 during 2015-2018 169
5.15 Ground tracks of the flights conducted on Airbus A321 within DUFMAN project 170
5.16 Ground tracks of the flights conducted on DLR's Dassault Falcon . . . 170
5.17 Code error due to the absolute antenna group delay of the Javad AirAnt antenna for GPS L1 signal (a), Galileo E1 (b) and GPS L5/Galileo E5a (c) 171
5.18 Effect of the cycle slip algorithms on airborne multipath models 172
5.19 Standard deviation of the estimated 100 seconds smooth airborne multipath and noise errors for GPS signals before and after antenna errors removal 174
5.20 Standard deviation of the estimated 100 seconds smooth airborne multipath and noise errors for Galileo signals before and after antenna errors removal 174
5.21 Example of overbounding for one elevation bin 175
5.22 Inflation factor derived for all elevation bins to account for heavy tails for GPS 176
5.23 Inflation factor derived for all elevation bins to account for heavy tails for Galileo signals 176
5.24 Median autocorrelation function of the unsmoothed and smoothing multipath and noise error 178
5.25 Inflation factor for 95% confidence limit function of number of samples 178
5.26 Number of samples and inflation factors for different elevation bin sizes 179
5.27 Number of samples and inflation factors for equal elevation bin sizes . 180
5.28 Overbounding aiborne multipath models for 30 seconds smoothed multipath and noise errors for GPS signals 181
5.29 Overbounding aiborne multipath models for 100 seconds smoothed multipath and noise errors for Galileo signals 181
5.30 Overbounding aiborne multipath models for 30 seconds smoothed multipath and noise errors for GPS signals 183
5.31 Overbounding aiborne multipath models for 30 seconds smoothed multipath and noise errors for Galileo signals 184
5.32 Airborne multipath models for GPS for different smoothing time constants 185
5.33 Airborne multipath models for Galileo for different smoothing time constants 186
5.34 Skyplot of the GPS and Galileo satellites tracked during the two flight tests conducted on Airbus A321 in aircraft body frame 187

5.35 Skyplot of the GPS and Galileo satellites tracked during the flight tests conducted on Dassault Falcon aircraft in aircraft body frame 187
5.36 Overbounding airborne multipath models for 100 seconds smoothed multipath and noise obtained from the measurements on A321 for GPS and Galileo signals 188
5.37 Overbounding airborne multipath models for the 100 seconds smoothed multipath and noise obtained from the measurements on Falcon aircraft for GPS and Galileo signals 189
5.38 Allowed E-L Discriminator Tracking of GPS satellites as specified in [18] 190
5.39 Standard deviation for the noise and multipath error obtained for two different smoothing time constants 190
5.40 DFDC airborne receiver design characteristics as specified in [92] . . . 191
5.41 Impact of the receiver parameters on the airborne multipath models for GPS signals 192
5.42 Impact of the receiver parameters on the airborne multipath models for Galileo signals 193
5.43 Initial airborne multipath models derived within DUFMAN project . . 194

6.1 Differential code bias using a ground receiver with the configuration of 0.1 chips for L1 and 16 MHz bandwidth and the airborne receiver taking the values from the dingle frequency design space for GPS PRN 9 (a),GPS PRN 24 (b) and GPS PRN 27 (c) 204
6.2 Differential satellite code biases on L1 for three GPS satellites 205
6.3 Differential satellite code biases on L5 for three GPS satellites 205
6.4 Differential satellite code bias for the Ifree combination for GPS satellites 205
6.5 $s_{\mathrm{apr_vert}}$ values (a) and $s_{\mathrm{apr_lat}}$ values obtained during a flight tests for dual-constellation GPS Galileo solution 209
6.6 Simulated $\Delta VPL_{\mathrm{H_0}}$ term (to be added to the nominal $VPL_{\mathrm{H_0}}$) for L1/E1, L5/E5a and Ifree solutions. The solid lines represent the worst case and the dashed lines the case when the sign is taken into account 211
6.7 Simulated $\Delta LPL_{\mathrm{H_0}}$ term (to be added to the nominal $LPL_{\mathrm{H_0}}$) for L1/E1, L5/E5a and Ifree solutions 212

7.1 Ground track of the flight considered in evaluations 214
7.2 East-north errors during flight for different processing modes 215
7.3 Vertical errors in flight for different processing modes 215
7.4 Total number of GPS Block IIF and Galileo satellites used in GBAS position error evaluation 216
7.5 VPL versus time for different processing modes 219
7.6 Aircraft speed and distance to the GBAS reference station during the flight used in evaluation 220
7.7 Vertical Protection Level (VPL) versus distance for different processing modes using DLR airborne multipath model and CONUS ionospheric threat model 221

7.8 VPL versus distance for different processing modes using DLR airborne multipath model and Germany ionospheric threat model 222
7.9 VPL versus distance for different processing modes using DLR and DUFMAN airborne multipath model and CONUS ionospheric threat model 222
7.10 VPL versus distance for different processing modes using DLR and DUFMAN airborne multipath model and Germany ionospheric threat model 224

List of Tables

2.1 Precision landing categories ([30]) 8
2.2 Available documents for GBAS used in this thesis 11
2.3 Parameters in FAS data 19
2.4 Performance requirements 22
2.5 Parameters for ground accuracy models 28
2.6 Fault free missed detection multiplier k_{ffmd} [18] 36
2.7 Missed detection multiplier k_{md} [18] 36
2.8 Faults and monitors in GAST-C 37
2.9 Parameters of the Conterminous United States (CONUS) Ionopheric threat model 43
2.10 Touchdown requirements 50
2.11 Linear approximation for P_{md} for limit case 55

4.1 Notations used for the derivation of $\sigma_{\mathrm{pr_gnd}}$ 103
4.2 Minimum and maximum power levels for GPS and Galileo signals . . 112
4.3 Minimum and maximum ratios for different signals pairs 116

5.1 Errors in multipath estimation 160

6.1 Design spaces considered for correlator-spacing and bandwidth for airborne receiver and ground reference receiver 203

Acronyms

AAD Airborne Accuracy Designator
AAD-A Airborne Accuracy Designator A
AAD-B Airborne Accuracy Designator B
ALs Alert Limits
APV Approach with Vertical Guidance
APV-I Approach with Vertical Guidance I
APV-II Approach with Vertical Guidance II
ARAIM Advanced Receiver Autonomous Integrity Monitoring
ARNS Aeronautical Radio Navigation Service
ASV Approach Service Volume
ATRA Advanced Techonology Research Aircraft
BDS BeiDou Navigation Satellite System
BGDs Broadcast Group Delays
BOC Binary Offset Carrier
BPSK Binary Phase Shift Keying
C/A Coarse/Aquisition
CAT-I Category I
CAT-II Category II
CAT-III Category III
CAT-IIIa Category IIIa
CAT-IIIb Category IIIb
CAT-IIIc Category IIIc
CBOC Composite Binary Offset Carrier
CCD Code Carrier Divergence
CDF Cumulative Distribution Function
CDMA Code Division Multiple Access
CMC Code Minus Carrier
CONUS Conterminous United States
CRC Cyclic Redundancy Check
CS-AWO Certification Specifications for All-Weather Operations
CUSUM Cumulative Sum
CW Course Width
DCBs Differential Code Biases
DFDC Dual-Frequency Dual-Constellation
Dfree Divergence-free
DH Decision Height
DLR Deutsches Zentrum für Luft- und Raumfahrt e.V.

Dmax Maximum Use Distance
D-RAIM Differential Receiver Autonomous Integrity Monitoring
DSIGMA Dual-Solution Ionospheric Gradient Monitor
DUFMAN Dual Frequency Multipath Models for Aviation
ECEF Earth-Centered Earth-Fixed
EGNOS European Geostationary Navigation Overlay Service
EIRP Equivalent Isotropic Radiated Power
Eurocae European Organization for Civil Aviation Equipment
EWMA Exponential Weighted Moving Average
FAA Federal Aviation Administration
FAS Final Approach Segment
FDMA Frequency Division Multiple Access
FOC Full Operational Capability
FPAP Flight Path Alignment Point
FTE Flight Technical Error
FTP Fictious Threshold Point
GAD Ground Accuracy Designator
GAD-A Ground Accuracy Designator A
GAD-B Ground Accuracy Designator B
GAD-C Ground Accuracy Designator C
GARP GNSS Azimuth Reference Point
GAST GBAS Approach Service Type
GAST-A GBAS Approach Service Type A
GAST-B GBAS Approach Service Type B
GAST-C GBAS Approach Service Type C
GAST-D GBAS Approach Service Type D
GAST-E GBAS Approach Service Type E
GAST-F GBAS Approach Service Type F
GBAS Ground Based Augmentation System
GERP GNSS Elevation Reference Point
GLONASS Global Navigation Satellite System
GNSS Global Navigation Satellite System
GPA Glide Path Angle
GPIP Glide Path Intercept Point
GPS Global Positioning System
GRP Guidance Reference Point
ICAO International Civil Aviation Organization
ICD Interface Control Document
IEV Ionosphere-induced Error in Vertical
IFB Inter-frequency bias
Ifree Ionosphere-free
IGM Ionospheric Gradient Monitor
IGN Instituto Geografico Nacional
IGS International GNSS Service
IGWG International GBAS Working Group

ILS Instrument Landing System
IOV In Orbit Validation
IPP Ionospheric Pierce Point
ISCs Inter-Signal Corrections
LAAS Local Area Augmentation System
LAL Lateral Alert Limit
LATO Landing & Guided Take-Off Task Force
LDACS L-band Digital Aeronautical Communications System
LPL Lateral Protection Level
LTI Linear Time Invariant
LTP Landing Threshold Point
MDE Minimum Detectable Error
MIEV Maximum Ionosphere-induced Error in Vertical
MLA Multipath Limiting Antenna
MOPS Minimum Operational Performance Standards
MQM Measurement Quality Monitor
MT Message Type
NED North-East-Down
NextGen Next Generation Air Transportation System
NSE Navigation System Error
NSP Navigation System Panel
NTDP Nominal Touchdown Point
OCS Obstacle Clearance Surfaces
PAR Precision Approach Region
PDF Probability Distribution Function
PPD Personal Privacy Devices
PRN Pseudorandom noise
RAIM Receiver Autonomous Integrity Monitoring
RF Radio Frequency
RFI Radio Frequency Interference
RMS root mean square
RTCA Radio Technical Commission for Aeronautics
RVR Runway Visibility Range
SARPS Standards and Recommended Practices
SBAS Satellite Based Augmentation System
SESAR Single European Sky ATM Research
SiS signal-in-space
SQM Signal Quality Monitor
TCH Threshold Crossing Height
TCP Threshold Crossing Point
TEL Tolerable Error Limit
TSE Total System Error
TTA Time to Alert
US United States
VAL Vertical Alert Limit

VDB Very High Frequency Data Broadcast
VHF Very High Frequency
VPL Vertical Protection Level
WAAS Wide Area Augmentation System
WGS84 World Geodetic System 1984
YETE Yesterday Ephemeris minus Today Ephemeris

Nomenclature

Measurements and measurements errors

Symbol	Description	Unit
ρ	Pseudorange (referred also as code) measurement	m
ϕ	Carrier phase measurement	m
R	Geometric range	m
δt	Clock bias	s
T	Tropospheric error	m
I	Ionospheric error	m
e	Ephemeris error	m
MP	Pseudorange multipath error	m
ε	Pseudorange receiver thermal noise error	m
mp	Carrier phase multipath error	m
η	Carrier phase noise error	m
wu_ϕ	Carrier phase windup error	m
N	Carrier phase ambiguity	cycles
B_r	Receiver instrumental error on pseudorange measurements	m
B^s	Satellite instrumental error on pseudorange measurements	m
β_r	Receiver instrumental error on carrier phase measurements	m
β^s	Satellite instrumental error on carrier phase measurements	m
ξ_r	Receiver antenna error on pseudorange measurements	m
ξ^s	Satellite antenna error on pseudorange measurements	m
ζ_r	Receiver antenna error on carrier phase measurements	m
ζ^s	Satellite antenna error on carrier phase measurements	m
CMC	Code-minus-carrier	m
θ	Satellite elevation	deg
ψ	Satellite azimuth angle	deg
λ	Wavelength	m
τ	Smoothing time constant	s
ΔT	Measurements sampling rate	s
c	speed of light in vacuum	m/s
θ_{GPA}	Glide path angle	deg
k	Measurements epoch	

N_{k}	Number of epochs	
$\mathrm{C/N_0}$	Carrier-to-noise ration	dB-Hz
g_{iono}	Slope of the ionospheric gradient	
w_{iono}	Width of the ionospheric gradient	km
v_{iono}	Speed of the ionospheric gradient	m/s
D_{iono}	Maximum differential delay	m

For a given measurement, e.g. $\rho^{s}_{r,i}(t)$, the indexes refer to the satellite s, recorded by receiver r on frequency band i at time t. If one of the indexes is missing, it means that the parameter is not a function of that parameter. The parameters indicated with an overline ($\overline{x}$) indicates the smoothed measurements (after the application of the smoothing filter) .

Dual-frequency measurements combinations

For the dual-frequency measurements combination, the indexes Dfree, for the divergence-free combination, and Ifree, for ionospheric-free combination are added to the variables.

Symbol	**Description**	**Unit**
ρ_{Dfree}	Divergence-free combination of pseudorange measurements	m
ϕ_{Dfree}	Divergence-free combination of phase measurements	m
$CMC_{\mathrm{Dfree,bias}}$	Code minus carrier divergence-free combination before carrier phase ambiguties removal	m
CMC_{Dfree}	Code minus carrier divergence-free combination after carrier phase ambiguties removal	m
mp_{Dfree}	Divergence-free combination of the carrier phase multipath error	m
η_{Dfree}	Divergence-free combination of the carrier phase noise error	m
a_{Dfree}	Divergence-free combination of the carrier phase hardware error	m
ρ_{Ifree}	Ionospheric-free combination of pseudorange measurements	m
ϕ_{Ifree}	Ionospheric-free combination of carrier phase measurements	m
$CMC_{\mathrm{Ifree,bias}}$	Code minus carrier ionospheric-free combination before carrier phase ambiguties removal	m
CMC_{Ifree}	Code minus carrier divergence-free combination after carrier phase ambiguties removal	m

The indexes follow a similar notation as explained above with the inclusion of two frequencies, e.g. the notation ${\rho_{\mathrm{Ifree}}}^{s}_{r,i,j}(t)$ refers to the ionosphere-free combination of

the code measurements from frequency bands i and j, from satellite s, recorded by receiver r at epoch time t.

GBAS ground subsystem parameters

Symbol	Description	Unit
PRC	Pseudorange correction	m
PRC_{CSC}	Smoothed pseudorange correction	m
PRC_{SCA}	Smoothed receiver clock adjust pseudorange correction	m
PRC_{TX}	Smoothed transmited pseudorange correction	m
RRC_{TX}	Smoothed transmited range rate correction	m
B	B-value	m

The ground system parameters follow the same nomenclature, the indexes for a variable, e.g. $PRC^{s}_{r,i}(t)$, refer to the pseudorange correction of the satellite s, receiver r, on frequency band i at epoch time t. For the dual-frequency combinations, the indexes Dfree and Ifree are used with the indication of the two frequencies used.

Position solution and deviations

Symbol	Description	Unit
$\boldsymbol{X}$	Position vector	
x_{BF}	Position coordinate in body-frame	m
x_{ECEF}	Position coordinate in Earth-Centered Earth-Fixed (ECEF)	m
x_{NED}	Position coordinate in North-East-Down (NED)	m
lat	Latitude	deg
$long$	Longitude	deg
H	Aircraft heading angle	deg
P	Aircraft pitch angle	deg
R	Aircraft roll angle	deg
$\boldsymbol{G}$	Geometry matrix	
g_{pq}	G-matrix element in row p, column q	
$\boldsymbol{S}$	Weighted least-squares projection matrix	
s_{pq}	S-matrix element in row p, column q	
$\boldsymbol{W}$	Weighting matrix	
w_{pq}	W-matrix element in row p, column q	
d_{lat}	Lateral deviation	m
d_{vert}	Vertical deviation	m
α_{lat}	Angular lateral deviation	deg
α_{vert}	Angular vertical deviation	deg
$\vec{r}$	Vector from the center of the Earth to the user coordinate	
$\vec{r}_{\mathrm{GRP}}$	Vector from the center of the Earth to the Guidance Reference Point (GRP) in ECEF	

$\vec{r}_{\mathrm{GARP}}$	Vector from the center of the Earth to the GNSS Azimuth Reference Point (GARP) in ECEF
$\vec{r}_{\mathrm{GERP}}$	Vector from the center of the Earth to the GNSS Elevation Reference Point (GERP) in ECEF
$\vec{u}$	Vector from the center of the Earth to the Landing Threshold Point (LTP) in ECEF
$\vec{u}_{\mathrm{lat}}$	Unit vector in lateral direction
$\vec{u}_{\mathrm{rw}}$	Unit vector in the longitudinal (runway frame) direction
$\vec{u}_{\mathrm{vert}}$	Vertical unit vector

Integrity parameters and requirements

Symbol	Description	Unit
σ_{GBAS}	Standard deviation of the total GBAS fault-free error	m
$\sigma_{\mathrm{pr_gnd}}$	Standard deviation of the ground pseudorange error x	m
$\sigma_{\mathrm{pr_air}}$	Standard deviation of the airborne residual error	m
σ_{iono}	Standard deviation of the residual ionosperic error	m
σ_{tropo}	Standard deviation of the residual tropospheric error	m
σ_{vig}	Standard deviation of nominal ionospheric uncertainty	m
σ_{ref}	Standard deviation refractivity uncertainty	m
σ_{n}	Standard deviation of code receiver noise	m
σ_{mp}	Standard deviation code multipath error	m
$s_{\mathrm{apr_vert}}$	Projection of S-onto the vertical component	m
$s_{\mathrm{apr_lat}}$	Projection of S-onto the lateral component	m
$B_{\mathrm{apr_vert}}$	Projection of B-value onto the vertical component	m
$B_{\mathrm{apr_lat}}$	Projection of B-value onto the lateral component	m
σ_{divg}	Error of the smoothing filter deviation	m
$\sigma_{\mathrm{H_1}}$	Range domain overbound of under H_1 faults	m
VAL	Vertical alert limit	m
LAL	Lateral alert limit	m
$VPL_{\mathrm{H_0}}$	Vertical protection level fault free	m
$VPL_{\mathrm{H_1}}$	Vertical protection level H_1	m
$VPL_{\mathrm{H_2}}$	Vertical protection level H_2	m
$LPL_{\mathrm{H_0}}$	Lateral protection level fault free	m
$LPL_{\mathrm{H_1}}$	Lateral protection level H_1	m
$LPL_{\mathrm{H_2}}$	Lateral protection level H_2	m
VPB	Vertical ephemeris protection level	m
LPB	Lateral ephemeris protection level	m
x_{air}	Horizontal distance from the airplane to the GBAS reference point	km
v_{air}	Aircraft speed	m/s
P_x	Ephemeris decorrelation parameter	m
D_{v}	Difference in vertical position between 30 seconds smoothed and 100 second smoothed position solution	m

D_{l}	Difference in lateral position between 30 seconds smoothed and 100 second smoothed position solution	m
P_{md}	Probability of missed-detection	
P_{fa}	Probability of false alarm	
k_{ffmd}	Sigma multiplier for the required integrity risk under the fault-free case	
k_{md}	Sigma multiplier for missed detection probability	m
$k_{\mathrm{md_e},x}$	Sigma multiplier for the missed detection probability needed to cover the ephemeris faults for the GBAS Approach Service Type (GAST) x	
k_{fa}	Sigma multiplier fot he false alarm probability	
MDE	Minimum detectable error	m
$\sigma_{\mathrm{monitor}}$	Standard deviation for the monitor errors under the fault condition for monitoring	m
$\sigma_{\mathrm{nominal}}$	Standard deviation of the range error under nominal case for monitoring	m
T	Monitor threshold	m
TSE	Total system error	m
FTE	Flight technical error	m
NSE	Navigation system error	m
NSE_{v}	Vertical navigation system error	m
$NSE_{\mathrm{v,ff}}$	Vertical navigation system error in fault-free condition	m
σ_{NSE}	Standard deviation of the navigation system error	m
$\sigma_{\mathrm{NSE,v}}$	Standard deviation of the vertical navigation system error	m
σ_{FTE}	Standard deviation of the flight technical error	m
σ_{TSE}	Standard deviation of the technical system error	m
E_{v}	Vertical error	m
E_{l}	Lateral error	m
$E_{\mathrm{v,max}}$	Maximum vertical error	m
E_{r}	Range error	m
$E_{\mathrm{r,max}}$	Maximum range error	m
$P_{UL\|E_{\mathrm{v}}}$	Probability of unsuccessful landing given the vertical error E_{v}	
$P_{UL\|E_{\mathrm{v}}_\mathrm{undetected}}$	Probability that an unsuccessful landing occurs giving the error E_{v} is not detected	
P_{fault}	Fault probability	
E_{IG}	Range error due to an ionospheric gradient	m
Y_{EIG}	Maximum value of the E_{IG}at 0 distance from GBAS reference point	m
M_{EIG}	Slope of the maximum E_{IG} versus distance	m/km

The indexing of the variables respect the measurements nomenclature. In addition, some of the variables are dependent of the GBAS Approach Service Type (GAST) and in this case the notation $\sigma^{n}_{\mathrm{GBAS},D}$ which denotes the standard deviation of the

total GBAS fault-free error for GAST-D for satellite n.

Satellite code biases

Symbol	Description	Unit
T_{gd}	Time group delay	s
scb	Satellite code bias	m
Δscb	Differential satellite code bias between two different receiver configurations	m
$\Delta\mathrm{scb}_{\mathrm{GBAS}}$	GBAS differential satellite code bias between ground and airborne receiver	m
$\Delta\mathrm{scb}_{\mathrm{GBAS,brdg}}$	Broadcast GBAS differential satellite code bias	m

1 Introduction

1.1 Background

Mobility is an essential human need in today's globalized world. Air transport of people and goods is one important element of this factor. Thus, the air transport system plays a vital role for the global economy and society [4, 5].

Different studies [5, 6, 7, 8] predict an increase in the air traffic by 1-2% per year for Western Europe, 2.6% for Southern and Eastern Europe, 5% for Asia and about 1% for the United States. But meanwhile, the air traffic capacity is not growing at the same rate and the air trafic flow management from Eurocontrol shows the airport capacity being one of the major reasons for delays [9, 10].

Single European Sky ATM Research (SESAR) in Europe and Next Generation Air Transportation System (NextGen) in the United States are two major initiatives to make the air transport systems more efficient, predictable and safer [11, 12]. In order to cope with the increasing traffic, new air traffic management methods are being developed. One of the key enablers is the use of Global Navigation Satellite System (GNSS) [13]. GNSS is a cornerstone of the performance based navigation concept and enables airspace users to ensure that their navigation capabilities meet significantly higher levels of performance enabling more efficient use of airspace and aerodrome capacity.

Different levels of integrity, accuracy and availability are required for different phases of flight [13]. The requirements for position errors reach from rather generous error budgets in the order of several nautical miles horizontally with a 95% probability confidence for the en-route phase, down to 10 meters vertical with an integrity risk of just 10^{-7} for precision approaches.

Today different methods (standalone or augmented by different systems) for achieving the required performance are already in use or being developed. Currently, Receiver Autonomous Integrity Monitoring (RAIM) is already performed within the avionics receivers in order to detect and exclude potentially corrupted ranging signals. Augmentation systems include space based (Satellite Based Augmentation System (SBAS)) and ground based (Ground Based Augmentation System (GBAS)) augmentations. In SBAS, corrections and integrity parameters are provided based on a network of ground reference stations spread over a continent. The corrections are provided through geostationary satellites to the user. SBAS is certified as precision approach guidance system for approaches down to a decision height of 200 ft for Wide Area Augmentation System (WAAS) (the United States (US) system) and European

Geostationary Navigation Overlay Service (EGNOS) (the European system) [14, 15]. However, for precision approach guidance under visibility conditions lower than this, local augmentation in form of a GBAS is necessary to meet the stringent performance requirements [13, 16, 17]. The standards to support approaches under all weather conditions were developed and standardized by the end of 2018 [13].

1.2 State of the art

GBAS is a local airport-based system that provides differential corrections and integrity monitoring of GNSS. GBAS provides precision approach service in the vicinity of the airport, serving all runways with one installation. The corrections and integrity parameters are broadcast via a VHF radio data link, termed as Very High Frequency Data Broadcast (VDB).

Stations supporting approaches under Category I (CAT-I) weather condition, the so-called GBAS Approach Service Type C (GAST-C) [18], have been certified and are fully operational [19]. In the last couple of years an increasing number of stations are used on a regular basis for approach guidance in several airports such as Newark Liberty International Airport, Houston, Sydney, Malaga, Frankfurt and Zurich). More information on the available installations are available at [17] and [19]. The so-called GBAS Approach Service Type D (GAST-D) is designed to support Category II (CAT-II)-Category III (CAT-III) operations [18, 19]. While the standards have been published, currently there are no stations or avionics equipment available.

The current GBAS architecture for both GAST-C and GAST-D is based on the use of GPS satellites and single frequency, L1 C/A code only. Several studies have shown that ionospheric anomalies may cause large spatial ionospheric gradients [1, 3, 20]. In order to protect users against these phenomena, different approaches are taken. These mitigation strategies may have a significant impact on the availability of the service. This effect is a major drawback for global deployment of the current GAST-C and GAST-D systems.

For stations supporting CAT-I operations, the GAST-C, it is the sole responsibility of the ground subsystem to ensure the mitigation of the ionospheric errors. The threat mitigation strategy requires the definition of an ionospheric threat model that specifies the largest gradient that can occur in the region of operation [1, 21]. Based on this information, the ground station inflates integrity parameters to ensure that the service will be unavailable at the GBAS user for satellite geometries that would result in an intolerable position error [22]. This inflation leads to a decrease in availability [2, 23].

In GAST-D system, the mitigation strategy is different and the inflation of the integrity parameters is removed. In this case, the ground and airborne systems share the responsibility to ensure that no large differential errors can occur without being detected. The integrity design requires implementation of additional monitors for ionospheric gradient detection in the aircraft receiver and the ground station [24].

These measures have also an impact on the availability of the service [3].

For mid-latitudes that are characterized by relatively small and slowly varying ionospheric gradients the achievable availability is sufficiently high (larger than 99.9%). However, at low and high latitudes the behavior of the ionosphere is different and very large nominal gradients have been observed [1, 2, 20, 3]. Under these conditions the availability is reduced significantly for both service types. In addition, in these regions scintillation events occur very often [25, 26]. The scintillation effect may cause the receiver to lose lock of one or more satellites signals leading to weaker satellite geometries and degraded navigation performance. Taking the aforementioned limitations into account, the global coverage of GAST-C and GAST-D is questionable.

One solution to mitigate the ionospheric problems is the use of signals of two frequency bands and multiple constellations. Using the dispersive characteristic of ionosphere propagation, the linear combination of signals from two frequency bands allows the removal of the ionospheric delay (to a first order) and thus eliminates the ionospheric gradient threat. On the other hand, the use of signals from different constellations provides increased robustness against ionospheric scintillations which would typically only affect one part of the sky and thus few satellites at the same time.

With the launch of 12 Block IIF GPS satellites and the 22 usable satellites of the Galileo constellation (as of end of 2019), signals from a large number of satellites are already available in the L5/E5a frequency band - a second frequency band that is part of the ARNS and which can be used for air navigation. Therefore, the use of dual-frequency dual-constellation algorithms has become a promising solution. Until today there is, however, no clear concept defined on how to use the new signals to provide better performance compared to the current system. Different options for DFDC are under discussion.

1.3 Objectives and research questions

Dual-Frequency Dual-Constellation (DFDC) GBAS is a promising approach for solving the aforementioned drawbacks of GAST-C and GAST-D. However, a new dual-frequency dual-constellation system will have different potential error sources and failure modes which have to be considered and bounded. For this, all performance and integrity assumptions of the existing single frequency GBAS must be carefully reviewed before they can be applied to a DFDC system. A central element for ensuring the integrity of the estimated position solution is the calculation of so-called protection levels which are error bounds to the estimated position. This is done by modeling all disturbances of the navigation signals in a conservative way and then deriving a bound on the resulting positioning errors that is valid at an allocated integrity risk probability.

This work aims at providing essential contributions to the development, stan-

dardization and implementation of a future DFDC GBAS. The new service type shall be able to provide sufficient availability, integrity and continuity to be usable globally. Relevant contributors to the error budget, and thus, to the protection levels are reviewed, characterized and modeled in an appropriate way. While the main contributors are being discussed and investigated, it is beyond the scope of this work to develop a complete integrity concept for DFDC GBAS.

For achieving this objective, the following questions should be answered:

- How can the processing for a future DFDC GBAS look like?
- What changes are required in the DFDC GBAS integrity concept?
- How can the ground multipath error models for the new signals be handled?
- How can the airborne multipath error models for the new signals be established and standardized?
- How do the satellite code biases affect the DFDC GBAS and how can they be accounted for in the integrity budget?
- Which performance can be achieved by the dual-frequency dual-constellation processing modes?

1.4 Outline of work and associated contributions

To achieve the above mentioned objectives and answer the research questions, the thesis is organized into the following main chapters:

After this Introduction, Chapter 2 provides a detailed overview of the existing integrity concept for the single frequency GBAS. First, a short overview of the GBAS fundamental and the existing service types is given. Next, the generation of the ground corrections and the airborne position solutions are described. Then after discussing the error sources and the threats affecting the GBAS, the details of the integrity concepts are given. This includes the calculation of the protection levels and the discussion of the specific monitors implemented for each service type.

Chapter 3 discusses different aspects for the implementation of DFDC GBAS concept. It starts with a general overview of the possible processing modes enabled by the use of dual-frequency dual-constellation signals. Next, it discusses the current constrains for a future systems and narrows down the processing modes to the most promising ones. Based on these selected processing modes, the modification for the ground system and airborne equipment are discussed. Finally, the chapter discusses the modifications to the integrity concept.

The contribution of this chapter is the definition of the required elements for the integrity concept. This includes the need for new ground multipath models, new airborne multipath models and consideration of the satellite code biases in the integrity concept. Each of the aspects are discussed and developed in Chapters 4 to 6.

Chapter 4 evaluates and studies the multipath affecting the GBAS ground sta-

tions. The chapter starts with the methodology used to derive the residual errors due to the ground multipath ($\sigma_{\text{pr_gnd}}$). Next, evaluation of the performance in terms of multipath and noise are discussed. The evaluations are based on measurements from the DLR GBAS test bed. The chapter focuses on the difference between the evaluation of the GPS and Galileo signals.

The major contribution in this chapter is the derivation of single frequency ground multipath models for GPS L5 and Galileo E1 and E5a signals using measurements from the DLR GBAS test bed. The second contribution is the investigation of the applicability of the existing method to the Galileo constellation for which the ground track repeatability is different compared to GPS. The third contribution is the comparison of two different methods used to derive the ground multipath models and discusses the possible difference. The fourth contribution is the investigation of the effect of different smoothing time constant and the receiver parameters on the residual ground multipath error. The final contribution of this chapter is the development of the dual-frequency ground multipath models that differ from combining the single frequency models mentioned earlier.

Chapter 5 is the main focus of this work and includes the development of the airborne multipath models for the new signals broadcast on GPS L5 and Galileo E1 and E5a signals. The chapter starts with an overview of the existing methodology used to derive the multipath error and the improvements and the developed extensions made in this work. Next, each step from the defined methodology is described in detail. One main contributor in the airborne multipath estimation process are the antenna induced errors. A concept for separating the antenna errors from the multipath errors is proposed and described in this chapter. Based on the established methodology, preliminary airborne multipath models are derived using measurements from an experimental installation on DLR's A320 aircraft. The effect of the different factors of influence such as smoothing time constant, receiver parameters, airframe and antenna is also studied.

The first contribution to this chapter is the suggestion of a new improved methodology to derive the airborne multipath models. This includes the separation of the antenna group delay related errors, an improved estimation of the bias introduced by the carrier phases ambiguities and suggestion for overbounding of the estimated values from the measurements in order to account for non-Gaussian distribution and limited number of samples. The next contribution includes the derivation of the preliminary multipath models for GPS L5 and Galileo E1 and E5a using measurements from flight tests conducted on DLR's A320. The final contribution in this chapter is the investigation of different factors of influence to the airborne multipath models including the smoothing time constant, the antenna and the airframe and the receiver parameters. This thesis contributed to the DUFMAN project funded by European Commission which aims at the development and standardization of the airborne multipath models. The methodology and the results derived in this work were presented at a number of standardization group meetings.

Chapter 6 discusses the effect of satellite code biases on DFDC GBAS. First,

the chapter provides a short description of these biases and the existing parameters used to account for them. The existing parameters include the broadcast terms in the satellite navigation messages and offline corrections provided by the International GNSS Service (IGS) analysis centers. They can not be used in the GBAS concept because they neglect the impact of the local receivers configuration and, therefore, cancel out when applying the corrections from the ground system. Another method to estimate the satellite biases relies on measurements from a high gain antenna and provides the code errors for different satellites as a function of receiver correlator spacing and bandwidth. Based on these estimates, an analysis of the GBAS residual code errors introduced by the satellite biases is performed. Next, different proposals of integration of these biases in the integrity concept are discussed. The different concepts propose the calibration of these errors or the integration of a maximum differential range error in the protection levels.

The contributions in this chapter are a first analysis of the impact of the differential satellite code biases on a GBAS user and the first proposal of their inclusion in GBAS integrity concept.

Chapter 7 presents the expected performance for different processing modes for a future DFDC GBAS. The evaluations are based on measurements collected during one flight trial conducted on DLR's A320. The integrity parameters developed in the previous chapters are used as input for the study. First, the chapter includes an evaluation of the position errors obtained for different processing modes during the flight. Next, the performance of the nominal protection levels is assessed. The impact of using different models for the airborne multipath and the ionospheric residual error are shown and discussed.

The contributions of this chapter are the first assessment of the position errors and protection levels for different processing modes using measurements collected in flight test and the impact of using different error models that were discussed in the previous chapter.

Chapter 8 contains the conclusion of this thesis and discusses the significance of this work in the GBAS context. It concludes with recommendations for further research.

2 Current single frequency GBAS

This chapter provides an overview of GBAS and describes the architecture and integrity concept of the existing single frequency system. The scope of the chapter is to set the background and framework and to identify what is needed in the development of the DFDC GBAS. Thus, the contribution focuses on a detailed and updated review of the current system and integrity concept, without providing any technical change or recommendations.

2.1 Fundamentals of GBAS and Approach Service Types

GBAS is a local, airport-based system that has been developed from the differential GPS concept. The system broadcasts differential corrections for pseudorange measurements and in addition provides real time integrity parameters. The system consists of three elements:

1. The satellite system which provides the ranging signals. The current GBAS is based only on the use of GPS C/A signals on the L1 frequency band.

2. The ground subsystem which provides the pseudorange corrections for the satellite measurements. The system includes four (or more) reference receivers and antennas installed in a carefully surveyed location inside the area of an airport. The antennas are separated by a distance large enough to avoid correlation of the multipath. Furthermore, the antennas are designed to minimize the multipath errors at each reference receiver [27]. This is important because these errors are not correlated with the GBAS user errors and are not removed through differential corrections. A master control facility located near the reference receivers gathers all the measurements and computes the pseudorange corrections and the integrity parameters. Several monitors are implemented in the control facility to ensure the safe use of the measurements from the satellites as will be discussed further in this chapter. The corrections together with the integrity parameters are packed in different message types and sent via Very High Frequency Data Broadcast (VDB) transmitter located also on the airport area.

3. The airborne subsystem which uses the GPS signals and the ground pseudorange corrections to compute a differentially corrected position solution. Based on the calculated position solution, the airborne subsystem outputs the deviations relative to the approach path. The outputs are defined in ILS-like deviations in order to be compatible with the current approach guidance system.

In contrast with the conventional Instrument Landing System (ILS) in use today, GBAS can provide approach guidance to multiple runway ends at an airport with only one system. It can, therefore, significantly reduce the required amount of infrastructure at an airport and the associated costs [16, 17]. Furthermore, GBAS requires less flight inspection and was shown to provide much steadier approach guidance signal compared to ILS [28].

According to the current standards [13], the GBAS coverage is specified by two parameters that are defined by the service provider and broadcast by the ground system in the GBAS message: the Approach Service Volume (ASV) and the Maximum Use Distance (Dmax). The ASV represents the region where the system provides service and integrity according to the standards and is defined depending upon the operational requirements and runway or airport. Dmax refers to the maximum distance from the GBAS reference point to the airplane where pseudorange corrections can be applied, but without ensuring integrity (ASV). The two values are introduced to allow the use of service at larger distances. The values of Dmax is defined by the service provider. Initially, the maximum use distance for the service was set to 43 km and no service was provided outside this range. However, the pilots start the approach preparation beyond this limit. Thus, introducing the Dmax and ASV concept allows the aircraft to receive and display information before the actual use of the guidance and navigation along the approach and provides a more ILS like operation (e.g. 60 km) [29].

GBAS offers approach service for different categories of precision approach. The different categories refer to different levels of Runway Visibility Range (RVR) and a Decision Height (DH) which represents the minimum altitude to which an aircraft can descend without having visual contact to the runway. Table 2.1 describes the limits on the RVR and DH for the different precision landing categories.

Category	**RVR** [m]	**DH** [m]
CAT-I	550	60
CAT-II	350	30 < DH< 60
CAT-III	350	0 < DH< 30
CAT-IIIa	200	0 < DH< 30
CAT-IIIb	50 < RVR < 200	30 < DH< 60
CAT-IIIc	RVR < 50	0

Table 2.1: Precision landing categories ([30])

Four GAST are currently defined for different levels of performance [13], [18]. In addition to the precision approaches, GBAS supports Approach with Vertical Guidance (APV) operations. The requirements for these services are defined by GBAS Approach Service Type A (GAST-A) and GBAS Approach Service Type B (GAST-B) which refer to the Approach with Vertical Guidance I (APV-I) and Approach with Vertical Guidance II (APV-II), respectively. GAST-C and GAST-D provide precision approach guidance similar to the performance of the ILS. The GAST-A and GAST-B were the initial development of GBAS and are not anymore used. The de-

fined standards for this approach service types are similar to the ones for GAST-C. In this thesis the detailed implementation for the GAST-C and GAST-D will be further discussed and used as a starting point for future DFDC GBAS.

GAST-C supports operations to the CAT-I minima while GAST-D includes further low-level monitoring requirements to support approaches and automatic landings under CAT-III weather conditions. No separate service has been defined to support the CAT-II minima. One way of supporting CAT-II operations is by using the GAST-D service type with the same functions implemented to support the CAT-III. Furthermore, the CAT-II might be supported also by GAST-C stations with additional integration (e.g. use of SBAS). These solution is still under discussion at the time of writing.

GAST-C stations have been certified and are fully operational. In the last couple of years an increasing number of stations are used on a regular basis for approach guidance (e.g. Newark, Houston, Sydney, Malaga, Frankfurt and Zurich) [17]. Standards for GAST-D stations have been published by International Civil Aviation Organization (ICAO) in 2018, but no stations or avionics are yet commercially available as of end of 2019.

2.2 Short discussion on the available documents

There are several applicable standards specifying the different GBAS service types and their architecture and implementation. The main high level requirements are given in the Standards and Recommended Practices (SARPS) in the Annex 10 ("Aeronautical Telecommunications") to the Convention on International Civil Aviation of the International Civil Aviation Organization (ICAO) with the newest version published in 2018 [13]. The SARPS are generally used as basis for certification by all ICAO member states; however, any state may deviate from them in its own national rule-making if it is deemed necessary or practical.

The Radio Technical Commission for Aeronautics (RTCA) and the European Organization for Civil Aviation Equipment (Eurocae) are developing further technical specifications that support manufacturers and users to design, deploy and use equipment in a way compliant with the SARPS and carrying out its intended function. In the case of GBAS there is the RTCA DO-253 document "Minimum Operational Performance Standards (MOPS) for GPS Local Area Augmentation System (LAAS) airborne equipment" [18] that specifies the performance and processing of the airborne GBAS equipment. The interface between the GBAS ground and airborne systems are specified in the DO-246 document, "GNSS-Based Precision Approach Local Area Augmentation System Signal-in-Space Interface Control Document (ICD)" [31]. This document specifies the different message types that are used to transmit the necessary information (corrections, integrity parameters, approach data) from the ground station to the airborne user. The specifications of the GBAS ground station are given in the Eurocae ED-114A "MOPS for Global Navigation Satellite Ground Based Augmentation System Ground Equipment to Support Category I Operations" [32]. A

new version that also specifies the additions necessary to support CAT-II/III operations is currently under development. For the United States, the Federal Aviation Administration (FAA) developed a similar requirement: the "non-fed Specification FAA-E-AJW44-2937A Category I Local Area Augmentation System Ground Facility" [33]. Note that due to the challenging task of proper siting of GBAS reference antennas, the FAA also developed and released a siting order [34]. It has the purpose of ensuring that the reference sites are protected enough so that the generation of the corrections is not significantly affected by any distortions of the measurements e.g. due to multipath effects.

The documents mentioned in this paragraph are the main documents ensuring safe and efficient GBAS operations. Other specifications (e.g. hardware specifications for the airborne antenna equipment in DO-301 [35]) are also applicable and are used in the GBAS context. Table 2.2 contains a list of all the documents used in this chapter. The second column and the third columns contain the title and a short description of the content of the document, while in the fourth column the reference to the document is given. The documents listed will be used as basis for the overview of the current GBAS architecture.

2.3 GBAS Positioning

The GNSS measurements are based on the transit time of a signal from a satellite to the receiver to be localized. The receiver measures the difference between its reception time and the transmission time that is contained in the navigation message broadcast by the satellite. Multiplying the transit time with the speed of light, the receiver computes the so-called pseudorange or code measurements (both names will be used through the thesis).

Since the user clock is not synchronized with the satellite clocks, the pseudoranges are affected by the user and the satellite clock errors. In addition, ephemeris errors, errors introduced by the propagation medium (ionospheric and tropospheric errors) and errors coming from the user side such as multipath, noise and interference sum up in the pseudorange estimation. Additional to the pseudorange measurements, the carrier phase of the signals is measured and available as observables at the output of the receiver. These measurements are very precise, but ambiguous because the total number of cycles between the satellite and the receiver is not known. The equation for the code (pseudorange) and carrier phase measurements for a frequency i, receiver r and satellite n are described by:

$$\rho^n_{r,i} = R^n_r + c \cdot (\delta t_r - \delta t^n) + T^n_r + I^n_{r,i} + e^n_{r,i} + MP^n_{r,i} + \varepsilon^n_{r,i} + B^n_i + B_{r,i} + \xi_{r,i} + \xi^n_i, \tag{2.1}$$

$$\phi^n_{r,i} = R^n_r + c \cdot (\delta t_r - \delta t^n) + T^n_r - I^n_{r,i} + e^n_{r,i} + N^n_{r,i} \cdot \lambda_i + mp^n_{r,i} + \eta^n_{r,i} + \beta^n_i + \beta_{r,i} + \zeta_{r,i} + \zeta^n_i, \tag{2.2}$$

Document	Title	Description	Reference
DO-301	Minimum Operational Performance Standards for GNSS Airborne Active Antenna Equipment for the L1 frequency band	Contains the standards and requirements for the L1 avionics antennas	[35]
DO-253D	Minimum Operational Performance Standards for GPS Local Area Augmentation System airborne equipment	Describes the performance and the processing of the airborne GBAS equipment including the GAST-D updates	[18]
SARPS	Standards and Recommended Practices in Annex 10 — Aeronautical Telecommunications, Volume I — Radio Navigation Aids from July 2018	Specify the high level requirements of the GBAS system and are used as basis for certification. This version includes the changes included for supporting CAT-III operations	[13]
DO-246E	GNSS-Based Precision Approach Local Area Augmentation System Signal-in-Space Interface Control Document	Represents an interface between the ground and the airborne systems and specifies the message types that are used to broadcast the integrity parameters from the ground station to the airborne	[31]
ED-114A	MOPS for Global Navigation Satellite Ground Based Augmentation System Ground Equipment to Support Category I Operations	Contains the specification of the ground system and is developed by Eurocae. This version includes only the standards for GAST-C	[32]
FAA-2937a	non-fed Specification FAA-E-AJW44-2937A Category I Local Area Augmentation System Ground Facility	Specifies the ground requirements in a similar way to the ED-114A and is developed by FAA	[33]
Order 6884.1	Siting Order for Ground Based Augmentation System	Specifies the requirements on the installation and siting of the ground station (e.g. reference GNSS antennas, VDB antenna)	[34]

Table 2.2: Available documents for GBAS used in this thesis

where R_r^n is the geometric range from the receiver r to the satellite n (in m), c the speed of light (in m/s), δt_r the receiver clock bias (in s), δt^s the satellite clock bias (in s), $I_{r,i}^n$ is the ionospheric delay for frequency i (in m), T_r^n is the tropospheric delay (in m), $e_{r,i}^n$ the ephemeris error of the satellite n on the frequency i observed by the receiver r (in m), $N_{r,i}^n$ and λ_i the integer ambiguity (in cycles) and the corresponding wavelength of the frequency i the $MP_{r,i}^n$, $\varepsilon_{r,i}^n$ and $mp_{r,i}^n$, $\eta_{r,i}^n$ represent the multipath and thermal noise errors on the code and carrier phase measurements, respectively (in m), the B_i^n, $B_{r,i}$ represent the satellite and receiver instrumental errors (in m) and β_i^n, $\beta_{r,i}$ represent the carrier-phase receiver and satellite instrumental errors (in m). The $\xi_{r,i}$ and ξ_i^n describe the errors introduced by the satellite and receiver antenna on code measurements on frequency i and the $\zeta_{r,i}$ and ζ_i^n describe the satellite and receiver antenna errors introduced on the carrier phase measurements on frequency i. For simplicity, in this chapter the additional errors introduced by the receiver and transmitter hardware (e.g. instrumental errors or antenna) on code and carrier phase measurements are comprised in the terms $A_{r,i}^n$ and $a_{r,i}^n$ with $A_{r,i}^n = B_i^n + B_{r,i} + \xi_{r,i} + \xi_i^n$ and $a_{r,i}^n = \beta_i^n + \beta_{r,i} + \zeta_{r,i} + \zeta_i^n$

The satellite errors (clock offset, ephemeris, hardware errors) and the atmospheric errors (ionosphere and troposphere) are correlated over short distances and thus can be removed by the the application of the corrections. GBAS is a code-based differential system; the ground system computes the corrections to the code measurements for each satellite visible based on the well known position of the reference receivers and the satellite position broadcast in the navigation message. The GBAS users receive the broadcast information and add the pseudorange correction to their own measurements. With this, the common errors between ground and airborne are removed, providing more accurate positioning.

One of the main sources of errors that are not correlated between ground and airborne receivers are the noise and multipath errors. While many receiver techniques are available to mitigate the multipath, they are not applicable in the aviation application. The high frequency noise and multipath from the pseudorange measurements of the ground and airborne receiver (independently) are removed through carrier-smoothing that makes use of the rate of change of the precise carrier phase measurements [36]. The carrier smoothed code measurements are determined by giving a large weight to the increments of the carrier phase measurements between two epochs and adding it to the previous smoothed pseudorange. The expression of the smoothed pseudoranges at an epoch k is expressed as

$$\overline{\rho}_{r,i}^n(k) = \frac{\Delta T}{\tau} \cdot \rho_{r,i}^n(k) + (1 - \frac{\Delta T}{\tau}) \cdot \left[\overline{\rho}_{r,i}^n(k-1) + \phi_{r,i}^n(k) - \phi_{r,i}^n(k-1)\right], \qquad (2.3)$$

with τ and ΔT being the smoothing time constant and the measurements sampling interval.

As shown in Appendix A, the carrier smoothed pseudorange at epoch k is formed by the Exponential Weighted Moving Average (EWMA) of the previous $k-1$ epochs of the Code Minus Carrier (CMC) series to which the current carrier phase measurement (at epoch k) is added to reconstruct the geometry. Expanding the terms, the

smoothed pseudorange at epoch k can be written as

$$\overline{\rho}^n_{r,i}(k) = R^n_r(k) + c\cdot(\delta t_r(k) - \delta t^n(k)) + e^n_{r,i}(k) + T^n_r(k) + \underbrace{(-I^n_{r,i}(k) + 2\cdot\overline{I}^n_{r,i})(k)}_{I(k)+\Delta I(k)=\overline{I}(k)} + \\ + \underbrace{mp^n_{r,i}(k) + \eta^n_{r,i}(k) + a^n_{r,i}(k)}_{\text{from } \phi^n_{r,i}(k)} + \underbrace{\overline{MP}^n_{r,i}(k) + \overline{\varepsilon}^n_{r,i}(k) + \overline{A}^n_{r,i}(k) + \overline{mp}^n_{r,i}(k) + \overline{\eta}^n_{r,i}(k) + \overline{a}^n_{r,i}(k)}_{\text{from } \overline{CMC}^n_{r,i}(k)}. \tag{2.4}$$

Typically, the multipath and noise errors added by the phase measurements are considered to be negligible, as they are some orders of magnitude lower compared to the multipath and noise code errors. The carrier smoothing is beneficial in reducing the multipath and noise errors if they are not fully correlated over time, but it introduces additional delay on the time-varying error sources such as the ionospheric error ($\overline{I}^n_{r,i} = I^n_{r,i} + \Delta I^n_{r,i}$). Thus, in order to keep the error common between ground and airborne receivers, the algorithm described above is applied on both systems using the same smoothing time constant. After the carrier smoothing process, the pseudorange corrections are computed and broadcast to the aircraft user. The user corrects its measurements and estimates its position. The specific functions of the ground and airborne systems are described further in the next sections.

2.3.1 Ground System. Generation of corrections

Based on the measurements from the reference receivers, the ground system computes carrier-smoothed pseudorange corrections for the satellites in view. Each reference receiver calculates the geometric range based on the precisely known position of the reference antennas and the satellites position computed from the navigation message. The smooth pseudorange corrections (noted PRC_{CSC}) are computed for each receiver m and satellite n from the geometric ranges and the smoothed pseudoranges. This is done by subtracting the smoothed pseudorange and the satellite clock bias (as computed from the navigation message) from the estimated geometric range [32]:

$$PRC_{\text{CSC}}{}^n_m = R^n_m - \overline{\rho}^n_m - c\cdot\delta t^n, \tag{2.5}$$

with R^n_m being the geometric range from the receiver m to the satellite n, $\overline{\rho}^n_m$ the smoothed pseudorange for satellite n calculated by receiver m, δt^n the clock bias for satellite n and c the speed of light. Replacing the $\overline{\rho}^n_m$ with the terms from Eq. (2.3), the $PRC_{\text{CSC}}{}^n_m$ become

$$PRC_{\text{CSC}}{}^n_m = -[c\cdot\delta t_m + T^n_m + \overline{I}^n_m + e^n_m + \overline{MP}^n_m + \overline{\varepsilon}^n_m + \overline{A}^n_m + \overline{mp}^n_m + \overline{\eta}^n_m + \overline{a}^n_m]. \tag{2.6}$$

Note that all the equations in this chapter refer to the measurements from the L1 band at time t. The indexes for the frequency and time are dropped for brevity and are included only if necessary.

The smoothed pseudorange corrections contain the errors that are common between ground and airborne receivers (atmospheric errors, ephemeris errors) and the

errors that are characteristic only for the ground system (noise and multipath errors, hardware errors and the receiver clock error). The largest contribution is the receiver clock bias, which is common to all satellites visible to one reference receiver, but is different for each reference receiver. In order to limit the range of the broadcast pseudorange corrections and to allow a cross comparison between the reference receivers, the receiver clock bias is removed from the corrections. Being common to all satellites in view, the receiver clock bias can be estimated by taking the average over the smoothed pseudorange corrections for a given receiver. The estimated average contains not only the receiver clock bias, but also an average of all common errors between satellites (e.g. atmospheric errors). After this process, the smoothed and clock adjust pseudorange corrections (PRC_{SCA}) for a receiver m and satellite n are obtained and described in [32] as

$$PRC_{\mathrm{SCA}}{}_m^n = PRC_{\mathrm{CSC}}{}_m^n - \sum_{n=1}^{N} w_m^n \cdot PRC_{\mathrm{CSC}}{}_m^n, \tag{2.7}$$

where N represents the total number of satellites visible at receiver m and w_m^n represent the weights for each satellite. Minimum four satellites have to be available at each receiver for computing a smooth and clock adjust correction. No clear definition for the computation of the weights is given in standards [32], only the requirement that $\sum_{n=1}^{N} w_m^n = 1$. Typically equal weights or elevation based weights are used, but it is the decision of the ground manufacturer on the exact implementation. Different implementation chosen will yield to a different projection in the user clock estimation, but does not affect the position solution if the $\sum_{n=1}^{N} w_m^n = 1$ is satisfied. The weighting might be beneficial for example in setting a low contribution to the measurements affected by high multipath errors.

The broadcast candidate correction for each satellite n (PRC_{TX}^n) is computed [32] as the average over the smoothed and clock adjusted corrections from all M receivers for that satellite as

$$PRC_{\mathrm{TX}}^n = \frac{1}{M(n)} \cdot \sum_{m=1}^{M(n)} PRC_{\mathrm{SCA}}{}_m^n, \tag{2.8}$$

with $M(n)$ representing the set of receivers approved for satellite n.

To ensure consistency of the broadcast corrections, the smooth and clock adjust corrections from each reference receiver (PRC_{SCA}) are compared against each other. Potential large differences enable the detection of faults or excessive measurement errors in one receiver. In order to detect these differences, the so-called B-values are computed. For each satellite-receiver pair $(n - m)$ they are determined as the difference between the broadcast candidate corrections for satellite n computed using all the receivers (as described in Eq. (2.8)) and an average over the smoothed and clock adjust correction from all other receivers excluding the receiver m:

$$B_m^n = PRC_{\mathrm{TX}}^n - \frac{1}{M-1} \cdot \sum_{\substack{m'=1 \\ m' \neq m}}^{M} PRC_{\mathrm{SCA}}{}_{m'}^n. \tag{2.9}$$

The summation computes the average correction over $M-1$ receivers except the receiver m. This allows the detection and exclusion of the receiver m if it is faulty. If all B-values are below their threshold, the candidate correction PRC^n_{TX} is approved and transmitted (referred as broadcast smoothed pseudorange corrections). If not, the PRC_{TX} and B-values are recalculated excluding the correction that exceeded the threshold. The process is repeated until all B-values are below their threshold. The exceed limit for the B-values is expressed as [32]:

$$B^n_m \leq \frac{K_B \cdot {\sigma_{\mathrm{pr_gnd}}}^n_m}{M}, \tag{2.10}$$

with K_B being the B-value threshold that should be configured with a permitted value in line with the integrity and continuity allocation for the ground subsystem, ${\sigma_{\mathrm{pr_gnd}}}^n_m$ the residual uncertainty associated with ground multipath and noise error for receiver m and satellite n and M the number of reference receivers.

Note that, under nominal conditions using only single frequency measurements, the B-values are mainly affected by the residual code multipath and noise remained after the carrier-smoothing and the remaining hardware biases (if any). Figure 2.1 and Figure 2.2 shows the broadcast 100 seconds smoothed PRC^n_{TX} values and the 100-second smoothed B^n_m-values (for one reference receiver), respectively. The results are computed using L1 measurements over 24 hours from DLR GBAS test bed. The test bed consists of four reference receivers connected to Leica AR25 antennas. A more detailed description of the test bed is given in Chapter 4. The different lines in both figures represent the PRC^n_{TX} for different satellites The shape of the pseudorange corrections is mainly driven by the ionospheric error. For the B^n_m-values, the absolute values stay below 0.5 m for elevation above 15°. The increase of the values for low elevation is explained by the choke ring antenna gain pattern and design yielding higher noise and multipath for low elevations.

In addition to the broadcast pseudorange corrections and B-values, the ground also provides range rate corrections used to interpolate the smoothed pseudorange corrections over the resulting time difference between the time used to generate the corrections on the ground station and the time of the application of the correction to the airborne measurements. The range rate corrections at a time t for a satellite n are computed as the difference between the current and the previous broadcast smoothed pseudorange correction divided by the time between them (in nominal case 0.5s) [32]:

$$RRC^n_{\mathrm{TX}}(t) = \frac{PRC^n_{\mathrm{TX}}(t) - PRC^n_{\mathrm{TX}}(t-1)}{\Delta T}\Big|_{\Delta T = 0.5s}. \tag{2.11}$$

The measurements in each reference receiver are updated with a minimum 2 Hz rate and the broadcast parameters are computed based on a minimum number of 2 receivers.

2.3.2 Airborne System. Position solution

The airborne subsystem receives the broadcast pseudorange corrections and range rate corrections and applies them to its own smoothed pseudorange measurements.

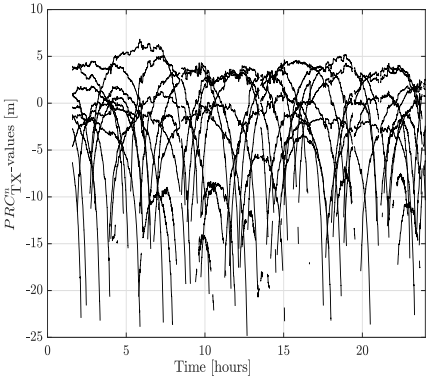


Figure 2.1: Broadcast PRC^n_{TX} for GPS L1 signals for N satellites over 24 hours from DLR GBAS test bed.

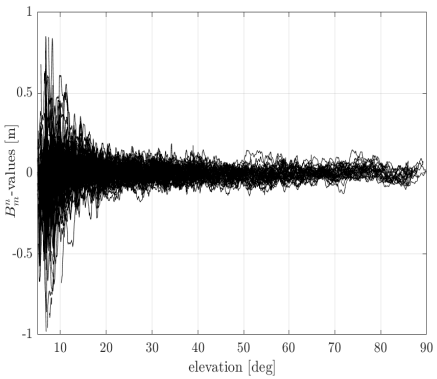


Figure 2.2: B^n_m-values versus satellite elevation from one reference receiver in DLR GBAS test bed

On the airborne measurements, the carrier smoothing algorithm is used with the same parameters (smoothing time constant) as in the ground system to ensure no additional errors are added. The application of the correction at time t (time for epoch k) for a satellite n is described as [18]:

$$\overline{\rho}^n_{\mathrm{air,corr}}(t) = \overline{\rho}^n_{\mathrm{air}}(t) + PRC^n_{\mathrm{TX}}(t_{PRC_{\mathrm{TX}}}) + RRC^n_{\mathrm{TX}}(t - t_{PRC_{\mathrm{TX}}}) + TC^n_{\mathrm{air}}(t) + c \cdot \delta t^n(t), \tag{2.12}$$

where $\overline{\rho}^n_{\mathrm{air}}$ is the airborne smoothed pseudorange for the satellite n, PRC^n_{TX} is the broadcast correction at time $t_{PRC_{\mathrm{TX}}}$, RRC^n_{TX} is the range rate correction broadcast at time $t_{PRC_{\mathrm{TX}}}$, TC^n_{air} is the differential tropospheric correction and the δt^n the clock bias for satellite n computed by the airborne receiver. To ensure the ground and the airborne receivers use the same navigation data, the ground system broadcasts a 16 bit encoded ephemeris Cyclic Redundancy Check (CRC) for each satellite for which a correction is transmitted. The user confirms the match by executing the same algorithm [31]. The $t_{PRC_{\mathrm{TX}}}$ represents the time at which the corrections and the range rate corrections are generated. The temporal variation of the errors during the time delay between the generation of the corrections and their application to the airborne measurements is compensated by the application of the range rate corrections. The user computes the latency time between the current time of application of the corrections and the time when the correction was transmitted by the ground system. It this is within the specified time to alert, the airborne receiver linearly extrapolates the correction rate from the corrections time to its current application time.

The tropospheric error is function of the altitude of the aircraft. As the pseudorange corrections contain the delay with respect to the ground station, a differential tropospheric correction needs to be applied due to the difference in altitude between the ground station and the airborne receiver. The delay correction is computed as

function of the altitude difference between the ground station and aircraft as [18]:

$$TC^n_{\text{air}} = N_R \cdot h_0 \cdot \frac{10^{-6}}{\sqrt{0.002 + \sin^2(\theta^n_{\text{air}})}} \cdot \left(1 - e^{\Delta h / h_0}\right), \tag{2.13}$$

where Δh is the height of the aircraft above the reference station, θ^n_{air} is the elevation of the satellite n computed by the airborne receiver. The parameters N_R and h_0 are the refractivity index and the troposphere scale height which are parameters specific to the ground station and broadcast in the GBAS message. Note that the user is able to use only the satellites for which corrections were broadcast, even if more satellites might be tracked by the airborne receiver (e.g. the receiver on the aircraft might track lower elevations satellites or the ground system might have specific areas masked or excluded satellites in the monitoring). This however, is necessary for the ground station to protect the airborne user from different failures.

Based on the smoothed and corrected pseudorange measurements, the airborne receiver estimates its position (x_{air}, y_{air}, z_{air}) and its receiver clock bias (δt_{air}). The standard position algorithm is (as described in [37]) used to estimate the four states vector $\boldsymbol{X} = [x_{\text{air}}, y_{\text{air}}, z_{\text{air}}, c \cdot \delta t_{\text{air}}]$ for N (at least four) corrected measurements as

$$\boldsymbol{X} = \left(\boldsymbol{G}^{\text{T}} \cdot \boldsymbol{W} \cdot \boldsymbol{G}\right)^{-1} \cdot \boldsymbol{G}^{\text{T}} \cdot \boldsymbol{W} \Delta\rho, \tag{2.14}$$

where $\Delta\rho$ represents the difference between the smoothed corrected airborne measurements and the estimated geometric range computed as the distance between the estimated position at each step and the satellite position ($\Delta\rho = \overline{\rho}^n_{\text{air,corr}} - R^n_{\text{air}}$). $\boldsymbol{G}$ represents the $N \times 4$ geometry matrix containing on the n^{th} row the unit vectors from the user to satellite n as

$$\mathrm{g}_{n:} = \begin{bmatrix} -\cos(\theta^n) \cdot \cos(\psi^n) & -\cos(\theta^n) \cdot \sin(\psi^n) & -\sin(\theta^n) & 1 \end{bmatrix}, \tag{2.15}$$

with θ and ψ being the elevation and the azimuth angles (relative to horizon, in ECEF coordinate system) of the satellite n. The last column of 1 represents the receiver clock offset. $\boldsymbol{W}$-matrix represents the weighting matrix which is used for weighting the satellites according to their expected residual error (e.g. higher weight for the satellites with low residual error expected). The matrix is the inverse of the $N \times N$ diagonal covariance matrix of the differential corrected measurements error and is defined as

$$\boldsymbol{W} = \begin{bmatrix} 1/(\sigma^1_{\text{GBAS},x})^2 & 0 & \dots & 0 \\ 0 & 1/(\sigma^2_{\text{GBAS},x})^2 & \dots & 0 \\ \vdots & \vdots & \vdots & \vdots \\ 0 & 0 & \dots & 1/(\sigma^n_{\text{GBAS},x})^2 \end{bmatrix}, \tag{2.16}$$

where $\sigma^n_{\text{GBAS},x}$ represents the standard deviation of the nominal uncertainty of the residual differentially corrected smoothed pseudorange error for satellite n. The index x refers to the GBAS Approach Service Type (GAST). This standard deviation is the root-sum-square of uncertainties introduced by atmospheric effects (ionosphere,

troposphere) as well as of the contribution of the ground and airborne multipath and noise as (the upper index n is the notation for the satellite and the index x for the GAST used):

$$\sigma^n_{\mathrm{GBAS},x} = \sqrt{(\sigma^n_{\mathrm{iono},x})^2 + (\sigma^n_{\mathrm{tropo}})^2 + (\sigma^n_{\mathrm{pr_gnd},x})^2 + (\sigma^n_{\mathrm{pr_air}})^2}, \tag{2.17}$$

with $\sigma^n_{\mathrm{iono},x}$ representing the bound on the ionospheric residual error for satellite n for the GBAS Approach Service Type (GAST) used (the computation of this bound is dependent on the GAST used), $\sigma^n_{\mathrm{tropo}}$ the bound on the tropospheric residual error for satellite n and $\sigma^n_{\mathrm{pr_gnd},x}$ and $\sigma^n_{\mathrm{pr_air}}$ represent the bound of the ground (computed depending on the used GAST x) and airborne receiver residual noise and multipath after smoothing for satellite n (independent on the GAST used). The general assumption in deriving the weighting matrix is that the nominal measurement errors are uncorrelated between satellites and unbiased. Each of these terms and their definition for different approach types will be discussed in detail in Section 2.5.2. In order to enable the autopilot and the integration with the avionics system, the airborne receiver needs to provide not directly the position estimate, but lateral and vertical deviations. The derivation of the deviations is discussed in the next section.

2.3.3 Computation of deviations

For GBAS, the deviations from the defined reference approach track are calculated ILS-like signals and are based on the aircraft position estimate, called GRP. The necessary reference coordinates describing the localizer plane (for lateral deviation information) and the glide slope cone (for vertical deviations) are transmitted by the ground station in the Final Approach Segment (FAS) data contained in the GBAS Type 4 message. The important parameters contained in FAS data are summarized in Table 2.3 taken from [18, 31]. The Landing Threshold Point (LTP) is the main reference point on the ground and is located in the middle of the runway threshold. This point is the origin of a local level tangent coordinate system defined by unit vectors pointing in the runway direction ($\vec{u}_{\mathrm{rw}}$), in the upward direction of the local tangent ($\vec{u}_{\mathrm{vert}}$) and the lateral vector perpendicular to the previous two ($\vec{u}_{\mathrm{lat}}$).

For the complete definition of the approach geometry four more parameters need to be defined:

- Threshold Crossing Point (TCP) – the point above the LTP at Threshold Crossing Height (TCH) height
- GARP – point on the procedure centerline 305 m beyond the point where the vertical projection of the Flight Path Alignment Point (FPAP) intersects with the extended runway centerline
- Glide Path Intercept Point (GPIP) – the point where the final approach path intersects the local level point
- GERP – point at the GPIP or laterally offset by a fixed value of 150 m

FAS Data	Meaning	Definition
LTP / FTP	Landing Threshold Point / Fictious Threshold Point	(Latitude, Longitude, Height) in WGS-84 [31]
FPAP	Flight Path Alignment Point	(ΔLatitude, ΔLongitude)
TCH	Threshold Crossing Height	Desired height of the FAS at the LTP
GPA	Glide Path Angle	Angle between the glide path and the local-level plane at the LTP
CW	Course Width	Lateral displacement at th LTP
ΔLength Offset		Along Track offset of the end of the runway from the FPAP

Table 2.3: Parameters in FAS data

Lateral deviation: The computation of the lateral deviation is based on the definition of the vertical plane that contains the GARP, the LTP and the TCP. First, the rectilinear lateral deviation is computed as the distance (in m) between the GRP and the localizer plane. The angular ILS-like deviation, α_{lat}, representing the displacement with respect to the GARP is computed next from the rectilinear deviation. It is computed as the angle whose tangent is the ratio between and the horizontal distance between the GRP and GARP. Figure 2.3 shows the geometric situation for the lateral deviation computation and the equations for both the rectilinear and angular deviations are described as

$$\begin{aligned} d_{\text{lat}} &= \vec{u}_{\text{lat}} \cdot (\vec{r}_{\text{GRP}} - \vec{r}_{\text{GARP}}) \\ \alpha_{\text{lat}} &= \tan^{-1}\left[\frac{d_{\text{lat}}}{|\vec{u}_{\text{rw}} \cdot (\vec{r}_{\text{GRP}} - \vec{r}_{\text{GARP}})|}\right], \end{aligned} \tag{2.18}$$

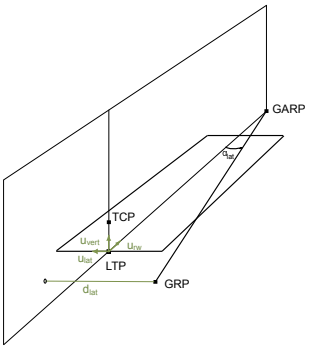


Figure 2.3: Lateral deviation definition

The vectors $\vec{r}$ represent the vectors from the center of the earth to the respective coordinates in an ECEF coordinate system.

Vertical deviation: For this case, initially the angular vertical deviation is computed and this is next transformed to compute the rectilinear vertical deviation. The rectilinear deviation is determined as the distance between the measured GRP and the surface of a vertically oriented cone, with the apex in the GERP and an angle defined by the GPA (θ_{GPA}). Figure 2.4 illustrates the geometrical situation of the vertical deviation calculations and the equations to compute the rectilinear and the angular deviation are computed as

$$\alpha_{\mathrm{vert}} = \tan^{-1} \frac{\vec{u}_{\mathrm{vert}} \cdot (\vec{r}_{\mathrm{GRP}} - \vec{r}_{\mathrm{GERP}})}{\sqrt{\left[\vec{u}_{\mathrm{lat}} \cdot (\vec{r}_{\mathrm{GRP}} - \vec{r}_{\mathrm{GERP}})\right]^2 + \left[\vec{u}_{\mathrm{rw}} \cdot (\vec{r}_{\mathrm{GRP}} - \vec{r}_{\mathrm{GERP}})\right]^2}} - \theta_{\mathrm{GPA}}$$
$$d_{\mathrm{vert}} = \sin(\alpha_{\mathrm{vert}}) \cdot |\vec{r}_{\mathrm{GRP}} - \vec{r}_{\mathrm{GARP}}|\,, \tag{2.19}$$

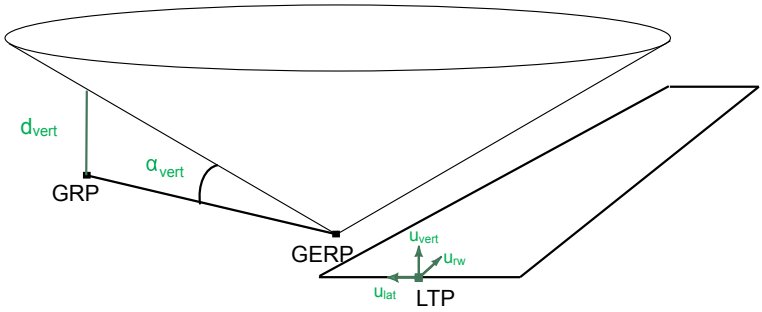


Figure 2.4: Vertical deviation definition

2.4 GBAS Threat Space

The application of the corrections removes most of the errors between the ground stations and the airborne receiver such as the satellite errors or the errors due to the propagation delays. This is done by assuming that under nominal conditions these errors are highly correlated over short distances. The temporal variation of the errors during the delay between the transmission time of the corrections and the application of the corrections at the user can be assumed to be linear and independent. This variation is taken into account using a linear extrapolation model by applying the correction rates as previously discussed in Section 2.3.2. However, faults or anomalies can occur either on the ground reference receiver, on the airborne receiver, or on the satellite. If the errors are occurring simultaneously on the ground station and on the airborne receiver and have the same magnitude, they could be removed by the differential corrections. Otherwise, they can lead to large errors for the GBAS users. Depending on their origin, these faults can be grouped into three categories [38]:

1. Faults within ground station

   This type of faults include failure in one of the reference receivers (hardware or software), failure in the VDB link or anomalous large multipath errors due to e.g. obstacles in the vicinity of the ground station or unexpected interference.

2. Faults in GNSS ranging sources

   These faults include failures within the satellite (hardware or software) or failures in the ground control stations responsible to upload the information to the satellite. The main threats created by these faults are:

   - *Code carrier divergence* which refers to a fault in the satellite that causes the code and the carrier to diverge excessively,
   - *Excessive acceleration* being a fault in the satellite that causes the carrier phase and the code to accelerate excessively,
   - *Ephemeris error threat* refers to a fault in the broadcast ephemeris parameters which can lead to large satellite position errors,
   - *Signal deformation threat* is a fault in the satellites that causes the code signal to be distorted. The actual distortion depends on the receiver parameters (bandwidth, correlator spacing) and thus affects different the ground and airborne measurements,
   - *Low power threat* is a fault in the satellite which leads to transmission of the signals with power below the minimum required level.

3. Environmental faults

   These faults are generated by anomalies in the propagation medium (ionosphere, troposphere) and affect differently the signal passing from the satellite to the ground and the airborne receiver. In addition to these faults, large errors can be created by local interference or spoofing of the ground receivers or the user receivers.

GBAS has to consider all the threats and to protect the users against each of them. This constitutes the integrity of the system and is achieved through bounding of the nominal errors and additional monitoring as is discussed in detail in the next section.

2.5 Integrity in GBAS

In civil aviation application, high performance in terms of integrity, accuracy, continuity and availability has to be achieved. The requirements are defined for each service level that provide guidance for the different categories of precision approach (see Section 2.1). Table 2.4 summarizes the requirements for accuracy, integrity and continuity for the different operations and their specific GAST [38].

Oper. type	GAST	Accuracy		Integrity				Continuity
		Lat.	Vert.	Integrity Risk	TTA	LAL	VAL	Probability
APV-I	GAST-A	16 m	20 m	$2 \cdot 10^{-7}$ in any approach	10 s	40 m	50 m	$1 - 8 \cdot 10^{-6}$ per 15 s
APV-II	GAST-B	16 m	8 m	$2 \cdot 10^{-7}$ in any approach	6 s	40 m	20 m	$1 - 8 \cdot 10^{-6}$ per 15 s
CAT-I / CAT-II	GAST-C	16 m	4 m	$2 \cdot 10^{-7}$ in any approach	6 s	40 m	10 m	$1 - 8 \cdot 10^{-6}$ per 15 s
CAT-III	GAST-D	5 m	2.9 m	$1 \cdot 10^{-9}$/ in any approach	2 s	17 m	10 m	$1 - 8 \cdot 10^{-6}$ per 15 s

Table 2.4: Performance requirements

The accuracy refers to the difference between the estimated and true position. The requirement is expressed as the 95^{th} percentile of the Navigation System Error (NSE).

The continuity refers to the capability of a system to offer navigation service without interruption during an ongoing operation and is expressed as a probability. For GBAS the "continuity exposure time is a minimum of 15 seconds, based on the time interval between 200 ft and 50 ft altitude" [38].

Integrity is a measure of trust put in the correctness of the position estimates and the capability of the system to warn the user in case the system should not be used. It is defined through three quantitative elements: integrity risk, alert limits, time to alert. The integrity risk refers to the probability that the integrity is lost during an approach. The alert limits represent the maximum position errors which can be accepted in the lateral and vertical domain. The time to alert refers to the times elapsed from the onset of an error until the system provides an appropriate alert or removes the erroneous measurements from the position solution. The integrity exposure in GBAS applies in "any one landing, which is a minimum of 15 seconds, based on the time interval between 200 ft and 50 ft altitude. If the operation includes lateral guidance through roll-out, the exposure time can be 30 seconds for lateral" (see Figure D-1 from [38]).

The availability refers to the percentage of time that the system is available and usable, meaning that the accuracy, continuity and integrity are met. The requirements are not included in the table as they may differ between airports.

Figure 2.5 shows the relations between the performance requirements. The accuracy of the system (the position accuracy) has a direct impact on the models needed for integrity. The integrity is provided through nominal bounds and monitors in order to protect the users from any threat. However, sometimes the defined monitoring scheme needed to cover a specific threat could increase the probability of the system to become unavailable (by often monitor triggers), decreasing the continuity and implicitly, the availability. Thus, one of the most challenging tasks is to tradeoff the integrity versus availability in order to be able to design a robust and safe system that meets all the requirements. The general concept to ensure integrity in GBAS against all possible threats is described in the following and detailed implementations of the different service types are presented as well.

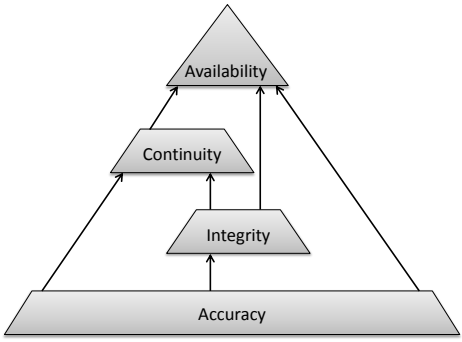


Figure 2.5: Relationship between performance parameters

Depending on their occurrence, the possible errors affecting GBAS positioning can be separated in small errors that occur very often, large errors with low probability of occurrence or faults and events that occur with a very low probability. The integrity for all faults is achieved through one of the three elements with their relation shown in Figure 2.6:

- Protection levels in the position domain which bound the impact of the small errors which occur with a high probability and are not easily detected in short time (nominal case),
- Monitoring which eliminates the large errors with a low probability of occurrence (fault case) that can lead to hazardous positioning errors,
- Bound on the probability of events with very low probability of occurrence. This is achieved by defining the integrity risk requirements and any errors that occur with a probability lower than the integrity risk do not have to be taken into account.

2.5.1 Protection levels in GBAS

Protection levels are bounds of the expected user errors (after the application of corrections) specified at very low probabilities ($2 \cdot 10^{-7}$) as required by the integrity risk allocated to them. The protection levels are computed by the airborne receiver using the differential residual uncertainty (σ_{GBAS}). The range error models are projected into the position solution using the current geometry available at the user. The Lateral Protection Level (LPL) bounds the lateral position error and the Vertical Protection Level (VPL) defines the bound for the vertical position error. The protection levels are unique for each user as they depend on the current satellite geometry and the specific pseudorange error models.

In GBAS, multiple protection levels are defined for each user: one for the nominal case and several protection levels for different fault conditions. Since it is not known

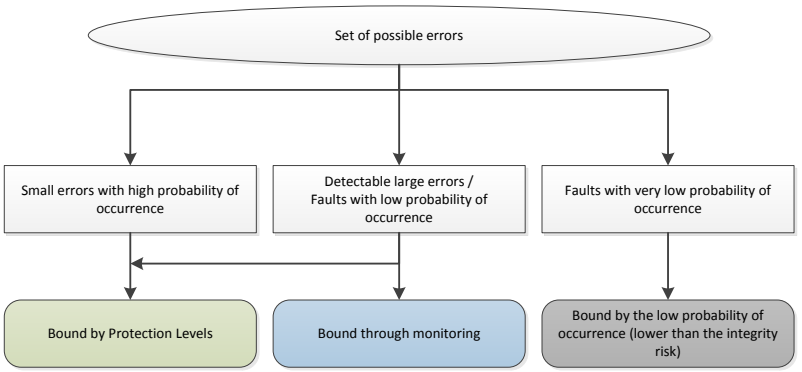


Figure 2.6: Error handling in GNSS

which case is true, the final protection level is computed as the maximum of over all of them. The integrity is ensured by comparing the final values with the corresponding safe error limits, so-called Alert Limits (ALs). In case any protection level exceeds the alert limit the system becomes unavailable.

The first protection levels discussed are the ones for the nominal case (referred as VPL_{H_0} and LPL_{H_0}). The nominal error components that affect the pseudorange after the application of the correction include the ground noise and multipath on the reference receivers, the ionospheric and tropospheric residuals and the airborne receiver noise and multipath. Each of these error components is modeled as a zero-mean Gaussian distribution that bounds the true distribution of the specific error. While this might not be possible for all nominal errors, gaussian overbounding techniques are applied to bound the observed range errors (e.g. multipath errors) [39, 40]. Based on these defined models, the total standard deviation of the differential corrected range error for the used GBAS Approach Service Type (GAST) ($\sigma_{\mathrm{GBAS},x}$) is computed as the root-sum-square of the variance of the components (see Eq. (2.17)). Using the bounds on the pseudorange errors, the nominal protection levels for a specific GAST x for the vertical and lateral position component are defined in [18] as

$$\begin{aligned} LPL_{\mathrm{H}_0 x} &= k_{\mathrm{ffmd}} \cdot \sqrt{\sum_{n=1}^{N} (s^n_{\mathrm{apr_lat}})^2 \cdot (\sigma^n_{\mathrm{GBAS},x})^2} + D_{\mathrm{l}}, \\ VPL_{\mathrm{H}_0 x} &= k_{\mathrm{ffmd}} \cdot \sqrt{\sum_{n=1}^{N} (s^n_{\mathrm{apr_vert}})^2 \cdot (\sigma^n_{\mathrm{GBAS},x})^2} + D_{\mathrm{v}}, \end{aligned} \tag{2.20}$$

where k_{ffmd} is a scalar factor that represents the required integrity risk under the fault-free (H_0) scenario, $s^n_{\mathrm{apr_lat}}$ and $s^n_{\mathrm{apr_vert}}$ represent lateral and vertical component

for a satellite n from the $\boldsymbol{S}$-matrix and are computed as

$$\begin{aligned} s^n_{\text{apr_lat}} &= \text{s}_{2n} \\ s^n_{\text{apr_vert}} &= \text{s}_{3n} + \text{s}_{1n} \cdot \tan(\theta_{\text{GPA}}), \end{aligned} \tag{2.21}$$

with θ_{GPA} being the glide path angle. The $\boldsymbol{S}$ matrix is the weighted pseudo-inverse of the geometry matrix $\boldsymbol{G}$ defined as

$$\boldsymbol{S} = \left(\boldsymbol{G}^{\text{T}}\boldsymbol{W}\boldsymbol{G}\right)^{-1}\boldsymbol{G}^{\text{T}}\boldsymbol{W}, \tag{2.22}$$

The D_{l} and D_{v} terms represent the difference in lateral and, respectively vertical position between 30 seconds smoothed and 100 second smoothed position solution. In GAST-C, only 100 seconds smoothing is used both on ground system and airborne system, while in GAST-D, the position solution is computed based on 30 seconds smoothing, but the integrity monitoring is still based on 100 seconds. The derivation of the error terms contained in $\sigma_{\text{GBAS},x}$ is shown in Section 2.5.2 and further details on the broadcast values for GAST-C and GAST-D are given in Sections 2.6 and 2.7, respectively.

Under a specific fault condition, the errors are not anymore zero mean, but contain a bias. Thus, the protection levels under this case are defined as the sum of the nominal error distribution from the fault-free measurements and the bias due to the faulted condition. A general form of the vertical protection level under a fault condition is defined as

$$VPL_f = |E_{\text{vert},f}| + k_{\text{md}} \cdot \sqrt{\sum_{n=1}^{N}(s^n_{\text{apr_vert}})^2 \cdot (\sigma^n_{\text{vert},f})^2}, \tag{2.23}$$

where $E_{\text{vert},f}$ represents the largest error projected in the vertical position domain due to the failure condition, k_{md} is the scalar multiplier for the missed detection probability for the fault integrity risk (which can incorporate also an apriori probability). For a given probability of missed detection requirement (P_{md}), the k_{md} factor is computed as

$$k_{\text{md}} = -\Phi^{-1}(0.5 \cdot P_{\text{md}}) = -\sqrt{2} \cdot \text{erf}^{-1}(P_{\text{md}} - 1). \tag{2.24}$$

Two failure types have defined protection levels in the current GBAS architecture: a failure in a single reference receiver and a failure in the satellite ephemeris.

The single receiver failure case is referred to as the H_1 case and the protection levels are defined as the sum of the nominal error distribution and the bias introduced by the faulty receiver m:

$$\begin{aligned} LPL_{\text{H}_1\,m} &= |B_{\text{apr_lat}_m}| + k_{\text{md}} \cdot \sigma_{\text{apr_lat_H}_1,x} + D_{\text{l}}, \\ VPL_{\text{H}_1\,m} &= |B_{\text{apr_vert}_m}| + k_{\text{md}} \cdot \sigma_{\text{apr_vert_H}_1,x} + D_{\text{v}}, \end{aligned} \tag{2.25}$$

with k_{md} being the scalar multiplier for the missed detection probability given that the ground system is faulty. Again, the D_{l} and D_{v} terms are the specific GAST-D

terms (set to 0 for GAST-C), as previously explained. The $B_{\text{apr_lat}_m}$ and $B_{\text{apr_vert}_m}$ represent the projection into the lateral and vertical position domain of the largest bias due to a failure in receiver m. The range domain errors due to a failure in a receiver m are accounted for in the broadcast B_m-values. Using the current geometry, the users can compute the maximum B-values contribution in the lateral and vertical domain for each receiver m as

$$\begin{aligned} B_{\text{apr_lat}_m} &= \sum_{n=1}^{N} s^n_{\text{apr_lat}} \cdot B^n_m, \\ B_{\text{apr_vert}_m} &= \sum_{n=1}^{N} s^n_{\text{apr_vert}} \cdot B^n_m, \end{aligned} \tag{2.26}$$

with $s^n_{\text{apr_lat}}$ and $s^n_{\text{apr_vert}}$ computed as in described in Eq. (2.21). The $\sigma_{\text{apr_lat_H}_1,x}$ and $\sigma_{\text{apr_vert_H}_1,x}$ for each satellite n are converted into the position domain in a similar manner as the nominal case

$$\begin{aligned} \left(\sigma_{\text{apr_lat_H}_1,x}\right)^2 &= \sum_{i=1}^{N} \left(s^n_{\text{apr_lat}}\right)^2 \cdot \left(\sigma^n_{\text{H}_1,x}\right)^2, \\ \left(\sigma_{\text{apr_vert_H}_1,x}\right)^2 &= \sum_{i=1}^{N} \left(s^n_{\text{apr_vert}}\right)^2 \cdot \left(\sigma^n_{\text{H}_1,x}\right)^2, \end{aligned} \tag{2.27}$$

with the $\sigma_{\text{H}_1,x}$ being the range domain overbound of the H_1 case. The value of this sigma is different than the value of the $\sigma_{\text{GBAS},x}$ because in this case one receiver less contributes to the total error distribution. It is defined as

$$\left(\sigma^n_{\text{H}_1,x}\right)^2 = \left(\sigma^n_{\text{iono},x}\right)^2 + \left(\sigma^n_{\text{tropo}}\right)^2 + \frac{M[n]}{M[n]-1} \cdot \left(\sigma^n_{\text{pr_gnd},x}\right)^2 + \left(\sigma^n_{\text{pr_air}}\right)^2, \tag{2.28}$$

with $M[n]$ being the number of receivers used to compute the corrections for satellite n.

The H_1 protection levels are computed for each receiver m and the maximum value over all reference receiver is taken. This is necessary as the actual faulty receiver is not known, and thus taking the maximum covers all the cases.

The second specific failure covered by its own protection level is the ephemeris error. The ground station includes an ephemeris monitor and broadcasts to the airborne the smallest error that is assured to be detected by the ground monitoring with a required probability (referred as P_x) [41]. However, the airborne user remains vulnerable to the errors smaller or equal to the ground ephemeris monitor threshold and these need to be covered by the ephemeris protection level. The lateral and vertical protection levels are thus computed for each satellite n as the sum of the bias

due to the ephemeris fault in the satellite n and the nominal error distribution as

$$\begin{aligned} LPB^n &= |s^n_{\text{apr_lat}}| \cdot x_{\text{air}} \cdot P^n_x + k_{\text{md_e},x} \cdot \sqrt{\sum_{n=1}^{N} (s^n_{\text{apr_lat}})^2 \cdot (\sigma^n_{\text{GBAS}})^2} + D_{\text{l}}, \\ VPB^n &= |s^n_{\text{apr_vert}}| \cdot x_{\text{air}} \cdot P^n_x + k_{\text{md_e},x} \cdot \sqrt{\sum_{n=1}^{N} (s^n_{\text{apr_vert}})^2 \cdot (\sigma^n_{\text{GBAS}})^2} + D_{\text{v}}, \end{aligned} \tag{2.29}$$

where $k_{\text{md_e},x}$ represents the service type dependent scalar multiplier for the missed detection probability needed to cover the ephemeris faults (broadcast by the ground). P^n_x is the ephemeris decorrelation parameter broadcast by the ground station. This value is computed by the ground station for each satellite n from the minimum detectable error MDE_{eph} as $P^n = \text{MDE}^n_{\text{eph}}/R^n$. R^n represents the minimum predicted geometric range from the reference receivers to the satellite n for the period of validity of P^n_x. The multiplication with the horizontal distance between the reference station and the user (x_{air}) is applied to account for the linear decorrelation of these errors with the distance. $s_{\text{apr_lat}}$, $s_{\text{apr_vert}}$ and σ_{GBAS} are the same as in the nominal case. After the protection levels for each satellite are computed, the maximum between them is selected as the vertical and lateral ephemeris protection level.

The other failures that occur with a high probability and do not have specific protection levels, have to be covered by one of these three previously defined. As the last two protection levels are very specific, the nominal (H_0) protection levels are responsible to bound all additional errors. Furthermore, specific large failures with low probabilities (e.g. ionospheric errors in GAST-C) are also bounded by the H_0 protection levels. Otherwise, an integrity monitor is responsible to bound the large failures. The concept of the monitoring in GBAS will be briefly introduced after the description of the nominal error models.

The main factor that contributes to the protection levels is the residual uncertainty of the differential errors which is described in the next section.

2.5.2 Error models

As defined previously, the standard deviation of the residual uncertainty of the the differential GBAS error (σ_{GBAS}) consist of the root sum square of the different uncertainties that contribute to the nominal error. The nominal error components include [13]:

- Ground subsystem contribution which is represented by $\sigma_{\text{pr_gnd}}$ and includes the reference receiver noise, multipath and hardware errors (e.g. error in the receiver antenna),
- Airborne receiver noise and multipath due to the airframe which is represented by $\sigma_{\text{pr_air}}$,

- Residual tropospheric error due to the altitude difference between the ground station and aircraft. This error is characterized by zero mean and its variance is accounted in the σ_{tropo} parameter broadcast by the ground station,
- Residual ionospheric error present due decorrelation of the ionosphere with the distance between the ground station and aircraft. An ionospheric parameter (σ_{vig}) broadcast by the ground bounds this effect in the nominal case.

2.5.2.1 Model of ground multipath and receiver noise

The ground system is responsible to broadcast the residual uncertainty of the ground noise and multipath ($\sigma_{\text{pr_gnd},x}$) for each satellite and each service type and processing mode. These values are derived apriori based on the respective B-value measurements from the ground receivers over minimum 24-hours and thus represent the actual multipath and noise characteristics. The 24-hours time for the data collection is chosen because the GPS satellites ground tracks repeat each sidereal day (23 hours, 56 minutes, 4.0916 seconds) and ensures all combination of elevation and azimuths are captured in the model derivation. The values estimated from the measurements using the methodology described in Chapter 4 are compared with the standard error models. These models are refer as Ground Accuracy Designator (GAD) models and have been derived to reflect different performance levels of GPS receiver technologies.

Three models have been defined for GPS L1 for the ground subsystem contributions using different types of antennas and receivers: GAD-A, GAD-B and GAD-C [42]. The GAD-C curve represents the model for the typical GBAS ground station that uses Multipath Limiting Antenna (MLA) and a narrow correlator receiver, while the GAD-B model represents the performances that can be achieved with advanced receiver technologies similar to GAD-C, but using conventional antennas instead of MLA. The GAD-A represents a level of performance that can be achieved with low-cost installations. The model is described as

$$\sigma_{\text{pr_gnd}}(\theta^n) = \sqrt{\frac{\left(a_0 + a_1 \cdot e^{-\theta^n/\theta_0}\right)^2}{M} + (a_2)^2}, \tag{2.30}$$

where M represents the number of receivers, θ^n the elevation of the satellite n. The parameters a_0, a_1, a_2 and θ_0 which depend on the ground accuracy designator type are defined in Table 2.5. Figure 2.7 shows the models as function of satellite angle. The models are defined for M=4.

GAD	**Elevation** [°]	$\mathbf{a_0}$ **[m]**	$\mathbf{a_1}$ **[m]**	$\mathbf{a_2}$ **[m]**	θ_0 [°]
GAD-A	≥ 5	0.5	1.65	0.08	14.3
GAD-B	≥ 5	0.16	1.07	0.08	15.5
GAD-C	≥ 35	0.15	0.84	0.04	15.5
	5 to 35	0.24	0	0.04	-

Table 2.5: Parameters for ground accuracy models

These models are used to classify the ground station and to define a maximum bound on the $\sigma_{\text{pr_gnd},x}$ values needed to detect anomalies on the ground stations.

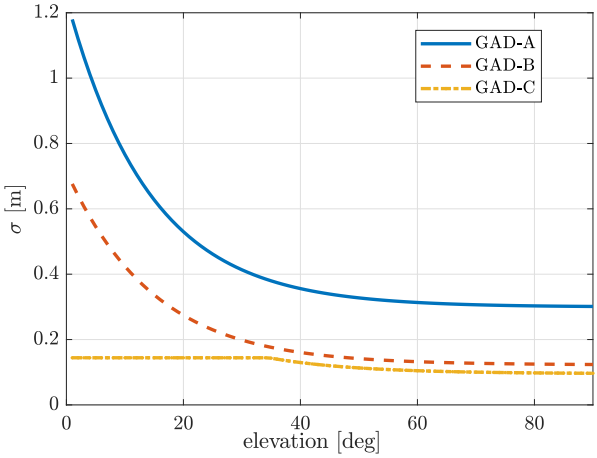


Figure 2.7: Ground accuracy models versus elevation angle

However, the ground subsystem broadcasts to the airborne the measurement-based values. Depending on the service type, these values might be inflated to account for other errors that need to be covered by the protection levels (e.g. ionospheric anomalies in GAST-C as described in Section 2.6.2), thus different values are broadcast for GAST-C and GAST-D. Furthermore, the GAST-D ground stations provide two types of corrections, based on 100 and 30 seconds smoothing. The shorter smoothing time constant (30 seconds) is introduced in GAST-D to mitigate the ionospheric anomalies (see Section 2.7). Thus two different set of values for $\sigma_{\text{pr_gnd},D}$: $\sigma_{\text{pr_gnd,D,100}}$ and $\sigma_{\text{pr_gnd,D,30}}$ are broadcast. The $\sigma_{\text{pr_gnd,D,30}}$ is used in the weighting in the position solution and the $\sigma_{\text{pr_gnd,D,100}}$ is used in the computation of the protection levels.

2.5.2.2 Model of the airborne multipath and receiver noise

Unlike the ground station, the residual uncertainty attributed to the airborne multipath and noise ($\sigma_{\text{pr_air}}$) is computed based on a standardized error model. The model is designed and applied to all aircraft types in order to avoid individual certification for each installation and each aircraft. In the current GPS L1 MOPS [18], the airborne error model is composed of receiver thermal noise and the multipath models. Both errors are parameterized as Gaussian overbound and the total error distribution is computed function of the satellite elevation as the root-sum-square of the variance of the two components. In addition, the variance of transient deviation of the airborne smoothing filter from the steady state response of the smoothing filter implemented in the ground station is taken into account as

$$\sigma_{\text{pr_air}}(\theta^n) = \sqrt{(\sigma_{\text{n}}(\theta^n))^2 + (\sigma_{\text{mp}}(\theta^n))^2 + (\sigma_{\text{divg}}(\theta^n))^2}, \tag{2.31}$$

where θ^n represents the elevation angle for the satellite n relative to the horizon. The σ_{divg} accounts for smoothing filter deviation. This error is induced in the differentially corrected pseudoranges when the airborne filter is initialized or re-initialized. Standard models for two performance classes of receiver/antenna combinations, called Airborne Accuracy Designator (AAD), provide parameters for the noise and multipath functions, where the multipath model is equal in both cases. They are defined in [18] as

$$\begin{aligned} \sigma_{\text{mp}}(\theta) &= 0.13 + 0.53e^{-\theta/10} \text{ [m]}, \\ \sigma_{\text{n}}(\theta) &= \begin{cases} 0.15 + 0.43e^{-\theta/6.9} \text{ [m] for AAD-A}, \\ 0.11 + 0.13e^{-\theta/6.9} \text{ [m] for AAD-B}. \end{cases} \end{aligned} \tag{2.32}$$

Figure 2.8 shows the multipath model versus elevation together with the two AAD models proposed for the receiver noise.

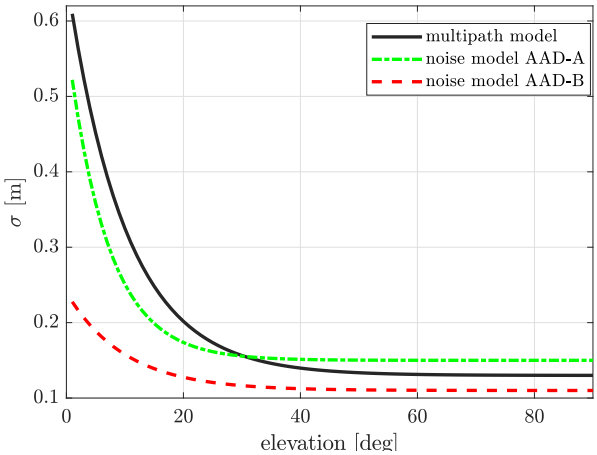


Figure 2.8: Multipath and airborne accuracy models versus elevation angle

The AAD-A represents the performance level achieved with low-cost general aviation equipment and early developed standard receiver or with wide correlator spacing (e.g. 1 chip for L1 band) and the AAD-B reflects the performance achievable with advance receiver technologies with narrow-correlator (e.g. 0.1 chips for L1 band) [42]. These models depend on the signal type and on the receiver parameters such as correlator spacing and are thus not applicable to other signals and modulation than GPS L1 C/A signal with Binary Phase Shift Keying (BPSK)(1) modulation.

2.5.2.3 Model of tropospheric residual uncertainty

The tropospheric error remaining after the application of the ground corrections decorrelates with the height between the aircraft and the reference station. The

standard deviation of the residual tropospheric error represents this tropospheric decorrelation and depends on atmospheric conditions and on the difference in altitude between the aircraft and the ground. The model used for σ_{tropo} is defined as function of elevation and altitude of the aircraft above the GBAS reference station (Δh) as described in [18], Section 2.3.12.2:

$$\sigma_{\text{tropo}} = \sigma_{\text{ref}} \cdot h_0 \cdot \frac{10^{-6}}{\sqrt{0.002 + \sin^2(\theta)}} \cdot (1 - e^{\Delta h / h_0}). \tag{2.33}$$

The parameters σ_{ref} and h_0 depend on the meteorological conditions at each site and the ground station is responsible to broadcast values that are representing the local conditions. An example of an algorithm to determine these values is given in [43].

2.5.2.4 Model of residual ionospheric error

The application of the corrections broadcast by the ground subsystem removes most of the ionospheric error from the user measurements. However, a residual error remains due to the spatial and temporal variation of the ionospheric error. The spatial variation refers to the difference in the observed ionospheric delay at the ground station and at the user due to the spatial separation. The temporal variation refers to the residual ionospheric error introduced during the time difference between the generation of the corrections and the time of the application. Of the two components, the spatial one is the larger one affecting the GBAS users as the distance between the ground reference stations and the aircraft can reach several tens of kilometers. The residual error due to the spatial decorrelation needs thus to be bounded and included in the calculation of the protection levels. This is done by the broadcast parameter $\sigma_{\text{vig},x}$ ($\sigma_{\text{vertical_iono_gradient}}$) which represents the standard deviation of the ionospheric delay variation in vertical (at 90°). The parameter is described based on the vertical delays in order to have a common value for each satellite regardless of its elevation. The conversion to the slant delay is done using a geometric mapping function that approximates the ionosphere with a thin-shell model located at 350 km above the Earth. This term is referred as the obliquity factor and is defined in [18] for a satellite n as

$$F_{pp}^{n} = \left[1 - \left(\frac{R_e \cdot \cos(\theta^n)}{R_e + h_I}\right)^2\right]^{-1/2}, \tag{2.34}$$

where R_e is the radius of the Earth (6371 km), h_I ionospheric shell height (350 km) and θ is the elevation angle of the satellite. The $\sigma_{\text{vig},x}$ parameter depends on the regional nominal ionosphere and has to be investigated for each region/country that intends to use GBAS. In the CONUS region, the typical one sigma variation of the σ_{vig} in nominal days for GPS L1 frequency is around 1 mm/km [44]. A value of 4 mm/km was determined in [45] as a conservative bound for $\sigma_{\text{vig},x}$ to bound nominal days and add margin to cover days with more active ionospheric activity. This value is considered representative for mid-latitudes, but variations in the regions outside the CONUS are expected, thus regional analysis need to be performed. For Germany,

for example, a $\sigma_{\text{vig},x}$ of 2.07 mm/km was derived as a sufficient bound to cover the ionospheric spatial decorrelation in this region [21]. In GAST-C $\sigma_{\text{vig},x}$ value might be inflated to account for large ionospheric gradients, thus ground broadcasts different values for different service types (GAST-C and GAST-D). More details are given later on in Section 2.6.2 and 2.7.3. Using the $\sigma_{\text{vig},x}$ term, the airborne user computes the total residual based on its estimated horizontal distance to the reference station (x_{air}) and the aircraft speed (v_{air}) as

$$\sigma_{\text{iono}} = F_{pp} \cdot \sigma_{\text{vig},x} \cdot (x_{\text{air}} + 2 \cdot \tau \cdot v_{\text{air}}), \tag{2.35}$$

with τ being the smoothing time constant (100 seconds for both GAST-C and GAST-D). As previously mentioned, for GAST-D the protection levels are defined based on the 100 seconds even if the output solution is based on the 30 seconds smoothed position solution. The difference to the shorter smoothing time constant is taken into acocunt through the D_{l} and D_{v} terms. However, the values of $\sigma_{\text{vig},C}$ and $\sigma_{\text{vig},D}$ broadcast by the ground station are different.

2.5.3 Integrity Monitoring

The purpose of the integrity monitors is to detect and exclude failures before they become hazardous to the users. Typically, the monitors are defined as an hypothesis testing (H_0 assumes no error is present and H_1 represents the case when the failure is present); the test observables are compared with a threshold and the failure is considered present if the threshold is exceeded. The thresholds for these monitors have to be high enough to ensure that under the nominal case the continuity requirement is met, meaning that the threshold is rarely violated but low enough to ensure integrity [1].

The monitors are designed with the assumption that the nominal test statistic has a zero mean Gaussian distribution and the faults are modeled by adding a fixed bias to the nominal test statistic. Figure 2.9 shows a graphical illustration of the monitoring and the definition of the nominal and faulty case. The green solid line represent the Probability Distribution Function (PDF) of the nominal error and the blue dashed line represents the PDF of the range errors under the fault condition. In the monitoring, two types of failure can occur: the error is present and is not detected (missed detection),P_{md} and the monitor triggers when no failure occurs (false alarm), P_{fa}. The two areas are represented in the figure with yellow and green, respectively. Based on a given P_{fa}, first a threshold T is derived as

$$\text{T} = k_{\text{fa}} \cdot \sigma_{\text{nominal}}, \tag{2.36}$$

with k_{fa} being the scalar multiplier needed to meet the required P_{fa} derived from the continuity requirement and σ_{nominal} representing the standard deviation of the test statistic under the nominal case. Under the fault case, the PDF is centered at the Minimum Detectable Error (MDE), which represents the error that will be detected by the monitor with a given P_{md} and is defined as [1]

$$\text{MDE} = \text{T} + k_{\text{md}} \cdot \sigma_{\text{nominal}}, \tag{2.37}$$

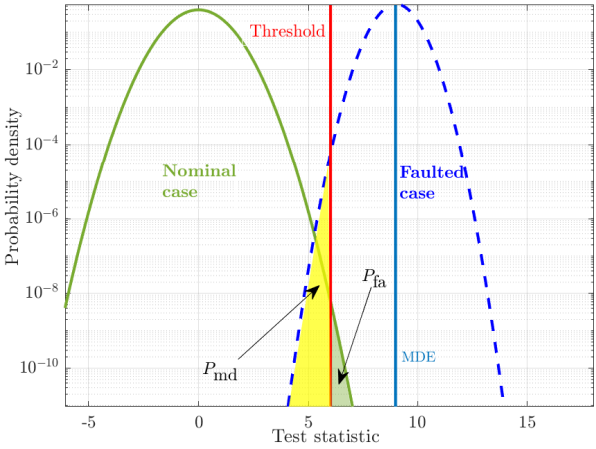


Figure 2.9: Monitoring used in GBAS integrity concept

with k_{md} being the scalar multiplier needed to meet the required P_{md} and the $\sigma_{nominal}$ as defined previously. Using Eq. (2.36) and (2.37), the MDE can be written as

$$MDE = (k_{fa} + k_{md}) \cdot \sigma_{nominal}, \tag{2.38}$$

Defining the P_{md} and P_{fa} is a trade-off between meeting the integrity and continuity requirements. The goal would be to decrease as much as possible the missed detection area which can yield hazardous failures to the user (integrity failure). However, decreasing this area increases the probability of the monitor to trigger, affecting the continuity and the availability of the system. Thus, the values are selected to meet both requirements.

Based on the MDE, the worst-case error in the range domain (maximum error before detection) that can occur at an user can be computed as [1]

$$E_{r,max} = E_{r,MDE} + k_{md} \cdot \sigma_{monitor}, \tag{2.39}$$

where $E_{r,MDE}$ represents the projection of the MDE in the range domain and $\sigma_{monitor}$ the 1-sigma range errors under the fault condition.

On the other side, for a given monitor for which the MDE and $\sigma_{monitor}$ are known, the monitor threshold in the range domain can be derived as

$$E_{r,threshold} = E_{r,MDE} - k_{md} \cdot \sigma_{monitor}. \tag{2.40}$$

From the above derivations, it can be concluded that the design of a monitor depends on

- The Minimum Detectable Error (MDE),

- The missed detection probability, P_{md}, which can take into account also an apriori probability,
- The standard deviation of the range error in the nominal case ($\sigma_{\mathrm{nominal}}$),
- The standard deviation of the range errors under fault case (monitor noise) ($\sigma_{\mathrm{monitor}}$).

This section provided an overview of the integrity in GBAS. The requirement definition and the specific implementation of the integrity concept is different for each service type. The next section discusses the derivation of the requirements and the integrity allocation for GAST-C. The approach considered for GAST-D is quite different from GAST-C adapted to provide the CAT-III service and will be discussed in Section 2.7.

2.6 Integrity in GAST-C

The requirements for GAST-C were derived in an ILS look-alike approach by extrapolating the equivalent NSE from the existing ILS signal-in-space (SiS) performance at a 200 ft height (the DH for CAT-I, see table 2.1).

For ILS, the integrity requirements are only specified for the ground subsystem and no requirements are defined on the aircraft subsystem. This means, that for GAST-C, the ground system is responsible to ensure the integrity to support CAT-I operations. However, compared to ILS, GBAS adds the satellite constellation with its specific failure modes and the effect of the atmosphere (ionosphere, troposphere) on the signal.

The standards for GAST-C are defined in terms of the SiS performance that is to be expected at the output of an airborne fault free receiver. This makes the ground subsystem responsible to broadcast integrity parameters which, when applied by the airborne user, bound the actual error with the given integrity risk. In addition, the ground has to monitor the faults that can lead to hazardous user position error.

Figure 2.10 presents the possible threats and errors (in gray boxes) and their integrity allocation for GAST-C. The diagram indicates that the nominal ranging source errors and the environmental conditions as well as the single reference receiver hardware failures are covered by the protection level (green boxes), while all the other errors due to faults in the ranging sources, ground facility or environment (ionosphere, troposphere, interference) are covered by the ground system integrity (blue boxes).

The total integrity risk budget which is defined to be less than 2×10^{-7} per approach [32] is thus allocated between protection level integrity risk and ground system integrity risk. From the total integrity risk, 25% ($0.5 \cdot 10^{-7}$ per approach) is allocated evenly to the H_0 (fault free) and H_1 (single receiver fault case) protection levels integrity risk. The remaining 75% of the total integrity risk is allocated to the other faults (described in Section 2.4) against which the ground system responsible to provide protection (Ground Subsystem Integrity). This allocation includes the faults

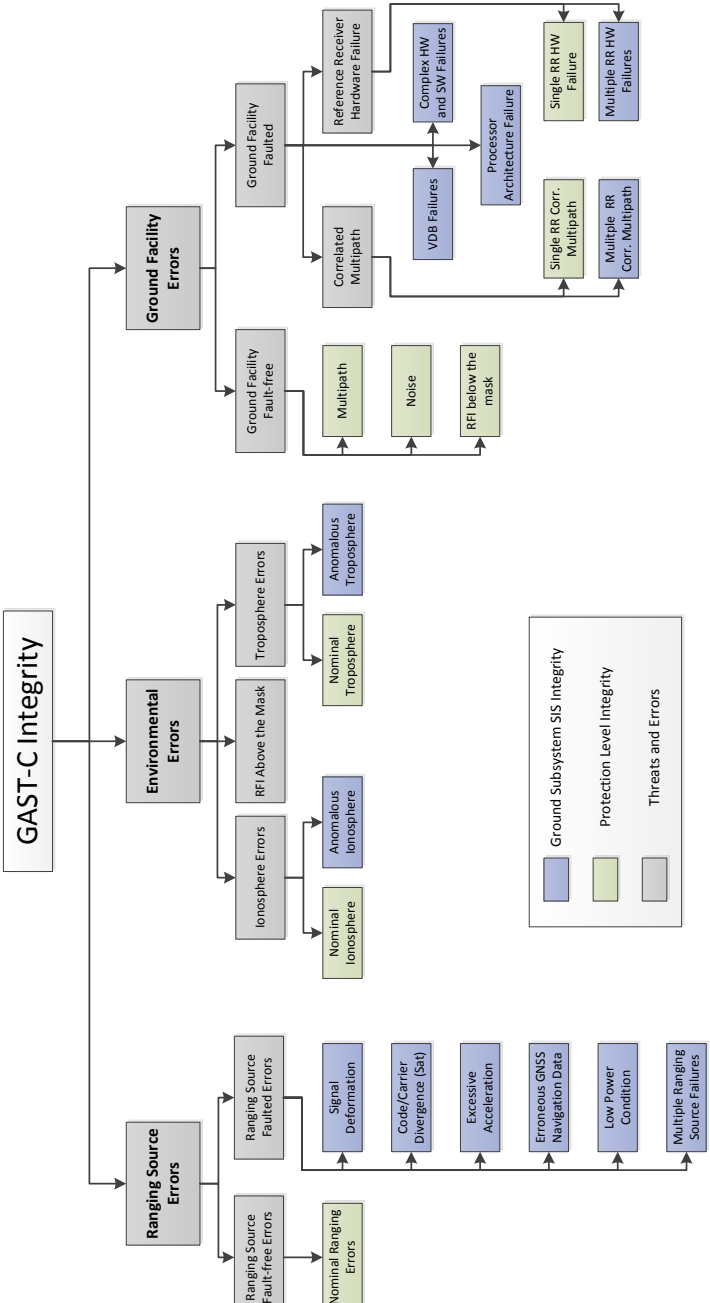


Figure 2.10: Errors and threats as part of integrity concept in GAST-C

in the ranging sources, the ground subsystem failures and the environmental failures. From these faults, only the ephemeris errors have allocated separate protection levels.

2.6.1 Protection levels in GAST-C

The $0.5{\cdot}10^{-7}$integrity risk (per approach) allocated to the protection levels include the H_0 and H_1 cases. The nominal protection levels bound the nominal errors affecting the differential position solution and are computed as described in Eq. (2.20) with D_{l} and D_{v} are set to 0. The scalar factor k_{ffmd} corresponding to the integrity risk allocation for nominal protection levels ($0.25 \cdot 10^{-7}$ per approach) values function of the number of the reference receivers are described in Table 2.6.

Number receivers	2	3	4
Value	5.763	5.810	5.847

Table 2.6: Fault free missed detection multiplier k_{ffmd} [18]

Similar, the H_1 protection levels are computed according to Eq. (2.25) with the values for k_{md} function on the number of receiver available as given in Table 2.7. In this case, the values for k_{md} are lower than the k_{ffmd} values for the fault free case even if the allocation of the integrity risk is made equally. This is because the k_{md} has to cover only the integrity risk given that a single reference receiver fault occurred while the k_{ffmd} has to cover the entire integrity risk under nominal conditions [1]. In other words, the derivation of the H_1 protection levels assumes an apriori probability of failures in reference receivers. The probability of one receiver being faulty is considered to be below 10^{-5} per approach as defined in [32] Section 3.3.4.2.

Number receivers	2	3	4
Value	2.935	2.898	2.878

Table 2.7: Missed detection multiplier k_{md} [18]

The output position solution in GAST-C is computed based on 100 seconds smoothed airborne code measurements and 100 seconds smoothed broadcast pseudo-range correction. Thus, the nominal GAST-C error models are defined to bound the 100 seconds smoothed measurement errors as

- $\sigma_{\mathrm{pr_gnd,C}}$: The GAST-C $\sigma_{\mathrm{pr_gnd}}$ is computed using the methodology described in Section 2.5.2.1 using the 100 second B-values. The broadcast parameter might be inflated to account for rare events and heavy tails of the ground multipath and noise distribution. Additional inflation is done in GAST-C to bound large ionospheric errors as will be further explained in Section 2.6.2,
- $\sigma_{\mathrm{iono},C}$: The residual error due to ionospheric decorrelation is computed using Eq. (2.35) with τ set to 100 seconds. The values broadcast for GAST-C $\sigma_{\mathrm{vig},C}$ is inflated to bound also the anoumalous ionospheric gradients,
- $\sigma_{\mathrm{pr_air}}$: The models defined in Section 2.5.2.2 were derived from 100 seconds measurements and are used to bound the airborne residual error for GAST-C,

- σ_{tropo} computed as described in Eq. (2.33) is function of the satellite and the height difference between the aircraft and the ground reference station.

Additional to the H_0 and H_1 protection levels, the ephemeris protection levels are computed as described in Eq. (2.29) with $\sigma_{\text{GBAS},C}$ being the fault free GAST-C differential error model (described above) and the k_{md} being the scalar corresponding to the allocation of the ephemeris failures. The protection levels are compared with the alert limits which decrease when the aircraft approaches the runway. Based on the error characteristic of the ILS, a minimum Vertical Alert Limit (VAL) of 10 m was established for CAT-I. The minimum LAL is 40 m at 200 ft DH. If any of the protection levels exceed these limits, the service becomes unavailable.

2.6.2 Ground subsystem signal-in-space integrity risk in GAST-C

The ground subsystem SiS integrity risk of $1.5 \times \cdot 10^{-7}$ is allocated to all the other errors that are not covered by the H_0 and H_1 protection levels. From these errors, the ephemeris errors are covered by a protection level, thus a fixed allocation for this fault is done (e.g. $2.3 \cdot 10^{-8}$ [1]). The allocation for all the other faults is not standardized as they do not have protection levels that require a fixed k values. These errors are referred to as H_2 faults and include failures in the ground subsystem. The protection against these failures is done through integrity monitoring. The monitors thresholds and requirements are derived based on the continuity and the specific integrity allocation for each fault.

Table 2.8 summarizes the faults and their specific monitors and the implementation of each monitor is then detailed in the remaining of the section.

Type	Fault	Value
Ranging source errors	Signal deformation	Signal Quality Monitor
	Code/carrier divergence	Code Carrier Divergence monitor
	Excessive acceleration	Excessive acceleration monitor
	Erroneous GNSS navigation data	Ephemeris monitor
	Low power condition	Low power monitor
Environmental errors	Anomalous troposphere	Accounted in $\sigma_{\text{vig},C}$
	Anomalous ionosphere	Ground geometry screening and inflation of the broadcast parameters
Ground Facility Faulted	Multiple reference receivers correlated multipath	Ground mean and sigma monitor
	Multiple reference receivers faulted	Ground mean and sigma monitor

Table 2.8: Faults and monitors in GAST-C

Ground mean and sigma monitor

The nominal models defined for the ground facility errors overbound the error of the pseudorange corrections under the assumption that these errors are zero mean and Gaussian distributed. This is true for the nominal case, but in case any anomaly occurs on the ground (sudden jump in multipath if environmental conditions change, hardware failure that can lead to a large receiver thermal noise error increase) it might affect the mean and the standard deviation of the pseudorange correction errors. Thus, a real time monitoring of the mean and of the standard deviation of the correction error is needed to ensure the true error distribution is bounded by the broadcast parameters.

In [46], Lee proposed two methods for the monitoring of the sigma: the sigma estimation method and the sigma Cumulative Sum (CUSUM) method. The first method computes in real-time an estimation of the standard deviation of the B-values and compares it with a time-dependent threshold which becomes lower as more samples are available. The B-values used as input are normalized by the standard deviation as

$$B_{\text{normalized}} = \frac{B}{\sigma_{\text{B}}} \text{ with } \sigma_{\text{B}} = \frac{\sigma_{\text{pr_gnd}}}{\sqrt{M-1}}, \tag{2.41}$$

with M being the number of receivers and $\sigma_{\text{pr_gnd}}$ represents the values computed based on the GAD models as defined in Table 2.5. These values are compared with a defined threshold, the derivation of which is presented in [46] and measurements that exceed it are removed from the corrections calculation.

The second method derived by Lee in [20] to monitor the sigma is based on CUSUM. This method collects cumulative sums of the squared and normalized B-values and compares them to a threshold which does not vary with time. If the sums accumulate above the threshold, an alert is raised. The cumulative sums are updated every 200 seconds (2 times the smoothing time constant) in order to ensure statistical independence. The details of the implementation of this method are given in Section 2.2 of [46].

In addition to the sigma monitoring, a real-time mean monitoring is required as any non-zero means of the error would affect the protection level calculation. In a similar manner as for the sigma estimation, Lee developed in the same work two methods for the mean monitoring: the mean estimation method and the mean CUSUM. The first method estimates the means of the normalized B-values and compares them with thresholds derived from the normal distribution of the estimated means. The mean CUSUM method is similar with the one described for the sigma monitoring, but the input to the running sums are the normalized B-values. Both methods detect large violations of the mean value almost instantaneously.

However, monitoring the sigma and the mean is not sufficient to guarantee that a zero mean Gaussian distribution with the broadcast sigma overbounds the true error due to the uncertainty in the error distributions. Thus, additional sigma inflation that overbounds the tails of the true error distribution of the corrections has to be

performed. In [47] Lee describes a method for determining the inflation factor of the broadcast $\sigma_{\text{pr_gnd}}$ which covers the limited number of samples, the non-Gaussian distribution of the tails in the true error and other limitation of the existing sigma monitor.

In addition to this, the ground has to monitor the failures in the VDB or any hardware or software failure and ensure a warning is sent when they occur. The exact implementation of these type of monitors is left to the manufacturer.

Ground Code Carrier Divergence Monitor

This monitor is working on the range domain and was originally designed for detection of the satellite failure causing code and carrier to diverge. However, the monitor is also used to detect anomalous large ionospheric gradients (which also cause the code and carrier to diverge) preventing large differential position errors introduced by these gradients.

The monitor is based on two consecutive 1$^{\text{st}}$ order Linear Time Invariant (LTI) filters. The input to the filtering is the time differential of the difference between code and carrier measurements for each satellite n on L1 frequency (in m):

$$d_{\text{z}}^{n}(k) = \frac{|\rho^{n}(k) - \phi^{n}(k)| - |\rho^{n}(k-1) - \phi^{n}(k-1)|}{\Delta t = t_k - t_{k-1}}. \tag{2.42}$$

The time differential removed from the Code Carrier Divergence (CCD) filter any constant or slowly changing bias on code or carrier phase such as the integer ambiguities (affecting the carrier phase measurements) or instrumental delays. Next the two LTI filters for the satellite n are defined as

$$\begin{aligned} Z^{n}(k) &= (1 - \frac{\Delta T}{\tau}) \cdot Z^{n}(k-1) + \frac{\Delta T}{\tau} \cdot d_{\text{z}}^{n}(k)t, \\ D^{n}(k) &= (1 - \frac{\Delta T}{\tau}) \cdot D^{n}(k-1) + \frac{\Delta T}{\tau} \cdot Z^{n}(k), \end{aligned} \tag{2.43}$$

with ΔT being the sampling rate (in s) and the and τ being the filter time constant and k the epoch counter. In GAST-C 100 seconds time constant is used for both filter.

This test statistic D is built for each tracked satellite and compared to a fixed threshold of 0.025 m/s [48]. This threshold was derived from the overbound of the expected ionospheric divergence rate of 0.00399 m/s and a normalized monitor threshold set to meet the continuity requirements ($k_{\text{fa}} = 5.83$). The filtered code measurements noise contributes to the standard deviation of the test statistic. However, its contribution shows to be about 10 times smaller than the nominal ionospheric divergence rate and it is thus neglected.

Any satellite whose test statistic exceeds the threshold is excluded from the processing and can be re-included at a later time, when the test statistic is below the threshold.

Excessive acceleration monitor

The excessive acceleration threat in the range domain is a fault condition of a (GPS) satellite. It is caused by a satellite suddenly moving relative to the expected satellite orbit, for example when performing a maneuver without setting the satellite health flag to false before. This fault causes code and carrier measurements to accelerate excessively, only limited by the properties of the satellite e.g. mass and propulsion.

To detect an event of excessive acceleration, the carrier phase measurements are used because they have the required low noise levels (the noise in the code measurements in some order of magnitudes larger). The low noise level is needed for this monitor because the required detection threshold is quite low (0.188 $\mathrm{m/s^2}$). This allows only an error of 1.41 m to build up within the defined time to alert and a missed detection probability of 10^{-4}. One drawback of using the carrier phase measurement, is that cycle slips can occur, which if undetected, might cause this monitor to trigger. However, as the monitor is performed on the ground station the cycle slips are not expected to occur often due to the strict siting requirements and high performance of the MLA antennas.

The detection itself can be performed comparing the rate of change of the carrier to the threshold of $0.0461 m/s^2$. The estimation of the acceleration at epoch k can be performed for example in the following:

$$a(k) = \frac{\phi(k) - 2 \cdot \phi(k-1) + \phi(k-2)}{\Delta T^2}. \tag{2.44}$$

The estimated $a(k)$ has to be compensated for the effect of the satellite movement so the value can be compared to the threshold. More sophisticated approaches are for example explained in [49].

Ephemeris monitor

In terms of ephemeris failures different types of faults can occur that can be classified as follows:

- Type A failure which refer to wrong broadcast ephemeris after a satellite maneuver. This case is further divided in two subcategories: the A1 faults and the A2 faults. The A1 fault denotes the case when the satellite maneuver is known to the ground facility (the satellite is marked as unhealthy), but erroneous or unchanged ephemeris are broadcast after the maneuver completed. The A2 faults refers to the case when an unintentional maneuver occurs without the awareness of the ground facility (the satellite is still set to healthy). The broadcast ephemeris are thus not valid and lead to a sudden divergence of the satellite position from the expected position.
- Type B faults occur during operation without any satellite maneuver, for example when a new set of ephemeris is uploaded.

As satellite maneuvers in general occur only once or twice per year, for CAT-I approaches in GAST-C Type A2 faults are not covered. Depending on the maneuver an

excessive acceleration event might occur in this case anyway as described in Section 2.6.2. Another general assumption is that only one satellite at a time is affected by an ephemeris failure. The SARPS mention different potential options to mitigate ephemeris threat which include:

- Long baseline in the ground system to optimize the MDE for ephemeris failures,
- The use of SBAS information, as SBAS continuously monitors the ephemeris validity using a wide area network. This approach makes small error detectable and provides optimum performance,
- Delta-V monitoring to detect sudden satellite maneuvers. This case is covered by the excessive acceleration monitoring (see Section 2.6.2),
- Ephemeris data monitoring which allows the detection of erroneous data. One implementation is the Yesterday Ephemeris minus Today Ephemeris (YETE) monitoring. This specifically covers the case when there is already a set of validated ephemeris available for a given satellite whenever a new set is being broadcast (Type B faults). When the satellite newly rises into view of the receiver, the old set of validated ephemeris will be likely from the previous day (thus the name). In case the satellite is already tracked for some time, the new set of ephemeris will be validated with the previous ephemeris. Validation is performed by comparing the satellite position computed by the previous, validated set of ephemeris with the position computed (for the same time) with the new ephemeris. Significant differences indicate an ephemeris fault.

Signal deformation monitor

One potential threat in the ranging sources is signal deformation. This describes the presence of harmful anomalous waveforms leading to unpredictable errors in the correlation loops within the receiver and therefore errors in the estimated ranges. This is particularly harmful when ground and airborne receiver have different characteristics (e.g. bandwidth, tracking loop correlator spacing) and thus observe different ranging errors. Note that carrier phase measurements are not affected by this threat.

Signal deformation monitoring basically checks whether the cross correlation (between the received signal and the local code replica) significantly differs from the nominal shape. This requires the receiver to provide multiple correlator outputs instead of only the prompt output. The Signal Quality Monitor (SQM) described in ED-114A [32] for examples bases on the outputs at ± 0.05, ± 0.075 and ± 0.1 chips. From this outputs different metrics are formed such as

$$\Delta_{\pm d} = \frac{I_{-d} - I_{+d}}{2 \cdot I_p}; R_{\pm d} = \frac{I_{-d} + I_{+d}}{2 \cdot I_p}; R_d = \frac{I_d}{I_p}, \tag{2.45}$$

where d is the offset from the prompt code (in chips), I_{-d}, I_{+d} are the outputs of the d correlator on the I channel, and I_p the output of the I prompt correlator. These metrics are then smoothed using low-pass filters with time constants smaller than the smoothing time constants of the Hatch-filters used for smoothing of the ranges. The

smoothed metrics are finally compared to predefined threshold and any satellite that exceeds it is marked as faulty.

The multipath can have large impact on this monitor because it can lead to deformation of the correlation peak. Deviations caused by multipath can exceed the nominal noise related errors in the test statistics by an order of magnitude which makes a strict siting with low multipath as well as the multipath limiting antennas essential for the SQM performance.

Low power monitor

The low power condition threat refers to a reduction in the satellite transmitted power below the minimum specified performance. As defined in the ED-114A document Section 3.3.4.1 [32], the level of the received RF signal at the output of a 3dBi linearly-polarized antenna should be within the range of -160 dBW to -153dBW for all antenna orientations orthogonal to the direction of propagation. Even if the low power might not cause a direct measurements error, it might indicate an abnormal operation of the ranging source or an environmental effect such as multipath or interference. Thus, the GBAS ground system has to monitor the signals levels and to exclude the satellites for which the power drops below the allowable values within 3 seconds. (Section 5.12.2.2 of [32]).

Radio Frequency Interference (RFI) above mask

A significant threat to GNSS users is RFI. The interference mask as specified in Attachment D of the DO-253D document [18] depends on the signal bandwidth. The requirement at the antenna output is to reject the out-of-band interference and to limit the in-band and near band interference. Even if limited, the in-band and near-band interference can harm the use of the GNSS signals (the equipment could receive interference up to -110.5dBm/MHz level in the frequency range of 1575.42 ± 10MHz).

The in-band and near-band interference can be classified in categories depending on the source and intention of the transmitter. In [50] three categories of the RFI are presented: the malicious interference, the uniformed interference and the accidental interference. The malicious interference represents the RF waveform produced intentionally with the harm the GNSS signal. The uninformed interference results from the waveform that are transmitted at or close to GNSS frequencies but do not aim to harm the GNSS signals. The last category, the accidental interference is a result of an unintentional transmission at GNSS frequency produces typically by a malfunction in the transmitted system. The most frequent is the uninformed interference and it can be created by Personal Privacy Devices (PPD) or by GNSS repeaters ([50],[51]).

Ionospheric anomalies monitoring

Under nominal conditions, the spatial ionospheric decorrelation is bounded by 4 mm/km σ_{vig}. However, during strong ionospheric storms or anomalies which are

characterized by steep gradients in the ionospheric delays over short distances. Under these conditions, the ionospheric error can grow larger than the derived σ_{vig} and threaten the GBAS user. This is because the ground system and the airborne user can experience different ionospheric delays and thus the errors are not canceled directly by the application of the differential correction.

The extremely large ionospheric anomalies were first observed in 2002 by analyzing data from WAAS reference stations [52, 53]. These anomalies produce large position errors and different strategies depending on the service type are used to mitigate the impact of the gradients on the GBAS users.

For GAST-C, the ground is solely responsible for mitigating the impact of the ionospheric gradients. The chosen approach to mitigate the ionospheric threat is to exclude geometries that if used by the airborne user, would lead to unacceptable large errors. This is done by inflating some combinations of the broadcast parameters such as the standard deviation of the ionospheric delay variation in vertical ($\sigma_{\text{vig,C}}$, the broadcast $\sigma_{\text{pr_gnd,C}}$ or the ephemeris decorrelation parameter (P_{C} value). The inflation methodology is done based on the assumption that the worst-case observed gradient is always present. Thus, no additional monitoring is required at the user.

In order to derive the inflation parameters,a model of the possible ionospheric anomalies that could occur is required. Using measurements from CONUS, a simplified threat model describing the dynamics of the ionospheric events was derived. The model provides bounding parameters for the ionospheric activities. The behavior of the ionospheric anomalies outside the model is considered to have negligible probability [41].

The ionospheric front geometry used in this threat model is shown in Figure 2.11. An anomalous ionospheric spatial gradient is modeled as a simplified linear semi-infinite wave front moving with constant speed. The main parameters in the GBAS ionospheric threat model are: the slope of the gradient (g_{iono}) in slant delay, the width of the wedge (w_{iono}), and the forward propagation speed of the ionospheric front relative to a fixed point on the ground (v_{iono}) and the maximum delay (D_{iono}) . The slant ionospheric delay is measured across the path of the satellite pseudorange through the ionosphere and not in the zenith direction. Thus, it is dependent on the satellite elevation.

The methodology employed in the data analysis that produced the current used values in CONUS is described in [54] and the parameters are summarized in Table 2.9.

Parameter		**Value**
Maximum front [mm/km]	Low elevation	375
	Medium elevation	375 + 50(θ - 15)/50
	High elevation	425
Front width [km]		25-200
Front speed [m/s]		0-750
Maximum differential delay [m]		50

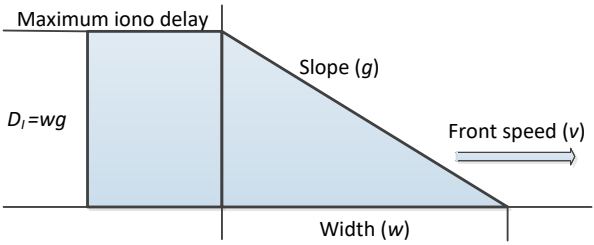


Figure 2.11: Ionospheric threat model

Table 2.9: Parameters of the CONUS Ionopheric threat model

Since the behavior of the ionosphere varies significantly around the world, the model in location dependent. Thus, each region which intends to use GBAS has to confirm that the CONUS model is bounding the actual local gradients or different parameters should be derived. If smaller gradients are discovered a less conservative threat model could be used.

Previous studies published results from the ionospheric threat models for Germany [21], and South Korea [55], which have shown that the gradients observed are lower than the CONUS bound. For these case the CONUS model would bound the observed gradients models, but adds unnecessary conservatism. However, recent studies have shown for low latitudes such as Brazil gradients up to 850.7 mm/km have been observed [2]. This makes the CONUS model not valid for low latitudes as it does not provide a bound for the expected ionospheric gradients.

Part of the large ionospheric gradients that affect the ground station are detected by the ground CCD monitor which is sensitive to temporal changes in the ionospheric delay (Section 2.6.2). The worst case scenarios for a GBAS user are the cases when the gradient is seen almost stationary from the fixed ground station (due to the motion of the satellite) or when the gradient is approaching from behind the aircraft without being visible at the ground station. The first scenarios result in small variations of the ionospheric delay over time and thus would not be detected by the CCD monitor while in the second cases large position errors might built at the aircraft before the gradient impacts the ground station and the CCD monitor triggers.

Thus, the ground station has to take the into account these cases and provide safety under such ionospheric conditions. This is done through an integrity algorithm known as geometry screening that inflates the broadcast VPL parameters. Only the VPL is taken into account as the most stringent requirements are defined for the vertical domain, while due to the satellite geometry the navigation performance is generally worse in the vertical than in the horizontal domain.

The geometry screening algorithm limits the maximum vertical position error

that can be experienced by a GBAS user. Applying the maximum gradients (e.g. 425 mm/km for CONUS) results in very large position errors and, thus, large vertical protection levels, which when compared to a 10 m (minimum VAL value) leads to low availability. Therefore, a relaxed requirement on the maximum Tolerable Error Limit (TEL) on the vertical error produced by an ionospheric anomaly was introduced based the definition on the Obstacle Clearance Surfaces (OCS) for CAT-I precision approaches. A value of about 28 m was derived using the CONUS model and the details of the methodology are presented in [56].

The geometry screening methodology was first proposed in [22] and adapted in [57], [58] and [20]. The main steps of the method are represented in Figure 2.12 and described next.

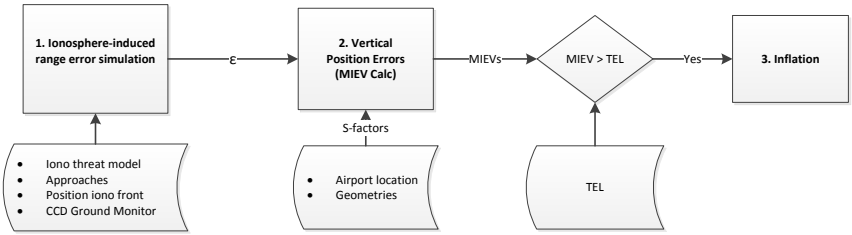


Figure 2.12: Steps for ionosphere mitigation in GAST-C

1. **Ionosphere-induced range error simulation**: The goal of this step is to determine the largest possible error in the vertical user position induced by an ionospheric gradient. The ionospheric-induced range errors are derived through exhaustive simulations which take as input the ionospheric threat model, all possible satellite geometries, user approach geometries and the positions of the ionospheric front. The largest error is limited by the ground CCD monitor, thus the simulations also take into account the detection of this monitor.

   For a given gradient slope and a relative speed between the front and the Ionospheric Pierce Point (IPP) of a satellite, the simulations look for all possible combinations of front widths and positions of the aircraft relative to the front to determine the worst-case differential error. Note that the IPP represents the intersection of the line of sight satellite-receiver and the ionosphere modeled as a thin shell located at 350 km above the Earth's surface. The simulations record the range errors for each setup and include in a look-up table the maximum differential range error (ε) as function of the ionospheric gradient slope (g) and front velocity relative to the IPP. A detailed discussion on the setup of the simulations performed for the CONUS threat model is given in [22].

   Further studies [57, 59] derived closed form equations for ionosphere-induced range errors based on the results of the extensive simulations and a mathemat-

ical model of the CCD monitor. The errors are expressed as a simple linear model function of the relative speed between the projected velocity of the IPP of the satellite and the front velocity. The closed-form equations derived for the acconus threat model are described in [57]. Recent research has shown that even if the closed-form equations are valid for regions where the gradients are below the ones observed in CONUS, the uncertainty of the model for larger gradients as it is the case for the low latitudes cannot be ignored. Thus, in [20] new closed-form expression based on the Brazilian threat model were derived.

2. **Vertical position errors**: Based on the ionospheric-induced range error per satellite ε derived in the previous step, user position errors can be computed considering satellite geometries. Based on a set of N satellites in view, the ground generates all possible subsets of geometries of all in view N satellite down to $N-2$ satellites. This because the airborne user can loose up to 2 satellites from the ones visible at the ground station (e.g due to aircraft maneuvering, filter convergence).

   The position errors are generated assuming that a maximum of two satellites are simultaneously affected by the ionospheric gradient. Two affected satellites generate the worst-case position errors (the largest position errors), because if more satellite are affected a part of the ionospheric range error becomes common to all satellites and will project into the receiver clock estimation. Since the worst possible satellite pair in terms of position error cannot be predicted a-priori, all possible satellite pairs of two satellites are tested for each subset. The Ionosphere-induced Error in Vertical (IEV) for each satellite pair (k_1, k_2) from each geometry subset is computed as :

$$IEV = \max \left\{ \begin{vmatrix} s^{k_1}_{\text{apr_vert}} \cdot \varepsilon^{k_1} + s^{k_2}_{\text{apr_vert}} \cdot \varepsilon^{k_2} \\ s^{k_1}_{\text{apr_vert}} \cdot \varepsilon^{k_1} - c \cdot s^{k_2}_{\text{apr_vert}} \cdot \varepsilon^{k_2} \\ s^{k_2}_{\text{apr_vert}} \cdot \varepsilon^{k_2} - c \cdot s^{k_1}_{\text{apr_vert}} \cdot \varepsilon^{k_1} \end{vmatrix} \right., \tag{2.46}$$

   with $s_{\text{apr_vert}}$ being the vertical position component of $\boldsymbol{S}$ (see Eq. (2.21)), ε^n the range error for satellite n computed as described in the previous step, and c is a constant between 0 and 1 used to overbound the errors introduced by any observed ionosphere anomaly [57].

   The Maximum Ionosphere-induced Error in Vertical (MIEV) of each subset geometry is computed as the maximum of the IEV from all satellite pairs in the subset. This value is then compared with the TEL for each subset geometry that might be used by the airborne user. If MIEV exceeds TEL computed for a subset geometry, the geometry must be made unavailable to the airborne user in order to mitigate the potential integrity risk. This is done by inflating the broadcast integrity parameters on ground. By inflating the broadcast parameters, the alert limits for the considered subset geometry will exceed the alert limits and thus the geometry will not be used by the airborne user. The inflation is performed until all potentially unsafe geometries become unavailable for the aircraft user.

3. **Inflation**: The aim of the inflation algorithm is to exclude all potentially hazardous geometries (for which the MIEV>TEL) by inflating the broadcast parameters such that the VPL would exceed the VAL. However, depending on which integrity parameters are inflated, also satellite geometries that are not hazardous might be screened out as well, leading to a loss of availability. Thus, it is important to select the most effective parameters to inflate among the broadcast ones. Several possibilities have been studied. The first parameter considered for inflation is σ_{vig} and the details of the procedure are given in [22, 57, 58]. Even if the σ_{vig} inflation meets the integrity requirements, as the parameter is not specific for each satellite it increases the VPL of all geometries potentially usable, including also the safe ones. Therefore, this could lead to an undesirable loss of availability. In order to solve this problem, other inflation methods have been studied and implemented throughout the literature which include the inflation of the $\sigma_{\text{pr_gnd}}$ and P_{C} value. Details are given in [22, 58, 59].

Prior to the installation of a new GBAS site, geometry-screening simulations are performed to cover all possible GPS satellite constellations, times of day, airborne subset geometries, user-GBAS ground station separations, and ionosphere anomaly permutations given by the ionosphere threat model. However, only performing the offline operation of this algorithm would produce inflation factors that would not bound possible variations of the GPS satellite constellation. For that reason, a real-time implementation of the geometry-screening is needed. Due to the computational effort required to perform all the geometry-screening simulations, the update interval of the inflation factors cannot meet the messages update rate of 2 Hz. In [57], the authors suggest that an inflation-factor update interval of 60 seconds could be enough.

2.6.2.1 Anomalous troposphere monitoring

As previously discussed, the ground subsystem is responsible to characterize and broadcast the parameters for the nominal state of the troposphere. In the current standards, the tropospheric anomalies are considered as part of the nominal behavior as they occur often enough and have a small impact into the total differential error. However, in [60] it was shown that a weather front between the reference station and the aircraft can cause significant measurement error, up to 0.41 m over a 5 km baseline. Different candidates were investigated for modeling the non-nominal tropospheric gradients and the wall model was selected as a good representation for the threat model [43]. The wall model represents a weather boundary with conditions within the wall being different from the conditions outside the wall. Thus, GNSS signals arriving to the ground station and to the airborne user will experience different errors as represented in Figure 2.13. The threat model assumes the worst case to be present always and computes a maximum error at a certain distance from the GBAS station. Note that this model only includes the lateral weather component because it is assumed that the vertical component is taken into account in the bounding of the nominal residual error (σ_{tropo}). The maximum bias is converted into a standard

deviation using the relation described as

$$\sigma_{\text{non_nominal_tropo}} = \frac{\mu_{\max} \cdot \sqrt{N}}{k_{\text{ffmd}}}, \tag{2.47}$$

with μ_{max} being the maximum bias on the range domain, N the number of satellites and k_{ffmd} the fault-free missed detection multiplier. The overbounding of the non-nominal tropospheric error is dependent on the lateral distance between the reference station and the aircraft. Thus, one solution suggested in [43] is to incorporate the bound of the anomalous troposphere in the residual ionospheric uncertainty (σ_{vig}) which is horizontal distance dependent as

$$\sigma_{\text{vig}} = \sqrt{\sigma_{\text{vig}}^2 + \sigma_{\text{non_nominal_tropo}}^2}, \tag{2.48}$$

A value of 5 mm/km is suggested in [43] to overbound the non-nominal troposphere standard deviation.

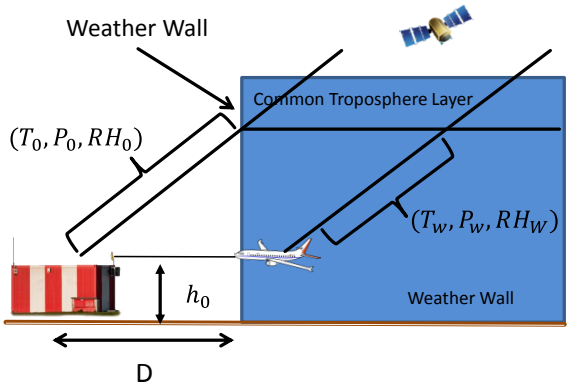


Figure 2.13: Tropospheric wall model (from Figure 3 from [43])

2.7 Integrity in GAST-D

Unlike GAST-C, the GAST-D integrity requirements are not derived based on an ILS look-alike approach. The GAST-C approach of placing the responsibility on the ground only requires the ground to make conservative assumptions which reduces the system availability. While this was acceptable for CAT-I, it is not feasible for more demanding CAT-III requirements. Thus, the rationale for GAST-D is different but leaves the GAST-C provisions unchanged for backwards compatibility. The adopted

methodology for deriving the integrity requirement for GAST-D is to ensure the safe landing of an aircraft represented by a longitudinal touchdown point on the runway.

The requirements are allocated to different systems as illustrated in Figure 2.14. The measure of performance considered in this concept is the Total System Error (TSE) which is defined as the difference between the true position and the desired position. The TSE includes two components: the Navigation System Error (NSE), representing the difference between the estimated position (by the navigation system) and the true position, and the aircraft Flight Technical Error (FTE) performance which refers to the accuracy with which an aircraft can follow the intended path. The path definition error is also a contribution to the TSE, but it is considered small enough to be neglected.

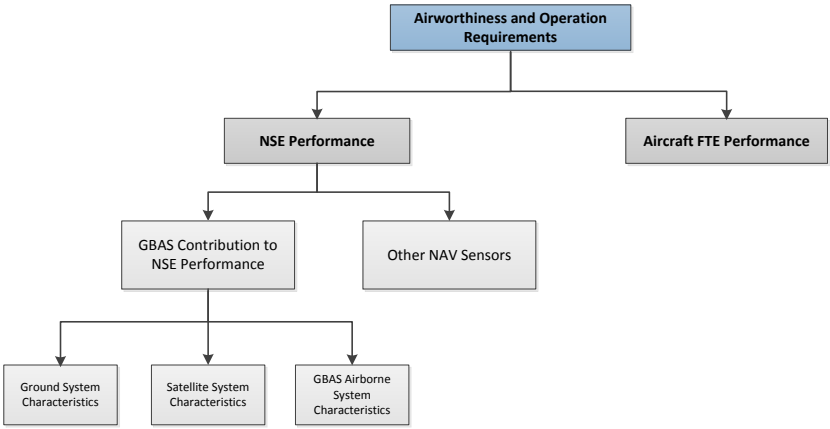


Figure 2.14: GAST-D requirements allocation from [61]

The consideration of both components is taken into account for CAT-III operations because the position accuracy is influenced not only by the navigation system, but also by the aircraft touchdown performance and they have to meet the airworthiness requirements together. For example, the closer to the limits the aircraft performance is, the better the navigation system has to be [61].

The FTE is aircraft dependent and is influenced by different factors such as the engine performance, the airframe, environmental conditions (wind) and the autopilot characteristics. In the derivation of the requirements, a fixed value for the FTE is used. Based on this value and the criteria for the safe landing, the required NSE for GAST-D can be derived.

The NSE includes the GBAS system contribution and the other aircraft sensors (e.g. inertial system or the radar altimeter) which are treated separately from the

GBAS errors. The GBAS errors include further the contributions of the ground system, the satellite system and the airborne equipment.

The airworthiness certification criteria necessary to meet the touch down requirements that refer to the safe landing of an aircraft are specified in Certification Specifications for All-Weather Operations (CS-AWO) [62] and the Advisory Circular AC 120-28D [63]. The requirements are specified for three conditions: the nominal condition where all influencing parameters vary according to their expected distributions, the malfunction case where one parameter is exceeding its limit and the limit case when one of the parameters is kept at its most critical value while the others vary in their expected manner.

According to the documents, a landing is considered to be safe if the aircraft touches down not less than 200 ft behind the runway threshold and not more than 2700 ft behind the threshold. In case of a limit case or malfunction condition the touchdown box extends to 3000 ft behind the threshold. The touchdown box for all cases is illustrated in Figure 2.15 and the dimensions together with the required probabilities are summarized in Table 2.10.

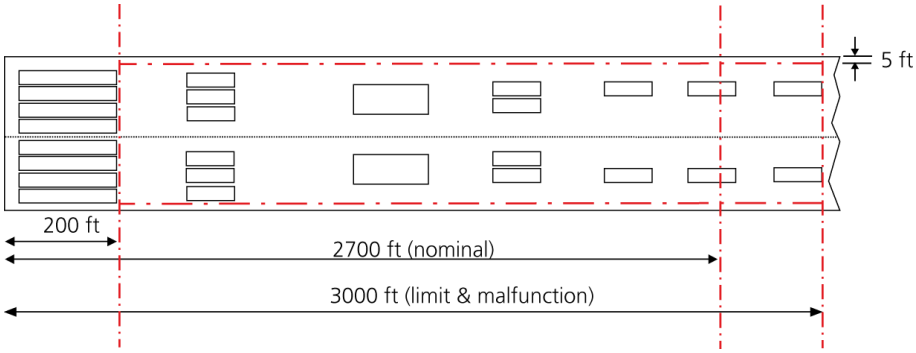


Figure 2.15: Box defining the touchdown requirements (from [64])

Performance case	Limit landing short (ft)	Limit landing long (ft)	Max. prob. of exceeding the limits
Nominal	200	2700	10^{-6}
Limit	200	3000	10^{-5}
Malfunction	200	3000	0

Table 2.10: Touchdown requirements

The three touchdown requirements have to be fulfilled at the same time and consist the basis in deriving the integrity concept. The nominal performance requirements are used to demonstrate that the aircraft lands safely in the touchdown box. The limit case applied to GBAS is used to derive a maximum limit on the NSE in case of a failure which is not detected by the monitors, which means the maximum error that

can build in the ranges before the monitor triggers. The malfunction case refers to the cases when a failure is present but not detected. It is applied to failures that have a probability larger than 10^{-9} and is used to derive the required monitor performance [61]. From this, it can be concluded that the nominal case applies to the fault free errors and impact the alert limits and the protection levels, while the limit and the malfunction case define the monitor requirements. The derivation of the requirements for each of the three cases and their relation with the integrity concept is detailed in the next section.

2.7.1 Relation between airworthiness requirements and integrity

The most stringent requirements are defined for the vertical domain, while due to the satellite geometry navigation performance is generally worse in the vertical than in the horizontal domain. Thus, in the derivation of the requirements it is assumed that if the conditions for the vertical domain are fulfilled, the horizontal will be within limits as well.

Before starting the derivation of the requirements, a relation between the logitudinal landing coordinates and the vertical domain used in the navigation solution is needed. Assuming that any vertical error translates into an along track position error, the translation from the longitudinal NSE to the vertical NSE is described as

$$NSE = \frac{NSE_{\mathrm{v}}}{\tan\theta_{\mathrm{GPA}}}, \tag{2.49}$$

This assumption is justified by the fact that the final phase (below 50m) of vertical guidance is accomplished by the radar altimeter and not on the navigation system. This means that an error on the vertical domain will shift the aircraft on the runway. The relation from the above equation has been validated on Boeing airplanes through simulation as described on [65].

Nominal condition

Under the nominal case it is assumed that all parameters vary according to their nominal distribution.

In order to meet the airworthiness requirements it is necessary that the Nominal Touchdown Point (NTDP) which is the point where the aircraft lands in the ideal case, and the standard deviation of the TSE, σ_{TSE}, are chosen such that the probability of exceeding any edge of the box is smaller than 10^{-6} in both cases landing short and landing long. The relation between the NTDP and σ_{TSE} for the landing short case is given by

$$NTDP - k \cdot \sigma_{\mathrm{TSE}} \geq 200\mathrm{ft}, \tag{2.50}$$

where σ_{TSE} is the standard deviation of the TSE (containing the navigation and flight technical errors) and k is the multiplier associated to the probability that the aircraft

landing outside the touchdown box. In the nominal case this probability is 10^{-6} (see Table 2.10) leading to $k = 4.75$.

In a similar manner, the condition for landing long can be expressed as

$$NTDP + k \cdot \sigma_{\mathrm{TSE}} \leq 2700\mathrm{ft}. \tag{2.51}$$

Generally, it is assumed that NSE and FTE are statistically independent so that the variance of the TSE can be considered as the sum of the variances of the two contributors

$$\sigma^2_{\mathrm{TSE}} = \sigma^2_{\mathrm{NSE}} + \sigma^2_{\mathrm{FTE}}. \tag{2.52}$$

The σ_{NSE} refers to the along-track touchdown performance which ca be translated to the vertical NSE using the relation from Equation 2.49 ($\sigma_{\mathrm{NSE}} = \frac{\sigma_{\mathrm{NSE,v}}}{\tan(\theta_{\mathrm{GPA}})}$)

The standard derivation of the vertical position uncertainty in the GBAS solution ($\sigma_{\mathrm{NSE,v}}$) can be related to the vertical protection levels (which represent the bounds on the vertical position domain) using Eq 2.20 and assuming $D_{\mathrm{v}} = 0$ as

$$\sigma_{\mathrm{NSE,v}} = \frac{VPL_{\mathrm{H_0}}}{k_{\mathrm{ffmd}}}. \tag{2.53}$$

The maximum value for the VPL is limited by the VAL, thus the maximum limit on the $\sigma_{\mathrm{NSE,v}}$ can be expressed as

$$\sigma_{\mathrm{NSE,v}} = \frac{VAL}{k_{\mathrm{ffmd}}}. \tag{2.54}$$

Replacing Eq. (2.52) and 2.54 in 2.50 and 2.51, the conditions become

$$\begin{cases} NTDP - k \cdot \sqrt{\sigma^2_{\mathrm{FTE}} + \left(\frac{3.28 \cdot VAL}{k_{\mathrm{ffmd}} \cdot \tan(\theta_{\mathrm{GPA}})}\right)^2} \geq 200\mathrm{ft}, \\ NTDP + k \cdot \sqrt{\sigma^2_{\mathrm{FTE}} + \left(\frac{3.28 \cdot VAL}{k_{\mathrm{ffmd}} \cdot \tan(\theta_{\mathrm{GPA}})}\right)^2} \leq 2700\mathrm{ft}. \end{cases} \tag{2.55}$$

As typically the VAL is given in meters, the factor 3.28 represents the conversion to feet. The FTE value has to be determined by the aircraft manufacturer. From these equations, it can be observed that the acceptable airplane autoland performance gets smaller as the vertical alert limit increases, which results in a larger tolerable navigation error. In [66] and [67] it was demonstrated that the landing system performance for Boeing airplanes is compatible with the previous VAL of 10 m derived for GAST-C.

In the derivation of the standards the values of the parameters for the nominal case were chosen as $NTDP = 1290$ m, $\sigma_{\mathrm{FTE}} = 150$ ft, $VAL = 10$ m and a glide path angle of 2.5° as a conservative value [61]. Taking these parameters, both constraints of landing long and landing short are fulfilled. Currently, a fixed value for the FTE is

assumed. The value was derived to accommodate different aircraft types. However, some aircraft might need to restrict the limit on the NSE to ensure airworthiness compliance. This can be achieved through lowering the VAL values internally in the GBAS airborne system. In [64] the authors show the potential benefits of using the deviations from the nominal approach path to assess the FTE performance during an approach instead of using conservative assumptions. A more realistic value for the FTE can optimize the landing or can increase the system availability by allowing a larger margin for the NSE.

Limit condition

The limit condition requires that under a fault condition that generates an error E, the airplane lands shorter than 200 ft from the threshold or longer than 3000 ft from the threshold with a probability not larger than 10^{-5} when the error for the fault is at its maximum value (before being detected by the monitor) and all the other errors vary according to their nominal distribution.

In this case, a vertical error is assumed to be composed of the fault-free component and an additional vertical error due to the fault (E_{v})

$$NSE_{\mathrm{v}} = NSE_{\mathrm{v,ff}} + E_{\mathrm{v}}. \tag{2.56}$$

The $NSE_{\mathrm{v,ff}}$ is the fault-free component as defined in the nominal case, Gaussian distributed with zero mean and standard deviation $\sigma_{\mathrm{NSE,v}}$. Assuming the $VAL = 10$ m and $k_{\mathrm{ffmd}} = 5.81$ (the value specified for three reference receivers, see Table 2.6) and using Eq. (2.54) results in a maximum value of $\sigma_{\mathrm{NSE,v}} = 1.72$ m.

The probability of an unsuccessful landing given the error E_{v} has to be lower than 10^{-5}. This probability can be defined as the conditional probability of having an error E_{v} without being detected by the monitor (P_{md}) and the probability that an unsuccessful landing occurs giving the error is not detected $P_{UL|E_{\mathrm{v}}_\mathrm{undetected}}$. This can be expressed as

$$P_{UL|E_{\mathrm{v}}} = P_{\mathrm{md}}(E_{\mathrm{v}}) \cdot P_{UL|E_{\mathrm{v}}_\mathrm{undetected}}(E_{\mathrm{v}}) \leq 10^{-5}. \tag{2.57}$$

Thus, the limit case requirement will be fulfilled if each monitor maintains the following condition on the monitoring probability of missed detection function of the error E_{v}

$$P_{\mathrm{md}}(|E_{\mathrm{v}}|) \leq \min\left(1, \frac{10^{-5}}{P_{UL|E_{\mathrm{v}}_\mathrm{undetected}}(|E_{\mathrm{v}}|)}\right). \tag{2.58}$$

The probability of unsuccessful landing can be determined from the landing short and landing long constraints (see Table 2.10). However, in the derivation of the standards [61], only the landing short condition is considered for the limit case as it is more stringent to be met. A short landing in the limit case occurs if the touchdown

point is more than 200ft behind the runway threshold which can be formulated using the same notations as in the nominal case as

$$NTDP - k \cdot \sigma_{\mathrm{TSE}} - \frac{E_{\mathrm{v}}}{tan(\theta_{\mathrm{GPA}})} \geq 200\mathrm{ft}. \tag{2.59}$$

Thus, the probability of an unsuccessful landing becomes:

$$P_{UL|E_{\mathrm{v}}_\mathrm{undetected}}(|E_{\mathrm{v}}|) = Q\left(\frac{NTDP - 200 - \frac{3.28 \cdot E_{\mathrm{v}}}{\tan(\theta_{\mathrm{GPA}})}}{\sqrt{\sigma_{\mathrm{FTE}}^2 + \frac{3.28 \cdot \sigma_{\mathrm{NSE,v}}}{\tan(\theta_{\mathrm{GPA}})}}}\right). \tag{2.60}$$

The monitor requirements for the limit case were derived assuming the same values as in the nominal case: $NTDP = 1290$ m, $\sigma_{\mathrm{FTE}} = 150$ft, $VAL = 10$ m, a glide path angle of 2.5° and the $\sigma_{\mathrm{NSE,v}} = 1.72$ m as derived above. This derivation defines a requirement for the monitor in the vertical domain. A translation of the vertical error E_{v} into the range domain for a satellite n, (E_{r}^n), can be computed using the vertical component of the $\boldsymbol{S}$ ($s_{\mathrm{apr_vert}}$ in Eq. (2.21)) as

$$E_{\mathrm{v}} = s_{\mathrm{apr_vert}}^n \cdot E_{\mathrm{r}}^n. \tag{2.61}$$

The maximum value is limited to 4.0 in the airborne receiver and ground reference station and the details of this threshold are given in Section 2.7.8. This limitation is needed for the monitors implemented in the ground system which does not have knowledge of the actual airborne geometry.

Figure 2.16 shows the resulting P_{md} function of the range error (E_{r}) (in meters) in black. For simplicity, a linear approximation of the $P_{\mathrm{md}}(E_{\mathrm{r}})$ is used in the standards shown by the red curve and the mathematical description of this approximation is described in Table 2.11.

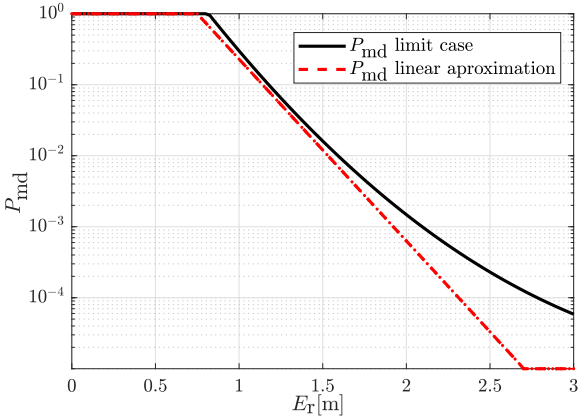


Figure 2.16: P_{md} in range domain for the limit case

Probability of missed detection (limit)	**Pseudorange error ($E_\mathbf{r}$) [m]**
$P_{\text{md}} \leq 1$	$0 \leq \lvert E_{\text{r}} \rvert \leq 0.75$
$P_{\text{md}} \leq 10^{-2.56 \cdot \lvert E_{\text{r}} \rvert + 1.92}$	$0.75 \leq \lvert E_{\text{r}} \rvert \leq 2.7$
$P_{\text{md}} \leq 10^{-5}$	$\lvert E_{\text{r}} \rvert \geq 2.7$

Table 2.11: Linear approximation for P_{md} for limit case

Malfunction condition

Under the malfunction condition the aircraft has to land safely in the landing box "under any malfunction scenario that is not extremely improbable (probability of occurrence on the order of 10^{-9} per landing)" [68]. Compared with the limit case which refers to the maximum error due to a fault that can build before detection, the malfunction refers to the case when a fault occurs on the NSE and is not detected by any monitor. In this case the landing has to be successful with complete certainty (probability of 1) for any error which occurs with a probability larger than 10^{-9}. However, providing a complete certainty is not possible due to the random nature of the NSE and FTE. Thus, in order to derive a maximum limit on the error, the NSE and FTE are taken at their 95^{th} percentile. Similar to the limit case, only the vertical contribution is considered in the derivation of the requirements as it has a more stringent impact and the maximum values for the E_{v} ($E_{\text{v,max}}$) is determined from the landing short constraints which again result in more restrictive requirements. The $E_{\text{v,max}}$ has to satisfy the landing short condition which can be formulated as

$$NTDP - k_1 \cdot \frac{3.28 \cdot \sigma_{\text{NSE,v}}}{\tan(\theta_{\text{GPA}})} - \frac{3.28 \cdot E_{\text{v,max}}}{\tan(\theta_{\text{GPA}})} - k_1 \sigma_{\text{FTE}} = 200\text{ft}. \tag{2.62}$$

The notations are the same as defined in the limit case and k_1 is the fixed value corresponding to 95^{th} percentile of the nominal NSE and FTE computed as $k_1 = Q^{-1}\left({}^{0.05}/_{2}\right) = 1.96$. The $E_{\text{v,max}}$ can be rewritten as

$$E_{\text{v,max}} = \frac{(NTDP - 200 - 1.96 \cdot \sigma_{\text{FTE}}) \cdot \tan(\theta_{\text{GPA}})}{3.28} - 1.96 \cdot \sigma_{\text{NSE,v}}. \tag{2.63}$$

For the derivation of the malfunction case the parameters were assumed similar with the limit case ($NTDP = 1290$ m, $VAL = 10$ m and $\theta_{\text{GPA}} = 2.5^\circ$ and $\sigma_{\text{NSE,v}} = 1.72$ m) but a values of 180 ft is used for σ_{FTE}. Using this value yields

$$E_{\text{v,max}} = 6.44\text{m}. \tag{2.64}$$

As this requirements is mainly used for the monitors on ground, the corresponding limit on the range domain is computed based on the maximum value on the $s_{\text{apr_vert}}$ (see Eq. (2.21)) which is set to 4 as

$$E_{\text{r,max}} = \frac{E_{\text{v,max}}}{4} = 1.6\text{m}. \tag{2.65}$$

Having a maximum value of E_r in order to defined the $P_{md}(E_r)$, a prior probability of occurrence of the fault must be assumed(P_{fault}). Then the requirements can be written as

$$P_{md}(E_r) = \begin{cases} > \dfrac{10^{-9}}{P_{fault}}, E_r > E_{r,max} \\ = 1, E_r \leq E_{r,max}. \end{cases} \tag{2.66}$$

Based on a satellite fault rate of 10^{-4} a duration of approach of 15 seconds and a maximum of 18 satellites, the value of P_{fault} is assumed to be [61]:

$$P_{fault} = \frac{10^{-4} \cdot 15 \cdot 18}{3600} = 7.5 \cdot 10^{-6}. \tag{2.67}$$

Figure 2.17 shows a graph on the P_{md} function of the range error E_r using the above derivation. The limit and the malfunction cases define the low-level requirements for GAST-D monitoring and the union of both constrained regions is shown in Figure 2.18. Each ground and airborne monitor defined in GAST-D has to meet the combined conditions and to ensure that any error is detected with the required probability.

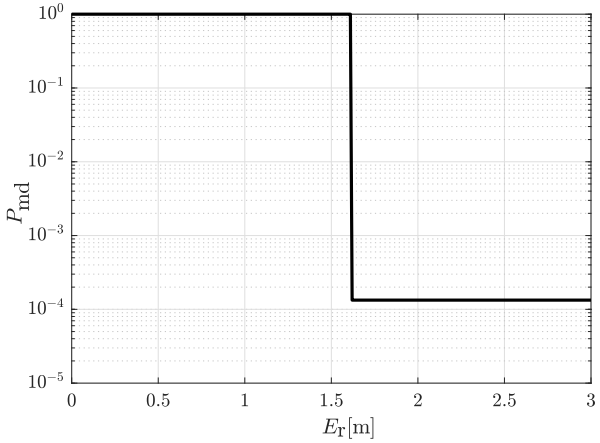


Figure 2.17: Limit on the P_{md} in range domain for the malfunction case

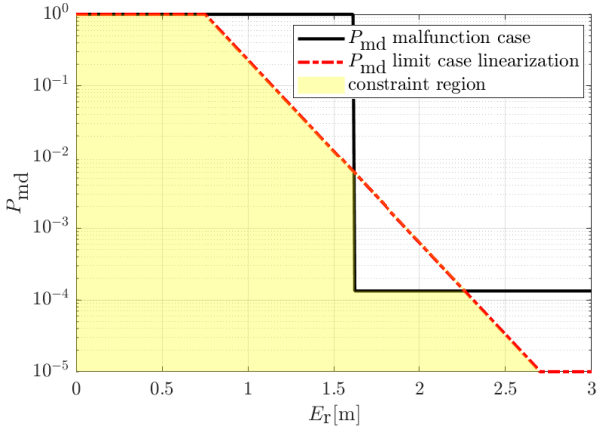


Figure 2.18: Limit on the P_{md} in range domain for the malfunction case

2.7.2 Integrity coverage for GAST-D

Figure 2.19 illustrates in a similar way as Figure 2.10 the integrity allocation for GAST-D. The fault free errors (including ground subsystem errors, airborne errors and environmental errors) are covered by protection levels similar to the GAST-C concept. However, some of the errors covered by the protection levels are also covered by the GAST-D ranging source monitoring requirement (e.g. the single receiver failure in ground subsystem). This is because the protection levels are not sufficiently sensitive to meet the GAST-D requirements and some of the errors have to be detected with higher integrity by specific monitors. Unlike the GAST-C concept, where the ground is solely responsible to provide integrity, in GAST-D this responsibility is shared between the airborne user and the ground system. The ground system is required to monitor the satellite ranging signals and to provide to the airborne receiver enabling the aircraft to assess its own integrity in the specific position solution [13]. Additionally, the GAST-D integrity requires the ground system design to mitigate failures of system components, monitor architecture and other design relevant faults. The ground requirements are defined in the range domain, and the aircraft is responsible to ensure the integrity in the position domain and to exclude geometries that do not meet the required performance. By shifting the integrity responsibility to the airborne user, the ground system does not have to make conservative assumption on the geometry used by the aircraft.

The diagram also indicates that the GAST-D integrity is specified differently for errors due to failures in the GNSS ranging sources and for anomalous ionospheric effects. The ranging source integrity requirement is given as a monitor requirement that limits the probability of missed detection function of the size of the error. The derivation of the monitor requirements is based on the conditions for limit and malfunction cases which have been presented previously.

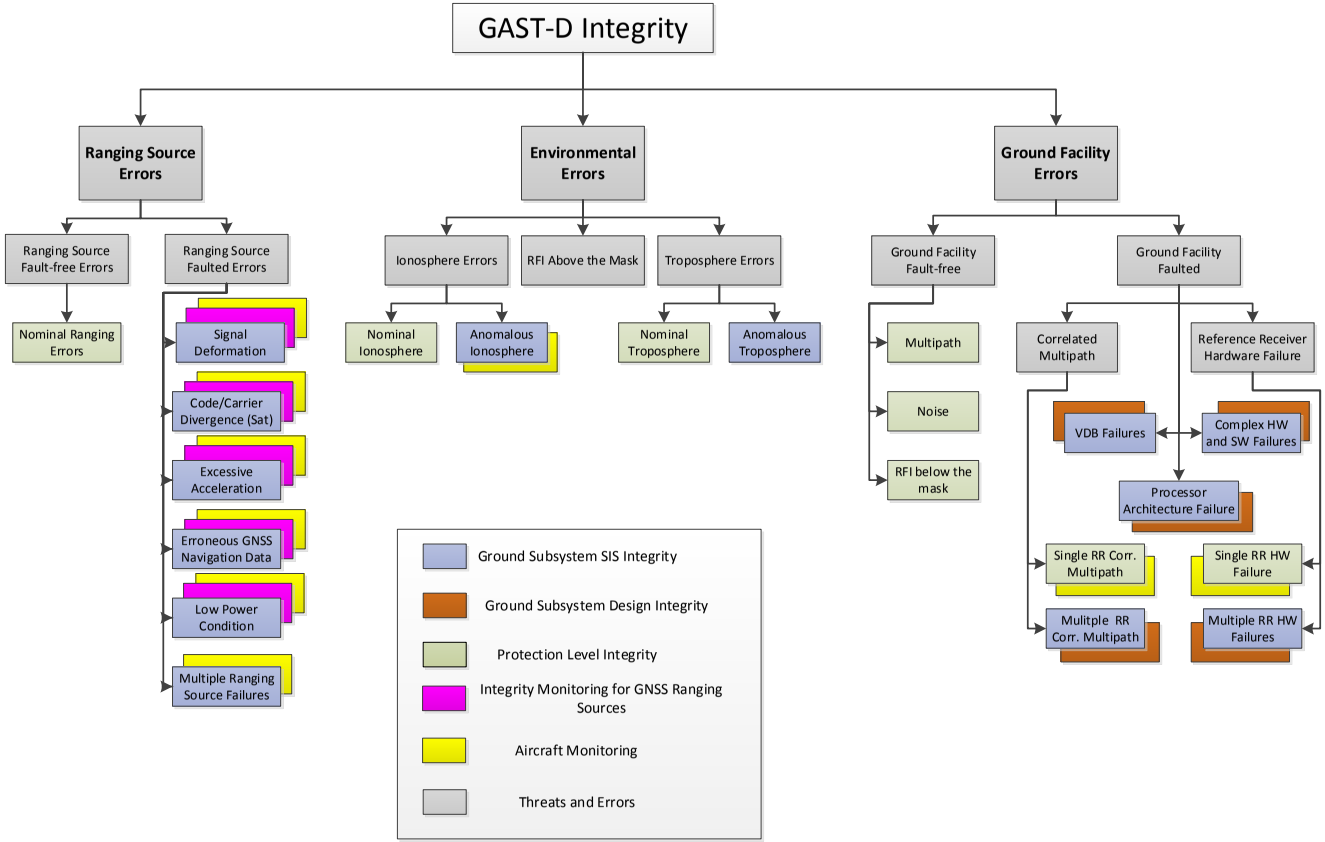


Figure 2.19: Errors and threats as part of integrity concept in GAST-D

One of the main differences between the two service types is the mitigation of the ionospheric threat. In GAST-C, the anomalous ionospheric errors are bounded by the protection levels by inflation integrity parameters broadcast by the ground system. The concept assumes that the worst case gradient is present all the time. This approach does not need additional monitoring, but it is very conservative and can lead to decrease of the system availability. In GAST-D, the detection of the ionospheric gradients is shared between ground and airborne monitoring and different modifications are implemented. First, 30 seconds carrier smoothed pseudorange corrections are introduced in addition to the 100 seconds smoothed pseudoranges. The airborne receiver forms both the 100 seconds and 30 seconds corrected pseudoranges to compute the two position solutions, but uses the later one for the calculation of the deviations. The advantage of the shorter smoothing time constant is that it makes the system less susceptible to the buildup ionospheric divergence in the filter. On the other side, the parallel use of 100 and 30 smoothed pseudoranges enables the airborne to monitor the ionospheric gradients (Dual-Solution Ionospheric Gradient Monitor (DSIGMA), see Section 2.7.8). Second, the CCD monitor is implemented also on the airborne receiver for the detection of large ionospheric gradients. On the ground subsystem, an ionospheric gradient monitoring is implemented that detects large ionospheric gradients that might not be visible to the airborne user. A version of this monitor is described in Section 2.7.8. Similar to GAST-C, the GAST-D ground includes the CCD monitor and its implementation is discussed in Section 2.7.8.

2.7.3 Protection levels in GAST-D

Similar to GAST-C, protection level integrity is allocated in GAST-D. The specified integrity risk for the protection levels that cover the fault free (H_0) and single reference receiver fault (H_1) is $2 \cdot 10^{-7}$, the same as in GAST-C. Thus, the same values for k_{ffmd} parameters are used (see Table 2.6). However, the algorithm and the broadcast parameters used in the implementation are different.

In GAST-C, the protection level parameters were used to bound the nominal errors and also the ionospheric anomalies. Under GAST-D, the protection levels cover only the nominal case. Thus, the ground subsystem does not have to provide inflated integrity parameters to bound the effect of the ionospheric gradients at the airborne user. Another difference is that the output position solution for GAST-D is based on 30 seconds smoothed and corrected pseudoranges. The weighting matrix, $\boldsymbol{W}$, in the position solution and in the calculation of the pseudoinverse matrix, $\boldsymbol{S}$, are based on 30 seconds models. However, in order to keep the equivalence with GAST-C error bounding, the GAST-D integrity concept is based on 100 seconds smoothing time constant. The ground equipment broadcasts thus new integrity parameters to enable the calculation of the protection levels for 100 seconds smoothing time constant. The airborne user is responsible to calculate the difference introduced in the 30 seconds position solution and apply the correction to the protection levels. This is achieved by adding the D_{l} and D_{v} terms which are calculated as the magnitude of the lateral and vertical projections between the 100 and 30 seconds smoothed position solu-

tions. The fault-free protection levels are computed using the relation described in Eq. (2.20). The variance of the residual uncertainty of the differential corrected solution for GAST-D for one satellite n is computed using the new parameters broadcast by the ground system as

$$(\sigma^n_{\mathrm{GBAS,D}})^2 = (\sigma^n_{\mathrm{pr_air}})^2 + (\sigma^n_{\mathrm{tropo}})^2 + (\sigma^n_{\mathrm{pr_gnd,D,100}})^2 + (\sigma^n_{\mathrm{iono,D}})^2, \tag{2.68}$$

where $\sigma_{\mathrm{pr_gnd,D,100}}$ is the parameter describing the uncertainty in the noise and multipath present in 100 seconds smoothed pseudorange corrections which removes any inflation performed in the $\sigma_{\mathrm{pr_gnd,C,100}}$ parameter. The $\sigma_{\mathrm{iono,D}}$ is the residual ionospheric uncertainty computed as shown in Eq.(2.35) based on 100 second smoothing time constant and the uninflated sigma vertical ionosphere gradient parameter broadcast by the ground system, $\sigma_{\mathrm{vig,D}}$.

The ground broadcasts also the parameters that bound the residual errors of the 30 seconds corrections, $\sigma_{\mathrm{pr_gnd,D,30}}$, used in the weighting matrix (see Eq. (2.16)).

The models for the airborne noise and multipath and the tropospheric uncertainty are identical to those for GAST-C.

The H_1 protection levels which cover the single reference receiver fault are computed in the same manner as described in Eq. (2.25) using the parameters specific for GAST-D described above.

Additional to the two protection levels, GAST-D also defines the ephemeris protection levels, specified in Eq. (2.29). For the computation of these bounds, the ground broadcasts new values for P_{D} and $k_{\mathrm{md_e,D}}$ which remove any inflation necessary for GAST-C.

A GAST-D station has to comply with all GAST-C requirements which means that they have to show compliance with the GAST-C integrity risk for all conditions [61]. This is because GAST-C is a fallback mode of GAST-D and airborne users equipped with GAST-C equipment should still be supported.

2.7.4 Ground subsystem signal-in-space integrity risk in GAST-D

For GAST-D the integrity risk allocated to all other faults not covered by protection levels is $1.5 \cdot 10^{-7}$. This requirement is similar to the GAST-C definition and includes all the faults discussed in Section 2.6.2 with the exception of the ionospheric anomalies and the single reference receiver fault which are not included in this allocation. These two types of faults are treated differently in GAST-D as will be discussed in the following sections. For all the other faults, the same integrity monitors discussed for GAST-C (see Table 2.8) apply.

2.7.5 Ground system integrity risk in GAST-D

In addition to the ground subsystem SiS integrity risk, GAST-D integrity requires the ground subsystem to ensure that internal failures due to system components, monitor

architecture or other design faults occur with a probability lower than 10^{-9} in any one landing [13]. This requirement is equivalent to the ILS CAT-III SiS integrity risk.

2.7.6 Integrity of the ranging source faults in GAST-D

The ranging source faults comprise the faults described previously in Section 2.4. These faults are covered by different monitors implemented in the ground system. For GAST-D, the monitor requirements are derived from the limit and malfunction case. This translate into the requirement that the ground system has to ensure that the probability of having a range error E_r in the 30 seconds smoothed and corrected pseudoranges due to any of these faults to be within the region defined in Figure 2.18.

2.7.7 Aircraft monitoring in GAST-D

In GAST-D new requirements for monitoring and geometry screening are included in the airborne system for mitigating possible errors due to the ionospheric anomalies. The ionospheric gradients mitigation and the specific monitors implemented in the airborne subsystem are discussed in the next section. Additionally, the airborne subsystem includes a B-values monitor check to detect reference receiver faults, a Differential Receiver Autonomous Integrity Monitoring (D-RAIM) algorithm used for fault detection, a monitor that checks the magnitude of the corrections as well as a measurements quality monitor. Each of the monitors is discussed in detail in the following.

Measurement Quality Monitor (MQM)

The Measurement Quality Monitor (MQM) checks for large jumps in the satellite tracked signals. These jumps can occur due to undetected cycle slip or to faults in the measurements that are not detected by other monitors. The jumps are detected by monitoring the difference between the raw pseudorange measurements and the projected smoothed pseudoranges (see Section 2.3.6.7 of DO-253D [18]). The threshold for the monitor is set to 10 m for the GPS L1 signals. As the monitor uses the raw measurements, large jumps in multipath would trigger the monitor as well. The defined threshold is only valid for GPS L1 signal and new thresholds need to be established if other signals are considered.

Reference Receiver Fault Monitor (RRFM)

In addition to the H_1 protection levels in GAST-D, the airborne user is responsible to monitor the magnitude of the broadcast B-values and to limit the impact of a single reference receiver fault on the total navigation error by using its actual geometry. The monitor test statistic uses the broadcast 100 seconds B-values and the difference between the 30 and 100 seconds smoothed position solutions (D_l and D_v) and

compares them with variable thresholds as

$$\begin{aligned} |B_{\text{apr_lat}_k}| + D_{\text{l}} &\leq T_{B_{\text{apr_lat}}}, \\ |B_{\text{apr_vert}_k}| + D_{\text{v}} &\leq T_{B_{\text{apr_vert}}}, \end{aligned} \tag{2.69}$$

with $B_{\text{apr_lat}_k}$ and $B_{\text{apr_vert}_k}$ being the projection into the lateral and vertical position domain of the largest bias due to a failure in receiver k (see Eq. (2.26)). The thresholds $T_{B_{\text{apr_lat}}}$ and $T_{B_{\text{apr_vert}}}$ are defined as

$$T_{B_{\text{apr_lat}}} = k_{ffd_B} \cdot \sqrt{\sigma^2_{B_{\text{apr_lat}}} + \sigma^2_{D_{\text{l}}}} \tag{2.70}$$

$$T_{B_{\text{apr_vert}}} = k_{ffd_B} \cdot \sqrt{\sigma^2_{B_{\text{apr_vert}}} + \sigma^2_{D_{\text{v}}}}, \tag{2.71}$$

where k_{ffd_B} is the multiplier for the probability of the fault free detection set to 5.5 [18]. The $\sigma_{D_{\text{l}}}$ and $\sigma_{D_{\text{v}}}$ represent the standard deviations of the lateral and vertical projection of the difference between 30 and 100 seconds smoothed position solutions which are computed as [18]

$$\sigma_{D_{\text{l}}} = 0.28 \cdot \sqrt{\sum_{n=1}^{N} (s^n_{\text{apr_lat}})^2 \cdot (\sigma^n_{\text{GBAS,D}})^2}, \tag{2.72}$$

$$\sigma_{D_{\text{v}}} = 0.28 \cdot \sqrt{\sum_{n=1}^{N} (s^n_{\text{apr_vert}})^2 \cdot (\sigma^n_{\text{GBAS,D}})^2}. \tag{2.73}$$

The $\sigma_{B_{\text{apr_lat}}}$ and $\sigma_{B_{\text{apr_vert}}}$ are defined as

$$\sigma_{B_{\text{apr_lat}}} = \sum_{n=1}^{N} \frac{(s^n_{\text{apr_lat}})^2 \cdot (\sigma^n_{\text{pr_gnd,D}})^2}{M_n}, \tag{2.74}$$

$$\sigma_{B_{\text{apr_vert}}} = \sum_{n=1}^{N} \frac{(s^n_{\text{apr_vert}})^2 \cdot (\sigma^n_{\text{pr_gnd,D}})^2}{M_n}, \tag{2.75}$$

$$\tag{2.76}$$

where $s_{\text{apr_lat}}$, $s_{\text{apr_vert}}$ are defined in Eq. (2.21), $\sigma_{\text{pr_gnd,D}}$ represents the broadcast GAST-D uncertainty error in the 100 seconds smoothed pseudorange corrections and M_n the number of receivers used to generate the correction for satellite n.

D-RAIM algorithm

The aircraft performs the D-RAIM algorithm for fault detection. This algorithm is enabled only when the aircraft is inside Precision Approach Region (PAR), if measurements from more than four satellites (with associated broadcast pseudorange corrections) are available. The test statistic and the threshold are based on the 100 seconds smoothed pseudoranges, the GAST-D error models derived for 100 seconds smoothing and the GAST-D projection matrix ($\boldsymbol{S}$) which is computed using error

models for 30 seconds smoothed measurements. If a fault is detected, the aircraft can either use a different geometry (for which the threshold is not exceeded) or downgrades to the GAST-C service.The D-RAIM algorithm for fault detection is performed also for including the satellites excluded by the airborne CCD monitor (which is described in the following section). This because the CCD monitor excludes the flag satellites for 20 minutes from the position solution. An earlier inclusion of the satellite in the position solution can be enabled by the use of the fault detection algorithm. A satellite is re-included if the protection levels (both lateral and vertical) are lower than the alert limits and the test statistic is below the threshold (see Section 2.3.9.7 of DO-253D, [18]).

2.7.8 Ionospheric anomaly mitigation in GAST-D

As previously discussed, in GAST-C the ground is fully responsible to protect the users against any ionospheric anomaly. This is achieved through inflation of broadcast parameters. The process can result in a decrease of the availability of the system because it inflates the values even when the gradients do not occur. In GAST-D, the responsibility to monitor ionospheric gradients is shared between the ground station and the airborne receiver. One first change in the GAST-D concept is the use of the 30 seconds smoothed position solution. Several monitors have been introduced on the airborne user for the detection of ionospheric gradients which will be discussed later in this section.

As the ground station and the airborne receiver share the responsibility to monitor the ionospheric gradient and they mitigate different threats, the complete ionospheric threat mitigate is difficult to demonstrate. Extensive studies have been conducted to validate that the performance requirements can be met by the combination of the ground and airborne monitors. The validation of the monitoring has been done through exhaustive simulations to show that the maximum errors at the output of the monitoring (on both the ground station and airborne receiver) meet the touchdown requirements. The work in [24] provides an overview of the validation methodologies and of the monitors integrated to tackle the ionospheric anomalies for the CAT-III service. As the ionospheric anomalies are treated as a malfunction, the integrity requirements are defined to limit the failures to a probability of 10^{-9} (see Table 2.10). An apriori probability (P_{fault} in Eq. (2.66)) can be taken into account in the derivation of the monitors requirements, but the validation studies have been performed assuming a probability of 1 [24]. In this case, the requirement allocated to the ionospheric anomalies translates into a limit on the differential corrected 30 second smoothed pseudorange error such that the probability of being larger than 2.75 m is lower than 10^{-9} per landing [24]. This value limits the maximum error on each satellite and thus its contribution to the position error. The value was derived such that when "translated into position domain, this performance is sufficient to enable suitably equipped aircraft to meet the requirements for CAT-III autoland" [24].

The ionospheric anomalies are modeled using the same wave front model mov-

ing with constant speed as described in Figure 2.11, but it was extended from the CONUS model to cover all mid-latitude measurements. The maximum gradient size was extended to 500 mm/km with widths between 25 km and 200 km and a maximum value of the gradient depth of 50 m (see Table 1 in [24]). The simulations also included different aircraft profiles speed as described in Table 2 in [24].

As previously mentioned, different monitors implemented in the ground station and the airborne receiver mitigate different parts of threat space. Figure 2.20 shows the main ionospheric gradient scenarios that can occur causing a threat for the GBAS user and need thus to be taken into account in the validation phase [69].

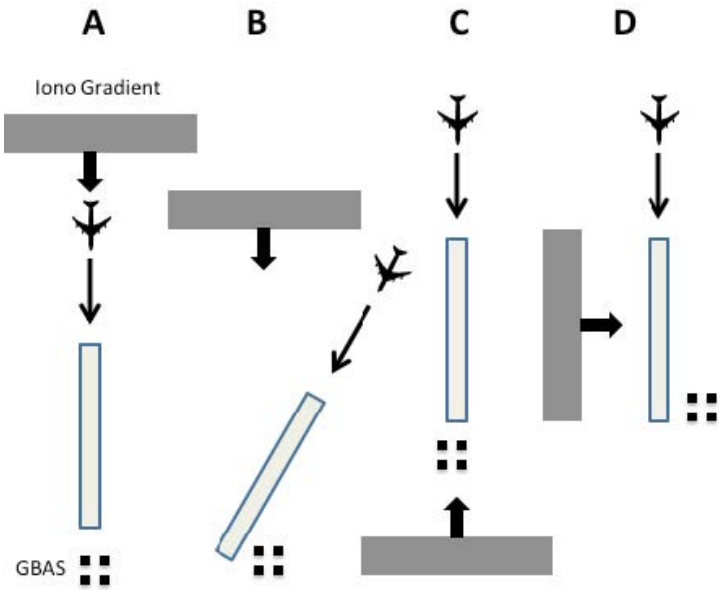


Figure 2.20: Ionospheric gradient orientations constituting a threat to GAST-D from [13]

Case A illustrates the situations when the ionospheric gradient approaches from behind the aircraft in the direction of the approach path. In this case, the airborne user is the first affected by the gradient (before it arrives to the ground stations). It is expected that most the time, the airborne monitors will detect the gradient and will either remove the affected satellites from the position solution or disable the GAST-D mode. The airborne monitoring will not be effective in this case if the ionospheric gradient front velocity is close to the speed of the airborne IPP. For this situation, a ground monitor is required to detect the gradient.

Case B represents the situation when the ionospheric front is at an angle to the approach direction. The gradient is visible first at the aircraft user and the airborne monitors can provide detection for all the cases and no additional ground monitoring

is required (due to the angle difference between the ionospheric front and the aircraft user).

In case C the front approaches from the opposite direction of the approach and will impact the ground station prior to the airborne. This scenario requires the ground monitoring as the airborne monitors may not able to detect the gradient before the build-up error is already large enough.

Case D represents the scenario where the gradient front velocity is orthogonal to the approach direction. This scenario is the most problematic because none of the ground or the airborne monitors might detect the gradient if it moves with a slow speed. One solution that can solve this issue is to restrict the distance between the ground station and the LTP to minimize the error that can build up at the user (e.g. to 5 km).

These scenarios highlight that the mitigation of the ionospheric gradients has to be done as a shared work between the ground and the airborne monitors because each of the monitors can cover a portion of the threat space. The ground subsystem includes a CCD monitor similar with the GAST-C one and the specific design will be discussed in next. However, this monitor will not detect gradients with front velocities close to the speed of the ground station IPP. Thus, an additional Ionospheric Gradient Monitor (IGM) is implemented in the ground system. This monitor is needed to detect mainly the gradients that approach from the opposite direction of the approach and the cases not covered by the CCD monitors.

On the airborne side two new monitors are part of the GAST-D architecture: a CCD monitor and a DSIGMA monitor which are responsible to detect the gradients that are visible at the aircraft, but not at the ground station. Furthermore, the airborne system performs a geometry screening algorithm to ensure that unacceptably large pseudorange errors due to ionospheric gradients do not occur. In following each of these monitors implemented in the ground system and airborne receiver are discussed.

Ground Ionospheric Gradient Monitor

The first version of the SARPS [38], required the ground to implement an ionospheric gradient monitor. A first implementation of a monitor that was adopted by the community was introduced by Khanafseh in [70]. The monitor uses the double difference carrier phase measurements between the known baselines of the reference receivers to detect instantaneous ionospheric fronts. The algorithm models the ionospheric front as a slant gradient and assumes that the baselines between the antennas in the GBAS ground station is aligned with the runway.

The details of the implementation are given in [70] which shows also the performance of the monitor considering different baseline lengths and different noise levels for the differential carrier phase measurements. Gradients between 470 - 1450 mm/km can be detected using a 100 m baseline and a standard deviation of the differential

carrier phase measurements of 6 mm/km. The monitor is sensitive to the quality of the carrier phase measurements and requires very small antenna phase center variation and carrier phase measurement noise less than 10 mm. Furthermore, the use of the monitor restricts the distance between the reference point of a ground station and the LTP of any runway which supports GAST-D to 5 km.

In 2014, during the performance analysis of a GAST-D IGM, increased noise of short duration (less than 2 minutes) was observed in the monitor test statistic [71]. The source of these gradients was small scale tropospheric noise, which became active during warm sunny days. Even if the size of these tropospheric gradients are small and of short duration, they lead to false detection in the ionospheric gradient monitor and impact the monitor performance.

Following this event, an IGM ad hoc team was formed to develop a reformulation of the ionospheric mitigation in GAST-D requirements. Different approaches were proposed and discussed. One of the approaches was to develop a monitor that could separate the signature of the tropospheric noise from true ionospheric gradients as the tropospheric errors show a higher autocorrelation [72]. However, it was not possible to utilize these characteristics to define a tropospheric error monitor [73].

The updated SARPS published in 2018 [13] replaced the previous requirements for the ground station. The change requires the ground system to implement an ionospheric gradient monitor with a more general requirement to limit the range error caused by an anomalous ionospheric gradient [73]. In this concept, the ground station broadcasts two additional parameters (Y_{EIG} and M_{EIG}) to represent the maximum error the ground system is able to protect. The first parameter, the Y_{EIG} represents the maximum value of the ionospheric gradient error (E_{IG}) at the GBAS reference point. The second parameter, M_{EIG} is the slope of the maximum E_{IG} versus distance. The maximum ionospheric gradient error, the E_{IG} is computed by the airborne receiver as

$$E_{\mathrm{IG}}(D) = Y_{\mathrm{EIG}} + M_{\mathrm{EIG}} \cdot D, \tag{2.77}$$

where D is the distance (in km) between the aircraft and the GBAS reference point.

The E_{IG} parameters are station specific and do not change over time. They are determined by the ionospheric monitoring capabilities of the ground station and the ionospheric threat space at the location of the GBAS installation. The use of these parameters allows larger distances between the reference point and the LTP (above 5 km) and has the potential to improve the system availability for approaches with short distance or reduced threat space [74]. The transition of the requirements on the range domain requires the ground manufacturer to limit the maximum range error due to the ionospheric anomalies to 2.75 m at the LTP taking into account all the ground and airborne monitoring.

Ground Code Carrier Divergence

The general concept of this monitor stays unchanged from GAST-C, but different time constants were considered. In the final validation of the ICAO requirements [24] a smoothing time constant of 25 seconds was used instead of 100 seconds in GAST-C and the monitor threshold was derived as 40.18 mm/sec based on an allocated false detection probability of $3/4 \cdot 10^{-9}$ [24]. In GAST-D, the main purpose of the CCD monitor is the detection of the ionospheric gradients.

Airborne Code Carrier Divergence monitor

Compared to GAST-C, the CCD monitoring was also introduced into the airborne system in GAST-D. The general principle of the monitor stays unchanged. Only the airborne filter uses a time constant τ of 100 seconds and furthermore a different detection threshold of 0.0415 m/s [24]. Initially the threshold was set to 0.0125 m/s [75]. The new values were derived from multiple flight data collected on different aicraft and receiver tyes in Europe, Japan and United States to meet an acceptable ranging source continuity level [24].

The monitor is effective in detecting fast moving ionospheric front that impact the airborne user prior to the ground station. In case the monitor threshold is exceeded, the specific satellite is excluded for 20 minutes from the GAST-D solution. The use of D-RAIM algorithm can, however reinclude the satellite faster.

Airborne Dual-Solution Ionospheric Gradient Monitor

The Dual Solution Ionospheric Gradient Monitoring Algorithm is specific to the GAST-D system as it compares the difference between the 30 second and the 100 second smoothed measurement. To be more specific, there are two DSIGMA implementations running in parallel, one is acting on the final position solution; the other one is acting on the pseudoranges. The position DSIGMA compares the difference of the position estimates calculated based on both smoothing time constants. The lateral and vertical difference between both solutions are called D_{l} and D_{v}, respectively. These two differences are used in the calculation of the protection levels for GAST-D (Section 2.7.3). Recall, that the integrity parameters in the protection level equation are based on a smoothing time constant of 100 seconds, whereas the position solution used in GAST-D is based on 30 seconds smoothing. Thus, the residual noise and multipath is somewhat larger than in the case of GAST-C where the 100 seconds smoothed solution is used. To account for the difference resulting from the shorter smoothing time constant, the D_{l} and D_{v} terms are added to the lateral and vertical protection levels.

The use of the D_{l} and D_{v} was originally also envisioned to be used for mitigation of part of the ionospheric threat space by comparing them to a threshold of 2 m [75]. However, it proved more useful to use the DSIGMA concept on a pseudorange level such that potentially affected satellites can be excluded. The difference between the

corrected 100 s and 30 s smoothed pseudoranges are evaluated. If the difference has exceeded 0.976 m at any time when the aircraft was inside the PAR and the difference has exceeded 0.348m in the last 60s, a DSIGMA range domain failure condition is assumed and the satellite shall be removed from the position solution (Section 2.3.9.7 of DO-253D, [18]).

Airborne geometry screening

The satellite geometry screening in the airborne system for GAST-D is completely different from the previously described geometry screening in the ground station for GAST-C. Its threshold values are determined by the characteristics of the airborne system, the autopilot performance of the aircraft as well as the capabilities of the GBAS ground station that provides the approach service. Under the term airborne geometry screening a series of evaluations are summarized.

First, the vertical and lateral alert limits are computed based on the position of the aircraft. They are then compared to an internal user-specified maximum value for the VAL and Lateral Alert Limit (LAL). That internal limit may be smaller than the values computed according to the GAST-D SARPS. Essentially, limiting the alert limits to an internal $\max(VAL)/\max(LAL)$ requires a better positioning accuracy, in order to meet the touchdown requirements in the nominal case (see Section 2.7.1). These internal alert limits values are determined by the airframe manufacturer in autoland simulations and are a trade-off between autopilot and navigation system performance.

Second, the projection factors $s_{\text{apr_lat}}$ and $s_{\text{apr_vert}}$ relating the pseudorange and the position domain are evaluated. Again, they are compared to user specified limits $\max(s_{\text{apr_lat}})$ and $\max(s_{\text{apr_vert}})$. This process ensures that not too much weight is given to a single satellite in the position solution. Thus, the maximum position error caused by a single satellite is limited. The parameters are again derived based on the individual characteristics of a specific installation.

Third, the maximum undetected pseudorange error E_{IG} on the 30 seconds smoothed pseudoranges due to an undetected ionospheric gradient is calculated based on integrity parameters and the FAS data transmitted by the ground station. It is defined as described in Eq. (2.77). The Y_{EIG} and M_{EIG} have to ensure that all predetermined potentially undetected pseudorange errors remain below the described linear relation. The E_{IG} is then used to compare $s_{\text{apr_vert}_2}$ (the sum of the largest two absolute values of $s_{\text{apr_vert}}$) and $s_{\text{apr_vert}_2}$ (the sum of the largest two absolute values of $s_{\text{apr_lat}}$) to thresholds $\max(s_{\text{apr_vert}_2})$ and $\max(s_{\text{apr_lat}_2})$ defined as

$$\max(s_{\text{apr_vert}_2}) = \frac{\max(E_{\text{v}})}{E_{\text{IG}}} \tag{2.78}$$

$$\max(s_{\text{apr_lat}_2}) = \frac{\max(E_{\text{l}})}{E_{\text{IG}}}, \tag{2.79}$$

where $\max(E_{\text{l}})$ and $\max(E_{\text{v}})$ are again user specified values for the largest allowable vertical and lateral position errors, respectively. These values again result from

autoland simulations and are the largest navigation system errors for which the touchdown requirements can be fulfilled (Section 2.3.9.4 of DO-253D [18]).

3 DFDC GBAS and considerations

The largest concern in ensuring integrity of the navigation solution in the current GBAS architecture results from ionospheric gradients that could potentially cause large position errors. As previously discussed in Chapter 2, in GAST-C this task is accomplished by inflating integrity parameters to protect users against the effect of worst case gradients. In GAST-D, additional monitoring algorithms are introduced to eliminate this conservatism. However, the monitors are highly sensitive and potentially cause undesired monitors triggers. Furthermore, they require very specific siting of the reference antennas. Especially at large, space constrained airports this causes significant problems in finding appropriate sites for the ground station. Both service types were designed with the CONUS ionospheric threat model in mind. However, significantly larger gradients and frequent scintillations were observed in equatorial regions [1, 3, 20]. Under these conditions the availability will be reduced significantly on both GAST-C and GAST-D due to the conservative overbounding or to the sensitive monitoring [2, 3, 23]. The scintillation effect, in particular, causes the receivers to lose lock of one or more satellite signals. Thus the satellite geometry is degraded, leading to increased protection levels. Current systems are thus mainly operational in mid-latitudes with quite ionospheric conditions. The development of the system to support operations also under more severe scenarios is still ongoing.

With the increased availability of additional GNSS constellations, signals from a large number of satellites are already available in the L5/E5a band. An international effort has been started to develop concepts and standards for the combination of signals and constellations for an improved GBAS service.

Four core constellation are currently considered in the standardization discussions [76]: the United States's GPS, the Russian constellation, Global Navigation Satellite System (GLONASS), the European constellation, Galileo, and China's BeiDou Navigation Satellite System (BDS).

The GPS constellation comprises already 12 Block IIF satellites that include signals on the L5 band - a second frequency band that is part of the ARNS. Furthermore, the new generation satellites (Block III), with the first launch in 2019 and more to come in the next years, also include signals on the L5 band. The GLONASS constellation comprises 24 satellites that are broadcasting on L1 frequency band. The current satellites use a Frequency Division Multiple Access (FDMA), but Code Division Multiple Access (CDMA) will be implemented on all satellites on L5 band by 2021. The Galileo constellation comprises at the time of writing (at the end of 2019) 22 operation satellites (26 in orbit from which 2 in elliptical orbit, 2 with technical issues) with activated E1(L1) and E5a(L1) signals and the full operation constella-

tion is planned by 2020. The BDS constellation is currently under deployment and 27 satellite providing B1C and B2A signals for use are planned to be operational from 2020.

An increased number of available satellites from different constellations adds sufficient redundancy to detect and remove potentially compromised satellites without significantly deteriorating the overall satellite geometry. In the same way, the larger number of satellites provides increased robustness against ionospheric scintillations which would typically only affect one part of the sky and thus few satellites at the same time. The combination of signals from two frequencies allows for effective detection of ionospheric gradients and bear the potential to significantly reduce the conservatism included in the current service types.

The addition of new signals from a second frequency and different constellations yields to significant amount of possible combinations of frequency and thus to many different processing modes that can be integrated in the GBAS system. Each processing mode comes with different advantages and disadvantages. However, a number of technical challenges still have to be overcome before a DFDC service can become operational.

Within Europe, the SESAR Program [11], founded by the European Union and Eurocontrol, is dedicated to define a concept of future DFDC GBAS service type. This new DFDC concept focuses on the use of the signals from GPS Block IIF and Galileo satellites on L1/E1 and L5/E5a bands and is intended to extend the CAT-II/CAT-III GBAS service.

This chapter discusses the possible architecture of a DFDC GBAS and the status of the development of a DFDC GBAS concept. The considered concept is based on the use of GPS and Galileo satellites. The chapter is organized as follows: Section 3.1 provides an overview on all the processing modes enabled by the use of new signals in GBAS. Next, a discussion on the current status is given in Section 3.2 including the constrains that have to be met when a new GBAS architecture is being developed and the initial concept proposed within SESAR activities. This work will extend the modes proposed within SESAR and the considerations made are detailed in Section 3.2.4. Based on this, the updates on the ground system and airborne equipment are then presented. Section 3.5 discusses the additional threats that should be considered for DFDC GBAS. The integrity aspects are finally detailed in Section 3.6

3.1 Candidate options for DFDC GBAS

The main goal of the DFDC GBAS service is to improve the ionospheric mitigation and increase the availability of the existing single frequency system. However, the use of a second frequency in GBAS enables several processing modes which have the potential to detect and mitigate the ionospheric anomalies. Two dual-frequency smoothing algorithms, Divergence-free (Dfree) and Ionosphere-free (Ifree), have been proposed to mitigate ionosphere gradients in GBAS [77, 78, 79]. The Dfree combi-

nation removes the ionospheric divergence introduced by the smoothing filter, while the Ifree combination removes completely the first order ionospheric delays.

The use of the Dfree and Ifree techniques require both the ground and the airborne receiver to use the same smoothing algorithm. In both cases, the position solution would be based either on the Dfree smoothed and corrected pseudoranges or the Ifree smoothed and corrected pseudoranges.

On the other side, another possible processing mode would be to provide the existing single frequency (single or dual-constellation) L1/E1 positioning and use the dual-frequency capability for ionospheric monitoring. The next section describes each of this processing modes and discusses their advantages and disadvantages.

3.1.1 Divergence free smoothing

Divergence-free smoothing eliminates the ionospheric delay from the smoothing filter input and, thus, removes the code-carrier divergence effect that affects the single frequency smoothing. This is achieved by using a linear combination of dual-frequency carrier phase measurements as the carrier input into the smoothing filter which is described as

$$\phi_{\mathrm{Dfree}_{i,j}} = \phi_i - \frac{2 \cdot f_j^2}{f_j^2 - f_i^2} \cdot (\phi_i - \phi_j), \tag{3.1}$$

with ϕ_i, ϕ_j being the carrier-phase measurements on frequency band i and j and f_i, f_j the central frequencies value for frequency bands i and j (1575.42 MHz for L1 and 1176.45 MHz for L5). The Dfree smoothed pseudorange (noted as $\overline{\rho_{\mathrm{Dfree}}}^{s}_{r,i,j}$) for a receiver r and a satellite s using frequencies i and j at epoch k is obtained as

$$\overline{\rho_{\mathrm{Dfree}}}^{s}_{r,i,j}(k) = \frac{\Delta T}{\tau} \cdot \rho^{s}_{r,i}(k) + (1 - \frac{\Delta T}{\tau}) \cdot \left[\overline{\rho_{\mathrm{Dfree}}}^{s}_{r,i,j}(k-1) + \phi_{\mathrm{Dfree}}{}^{s}_{r,i,j}(k) - \phi_{\mathrm{Dfree}}{}^{s}_{r,i,j}(k-1)\right]. \tag{3.2}$$

Similar to the single frequency smoothed pseudorange, the Dfree smoothed pseudorange at epoch k is formed by the EWMA of the previous $k-1$ epochs of the CMC series (in this case, $CMC_{\mathrm{Dfree}_{i,j}}$) to which the carrier phase $\phi_{\mathrm{Dfree}_{i,j}}$ measurement is added to reconstruct the geometry (see Appendix A.1):

$$\overline{\rho_{\mathrm{Dfree}}}^{s}_{r,i,j}(k) = \phi_{\mathrm{Dfree}}{}^{s}_{r,i,j}(k) + (1-\alpha)^{k-1} \cdot \underbrace{\left(\rho^{s}_{r,i}(1) - \phi_{\mathrm{Dfree}}{}^{s}_{r,i,j}(1)\right)}_{CMC_{\mathrm{Dfree}_{i,j}}} + \alpha \cdot \sum_{n=2}^{k} (1-\alpha)^{k-n} \cdot \left(\rho^{s}_{r,i}(n) - \phi_{\mathrm{Dfree}}{}^{s}_{r,i}(n)\right). \tag{3.3}$$

The EWMA of the $CMC_{\mathrm{Dfree}_{i,j}}$ does not contain the ionospheric error and, thus, the smoothed Dfree pseudoranges do not contain the single frequency filter-induced error in the ionospheric delay (code carrier divergence). However, they still contain the raw ionospheric error from the carrier-phase measurements ($\phi_{\mathrm{Dfree}}{}^{s}_{r,i,j}(k)$). Expanding

the terms in Eq. (3.3) the smoothed pseudorange $\overline{\rho_{\text{Dfree}}}^{s}_{r,i,j}(k)$ at epoch k becomes

$$\overline{\rho_{\text{Dfree}}}^{s}_{r,i,j}(k) = R^s_r + c\cdot(\delta t_r - \delta t^s) + T^s_r - I^s_{r,i} + e^s_{r,i} + mp_{\text{Dfree}}{}^{s}_{r,i,j} + \eta_{\text{Dfree}}{}^{s}_{r,i,j} + a_{\text{Dfree}}{}^{s}_{r,i,j} + \\ + \overline{MP}^s_{r,i} + \bar{\varepsilon}^s_{r,i} + \overline{A}^s_{r,i} + \overline{mp_{\text{Dfree}}}^{s}_{r,i,j} + \overline{\eta_{\text{Dfree}}}^{s}_{r,i,j} + \overline{a_{\text{Dfree}}}^{s}_{r,i,j}. \tag{3.4}$$

Note that "$-$" sign in the ionosphere comes from the carrier phase measurements. The notations used are the same as in Eq. (2.4) and the terms $mp_{\text{Dfree}}{}^{s}_{r,i,j}$, $\eta_{\text{Dfree}}{}^{s}_{r,i,j}$ and $a_{\text{Dfree}}{}^{s}_{r,i,j}$ represent the multipath, noise and hardware errors present in the Dfree smoothed pseudoranges described as

$$\begin{cases} mp_{\text{Dfree}}{}^{s}_{r,i,j} & = mp^s_{r,i} - \frac{2\cdot f_j^2}{f_j^2 - f_i^2}(mp^s_{r,i} - mp^s_{r,j}) \\ \eta_{\text{Dfree}}{}^{s}_{r,i,j} & = \eta^s_{r,i} - \frac{2\cdot f_j^2}{f_j^2 - f_i^2}\cdot(\eta^s_{r,i} - \eta^s_{r,j}) \\ a_{\text{Dfree}}{}^{s}_{r,i,j} & = a^s_{r,i} + \frac{2\cdot f_j^2}{f_j^2 - f_i^2}\cdot(a^s_{r,i} - a^s_{r,j}), \end{cases} \tag{3.5}$$

The main advantage of the Dfree solution is that it removes the additional ionospheric delay introduced by the smoothing filter and the output noise is similar with the one of the single frequency smoothing. This is because only one single frequency code measurement is used as code input (recall that the carrier phase noises are small and can be neglected). The impact of an ionospheric gradient is not affected by the smoothing filter and thus can be detected much faster, as shown in [79]. However, an additional ionospheric monitor has to be implemented by the ground system and the airborne receiver in order to mitigate the effect of ionospheric gradients [78]. Furthermore, this processing mode requires the provision of the Dfree corrections to enable the application of the Dfree smoothing on the airborne receiver.

3.1.2 Ionosphere free smoothing

A second dual-frequency technique is the Ifree smoothing. The Ifree smoothing removes the ionospheric error (to a first approximation) by using the ionosphere-free combinations of both code and phase as inputs to the smoothing filter. Both code and phase inputs combine dual-frequency measurements from frequency bands i and j, as

$$\phi_{\text{Ifree}}{}^{s}_{r,i,j} = \frac{f_i^2}{f_i^2 - f_j^2}\cdot\phi^s_{r,i} - \frac{f_j^2}{f_i^2 - f_j^2}\cdot\phi^s_{r,j}, \tag{3.6}$$

$$\rho_{\text{Ifree}}{}^{s}_{r,i,j} = \frac{f_i^2}{f_i^2 - f_j^2}\cdot\rho^s_{r,i} - \frac{f_j^2}{f_i^2 - f_j^2}\cdot\rho^s_{r,j}. \tag{3.7}$$

The Ifree smoothed pseudoranges at epoch k are formed as

$$\overline{\rho_{\text{Ifree}}}^{s}_{r,i,j}(k) = \frac{\Delta T}{\tau}\cdot\rho_{\text{Ifree}}{}^{s}_{r,i}(k) + (1 - \frac{\Delta T}{\tau})\cdot\left[\overline{\rho_{\text{Ifree}}}^{s}_{r,i,j}(k-1) + \phi_{\text{Ifree}}{}^{s}_{r,i,j}(k) - \phi_{\text{Ifree}}{}^{s}_{r,i,j}(k-1)\right]. \tag{3.8}$$

The Ifree smoothed pseudorange can also be obtained by forming the Ifree combination of the single frequency smoothed pseudoranges on frequencies i and j:

$$\overline{\rho_{\text{Ifree}}}^{s}_{r,i,j}(k) = \frac{f_i^2}{f_i^2 - f_j^2} \cdot \overline{\rho}^{s}_{r,i}(k) - \frac{f_j^2}{f_i^2 - f_j^2} \cdot \overline{\rho}^{s}_{r,j}(k). \tag{3.9}$$

The derivation of this equality is shown in Appendix A.2. The relation holds only if identical smoothing algorithm are applied to the single frequency pseudoranges with the same parameters (e.g. the same smoothing constant for both frequencies and the single frequency filters are reset at the same times for both frequencies). Differences in the filter parameters would lead to a different additional delay in the ionospheric divergence for different frequencies and are not completely removed by the Ifree combination.

The smoothed Ifree pseudoranges no longer contain ionospheric errors (to a first-order approximation), but they contain the combination of the errors (multipath, noise, hardware) from two code measurements. This increases the noise on the ranges error and the position solution. One solution to overcome this issue is the use of a larger smoothing time constant yielding to decreased noise and multipath errors in the Ifree pseudoranges. This is possible as the Ifree smoothing filter does not contain the ionospheric delay which was the main constraint in setting the smoothing time constant for single frequency. However, a different smoothing constant would, however, require additional corrections to be broadcast by the ground receiver.

One of the advantages of the Ifree processing mode is that it can be used by the airborne receiver either by broadcasting specific Ifree corrections (using any smoothing time constant) or by broadcasting single frequency smoothed corrections using the same smoothing time constant for both frequencies. The airborne receiver forms the Ifree combination using its own measurements based on the smoothing time constant used to process by the ground corrections.

3.1.3 Single-frequency with dual-frequency monitoring

While the Ifree combination eliminates the ionospheric gradients, it is not always beneficial due to the increased noise in the ranging errors and implicitly in the position errors. Thus, a likely scenario for the future service types would be to base the positioning on the single frequency methods and to use the second frequency only for ionospheric gradient monitoring. The dual-frequency Ifree processing could then be used in case an ionospheric gradients is detected.

In this case, the position solution can be based either on dual-constellation single-frequency L1/E1 smoothed and corrected pseudoranges or on dual-constellation L5/E5a smoothed and corrected pseudoranges. In the current system, the 100 seconds and 30 seconds smoothing time constants are used. The shorter smoothing time constant (30 seconds) is used for a faster detection of ionospheric gradients. The drawback of the shorter smoothing time is an increased noise in the position solution. If on the other side, the monitoring of the ionospheric gradients is done independently based

on dual-frequency measurements, the use of a shorter smoothing time constant is not necessary. However, the choice of the smoothing time constant depends on the technical constrains (e.g. VDB capacity) which are discussed in the next section. Compared to the current single frequency single constellation implementation, the increase in the number of satellites improve the geometry and yield to lower s-factors and thus lower protection levels. In case one of the constellations is not available, the performance of this processing mode would be similar to the current GAST-D processing mode.

The second frequency can be used to monitor the ionospheric gradients and remove the affected satellites from the position solution. Assuming that both the ground station and the aircraft receiver are capable to track dual-frequency signals, an ionospheric monitoring can be built by comparing estimates of the ionospheric delays from the pseudorange corrections with ionospheric delays estimates obtained from the measurements of the airborne receiver. A first concept of such a monitors was proposed in [80]. The algorithm is implemented in the airborne receiver and uses the current geometry without conservative assumptions made by the ground system. Due to the way the pseudorange corrections are generated, the ionospheric delays experienced at the ground station can not be directly estimated, but rather a pseudo-ionospheric estimate. This is because in the computation of the pseudorange correction, the mean over all satellites is removed to eliminate the receiver clock bias. The mean contains also a part of the ionospheric error common to all satellites. However, as shown in [80], applying a similar mean removal process on the ionospheric estimates from the aircraft allows a comparison of the two estimates. Based on the performance requirements and the actual geometry of the aircraft, the threshold can be defined in real time by the airborne receiver. Details of the implementation and evaluations of the monitor in flight tests are given in [80]. The advantage of the monitor is that it acts on the range domain and it excludes from the position solution only the satellites affected by ionospheric gradients. A switch to an Ifree solution could be performed in case a large portion of the sky is affected by ionospheric anomalies. Furthermore, this monitoring strategy moves the responsibility of the ionospheric gradient mitigation completely to the airborne system. The approach is less conservative than the existing GAST-C and GAST-D concepts because the derivation of the monitor threshold is based on the actual satellite geometry and, thus, reflects better the current positioning performance.

3.2 Discussion on service types and current status

Each of the processing mode discussed in the previous section represents a promising candidate solution for DFDC GBAS. However, several navigation and technical constraints have to be met when the architecture for the DFDC GBAS is defined. This section discusses some of these constrains and details the initial concept of future DFDC GBAS proposed within SESAR Program. The concept is based on the use of signals broadcast on L1/E1 and L5/E5a frequency bands by the GPS Block IIF and Galileo satellites.

3.2.1 Constrains for DFDC GBAS

A first constraint is that a new GBAS system has to be backwards compatible to the existing GAST-C and GAST-D systems. This is because a large number of users will be equipped with the current single-frequency single-constellation GAST-C or GAST-D hardware until a new service type will be standardized. Thus, the new service type has to provide the corrections and the integrity parameters necessary for GAST-C and GAST-D (see Chapter 2) through the existing VDB.

The additional corrections and integrity parameters needed to support a new service type have to be accommodated in the remaining VDB capacity. When adding a second constellation and a second frequency, one of the main constraints is thus, the limited VDB capacity. Within SESAR 15.3.7 project, a first concept of integrating corrections for an additional constellation and an additional frequency in the existing limited capacity of the VDB that is also backwards compatible to legacy VDB has been developed. The concept relies on the use of the current VDB structure and hardware.

The concept supports the broadcast of corrections and integrity parameters for a set of selected satellites from a second constellation for L1/E1 for the two smoothing time constants (100 seconds and 30 seconds) in a similar manner as in the current single constellation GAST-C and GAST-D architecture.

Based on this scheme, it is unlikely to have specific corrections for a dual-frequency smoothing technique (Dfree or Ifree) or corrections with two smoothing time constants for the second frequency (L5/E5a). The proposed solution includes broadcast pseudorange corrections for the second frequency (L5/E5a) for only one smoothing time constant. Details of this scheme are given in [81]. Using the relation from Eq.(3.9), the Ifree pseudorange corrections can be formed by the airborne receiver from the broadcast single frequency corrections on L1/E1 and L5/E5a. This solution works only under the condition that the same smoothing time constant is applied to both single frequency correction, which limits the smoothing time constant for the L5/E5a pseudorange corrections to 100 or 30 seconds. The proposed VDB scheme defined is discussed next.

3.2.2 Proposed VDB Scheme

The DFDC GBAS architecture needs additional messages in order to cover the different processing modes based on the second constellation and the second frequency. As previously discussed, within SESAR project a first concept of integrating the additional messages in the existing VDB link has been proposed. The concept relies on the use of the same hardware and implementation structure of the existing VDB for with the main goal to ensure backwards compatibility.

Two new messages are introduced to support the new functions: a message for the L5/E5a pseudorange corrections called Message Type (MT) 42. Unlike the message carrying the L1 pseudorange corrections in the current GAST-C and GAST-D

architecture, this message is split over multipath consecutive frames by reducing the minimum update rate for these corrections. The minimum required update rate for MT 42 is 2.5 seconds instead of 0.5 seconds [82]. Such a decrease in the update rate has several implications, such as the difficulty to ensure the Time to Alert (TTA) requirement. For this, an additional integrity message which is sent with a higher update rate is introduced. The message is refers as MT 50. This message is transmitted in different slot and contains two bits for each satellite of the two constellations. The first one indicates the usability of the L5/E5a corrections and the second bit the usability of the Ifree pseudorange corrections. In addition to these two new message types, additional data blocks are included in the existing messages to accommodate the pseudorange corrections and integrity parameters for the E1 signal. An example of the distribution of the MT within the slots for scenario with dual VDB transmit antennas is shown in Figure 3.1. The scheme assumes 8 slots per frame, 15 pseudorange corrections for L1/E1 signals and 7 L5/E5a pseudorange corrections [82]. A detailed and complete definition of the new message types and message content supporting such backward compatibility is included in [81] and in Appendix A of [82].

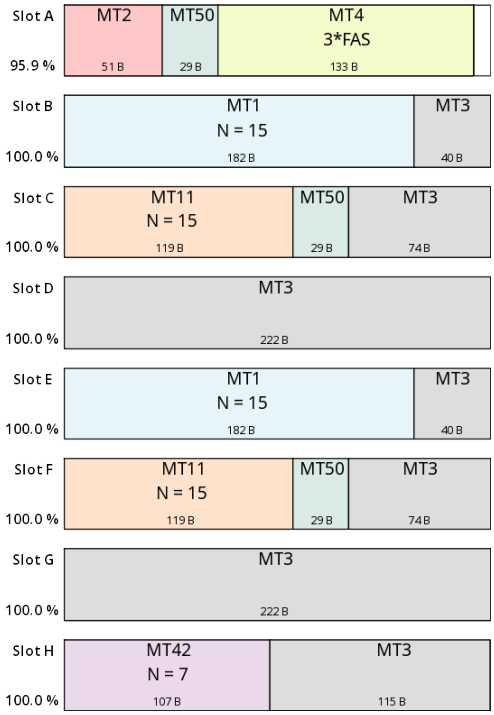


Figure 3.1: Example of distribution of VDB messages for a DFDC GBAS scenario with 2 VDB antennas (taken from [82])

3.2.3 Current proposed processing modes

Based on this VDB scheme, a preliminary concept for DFDC has been proposed within SESAR with the aim to optimize the benefits of the use of a second constellation and additional signal in order to offer robustness of the GBAS system under ionospheric anomalies conditions [82]. This concept introduces, two additional service types in addition to the existing GAST-C and GAST-D as follows:

- GAST-E which is based on the use of the L5/E5a correction and offers a CAT-I service. This mode is foreseen as a fallback mode in case the L1 frequency is not available.
- GAST-F which refers to the use of dual-frequency signals from GPS L1/L5 and Galileo E1/E5a bands.

Note that the names attributed to the new service types are still preliminary and might change in the future.

The GAST-E service providing a L5/E5a is currently foreseen only as a fall-back mode and a L5/E5a only mode is not taken into account as the future GAST-F service. The reason for this is that even if the signals on L5 show better performance in terms of noise and multipath, the ionospheric error on the signals from this band is 1.8 larger than the ionospheric error on the L1 signals [83]. It was thus considered that the decrease in noise does not compensate for the increase in the ionospheric error and a L5/E5a processing mode will lead to worse performance compared with L1/E1 processing mode.

The GAST-F service is defined to support operations under CAT-II/CAT-III conditions and two processing modes are currently studied in SESAR as primary modes:

- Single-frequency dual-constellation L1/E1 processing mode based on 100 seconds smoothing with dual-frequency ionospheric monitor.

  This processing mode is considered assuming that the Ifree positioning mode is insufficient for a CAT-III mode and corresponds to the processing scheme described in Section 3.1.3 Based on the proposed VDB scheme the position solution can be based either on 100 seconds or on 30 seconds as pseudorange corrections for dual-constellation satellites for both smoothing time constant are available. The shorter smoothing time constant is mainly beneficial for faster detection of the ionospheric gradients. As in DFDC concept, the ionospheric gradients are monitored based on the second frequency, the use of 30 seconds is not necessary and the 100 seconds smoothed position solution can be used. The advantage of he longer smoothing time constant is the lower noise and multipath errors (and thus lower position errors). Compared to a single-frequency dual-constellation L5/E5a only processing mode, the L1/E1 single frequency mode has the benefit of having a 0.5 seconds correction update interval, while for some GAST-F configurations any corrections containing L5/E5a measurements may be updated only every 2.5 seconds.

- Dual-frequency dual-constellation Ifree (L1/L5 E1/E5a) processing mode based on 100 seconds smoothing time constant

  This mode envisages the estimation of the position solution based on the dual-constellation Ifree 100 seconds smoothed and corrected pseudoranges. The Ifree pseudorange corrections are formed by the airborne receiver from the 100 seconds smoothed single-frequency L1/E1 and L5/E5a pseudorange correction (see Section 3.1.2). The advantage of this mode is that it does not require a specific ionospheric monitor and the system does not have to switch to a different processing mode during anomalous ionospheric conditions. However, the increase in the noise and multipath errors might degrade the overall performance and lead to loss of availability. Furthermore, for some ground stations the Ifree corrections might have a 2.5 seconds update interval. The decision on which of the processing modes will be considered as primary mode is not yet final and further studies analyze the benefits of each of the options.

3.2.3.1 Processing modes not considered

The proposed scheme disregards the use of the Dfree mode. The Dfree smoothing technique removes the ionospheric divergence, but still constrains the raw ionospheric error. Thus, compared to the Ifree processing mode that eliminates the first order components of the ionospheric error completely, a Dfree mode would still require an ionospheric monitor. Furthermore, in order to enable the Dfree smoothing on the airborne receiver, the ground system has to broadcast Dfree specific corrections. Due to the limited VDB capacity broadcasting these corrections would disregard the transmission of the L5/E5a corrections that enable both the L5/E5a mode only and the Ifree mode.

The use of an L5/E5a only processing mode for positioning is also excluded in the concept proposed in SESAR. It is considered that the improved performance in terms of noise and multipath on this signals is smaller compared with the increase in the ionospheric error on the L5/E5a band (1.8 times larger).

Furthermore, other smoothing time constants are not feasible in this proposed concept. Even if theoretically it might be beneficial to use longer smoothing time constant (especially for Ifree), these option are disregarded due to the limitation of the VDB capacity. The introduction of new smoothing time constant requires the ground receiver to broadcast new corrections for all signals in addition to the existing 100 and 30 seconds smoothing time constants for L1 corrections.

This section provided an overview of the current options that are considered and disregarded in Europe within SESAR project. Next, the author's view and the processing modes considered in this work will be presented.

3.2.4 Considerations in this thesis

The previous two section discussed the DFDC GBAS concept proposed within SESAR project which is used as base in this thesis. The goal of this work is, however, to investigate the performance of different processing models without an intent to propose a final DFDC GBAS. The assumptions and consideration regarding the future hardware architecture of DFDC GBAS such as the VDB capacity follow the current SESAR project.

In author's opinion, the most promising processing mode for the future DFDC GBAS is the one based on single frequency L1/E1 positioning and use of dual-frequency for ionospheric gradient monitoring. The extension of this mode from the existing single frequency system is straight forward and can provide improved availability compared to the current GAST-C and GAST-D service types. This is because the use of the second frequency for ionospheric gradients mitigation removes the conservative overbounding used in GAST-C and the sensitive monitoring implemented in the GAST-D service type. If the ionospheric monitor is implemented in the range domain [80], only the satellites affected by a gradient are removed from the aircraft position solution. The use of a second constellation increases the number of satellites available yielding still to good geometries after exclusion of satellites. Even if the second constellation is not available, the performance of this processing mode would be comparable (or even better) with the performance of the existing GAST-D service type which is certified for CAT-III operations.

The Ifree processing mode removes the ionospheric error, but the increase of the noise and the multipath errors in the Ifree ranges yields to larger position errors and thus large protection levels. Furthermore, the hardware biases from both frequency are combined (e.g. receiver antenna errors) which can be significant in the Ifree combination. This increase is especially an issue for the landing phase, where the maximum allowable errors (alert limits) decrease down to 10 m. Using measurements from two complete constellations errors below this limits could be achieved, but in case one of the constellation is unavailable, it is expected that the obtained protection levels will be above 10 meters. The unavailability of one constellation can occur if for example the ground station supports a different second constellation than the airborne receiver.

The issue of the increased noise and multipath error in the Ifree solution could be solved by using a longer smoothing time constant. Following the proposed VDB scheme, in this work the smoothing time constants are limited to 100 or 30 seconds and the Ifree pseudorange corrections are computed by the airborne receiver from the single frequency L1/E1 and L5/E5a pseudorange correction. The 100 seconds is recommended because the shorter smoothing time constant would lead further increase in the position errors. However, if a different VDB architecture and structure will be consider in future, a longer smoothing time constant such as 300 or 600 seconds could improve the performance of the Ifree solution. The use of the larger smoothing time constant would require either broadcast of Ifree pseudorange corrections or single frequency L1/E1 and L5/E5a pseudorange corrections smoothed with the longer

smoothing time constant in addition to the 100 seconds and 30 seconds L1 corrections needed for the current single frequency service types.

In addition to the single frequency L1/E1 and Ifree processing modes, it is considered that the L5/E5a positioning mode should be taken into account as a processing mode for a future DFDC GBAS. Even if the ionospheric error on the L5 band is 1.8 larger than the error on the L1 band, the smaller noise and multipath errors on the L5/E5a is beneficial when the aircraft is closer to the ground station (when the ionospheric spatial decorrelation is much smaller) and when actually a better performance is needed (alert limits decrease to 10m). This processing mode can enable also the use of GBAS for future services such as rolling and taxiing. Similar to the single frequency dual-constellation L1/E1 mode, the ionospheric gradient monitor can be based on dual-frequency. The increase in the ionospheric error on the L5 signals yields to larger monitors thresholds. This will not be an issue for the DFDC GBAS as the addition of new signals could enable lower nominal navigation errors and thus increased flexibility in the monitors design.

The Dfree processing mode is also disregard in this work for the same reasons discussed above. Having an ionospheric gradients monitor based on dual-frequency, the Dfree positioning does not bring a benefit compared to the single frequency L1/E1 mode. Enabling this mode on the airborne receiver requires additional corrections and additional computation power on both the ground stations and the airborne receiver.

Summarizing, the primary processing modes based on the use of GPS and Galileo signals that are be considered further in this thesis are as follows:

- single-frequency dual-constellation L1/E1 processing mode based on 100 seconds and 30 seconds positioning with dual-frequency ionospheric monitoring using the algorithm described in [80],
- single-frequency dual-constellation L5/E5a processing mode based on 100 seconds with dual-frequency ionospheric monitor using the algorithm described in [80],
- dual-frequency dual-constellation Ifree processing based on 100 seconds smoothing time constant. The Ifree pseudorange corrections are calculated by the airborne receiver based on the broadcast single frequency L1/E1 and L5/E5a single frequency pseudorange corrections.

In addition to these processing modes the derivation of the error models and the performance assessment of different modes will include also the 30 seconds smoothing time constant for the L5/E5a mode and Ifree mode.

The next two sections introduces the changes that need to be implemented in the DFDC GBAS ground station and the airborne receiver and the additional parameters that should be broadcast to enable the use of different processing modes.

3.3 Ground processing for DFDC GBAS

This section describes the updates and responsibilities of the DFDC GBAS ground station. The reference receivers and the antennas of the DFDC ground station need to be updated to use the signals from L1 and L5 band. In this work it is assumed that the ground reference receivers are able to track signals from L1/E1 and L5/E5a from GPS and Galileo constellation. The DFDC GBAS ground station will simultaneously broadcast pseudorange corrections and integrity parameters to enable several processing modes. These parameters are described in the following subsections.

3.3.1 Pseudorange corrections

A DFDC GBAS station needs to provide additional corrections and integrity parameters for a second constellation (in this case Galileo) and the L5/E5a frequency. The DFDC ground system will transmit all the corrections simultaneously to enable the proposed processing modes even if the airborne receiver does not use both of them. The airborne receiver is responsibility to select the nominal mode pr to switch to a fall-back mode. Thus in the proposed architecture, a DFDC ground station transmits the following pseudorange corrections:

- single frequency GPS L1 pseudorange corrections based on 100 seconds and 30 seconds smoothing time constants,
- single frequency Galileo E1 pseudorange corrections based on 100 seconds and 30 seconds smoothing time constants,
- single frequency GPS L5 pseudorange corrections based on 100 seconds smoothing time constant,
- single frequency Galileo E5a pseudorange corrections based on 100 seconds smoothing time constant.

When the 30 seconds smoothing time constants is used for the L5/E5a and Ifree processing a in the evaluations, it is assumed that the ground station computes and broadcasts these corrections instead of the 100 seconds ones.

The computation of the single frequency L1/E1 corrections will be performed in the same way as the presented in Chapter 2 Section 2.3.1 for both 30 and 100 smoothing time constants. Additionally, corrections for L5 and E5a signals are computed based on the same algorithm with the use of the L5/E5a 100 seconds smooth pseudoranges. The computation is performed independently for each constellation and each frequency. The separate computation for each constellation is especially important to be considered in the smooth clock adjust step, because the estimated receiver clock bias is different for each constellation. Furthermore, the satellite position is computed independently for each signal type based on different sets of information:

- LNAV data for GPS L1 signals
- CNAV data for GPS L5 signals
- INAV data for Galileo E1 signals
- FNAV data for Galileo E5a signals

The corresponding navigation data are used to compute the satellite position and the satellite clock bias. Together with the pseudorange corrections, the ground station broadcast the single frequency range rate corrections associated with each correction type.

3.3.2 Integrity parameters

Additional integrity parameters need to be broadcast by the ground system to enable the new processing modes at the airborne receiver. This includes for example the B-values corresponding to each processing and signal type and $\sigma_{\text{pr_gnd}}$ values. Furthermore, specific parameters will be transmitted by the ground system such as the multiplier for the ephemeris error position bound for the different service types and constellations ($k_{\text{md_e},x,c}$). These parameters will be different from the current GPS only parameters as different ephemeris monitors, and thus different missed detection probabilities might be implemented for different service types. The main parameters that need to be integrated are discussed in the following.

3.3.2.1 B-values

As described in Chapter 2, the B-values are integrity parameters associated with the pseudorange corrections. They are mainly affected by the noise and multipath errors of the ground receivers and are thus different for each signal type (because each signal has different modulation). The DFDC ground system computes and provides B-values the corresponding broadcast pseudorange corrections such as single-frequency L1 and E1 B-values based on 100 seconds and 30 seconds smoothing time constant, single-frequency L5 and E5a B-values based on 100 seconds smoothing time constant. For the Ifree combinations, the ground station can broadcast separate Ifree B-values or the airborne receivers can form the dual-frequency combination from the single frequency values. The correlations of the multipath and noise errors will affect the derivation of these values and the different cases are analyzed in Chapter 4.

3.3.2.2 Residual error associated to the pseudorange corrections

The ground system needs to compute and transmit $\sigma_{\text{pr_gnd}}$ values for new signals and new processing modes as follows:

- $\sigma_{\text{pr_gnd}_{\text{E1,100}}}$ and $\sigma_{\text{pr_gnd}_{\text{E1,30}}}$ which represent the residual uncertainty due to the noise and multipath errors associated to the Galileo E1 100 seconds and 30 seconds smoothed broadcast pseudorange corrections which will be used for the single frequency dual-constellation L1/E1 processing mode. These values are not inflated to account for ionospheric anomalies (as in GAST-C),
- $\sigma_{\text{pr_gnd}_{\text{E5/L5a,100}}}$ which represent the residual uncertainty if the 100 seconds smoothed noise and multipath error associated to the Galileo E5a/GPS L5a 100 seconds smoothed broadcast pseudorange corrections (not inflated),

- $\sigma_{\text{pr_gnd}_{\text{Ifree,100}}}$ which represent the residual uncertainty of the 100 seconds noise and multipath errors associated to the Galileo and GPS Ifree 100 seconds smoothed broadcast pseudorange corrections.

The derivation of these error models will be discussed in detail in Chapter 4.

3.3.2.3 Integrity parameters for the ionospheric uncertainty

The uncertainty for the ionospheric error decorrelation is computed on the airborne based on the broadcast σ_{vig} terms. The current single frequency GPS GBAS station broadcast two values for this parameters $\sigma_{\text{vig,C}}$ and $\sigma_{\text{vig,D}}$ for GAST-C and GAST-D, respectively (see Chapter 2). The bounding of the ionospheric errors on the L5/E5a can be computed by the airborne receiver by multiplying the values broadcast for L1 values with 1.8. For the Ifree processing mode the $\sigma_{\text{vig,Ifree}} = 0$ and no additional value should be broadcast. However, in the current GBAS architecture, the σ_{vig} terms also contain a bound for the anomalous troposheric gradients. Those gradients can also affect the Ifree pseudoranges, thus an additional value for the $\sigma_{\text{vig,Ifree}}$ might need to be included in the broadcast parameters to account for the tropospheric gradients.

3.4 Airborne processing for DFDC GBAS

Using the corrections from the ground station, the airborne receiver will perform in parallel different position solutions as follows:

- the legacy single-frequency GAST-C position solution based on 100 seconds smoothed pseudoranges and corrections and GAST-D position solutions based on 100 and 30 seconds smoothed and corrected pseudoranges and the specific integrity parameters described in Chapter 2,
- the single-frequency dual-constellation L1/E1 position based on 100 seconds smoothing time constant using the 100 seconds smoothed pseudoranges corrected with the corrections provided from the extended legacy message types and the extended integrity parameters that cover the E1 signals,
- single-frequency dual-constellation L5/E5a position solution based on 100 seconds smoothing time constant (or 30 seconds smoothing time constant) using 100 seconds (or 30 seconds) smoothed and corrected pseudoranges. The projection matrix, $\boldsymbol{S}$, used to compute the position solution (defined in Eq. (2.22)) will be computed based on a new total residual uncertainty σ_{GBAS} specific for L5/E5a signals with $\sigma_{\text{pr_gnd}_{\text{E5/L5a}}}$, $\sigma_{\text{iono}_{\text{E5/L5a}}}$ broadcast by the DFDC GBAS ground station and a new defined $\sigma_{\text{pr_air}_{\text{E5/L5a}}}$,
- the dual-frequency dual-constellation Ifree L1/E1-L5/E5a position solution based on 100 seconds (or 30 seconds) smoothing time constant. The Ifree smoothed pseudoranges are corrected using the Ifree combination of the single frequency L1/E1a and L5/E5a broadcast pseudorange corrections.

The measurements on the airborne are smoothed using the same carrier smoothing algorithm as implemented by the ground receiver. For the Ifree solution, the airborne

receivers computes the Ifree smoothed pseudoranges using the relation defined in Eq. (3.9). As the ground receiver does not broadcast directly the Ifree smooth corrections, they are formed by the airborne receiver from the single frequency corrections as (based on Eq. (3.9))

$$PRC_{\mathrm{TX}}{}^{s}_{i,j\,\mathrm{Ifree}} = \frac{f_i^2}{f_i^2 - f_j^2} \cdot PRC_{\mathrm{TX}}{}^{s}_{i} - \frac{f_j^2}{f_i^2 - f_j^2} \cdot PRC_{\mathrm{TX}}{}^{s}_{j}. \tag{3.10}$$

The computation of the Ifree corrections on the airborne receiver requires the single frequency corrections to be smooth with the same filter parameters (the same smoothing time constant and the same filter reset time). In this way, the ionospheric divergence introduced in the single frequency smoothing filters is removed. As different sets of satellites might be used to compute the single frequency pseudorange corrections for the two frequencies, the estimated receiver clock bias on the ground receivers might be different. This error projects however, into the airborne receiver clock and will not affect the position solution. One way to account for remove this additional error on the airborne receiver clock estimation is to perform a mean removal over the formed Ifree pseudorange corrections.

The position solution for each processing mode are then estimated as described in Chapter 2 Eq. (2.14) as

$$\boldsymbol{X} = \left(\boldsymbol{G}^{\mathrm{T}} \cdot \boldsymbol{W} \cdot \boldsymbol{G}\right)^{-1} \cdot \boldsymbol{G}^{\mathrm{T}} \cdot \boldsymbol{W} \Delta\rho. \tag{2.14 revisited}$$

where the n^{th} row of the $\boldsymbol{G}$ for dual-constellation is defined as

$$\boldsymbol{g}_{n:} = \begin{bmatrix} -\cos(\theta^n) \cdot \cos(\psi^n) & -\cos(\theta^n) \cdot \sin(\psi^n) & -\sin(\theta^n) & 1 & 0 \end{bmatrix}, \tag{3.11}$$

for GPS satellites and

$$\boldsymbol{g}_{n:} = \begin{bmatrix} -\cos(\theta^n) \cdot \cos(\psi^n) & -\cos(\theta^n) \cdot \sin(\psi^n) & -\sin(\theta^n) & 0 & 1 \end{bmatrix}, \tag{3.12}$$

for the Galileo satellites with θ^n and ψ^n being the satellite elevation and azimuth angle of the n-th satellite.

The additional column of 1 is needed to account for the clock offset difference between the two constellations. The weighting matrix $\boldsymbol{W}$ is computed based the $\sigma_{\mathrm{GBAS},x}$ for the corresponding processing mode and signal (e.g. signals from different constellation will be based on different models). The calculation of the residual uncertainty for each mode is detailed in the next sections.

After the modifications on the ground and airborne receivers were presented, the next section discusses the threats that need to be taken into account in a DFDC GBAS system.

3.5 Threat space for DFDC GBAS

The components of the threat space described and discussed for the current single frequency GBAS in Chapter 2 (Section 2.4) apply also to the DFDC GBAS. However, with the inclusion of new signals from the second frequency and a second constellation, the threat space should be extended to cover also new faults. The following threats add to a DFDC GBAS for each category described in Section 2.4:

1. Faults in the ground stations which can occur due to a hardware fault in the reference receiver caused by a failure in the E1, L5 or E5a tracking loops.
2. Faults in the GNSS ranging sources introduced by the addition of the new signals. Similar faults that can occur on the GPS L1 satellites have to be considered also for the GPS satellites brodcasting on L5 and the Galileo satellites. This includes the signal deformation faults, the code carrier divergence fault, the ephemeris faults in the navigation messages, the Galileo power condition.
3. Anomalous ionospheric conditions: The DFDC GBAS should be able to offer more robustness and to possibly reduce the impact of the ionospheric effects by using a second frequency. However, this threat refers to the situation when the ionospheric monitors designed for DFDC are not able to support the required integrity.
4. GNSS L5 band RFI. In addition to the L1 RFI, DFDC GBAS is also prone to interference and local spoofing of the L5/E5a band threat.

3.6 Integrity in DFDC GBAS

In the curent concept developed in SESAR the main service type for DFDC GBAS is the GBAS Approach Service Type F (GAST-F) that intends to support CAT-II/CAT-III approaches using the signals broadcast on GPS L1/L5 and Galileo E1/E5a bands. The GBAS Approach Service Type E (GAST-E) service type, based on the use of GPS L5 and Galileo E5a signals is foreseen only as fallback of GAST-F in case of RFI on L1/E1 band. GAST-E is envisioned to support only CAT-I service, similar to GAST-C service. The switch to this service type is envisioned only in case the L1 frequency is unavailable. The integrity concept of the GAST-E could be developed based on the GAST-C concept. As the ionospheric errors on L5/E5a is 1.8 times larger, new simulations to derive the inflation factors for the ground parameters will need to be performed to enable the use of this processing mode.

In this thesis, the different service types GAST-E and GAST-F will not be considered when discussing the future DFDC integrity concept. The focus is to discuss the high level changes that need to be taken into acount when defining the integrity concept that will provide CAT-III services.

The integrity concept for DFDC GBAS is based on the definition of the GAST-C and GAST-D requirements. As discussed in Chapter 2, the main difference between the GAST-D and GAST-C integrity concept definition is the approach to derive the performance allocation. For GAST-C, an ILS-like approach was followed and the

ground system is responsible to provide the integrity. However, compared with an ILS system, for GBAS the ground system is only one component of the navigation error. The provision of the integrity for the whole system is achieved by making assumption about the quality and the geometry used by the airborne receiver which are usually very conservative.

For GAST-D a different approach was chosen, based on the touchdown performance. In this concept, the responsibility to provide integrity is shared between the ground and the airborne system. The advantage of shifting the integrity on the airborne system is that the actual geometry used by the airborne receiver can be used, allowing less conservative overbounding and monitoring.

The split of the performance allocation it is also important and desired for DFDC GBAS concept, especially because the ground system can not know which constellation and signals supported by the ground receivers are actually used by the airborne receiver. In the GAST-D concept, the requirements for ground and airborne have been derived from the airworthiness certification criteria necessary to land an aircraft. This includes the probabilities to land in the touchdown box (see Figure 2.15) under three conditions: the nominal condition, the limit case condition and the malfunction case. The requirements of each of the case are detailed in previous chapter, Section 2.7.1. The same approach based on the airworthiness criteria can be applied to derive the requirements for DFDC GBAS and the possible changes are discussed next.

3.6.1 Airworthiness requirements and modifications for DFDC GBAS

The derivation of the GAST-D requirements were done based on several assumption such as:

- the NSE and FTE are Gaussian distributed and independent,
- the FTE was modeled using a σ_{FTE} of 150 ft for the nominal and limit case and 180 ft for the malfunction case,
- a maximum value of the standard deviation of the vertical NSE, $\sigma_{\mathrm{NSE,v}}$ of 1.72 m was considered in order to meet the maximum VAL of 10 m with a k_{ffmd} of 5.81 for a ground system with four reference receivers (see Eq. (2.53)). The maximum value of VAL was used to show that touchdown condition under the nominal case is fulfilled and also to derive the requirements in the limit and malfunction case,
- the minimum glide path angle of 2.5° was used for the transformation from the vertical to longitudinal NSE (see Eq. (2.49)),
- a maximum conservative value of 4 was used for the $s_{\mathrm{apr_vert}}$ terms (which represents the projection from the position domain to the range domain).

Some of these parameters need to be reviewed in the DFDC GBAS requirements derivation. The standard deviation of the vertical NSE is an important parameter in the derivation of the monitoring requirements for the ground station. The monitor requirements are derived from the limit and malfunction case and set a limit on the

probability of missed detection (P_{md}) and the maximum tolerable range error ($E_{\mathrm{r,max}}$) (Section 2.7.1).

The value of $\sigma_{\mathrm{NSE,v}}$ reflects the expected accuracy on the vertical NSE and is set to 1.72 m for for the current GAST-D. The assumption is based on a maximum VAL of 10 m and a fault free missed detection k_{ffmd} of 5.81 which corresponds to the allocated integrity risk for a ground station with fours reference receivers. The use of signals from a second constellation and a second frequency can lead to an improved navigation performance and a better accuracy. This enables a lower the maximum VAL, and thus a lower standard deviation of the vertical NSE. Initial studies performed within SESAR project suggest lowering the maximum VAL to 7 m, yielding to $\sigma_{\mathrm{NSE,v}} = 1.2$ m. Lower value for the vertical NSE would enable on one side larger FTE values and, on the other side would relax the ground monitor requirements allowing larger tolerable errors. In [84] initial simulations for different processing modes have been performed to study the impact of adding an additional constellation as well as the protection levels obtained for the different protection levels. The simulations were performed considering nominal constellation of 24 satellites GPS and 24 Galileo satellites for the single-frequency dual-constellation L1/E1 processing modes, single frequency L5/E5a processing modes and the dual-frequency dual-constellation Ifree mode. The protection levels integrity allocation was considered unchanged and the used error models were based on preliminary results derived in [85] and [86]. The results suggest, as expected, that the addition of a second constellation yields lower protection levels. The L5/E5a processing mode shows lower protection levels closeby the airport, but increase faster with distance compared with the L1/E1 protection levels due to the larger ionospheric error. In a complete dual-constellation scenario, the Ifree protection levels are below 6 m. Based on these initial results, extended availability studies for a VAL of 7 m have been performed within SESAR project considering also satellites outages (e.g. due to aircraft maneuvering). The study showed that lowering the VAL has a very limited impact on the availability, especially for the single frequency mode. The increase in the noise for the Ifree solution leads to larger protection levels and has a larger impact in the availability in case satellite outages occur. Thus it can be considered that a VAL of 7 m is an option for the future DFDC without a strong effect on the availability of the system.

On the other side, using signals from a second constellation increases the number of satellites in the position solution and can potentially allow lower maximum values for lateral and vertical projection factors ($s_{\mathrm{apr_vert}}$ and $s_{\mathrm{apr_lat}}$). This would yield again to more flexibility and larger tolerable errors in the ranging source requirements for the ground subsystem.

Figure 3.2 shows the constraint on the P_{md} versus allowable range error E_{r} when a value of 1.2 m is considered for $\sigma_{\mathrm{NSE,v}}$ and $s_{\mathrm{apr_vert}} = 1.4$. The black line represents the constraint derived from the malfunction case, while the blue line shows the limits on the P_{md} for the limit case with the red line being the linear approximation. The derivation of the results was done following the logic presented in the Chapter 2, Section 2.7.1. Comparing the constraint region (the yellow area) in this case

with the one obtained in GAST-D (see Figure 2.18) it becomes clear that lowering the $\sigma_{\mathrm{NSE,v}}$ and $s_{\mathrm{apr_vert}}$ values yields to larger monitors thresholds (e.g. maximum tolerable error increases to 4.6 m compared to 1.6 in GAST-D). While decreasing the maximum values for VAL would be beneficial for monitoring, it requires that the system broadcasts different VAL values for different service types which might be undesirable. Furthermore, the use of Ifree processing mode (e.g. in areas with active ionosphere) with a lower values of alert limit might lead to poor availability. Thus, the final decision of these values needs to be done based on all operational aspects.

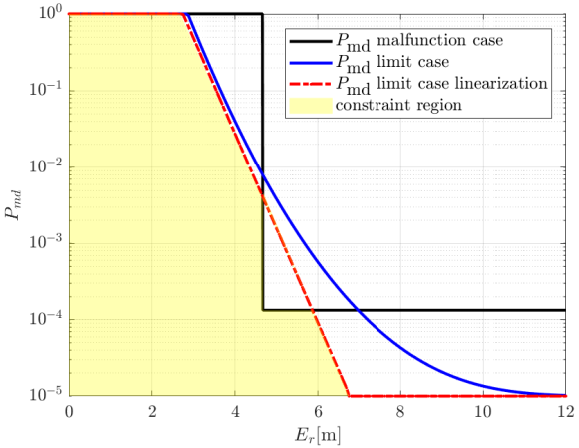


Figure 3.2: Limit on the P_{md} in range domain for limit and malfunction case for DFDC

Another change that can be made in the derivation of the DFDC GBAS requirements regards the glide path angle. As mentioned above, in the derivation of the GAST-D requirements a fixed to 2.5° is used. However, the actual value of the glide path angle used for each approach is known by the ground stationd and broadcast to the airborne receiver. Using the actual value would lead to less conservatism and larger threshold values for the monitors.

3.6.2 Integrity coverage for DFDC GBAS

In this work, the DFDC integrity concept is assumed to be similar to the GAST-D, but extended to include the new signals from the second frequency and the Galileo constellation and the new threats specific to them. In GAST-D, the ground and the airborne share the responsibility to provide integrity coverage; the ground system is responsible to monitor its ranging signals in the pseudorange domain and the airborne is responsible to assess whether the performance is enough to continue the approach. As shown in Figure 2.19, the integrity allocation in GAST-D is split in five categories: ground system SiS integrity, ground system integrity, protection levels integrity, integrity monitoring for ranging source faults, aircraft monitoring.

The simplest way is to keep for the DFDC integrity scheme the same allocation and include the integrity coverage and monitors required by the addition of the new signals. The modification for each category are discussed in the following.

1. **Ground SiS integrity**

   This allocation refers to the faults that occur in the ground satellite signals and are not addressed by the protection levels. This comprises failures in the ground ranging sources, hardware or software failures that occur in more than one reference receiver failures (single reference receivers faults are covered by the protection levels), failures due to ionospheric anomalies or faults due to correlated multipath that affect more receiver simultaneously. The integrity risk allocated to this category is $1.5 \cdot 10^{-7}$ and a DFDC ground station needs to cover also the faults introduced by the new signals. For the single frequency, six main ranging sources faults have been identified including: signal deformation, code carrier divergence, excessive pseudorange acceleration, erroneous GNSS navigation data, low signal power and multiple ranging source failure due to a constellation fault and an integrity monitor has been designed for each of this threat. All these faults are applicable to the GPS L5 (with a BPSK(10) modulation) and Galileo E1 (with a Binary Offset Carrier (BOC)(1,1) modulation) and E5a(with a BPSK(10) modulation) signals. Because the new signals are based on different modulations, new threat models and monitors need to be designed to cover these new signals and the new constellation. Furthermore, a satellite fault rate needs to be established for Galileo constellation.

   A second category of faults includes the errors generated by failures in multiple reference receiver. While the single reference receivers faults are included in the $VPL_{\mathrm{H_1}}$ and $LPL_{\mathrm{H_1}}$, the ground system is responsible to ensure integrity in case multiple reference receivers are affected. Compared to the single frequency system, a DFDC ground station needs to take into account the errors due to a failure in the tracking loops for E1, L5 and E5a. Furthermore, the effect of correlated multipath affecting more reference receivers should be extended to signals on L5/E5a and E1.

   For the environmental errors, in GAST-D, a part of the allocation of the ground SiS integrity covers the errors introduced for the anomalous ionospheric and tropospheric gradients. The mitigation of the ionospheric gradients will be different in the DFDC GBAS concept. Depending on the final processing scheme that will be chosen for the DFDC GBAS, the ionospheric gradients can be mitigated by making use of the dual-frequency. If the dual-frequency Ifree combination is selected as a processing mode, the impact of the ionospheric can be removed and no additional monitoring and thus, integrity allocation is needed on the ground system. If, on the other side the single frequency, dual-constellation L1/E1 mode is selected as primary mode, the ionospheric gradient mitigation can be done through a combination of the dual-frequency monitors on ground and on the airborne. In this case, the integrity allocation on the ground system for anomalous gradients depends on the final monitoring scheme

and its performance.

The bound for the errors due to non-nominal tropospheric errors are incorporated in the current single frequency GAST-C and GAST-D implementation in the residual ionospheric uncertainty (σ_{vig}) because it has been demonstrated to be dependent on the horizontal distance between the aircraft and the ground station (see Section 2.6.2.1). In the last years, larger tropospheric anomalies have been observed and several studies have been performed to investigate the impact of non-nominal tropospheric errors on the protection levels. In [87] the author proposed a new approach to bound these errors by including an additional term in the protection levels which can be a solution for the DFDC GBAS.

2. **Ground system integrity**

   In addition to the SiS allocation, a DFDC ground station should include mitigation to ensure that failures in the system components (e.g. ground receivers, VDB failures) or other faults in the design occur with a probability less than 10^{-9}.

3. **Protection level integrity**

   The integrity allocation for the protection levels in the DFDC GBAS should be the same as for GAST-C and GAST-D service types set to $2 \cdot 10^{-7}$ for both fault free protection levels (H_0) and the ones covering the single reference fault and the ephemeris fault (H_1). However, the parameters used in the computation and possible the algorithms might change to cover the new signals. The calculation of the protection levels and the changes in the integrity parameters are discussed further in Section 3.6.3.

4. **Integrity monitoring for ranging source faults**

   Similar to GAST-D, in order to ensure a CAT-III service and a successful landing inside the touchdown box, the DFDC integrity concept needs to limit the worst case error that can be generated by a fault in a ranging sources, in case the fault cannot be demonstrated to be extremely improbable. This allocation puts a requirements on the monitors of the ground system using a constraint region which is defined through the probability of missed detection versus the maximum differential pseudorange error. This requirement is derived from the airworthiness condition for limit and malfunction case.

   As discussed in Section 3.6.1 of this chapter, using signals from a second constellation and a second frequency is expected to improve the navigation performance. Adding more satellites in the position solution would also yield lower $s_{\text{apr_vert}}$ factor. Thus, the constrain region could be more relaxed allowing larger threshold for DFDC ground monitors. The extended constraint region when considering a $\sigma_{\text{NSE,v}}$ of 1.2 m and a maximum $s_{\text{apr_vert}}$ of 1.6 for the dual-constellation dual-constellation mode was shown in Figure 3.2.

The derivation of the final parameters depend of course on the primary processing that will be chosen for the DFDC concept and on operational constraints.

5. **Aircraft monitoring**

   As not all the NSE threats can be mitigated by the ground system, airborne monitoring will be required in the DFDC GBAS, similar to the GAST-D concept. For GAST-D, several monitors have been defined on the airborne which are described in Section 2.7.7.

   Similar to the ground system, some of the monitors need to be adapted to include the new signals broadcast on GPS L5 and Galileo E1 and E5a bands. Some of these monitors are:

   - MQM: this monitor is designed to limit the impact of ground multipath and of undetected cycle slips. The performance of the monitor is a function of the noise and multipath error and a threshold of 10 m is currently used for L1 C/A GPS signal. As the new signals have different modulations and different characteristics in terms of noise and multipath, a new threshold should be defined for Galileo E1 and GPS L5/Galileo E5a signals. Furthermore, if the Ifree combination is used, it has to be established if a separate monitor is defined for the combination or independent single frequency monitors are sufficient. The disadvantage of using a monitor on the dual-frequency combination is that the amplification in the noise and multipath error can lead to undisered false alarms.

   - Reference receiver monitors: a DFDC airborne receiver should monitor in addition to the B-values broadcast for L1, the E1, L5 and E5a B. For E1 a similar threshold as for L1 can be applied. However, as the performance of the signals broadcast on L5/E5a band are expected to have better performance a new threshold should be considered. Furthermore, the GAST-D monitor includes the D_{l}, D_{v} terms which are not needed in the DFDC processing.

   In addition to these monitors the GAST-D airborne system requires several monitors to mitigate the ionospheric gradients. Some of these monitors will not be needed in the DFDC airborne processing as the mitigation of the errors due to anomalous ionosphere will be based on the use of second frequency either by implementing dual-frequency monitors or by switching to Ifree processing mode. The integrity monitoring scheme for ionospheric gradient monitors depends on the final concept and design of the DFDC GBAS architecture and is out of scope of this thesis.

Other additional monitors might be integrated in the future DFDC GBAS concept. However, they will depend on the final concept and thus cannot be discussed at this point.

3.6.3 Integrity aspects considered further in this thesis

The previous section gave an overview of the DFDC GBAS concept and a summary description of the integrity. While many aspects still need to be investigated in order to define the final integrity concept and the monitors to cover all the faults, this work will focus further on the nominal performance of a DFDC GBAS.

The nominal performance is covered in the nominal protection levels (H_0) which are the statistical bounds for the expected position errors. Two more protection levels are defined in the single frequency system: the H_1 protection levels which cover the case of a single fault in the ground reference receivers and ephemeris protection levels which bound the error due to failure in the ephemeris data that builds at the airborne receiver until the ground system is able to detect it. The equations for the protection levels calculations for single-frequency are described in Eq. (2.20), Eq. (2.25) and Eq. (2.29). The protection levels are mainly affected by two factors: the satellite geometry and the residual differential error bounds (σ_{GBAS}). The satellite geometry is included in the calculation of the $\boldsymbol{S}$-matrix (Eq. (2.22)) done at the airborne receiver. The variance of the residual differential bounds plays a role in the calculation of the geometry being used for the weighting in $\boldsymbol{S}$-matrix. As shown in Eq. (2.17), the standard deviation of the uncertainty in the residual differential error consists of the root sum square of the uncertainties introduced by the ionospheric and tropospheric errors decorrelation as well as the contribution of the ground and airborne multipath and noise errors. These bounds are different for different service types. For GAST-C, residual uncertainty model bounds the errors expected in the 100 seconds smooth and corrected position solution and includes also the effect of the ionospheric effects. For GAST-D, the position solution used for the calculation of the deviation is based on the 30 seconds and the position residual error with respect to 100 seconds smoothing is accounted by the airborne receiver through the D_{v} and D_{l} terms.

Until now, no multipath models have been defined for signals foreseen to be used in the DFDC GBAS. When using signals from a second frequency and different GNSS constellation, the performance under nominal and conditions has to be assessed and new models for the uncertainty in the residual differential error have to be defined. While the tropospheric error is not frequency dependent and will not change for different processing type, the ionospheric error amplifies on the L5/E5a and needs to be taken into account when new processing modes are defined.

The remaining of the section will discuss each of the contributor to the uncertainty of the residual differential error for the different processing modes considered in DFDC GBAS concept.

3.6.3.1 Tropospheric residual uncertainty for DFDC GBAS

The standard deviation of the residual tropospheric error represents the tropospheric decorrelation between the aircraft and the ground station. The residual error depends on atmospheric conditions and on the difference in altitude between the aircraft and the ground station and the model used of this contribution is described in Eq. (2.33).

As the troposphere is non-dispersive and does not change with frequency the σ_{tropo} is the same for all single frequency and dual-frequency modes (Ifree). Thus, in this work the model from Eq. (2.33) the is used for all processing modes. Note that in the final DFDC GBAS additional terms might be considered in the protection levels to bound the observed tropospheric gradients as suggestes in [87]. These terms will be however neglected in this work, as they are not considered dominant in the evaluations performed.

3.6.3.2 Ionospheric residual uncertainty for DFDC GBAS

Unlike the troposphere, the ionosphere is frequency depend. Thus, σ_{iono} will be different for each processing mode. The model for the residual ionospheric error is discussed in Section 2.5.2.4. Eq. (2.35) describes the relation used in the computation of this term. The calculation of the ionospheric residual uncertainty is done by the airborne receiver based on the current aircraft speed and distance to the reference station and on the standard deviation of the ionospheric delay variation in vertical which is broadcast by the ground station.

In GAST-C the ground station is responsible to protect the user against any ionospheric gradient within the locally valid threat model and thus broadcasts an inflated σ_{vig} in order to make vulnerable geometries unavailable. In GAST-D the ground and airborne subsystems share the responsibility of detecting large ionospheric gradients and additional monitors are added. Thus the inflation of σ_{vig} becomes unnecessary. The broadcast σ_{vig} depends on the signal frequency and on the region where the GBAS station is installed.

For L5/E5a frequency the ionospheric delay increases by a factor of 1.8 due to the relation of the ionospheric delay between frequencies. As the nominal ionospheric decorrelation is a physical property of the ionosphere the σ_{vig} for L5 is 1.8 times larger than σ_{vig} for L1 which leads to $\sigma_{\text{iono}\,L5} = 1.8 \cdot \sigma_{\text{iono}\,L1}$. This would apply only in case the L5/E5a is used as primary mode to provide the CAT-III service, for which the model bounds only the nominal ionospheric errors. However, if the L5/E5a mode is used only as a fallback mode and provides a CAT-I service, the inflation factor to account for the ionospheric gradients needs to be established.

For the Ifree processing mode the first order ionospheric error is completely removed thus the σ_{iono} can be set to 0. It might still be necessary to include the effects of the higher orders. By setting the σ_{iono} to 0 means that the ground system does not have to broadcast any parameter for the $\sigma_{\text{ionoIfree}}$ which might be an issue if the errors due to tropospheric gradients are not treated separate in the protection levels

3.6.3.3 Residual uncertainty for ground multipath for DFDC GBAS

The ground system is responsible to broadcast $\sigma_{\text{pr_gnd}}$ values for each satellite and each processing mode. For GPS L1 these broadcast values are derived based on measurements from the ground receivers over 24-hours and thus represent the actual

multipath and noise characteristics. However, as the Galileo constellation repeats every 10 days the models for the Galileo signals should be computed over a minimum period of 10-days in order to consider all azimuth and elevation angles. In the current GBAS implementation the ground broadcasts $\sigma_{\text{pr_gnd}}$ values for GPS L1 for 100 and 30 seconds smoothing time constant. As the ground multipath and noise are mainly dependent on the signal modulation and signal bandwidth they will be different for different signals. Chapter 4 focuses on the characterization of the ground multipath for the single frequency and dual-frequency processing. Furthermore, changes that need to be included in the derivation of the $\sigma_{\text{pr_gnd}}$ for the new signals are discussed.

3.6.3.4 Airborne multipath models for DFDC GBAS

Unlike the ground, the residual uncertainty attributed to the airborne multipath and noise after carrier smoothing, ($\sigma_{\text{pr_air}}$), is defined based on standardized error models as opposed to actual measurements of an installation. These models have to be conservative to cover all the aircraft installations with different antennas and receivers. In the current single frequency GBAS the airborne error model, the code tracking noise and multipath error are parameterized as zero-mean Gaussian overbounds and together they form an error distribution expressed as a function of the elevation angle of the satellite (relating to the horizon) as described in Eq. (2.31) in Section 2.5.2.2. The model describes the distribution of the airborne error for the 100 seconds smoothed measurements. For DFDC aviation user, the airborne multipath and noise errors gain a significantly more important role in the error budget because the previous dominant ionopheric error can be removed. It is essentially thus that the errors are well understood and assessed in order to be able to properly bound the residual errors and ensure integrity. Chapter 5 of this thesis investigates and proposes new models for the airborne multipath for single frequency L1/E1 and L5/E5a signals as well as for Ifree combination.

3.6.3.5 Additional terms

Another aspect which has to be considered in a dual-frequency implementation is the satellite code biases. These biases affect the single frequency and dual-frequency signal processing and positioning in the GNSS receiver and depend mainly on the receiver parameters and are different for each satellite. In GBAS, the ground and airborne equipment can differ; consequently the satellite code biases cannot be removed by differential corrections. They are specially relevant for the Ifree combination, on which the biases from the single frequency get combined.

Until now, no studies have investigated how to include these errors in the integrity concept. Chapter 6 will discuss the impact of the satellite code biases on the dual-frequency GBAS user and will propose different methods to account and bound these biases in the protection levels.

4 Ground multipath in DFDC GBAS

4.1 Objectives and contributions

One of the parameters which is different for the new signals and which has to be re-characterized is the residual uncertainty attributed to the smoothed pseudorange corrections from the ground system ($\sigma_{\text{pr_gnd}}$). These parameter is mainly affected by the multipath and noise error present in the code measurements from the ground receivers. These errors affect the computation of the pseudorange corrections and need to be taken into account in the calculation of the protection levels.

Until now, the derivation of the $\sigma_{\text{pr_gnd}}$ has been performed only for GPS L1 C/A code signals. However, the signals broadcast by the new Block IIF GPS satellites on L5 are expected to have lower noise and multipath mainly due to the higher chipping rate of L5 signals relative to L1 C/A code [41, 85]. For Galileo constellation, the signals broadcast on the E1 (L1) band adopt Composite Binary Offset Carrier (CBOC)(6,1,1/11) modulation and the BPSK(10) modulation for the E5a (L5) band. The multipath and noise errors are depend on the signal modulation and signal characteristic. As both new modulations are different from the GPS L1 C/A code, new evaluation of the ground multipath models ($\sigma_{\text{pr_gnd}}$) need to be performed.

This chapter shows the evaluation of GPS L5 noise and multipath using unsmoothed measurements and also the impact of the carrier-smoothing filter on the residual noise and multipath that form the largest component of $\sigma_{\text{pr_gnd}}$. Furthermore, this work investigates the applicability of the suggested methods to the Galileo constellation and provides an evaluation of the $\sigma_{\text{pr_gnd}}$ for the signals broadcast on E1 and E5a bands. The affecting multipath and noise errors are dependent on the signal modulation and signal bandwidth, but also by the receiver parameters such as correlator spacing. Different receiver configurations (e.g. correlator spacing) would lead to different $\sigma_{\text{pr_gnd}}$ curves. In order to show the impact of the different correlator, measurements with different correlator spacing values are compared. In addition to the single frequency processing modes, in the DFDC GBAS concept, the Ionosphere-free (Ifree) combination is one of the considered modes. This chapter provides an evaluation of errors expected in the Ifree pseudorange corrections and discusses the aspects that need to be taken into account for the broadcast of the $\sigma_{\text{pr_gnd}_{\text{Ifree}}}$ parameters.

This chapter is structured as follows: Section 4.2 discusses the methodology and metrics used to derive the multipath and noise error and $\sigma_{\text{pr_gnd}}$ models. This includes two different methods based on Code Minus Carrier (CMC) and based on B-values method and relations to compute the values of the $\sigma_{\text{pr_gnd}}$ are detailed. Section 4.3

gives an overview on the facilities and measurements used in this chapter. The results and the conclusions are presented in Section 4.4 including:

- Derivation of $\sigma_{\text{pr_gnd}}$ for GPS L5 and Galileo E1 and E5a,
- Applicability to the suggested method for Galileo constellation for which the ground track repeats every 10 days,
- Impact of the smoothing time constant in the $\sigma_{\text{pr_gnd}}$ curves,
- Comparison of the results obtained from the two methods used to derive $\sigma_{\text{pr_gnd}}$ and discussion on the difference,
- Models for the Ifree combination.

4.2 Methodology, metrics and assumptions

The broadcasts values for $\sigma_{\text{pr_gnd}}$ are based on combinations of theoretical models and measurements collected from the ground reference receivers that represent actual system characteristics. This sections presents the methods used to derive these values. In addition, the estimation of the method to directly estimate the raw multipath and noise errors on the code measurements are presented.

4.2.1 Raw multipath and noise

Before discussing the derivation of the $\sigma_{\text{pr_gnd}}$, an analysis of the raw multipath and noise error present in each signal will be performed. This analysis is useful for understanding the different performance for the new signals. The raw multipath and noise error in the pseudorange can be estimated directly by differentiating the code and carrier phase measurements (linear CMC combination) from which the ionospheric divergence removed. The obtained estimates are referred as CMC divergence-free and noted in this thesis as $CMC_{\text{Dfree,bias}_{i,j}}$. The equation for $CMC_{\text{Dfree,bias}_{i,j}}$ for the receiver m, satellite s and frequency bands i and j is expressed as

$$CMC_{\text{Dfree,bias}}{}^{s}_{m,i,j} = \rho^{s}_{m,i} - \phi^{s}_{m,i} - \frac{f_j^2}{f_i^2 - f_j^2} \cdot (\phi^{s}_{r,i} - \phi^{s}_{m,j}), \tag{4.1}$$

with $\rho^{s}_{m,i}$ representing the code measurement on frequency i, $\phi^{s}_{m,i}$, $\phi^{s}_{m,j}$ the carrier phase measurements from the frequency bands i and j, f_i and f_j the center frequency values for frequency i and j. The estimation contains the code multipath and noise, the hardware errors on the phase and code measurements and the combination of the carrier phase ambiguities from the two frequencies i and j. The integer ambiguities remain constant if no cycle slip occurs. As typically the measurements from the ground reference receiver are not highly affected by cycle slips (due to the location of the antenna in open-sky environments), the satellites are continuously tracked over the entire pass. Thus, the carrier phase ambiguities can be estimated by removing the mean over a continuous pass for each satellite. Remaining biases are assumed to be constant during the duration of each data set and are removed by subtracting the corresponding average. This assumption can hold since the parameter of interest,

i.e. multipath errors and tracking noise, are zero-mean distributed for a sufficiently long observation time. Other signal components in the data set include the hardware biases. They can be assumed approximately constant except the error introduced by the satellite and receiver antennas. The antennas introduce on one side errors on the carrier phase measurements due to the phase center variations and, on the other side, code error due to group delay variations. The errors introduced by the satellite antennas are typically much smaller compared with the errors introduced by the receiver antennas and are considered negligible. For the receiver antennas, high performance antennas (e.g. choke ring antennas or MLA) are used in the ground installation for which the errors are small enough to be neglected. Furthermore, for certified station calibration tests take place at the initialization of the ground facility which reduce these errors.

The final equation for the estimation of the multipath and noise error after the mean removal for the receiver m, satellite s and frequencies i and j ($CMC_{\mathrm{Dfree}}{}^{s}_{m,i,j}$) is then expressed as

$$CMC_{\mathrm{Dfree}}{}^{s}_{m,i,j} = CMC_{\mathrm{Dfree,bias}}{}^{s}_{m,i} - \frac{1}{N_{\mathrm{k}}} \sum CMC_{\mathrm{Dfree,bias}}{}^{s}_{m,i,j}, \tag{4.2}$$

with N_{k} being the number of epochs of the continuous track of the satellite s. More details on the derivation of the equation are given in the next chapter, which discusses the estimation of the multipath error on the measurements from the airborne receiver.

4.2.2 Derivation of $\sigma_{\mathrm{pr_gnd}}$

The errors that are characterized by the $\sigma_{\mathrm{pr_gnd}}$ are the errors present in the broadcast smoothed pseudorange corrections. Typically these errors are driven by the effect of the ground multipath and receiver thermal noise. Two methods have been proposed to derive the empirical standard deviation from the measurements. The first method is based on the evaluation of a set of B-values, which gives an estimate of the error contribution from a single reference receiver to the average broadcast pseudorange correction. This method is shown in Section 4.2.2.1. The second method is based on the analysis of the smoothed dual-frequency CMC combination that provide a direct estimation of the noise and multipath errors on the pseudorange. This technique is described as well in Section 4.2.2.2.

4.2.2.1 B-values method

This method relies on the use of the B-values to derive the $\sigma_{\mathrm{pr_gnd}}$ values. The B-values for each satellite-receiver pair (n-m) are calculated as the difference between the broadcast corrections for satellite n computed using all the receivers (PRC^{n}_{TX}) and the average over the smoothed and clock adjust corrections from all other receivers excluding the receiver m ($PRC_{\mathrm{SCA}}{}^{n}_{r}$). The relation used to compute the B-values for

receiver r is described in Eq. (2.9) and shown again for simplicity

$$B_m^n = PRC_{\mathrm{TX}}^n - \frac{1}{M-1} \cdot \sum_{\substack{r=1 \\ r \neq m}}^{M} PRC_{\mathrm{SCA}_r}{}^n, \tag{2.9 revisited}$$

with M being the total number of receivers. This equation can be rewritten as

$$\begin{aligned} B_m^n &= \frac{(M-1)PRC_{\mathrm{TX}}^n - \sum_{\substack{r=1 \\ r \neq m}}^{M-1} PRC_{\mathrm{SCA}_r}{}^n}{M-1} = \frac{(M \cdot PRC_{\mathrm{TX}}^n - PRC_{\mathrm{TX}}^n - \left(\sum_{r=1}^{M} PRC_{\mathrm{SCA}_r}{}^n - PRC_{\mathrm{SCA}_m}{}^n\right)}{M-1} = \\ &= \frac{(M \cdot \frac{1}{M} \cdot \sum_{r=1}^{M} PRC_{\mathrm{SCA}_r}{}^n - \sum_{r=1}^{M} PRC_{\mathrm{SCA}_r}{}^n + PRC_{\mathrm{SCA}_m}{}^n - PRC_{\mathrm{TX}}^n}{M-1} = \\ &= \frac{PRC_{\mathrm{SCA}_m}{}^n - PRC_{\mathrm{TX}}^n}{M-1}. \end{aligned} \tag{4.3}$$

To understand the error contributions to the B-values the computation of the pseudorange corrections described in Chapter 2 is recalled focusing on the errors contained at each step. Knowing the exact position of the reference antennas and the satellite position, the true geometric range between the phase center of each reference receiver antenna and the satellite (noted as R_m^n) can be computed. The smoothed pseudorange corrections (PRC_{CSC}) are calculated by subtracting from the geometric range the smoothed measured pseudorange corrected by the satellite clock bias as shown in Eq. (2.5)

$$PRC_{\mathrm{CSC}}{}_m^n = R_m^n - \overline{\rho}_m^n - c \cdot \delta t^n. \tag{2.5 revisited}$$

The remaining errors in the smoothed pseudorange corrections can be separated in two types: errors common between the receivers from the ground facility and errors that are different for each of to the reference receivers as shown in Eq. (2.6)

$$PRC_{\mathrm{CSC}}{}_m^n = -\underbrace{\left[T_m^n + \overline{I}_m^n + e_m^n + \overline{A}_m^n + \overline{a}_m^n\right]}_{\substack{\text{common between} \\ \text{receivers}}} - \underbrace{\left[c \cdot \delta t_m + \overline{MP}_m^n + \overline{\varepsilon}_m^n + \overline{mp}_m^n + \overline{\eta}_m^n\right]}_{\substack{\text{different for each} \\ \text{receiver}}}, \tag{2.6 revisited}$$

with T_m^n, $\overline{I}_m^n$ representing the troposheric and ionospheric errors from receiver m to satellite n, e_m^n the ephemeris error, δt_m the clock bias of the receiver m, $\overline{MP}_m^n$ and $\overline{\varepsilon}_m^n$ the multipath and receiver noise error on the code measurement, $\overline{mp}_m^n$ and $\overline{\eta}_m^n$ the multipath and noise error on the phase measurement. The $\overline{A}_m^n$ and $\overline{a}_m^n$ represent the hardware errors on the code and respectively on the phase measurements.

As typically the distances between the receivers are short (below 2 km), it is reasonable to assume that the errors introduced by the atmospheric delay (ionosphere, troposphere) are the same. The same assumption holds also for the ephemeris error which is a function of the unit vector from the reference receiver to the satellite. The distance from a reference receiver to a satellite is much larger (20000 km) than the distance between the stations. The hardware errors ($\overline{A}_m^n$, $\overline{a}_m^n$) can also be considered

the same for all receivers because all of them use the same hardware (the same receiver type and the same receiver antenna).

Using the notations: $\Gamma^n = T^n + \overline{I}^n + e^n + \overline{A}^n + \overline{a}^n$ for the errors of a satellite n that are similar between the reference receivers (thus the index for the receiver is dropped), and $\gamma_m^n = \overline{MP}_m^n + \overline{\varepsilon}_m^n$ for the smoothed multipath and noise errors from the smoothed code measurements, Eq. (2.6) becomes

$$PRC_{\mathrm{CSC}}{}_m^n = -\Gamma^n - c \cdot \delta t_m - \gamma_m^n. \tag{4.4}$$

The largest contribution in the smoothed pseudorange corrections is the receiver clock bias. This bias is common to all satellites and can be estimated as explained in Section 2.3.1 by taking the average over the smoothed pseudorange corrections from each reference receiver. The clock bias is different for each receiver this calculation is computed for each receiver m independently. Using the above notations, the estimated clock bias ($\widetilde{\delta} t_m$) can be written as

$$\begin{aligned} c \cdot \widetilde{\delta} t_m &= \frac{1}{N} \sum_{j=1}^{N} PRC_{\mathrm{CSC}}{}_m^j = -\frac{1}{N} \cdot \sum_{j=1}^{N} \Gamma^j - \frac{1}{N} \cdot \sum_{j=1}^{N} c \cdot \delta t_j - \frac{1}{N} \cdot \sum_{j=1}^{N} \gamma_m^j = \\ &= -c \cdot \delta t_m - \frac{1}{N} \cdot \sum_{j=1}^{N} \Gamma^j - \frac{1}{N} \cdot \sum_{j=1}^{N} \gamma_m^j. \end{aligned} \tag{4.5}$$

In order to account for the different error variances for different satellites, a weighted average can be used. For simplicity, in the derivation in here no weighting is performed.

With the removal of the mean, the estimated clock contains also the common part of all the other errors that are contained in the pseudorange corrections. This will not affect the aircraft position solution because any error common to all satellites projects in the airborne clock state. It is thus important that the same set of satellites for all reference receivers is used to remove the clock bias; otherwise a difference in the estimate may result. The smoothed and clock adjust pseudorange corrections (PRC_{SCA}) are obtained by subtracting the estimated clock bias from the smoothed pseudorange corrections, (see Eq. (2.7)). Using Eq. (4.4) and 4.5, the PRC_{SCA} become

$$PRC_{\mathrm{SCA}}{}_m^n = -\left[\Gamma^n - \frac{1}{N} \cdot \sum_{j=1}^{N} \Gamma^j\right] - \left[\gamma_m^n - \frac{1}{N} \cdot \sum_{j=1}^{N} \gamma_m^j\right]. \tag{4.6}$$

The second term in Eq.(4.6) represents the residual clock bias error with the distribution given by the distribution of the sum of the errors contributing to the differential correction. Note that if the same set of satellites is used to estimate the clock bias, the errors contained in Γ^j will be similar for all receiver. The broadcast pseudorange correction for each satellite n (PRC_{TX}^n) is then computed as an average

of the smooth and clock adjust pseudorange corrections from all M receivers available (Eq. (2.8)). Using the above derivations, the PRC^n_{TX} result in

$$\begin{aligned} PRC^n_{\mathrm{TX}} &= -\frac{1}{M}\cdot\sum_{m=1}^{M}\left[\Gamma^n - \frac{1}{N}\cdot\sum_{j=1}^{N}\Gamma^j\right] - \frac{1}{M}\sum_{m=1}^{M}\left[\gamma^n_m - \frac{1}{N}\cdot\sum_{j=1}^{N}\gamma^j_m\right] = \\ &= -\left[\Gamma^n - \frac{1}{N}\cdot\sum_{j=1}^{N}\Gamma^j\right] - \left[\frac{1}{M}\cdot\sum_{m=1}^{M}\gamma^n_m - \frac{1}{M\cdot N}\sum_{r=1}^{M}\sum_{j=1}^{N}\gamma^j_r\right]. \end{aligned} \tag{4.7}$$

Substituting the broadcast pseudorange correction PRC^n_{TX} and the smooth and clock adjust pseudorange corrections in B-values equation described in Eq. (4.3), the B-value for satellite n and receiver m can be written as

$$\begin{aligned} B^n_m = \frac{1}{M-1}\cdot\Bigg\{ &-\left[\Gamma^n - \frac{1}{N}\cdot\sum_{j=1}^{N}\Gamma^j\right] - \left[\gamma^n_m - \frac{1}{N}\cdot\sum_{j=1}^{N}\gamma^j_m\right] + \\ &+\left[\Gamma^n - \frac{1}{N}\cdot\sum_{j=1}^{N}\Gamma^j\right] + \left[\frac{1}{M}\cdot\sum_{m=1}^{M}\gamma^n_m - \frac{1}{M\cdot N}\sum_{r=1}^{M}\sum_{j=1}^{N}\gamma^j_r\right]\Bigg\}. \end{aligned} \tag{4.8}$$

Reducing the terms, the B-values equation can be simplified to

$$B^n_m = -\frac{1}{M-1}\cdot\Bigg[\underbrace{\gamma^n_m}_{\substack{\text{multipath}\\ \text{and noise}\\ \text{for receiver } m}} - \underbrace{\frac{1}{M}\cdot\sum_{m=1}^{M}\gamma^n_m}_{\substack{\text{contribution from}\\ \text{other receivers}}} \underbrace{-\frac{1}{N}\cdot\sum_{j=1}^{N}\gamma^j_m + \frac{1}{M\cdot N}\sum_{r=1}^{M}\sum_{j=1}^{N}\gamma^j_r}_{\substack{\text{residual noise from}\\ \text{the imperfect removal of the clock}}}\Bigg]. \tag{4.9}$$

The B-values contains not only the noise and multipath error from the receiver m, but also the error from the other receivers (due to the averaging over the broadcast corrections) and the residual noise from the imperfect removal of the receiver clock bias. Based on the assumption that the multipath and noise from the ground receiver is zero mean (under nominal conditions), the expected value of the B-value is zero and the variance of the B-values can be computed as

$$\mathrm{Var}[B^n_m] = \mathrm{E}[(B^n_m - \mathrm{E}[B^n_m])\cdot(B^n_m - \mathrm{E}[B^n_m])^T] = \mathrm{E}[B^n_m \cdot B^{T\,n}_{\ m}]. \tag{4.10}$$

Including the therms Eq. (4.9), the variance of the B-value becomes

$$
\begin{aligned}
&(M-1)^2 \cdot \mathrm{Var}[B_m^n] = \\
&= \mathrm{E}[\gamma_m^n \cdot \gamma_m^n] - \frac{2}{M} \cdot \mathrm{E}\left[\gamma_m^n \cdot \sum_{r=1}^{M} \gamma_r^n\right] - \frac{2}{N} \cdot \mathrm{E}\left[\gamma_m^n \cdot \sum_{j=1}^{N} \gamma_m^j\right] + \frac{2}{M \cdot N} \cdot \mathrm{E}\left[\gamma_m^n \cdot \sum_{r=1}^{M}\sum_{j=1}^{N} \gamma_r^j\right] + \\
&+ \frac{2}{M^2} \cdot \mathrm{E}\left[\sum_{r=1}^{M} \gamma_r^n \cdot \sum_{r=1}^{M} \gamma_r^n\right] + \frac{2}{M \cdot N} \cdot \mathrm{E}\left[\sum_{r=1}^{M} \gamma_r^n \cdot \sum_{j=1}^{N} \gamma_m^j\right] - \frac{2}{M^2 \cdot N} \cdot \mathrm{E}\left[\sum_{r=1}^{M} \gamma_r^n \cdot \sum_{r=1}^{M}\sum_{j=1}^{N} \gamma_r^j\right] \\
&+ \frac{2}{N^2} \cdot \mathrm{E}\left[\sum_{j=1}^{N} \gamma_m^j \cdot \sum_{j=1}^{N} \gamma_m^j\right] - \frac{2}{M \cdot N^2} \cdot \mathrm{E}\left[\sum_{j=1}^{N} \gamma_m^j \cdot \sum_{r=1}^{M}\sum_{j=1}^{N} \gamma_r^j\right] + \frac{2}{M^2 \cdot N^2} \cdot \mathrm{E}\left[\sum_{r=1}^{M}\sum_{j=1}^{N} \gamma_r^j \cdot \sum_{r=1}^{M}\sum_{j=1}^{N} \gamma_r^j\right].
\end{aligned}
\tag{4.11}
$$

To calculate the variance of the B-value, the notations described in Table 4.1 are used:

Notation	Description
$\sigma^2_{B_m^n}$	variance of the B-values for receiver m and satellite n
$\sigma^{2\ n}_{\mathrm{pr_gnd}\ m}$	$\sigma_{\mathrm{pr_gnd}}$ for receiver m and satellite n
$\mathrm{Cov}(\gamma_{r_1}^{j_2}, \gamma_{r_2}^{j_2})$	the covariance of the multipath and noise errors between receiver k_1 and k_2 and satellites j_1 and j_2

Table 4.1: Notations used for the derivation of $\sigma_{\mathrm{pr_gnd}}$

The variance of the B-value can be written as function of the variances and covariance of the measurements errors from all receivers and satellites as

$$
\begin{aligned}
&(M-1)^2 \cdot \sigma^2_{B_m^n} = \\
&\frac{(M-2)\cdot(N-2)}{M\cdot N} \cdot \sigma^{2\ n}_{\mathrm{pr_gnd}\ m} + \frac{(N-2)}{M^2\cdot N} \cdot \sum_{r=1}^{M} \sigma^{2\ n}_{\mathrm{pr_gnd}\ r} + \frac{(M-2)}{M\cdot N^2} \cdot \sum_{j=1}^{N} \sigma^{2\ j}_{\mathrm{pr_gnd}\ m} + \frac{1}{M^2\cdot N^2} \cdot \sum_{r=1}^{M}\sum_{j=1}^{N} \sigma^{2\ j}_{\mathrm{pr_gnd}\ r} \\
&- \frac{2\cdot(N-2)}{M\cdot N} \cdot \sum_{\substack{r=1\\ r\neq m}}^{M} \mathrm{Cov}(\gamma_m^n, \gamma_r^n) - \frac{(N-2)}{M^2\cdot N} \cdot \sum_{r=1}^{M}\sum_{\substack{r_1=1\\ r_1\neq r}}^{M} \mathrm{Cov}(\gamma_r^n, \gamma_{r_1}^n) - \frac{2}{M\cdot N^2} \cdot \sum_{\substack{r=1\\ r\neq m}}^{M}\sum_{j=1}^{N} \mathrm{Cov}(\gamma_m^j, \gamma_r^j) + \frac{1}{M^2\cdot N^2} \cdot \sum_{r=1}^{M}\sum_{\substack{r_1=1\\ r_1\neq r}}^{M}\sum_{j=1}^{N} \mathrm{Cov}(\gamma_r^j, \gamma_{r_1}^j) \\
&- \frac{2\cdot(M-2)}{M\cdot N} \cdot \sum_{\substack{j=1\\ j\neq n}}^{N} \mathrm{Cov}(\gamma_m^n, \gamma_m^j) \frac{(M-2)}{M^2\cdot N} \cdot \sum_{j=1}^{N}\sum_{\substack{j_1=1\\ j_1\neq j}}^{M} \mathrm{Cov}(\gamma_m^j, \gamma_m^{j_1}) - \frac{2}{M^2\cdot N} \cdot \sum_{r=1}^{M}\sum_{\substack{j=1\\ j\neq n}}^{N} \mathrm{Cov}(\gamma_r^n, \gamma_r^j) + \frac{1}{M^2\cdot N^2} \cdot \sum_{r=1}^{M}\sum_{j=1}^{N}\sum_{\substack{j_1=1\\ j_1\neq j}}^{N} \mathrm{Cov}(\gamma_r^j, \gamma_r^{j_1}) \\
&- \frac{2}{M\cdot N} \cdot \sum_{\substack{j=1\\ j\neq n}}^{N}\sum_{\substack{r=1\\ r\neq m}}^{M} \mathrm{Cov}(\gamma_m^n, \gamma_r^j) + \frac{2}{M\cdot N} \cdot \sum_{\substack{r=1\\ r\neq m}}^{M}\sum_{\substack{j=1\\ j\neq n}}^{N} \mathrm{Cov}(\gamma_r^n, \gamma_m^j) - \frac{2}{M^2\cdot N} \cdot \sum_{r=1}^{M}\sum_{\substack{r_1=1\\ r_1\neq r}}^{M}\sum_{j_1=1}^{N} \mathrm{Cov}(\gamma_r^n, \gamma_{r_1}^j) - \frac{2}{M\cdot N^2} \cdot \sum_{\substack{r=1\\ r\neq m}}^{M}\sum_{j=1}^{N}\sum_{\substack{j_1=1\\ j_1\neq j}}^{N} \mathrm{Cov}(\gamma_m^j, \gamma_r^{j_1}) \\
&- \frac{2}{M\cdot N^2} \cdot \sum_{\substack{r=1\\ r\neq m}}^{M}\sum_{\substack{r_1=1\\ r_1\neq r}}^{M}\sum_{\substack{j=1\\ j\neq n}}^{N}\sum_{\substack{j_1=1\\ j_1\neq j,}}^{N} \mathrm{Cov}(\gamma_r^j, \gamma_{r_1}^{j_1}).
\end{aligned}
\tag{4.12}
$$

Under the assumption that the errors (multipath and noise) are uncorrelated between satellites and the reference receivers (all covariance terms are zero), the relation between the variance of the B-values and the $\sigma_{\mathrm{pr_gnd}}$ becomes

$$
(M-1)^2 \cdot \sigma^2_{B_m^n} = \frac{(M-2)\cdot(N-2)}{M\cdot N} \cdot \sigma^{2\ n}_{\mathrm{pr_gnd}\ m} + \frac{(N-2)}{M^2\cdot N} \cdot \sum_{r=1}^{M} \sigma^{2\ n}_{\mathrm{pr_gnd}\ r} + \frac{(M-2)}{M\cdot N^2} \cdot \sum_{j=1}^{N} \sigma^{2\ j}_{\mathrm{pr_gnd}\ m} + \frac{1}{M^2\cdot N^2} \cdot \sum_{r=1}^{M}\sum_{j=1}^{N} \sigma^{2\ j}_{\mathrm{pr_gnd}\ r}.
\tag{4.13}
$$

Furthermore, assuming that the errors variance from different receivers and different satellites are the same ($\sigma^2_{\text{pr_gnd}_m}{}^{j} = \sigma^2_{\text{pr_gnd}_r}{}^{n} = \sigma^2_{\text{pr_gnd}_m}$), the variance of the uncorrelated measurements error from the reference receiver m is related to the variance of the B-values by the approximate relation

$$\sigma^2_{\text{pr_gnd}_m} = \frac{M \cdot N \cdot (M-1)}{N-1} \cdot \sigma^2_{B^n_m}. \tag{4.14}$$

This equations expresses the relation of the variance of the uncorrelated measurements errors from one reference receiver to the B-values. However, the final corrections are computed as an average over all M reference receivers and thus the variance of the broadcast corrections becomes

$$\sigma^2_{\text{pr_gnd}} = \frac{1}{M^2} \cdot \sum_{m=1}^{M} \sigma^2_{\text{pr_gnd}_m} = \frac{1}{M} \cdot \sum_{m=1}^{M} \frac{1}{M} \cdot \sigma^2_{\text{pr_gnd}_m}. \tag{4.15}$$

This means that the composite variance can be expressed at the root mean square of the individual variances of each reference receiver divided by the number of the receivers (M). Then, the calculation of the variance from one single reference receiver can be written is:

$$\sigma^2_{\text{pr_gnd}_m} = \frac{N \cdot (M-1)}{N-1} \cdot \sigma^2_{B^n_m}. \tag{4.16}$$

Section 5.5.4 of ED-114A ([32]), defines a similar relation between the variance of the uncorrelated measurements error for one reference receiver and the variance of the B-values as

$$\sigma^2_{\text{pr_gnd}_m} = \frac{(N+1) \cdot (M-1)}{N} \cdot \sigma^2_{B^n_m}. \tag{4.17}$$

The main difference between the relation derived in this thesis and the one proposed in ED-114A is related to the multiplication factor for the number of satellites $\frac{N+1}{N}$. The ED-114A specifies that the relation is derived from the protection levels equation, but no further clarifications are provided. For the remaining of this chapter, the relation derived in (Eq. (4.16)) will be used for the evaluations of the $\sigma_{\text{pr_gnd}_m}$ for each m reference receiver. The difference in the multiplication factor will however not have a large impact in the final models.

Based on this relation, the steps to derive the $\sigma_{\text{pr_gnd}_m}$ for each reference receiver are as follows (described also in [32]):

- independent samples of the broadcast B-values are collected over 24 hours (for GPS) from all satellites in view for each reference receiver m. An independent samples is taken every 2 times the smoothing time constant [32],

- the B-values are sorted according to the corresponding satellite elevation and are grouped into bins. In order to account for the faster movement of the satellites at lower elevations and slow movement at high elevations, the bins are selected as 1° bin size for elevations below 30°, 2° for elevations between 30° and 50°, and 5° for elevations above 50°,
- the mean and the variance for each elevation bin is computed. The mean of the B-values in each bin should close to zero (below 0.05 m [32]),
- based on the variance of the B-value, the standard deviation $\sigma_{\text{pr_gnd}}$ for each bin and each reference receiver m is calculated,
- the broadcast $\sigma_{\text{pr_gnd}}$ is computed as the root mean square from all reference receivers.

4.2.2.2 Code-minus-carrier method

Another approach to estimate the $\sigma_{\text{pr_gnd}}$ is by using the dual-frequency code-minus-carrier method to estimate the multipath and noise error described in Section 4.2.1. The smoothed multipath and noise errors can be obtained by applying the smoothing filter to the raw estimateds errors (see Appendix A) as

$$\overline{CMC_{\text{Dfree}^{s}_{m,i,j}}}(k) = \frac{\Delta T}{\tau} \cdot CMC_{\text{Dfree}^{s}_{m,i,j}}(k) + (1 - \frac{\Delta T}{\tau}) \cdot \overline{CMC_{\text{Dfree}^{s}_{m,i,j}}}(k-1), \tag{4.18}$$

with k representing the current epoch, with τ being the smoothing time constant and ΔT the measurements sampling interval (0.5 for ground measurements). The estimation is performed independently for each reference receiver. The smooth multipath and noise are estimated for each reference receiver m. Similar steps as described in the B-values method are applied to derive the $\sigma_{\text{pr_gnd}}$ for each receiver m as

- independent samples of the smooth multipath and noise estimates are collected from all satellites in view for each reference receiver m. Similar to the B-values independent samples are selected after 2 times the smoothing time constant (e.g. every 200 seconds when 100 second smoothing time constant is applied),
- the smooth multipath and noise are sorted according to the corresponding satellite elevation and are grouped into bins using the same binning as prior introduced discussed,
- the mean and the variance for each elevation bins is computed. The $\sigma_{\text{pr_gnd}_m}$ for each receiver m is computed by dividing the obtained standard deviation by the total number of used reference receivers M.

4.2.2.3 Computation of broadcast values and GAD assessment

The two methods described above are used to determine the empirical values from measurements for each reference receiver. These values are used initially for the assessment of the type of the ground stations by comparing the curves obtained for each receiver against the GAD models (discussed in Chapter 2). The station type is decided by the lowest model that covers the results from all reference receivers.

However, as these values are based on a finite number of samples, a significant challenge is to ensure that these broadcast values provide a bound of the ranging errors. An approach to handle this challenge is to apply inflation factors to the estimated values. Several studies [88],[89], [90], [91] present several methodologies to derive inflation factors for the $\sigma_{\text{pr_gnd}}$ value broadcast to the aircraft. In [90] the following steps are suggested in the establishment of the broadcast sigmas (applied to the 1-*sigma* derived from the measurements):

- inflation of sample standard deviation due to the limited number of samples. This inflation is based on the χ^2-square distribution of the standard deviation,
- inflation for the correlation effects between the reference receivers. The inflation is applied as a multiplication factor to the measurements-based standard deviation which is derived as

$$\sigma_{\text{pr_gnd}_{\text{corr},m}} = \sigma_{\text{pr_gnd}_m} \cdot (1 + \sum_{j=1}^{M} p_{m,j}), \tag{4.19}$$

  where $p_{m,j}$ represents the positive correlation between all the receiver pairs $m-j$. The negative correlation is not considered because in this case no inflation is needed,
- inflation for the seasonal variation in derived standard deviation. This factor is computed by collecting measurements over longer periods (in different environmental conditions, e.g. snow, rain) and deriving factor to bound all the observed behaviors,
- inflation for non-Gaussian and non zero mean of the multipath error. A methodology to inflate for these effects is proposed in [91].

The process is repeated for each reference receiver and the composite $\sigma_{\text{pr_gnd}}$ is computed as the root mean square of the variances of the uncertainties as

$$\sigma_{\text{pr_gnd}} = \sqrt{\frac{1}{M} \cdot \sum_{m=1}^{M} \sigma'^2_{\text{pr_gnd}_m}}. \tag{4.20}$$

Note that the $\sigma'^2_{\text{pr_gnd}_m}$ refer to the variance of the uncorrelated measurements from the single reference receivers divided by the total number of reference receivers M (see Eq. (4.15)).

4.2.3 Assumptions

In the previous sections the two methods for computing the $\sigma_{\text{pr_gnd}}$ have been described. The methods should lead to similar results if all the assumption hold. However, in the current standards, the B-values method is preferred [32]. This because this method gives the best estimate of the residual error in the broadcast smoothed pseudorange corrections and it takes into account the monitors specific for the ground station. Furthermore, it is considered that the CMC methodology might have an influence in the obtained results. For example, the removal of the carrier phase ambiguities might suppress long multipath effects.

In the evaluations in this thesis, both methods will be used and the differences in the results will be discussed. The relation described in Eq. (4.16) will be initially used to estimate the $\sigma_{\text{pr_gnd}}$ from the variance of the B-values. The models for different single frequency processing modes are derived based on the corresponding computed B-values. This simplified relation is based on several assumptions such as the equal errors variance for all reference receivers and the non-correlation of the measurements errors from different satellites and different satellites. Measurements over one month will be used to derive the $\sigma_{\text{pr_gnd}}$ curves for the new signals. As previously discussed, the different modulations available in the signals broadcast by GPS Block IIF satellites on L5 and by Galileo satellites on E1 and E5a yield different multipath and noise error characteristics. The Galileo E1 signals is uses a CBOC(6,1,1/11) which is a combination of the BOC(1,1) and BOC(6,1) modulations. For aviation the current specifications require only the use of the BOC(1,1) component [92]. Thus, the receivers are configured to use the BOC(1,1) replica and all the results of the E1 signal refer to this component only.

For DFDC GBAS in addition to the single frequency ground multipath models, Ifree models are needed in order to enable the use of Ifree processing mode at the aircraft. Section 4.4.4 provides a discussion on the derivation of these models. The impact of the correlation of the L1/E1 measurements with the L5/E5a measurements on the $\sigma_{\text{pr_gnd}_{\text{Ifree}}}$ is shown and recommendations for the derivation of the broadcast models will be proposed.

The evaluation for the GPS are based only on the available 12 Block IIF satellites and from the Galileo constellation the 14 operations satellites available during March 2018 are considered. Note that in this work the evaluation of the $\sigma_{\text{pr_gnd}}$ refers only to the estimated values from the observations and no inflation is considered.

4.3 Facilities

This section provides an overview of the facility used for the data collections and the measurements recorded.

4.3.1 DLR GBAS Test bed

DLR has set up a GBAS prototype at the research airport in Braunschweig (ICAO identifier EDVE) near the DLR research facility. This ground station has been updated and consists of four Javad Delta TRE3 receivers connected to Leica AR 25 choke ring antennas that are mounted at heights between 2.5 meters and 7.5 meters above equipment shelters. All four receivers are capable of tracking GPS L5 (in addition to GPS L1 and L2 semi-codeless) and Galileo E1 and E5a signals. Figure 4.1 shows an overview of the ground station layout.

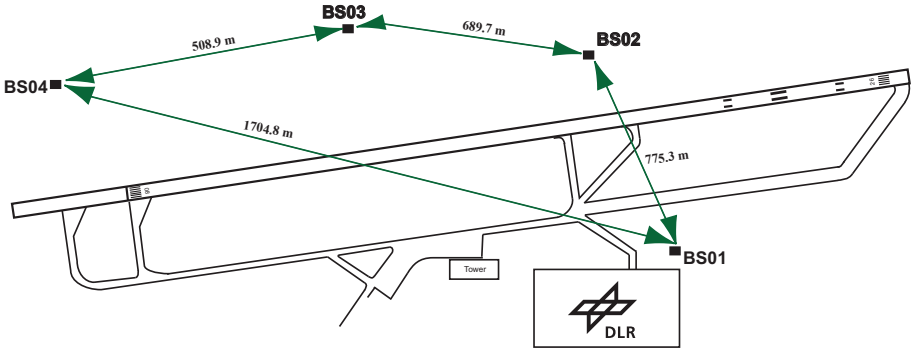


Figure 4.1: DLR GBAS Ground Facility close to Braunschweig Airport

Measurements over one month in March 2018 were collected to perform most of the analysis in this work. For this data collection, the ground reference receivers were configured with a correlator spacing of 0.1 chips for L1/E1 band and 1 chip for L5 band and a bandwidth of 30 MHz. The code and carrier phase observables in the L1/E1 and L5/E5a frequency bands from the available GPS Block IIF and Galileo satellites were collected at a rate of 2 Hz. Additionally, the carrier to noise ratios for all signals were collected at the same rate. During March 2018 all 12 Block IIF GPS satellites were available and the Galileo constellation comprised during that period 14 operational satellites from a total of 18 in orbit (from which 2 in elliptical orbit: PRN code 14 and 18 and 22 with technical issues PRN code 20 and 22). The PRN codes of the operational Galileo satellites used were 11 12 19 which are the first In Orbit Validation (IOV) satellites and the rest being the Full Operational Capability (FOC) satellites.

In the coming period, 8 more Galileo satellites were available launched the end of 2019, completing the set of FOC satellites (PRN 13, 15, 21, 25, 27, 31, 33, 36). The additional satellite have not been analyzed in this thesis. It is however expected that the performance of the complete set of satellites is not different from the one observed from the 14 satellites available. Figure 4.2 and 4.3 show the number of hours collected during the period of one month for each PRN available from the GPS Block IIF and each Galileo satellite, respectively.

The analysis covered in this chapter is similar with the one presented in [85] when measurements over a month from August 2015 from DLR GBAS test bed were used. During that period, 10 GPS Block IIF and only the 3 Galileo IOV satellites are available. Significant differences to this analysis will be shown and discussed in Section 4.4. In addition, data collected over one month in December 2014 will be used for analyzing the impact of the receiver parameters. The receivers were setup with a very narrow correlator spacing of 0.01 for L1/E1 frequency band and 0.1 for L5/E5a band. Again, during this period only the three IOV satellites (PRN code 11,12,19) were available.

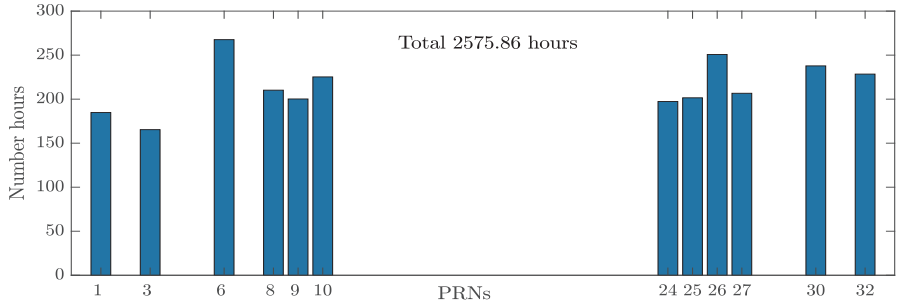


Figure 4.2: Number of hours collected over one month in March 2018 for each PRN from Block IIF GPS

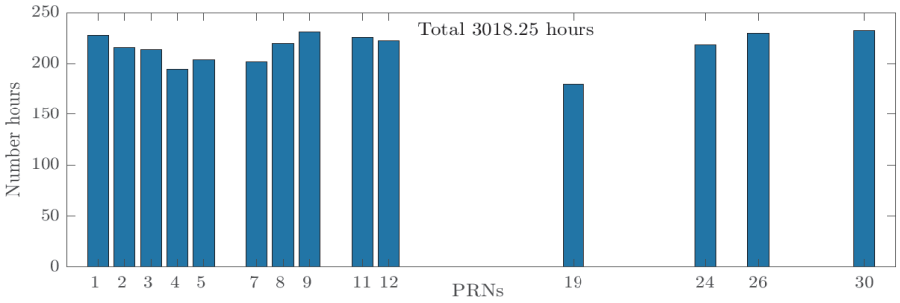


Figure 4.3: Number of hours collected over one month in March 2018 for each PRN from Galileo constellation

4.3.2 Additional data

In addition to the data collected from DLR GBAS test bed, 24 hours of measurements from a certified GAST-C station from Malaga airport are used. The GBAS station consists of four reference receivers connected to BAE multipath limiting antennas ([27]). More information on the site and the antennas landscape are given in [93]. Being a certified equipment, only single frequency (GPS L1) measurements were available from the GBAS station. Thus, dual-frequency phase measurements from a reference station close by Malaga airport are used to estimate the ionospheric delay need for the multipath and noise errors separation.

4.4 Results and discussion

This section discusses the performance results obtained for the different signals in terms of multipath and noise error and $\sigma_{\text{pr_gnd}}$ curves obtained using the relations previously presented.

4.4.1 Raw multipath and noise

The performance evaluation of the new signals starts with an estimation of the raw (unsmoothed) multipath and noise error on all new signals. The raw error is based on the linear combination described in Section 4.2.1. The analysis on the raw multipath shown in this section is based on measurements collected over the full period from one reference receiver (BS01).

Multipath and thermal noise on the newly available L5 signals broadcast by the Block IIF satellites are expected to be smaller compared to L1 C/A code, mainly due to an increased transmitted power and a 10-times-higher chip rate [94]. This is confirmed by the measurements from the DLR's GBAS test bed. In Figure 4.4 estimates of unsmoothed code multipath and noise errors on L1 and L5 are plotted as a function of satellite elevation using measurements from the 12 IIF GPS satellites during March 2018. Multipath and noise error on L5 is reduced substantially from L1 C/A code.

In the same manner, in Figure 4.5, the suppression of multipath and noise on the Galileo signals can be observed, where the code multipath and noise versus elevation for GPS L1 C/A, GPS L5, Galileo E1 and Galileo E5a signals are shown. The Galileo E1 results refer to the (BOC(1,1)) component as mentioned prior in the chapter. The modulation used on Galileo E5a is the same as on the GPS L5 band, the BPSK(10). The multipath on the Galileo E1 BOC(1,1) signal (the blue crosses) is slightly lower than the GPS BPSK(1) on L1 (black triangles), especially at medium elevations. The lower values can be explained by the wider transmission bandwidth on E1 and the structure of the BOC signal [95]. The Galileo E5a signals (cyan circles) show better performance than Galileo E1. As noted above, this is also expected due to the higher chip rate and higher signal power of the E5a signal [95]. Having the same modulation, the GPS L5 signal and the Galileo E5a signal shows similar performance. The slightly lower values on the GPS L5 signals can be attributed to the difference in the transmitted power which will be discussed later more in detail.

These results however, contain not only the effect of the multipath, but also the receiver thermal noise. In attempt to separate the effect of multipath and receiver noise, the expected receiver noise for each signal can be estimated. The expected noise curves are derived based on the theoretical model developed in [96] and [97], where it was shown that the standard deviation of the receiver noise can be computed as

$$\sigma_{\mathrm{n}} = \sqrt{\frac{1}{T_c} \cdot \frac{B_L}{\mathrm{C/N_0}} \cdot \frac{\int_{-B_r}^{B_r} S(f) \cdot \sin^2(\pi f \Delta) df}{\left(\int_{-B_r}^{B_r} 2 \cdot \pi \cdot S(f) \cdot \sin(\pi f \Delta) df\right)^2} \cdot \left(1 + \frac{\int_{-B_r}^{B_r} S(f) \cdot \cos^2(\pi f \Delta) df}{\left(T_p \cdot \mathrm{C/N_0} \cdot \int_{-B_r}^{B_r} S(f) \cdot \cos(\pi f \Delta) df\right)^2}\right)}, \tag{4.21}$$

with B_L being the one sided tracking loop bandwidth (1.5 Hz for reference receivers in DLR GBAS test bed), B_r the one sided bandwidth of the receiver (15 MHz for the DLR reference receivers), Δ the total correlator chip spacing early minus late (0.1 chips for L1/E1 and 1 chip for L5/E5a), T_c the code period, $\mathrm{C/N_0}$ the carrier

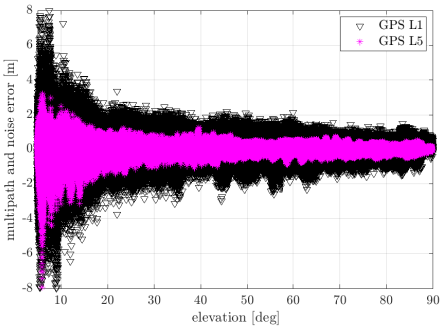


Figure 4.4: Raw multipath and noise as a function of elevation for GPS L1 C/A (black curves with $'\triangledown'$ marker) and GPS L5 (magenta $'\circ'$ curves) signals

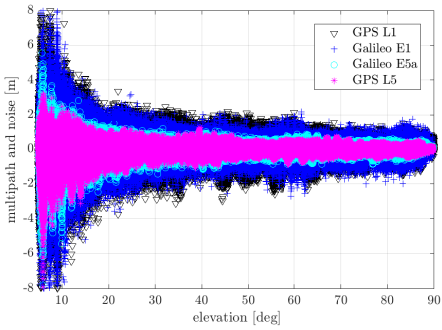


Figure 4.5: Raw code multipath and noise as a function of elevation for GPS L1 C/A (black curves with $'\triangledown'$ marker), GPS L5 (magenta $'*'$ curves), Galileo E1 (blue curve with $'+'$) and E5a (magenta $'\circ'$ curves)

to noise ratio, T_p the predetection integration time and $S(f)$ the power spectrum density. The power spectrum density for the BPSK modulation used on GPS L1, GPS L5 and Galileo E5a is

$$S_{BPSK}(f) = T_c \cdot \left(\frac{\sin(\pi f T_c)}{\pi f T_c} \right)^2, \tag{4.22}$$

with $T_c = \frac{1}{1.023 \cdot 10^6}$ for L1 and $T_c = \frac{1}{1.023 \cdot 10^7}$ for L5/E5a. The Galileo E1 signal uses a CBOC(6,1,1/11) modulation with a dominant BOC(1,1) modulation carrying 10/11 of the entire signal power. Therefore, for the power spectrum density the contribution of the BOC(1,1) component is

$$S_{BOC(1,1)}(f) = T_c \cdot \left(\frac{1 - \cos(\pi f T_c)}{\pi f T_c} \right)^2. \tag{4.23}$$

The calculation of this variance depends however not directly on the elevation, but it is a function of the C/N_0 values. In order to establish a model for the C/N_0 function of elevation, measurements from one reference receiver were used. Mean values over the full set of data was applied as very similar behavior of C/N_0 versus elevation was observed every day. The mean values of C/N_0 over one month of recorded data (March 2018) from the reference receiver BS01 are presented in Figure 4.6.

The measured C/N_0 values are affected mainly by the transmitted power of the satellite and the receiver antenna gain pattern, but local multipath also has an impact. It can be observed in Figure 4.6 that for low elevations, the C/N_0 values are very similar for GPS L1, Galileo E1 and Galileo E5a signals due to both satellite and receiver gain pattern and relatively high multipath. The largest C/N_0 values for all elevation are achieved by the GPS L5 signals because of the higher transmitted power.

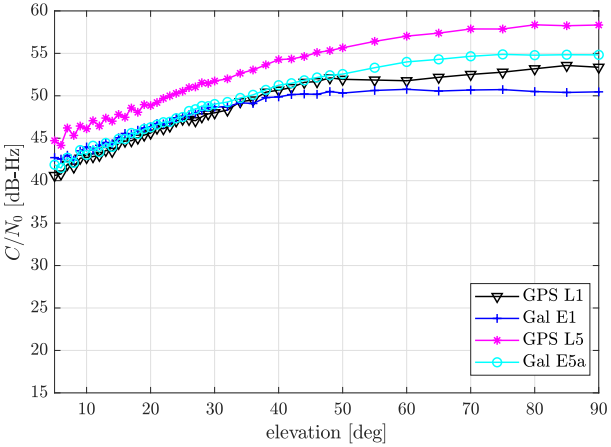


Figure 4.6: Mean C/N_0 over March 2018 for GPS L1 C/A signal (black curve with '$\triangledown$'), GPS L5 (magenta curve with '$*$'), Galileo E1 (blue curve with '$+$') and Galileo E5a (light blue with '$\circ$')

The Galileo E1 signal shows the lowest C/N_0 values over all elevations with an almost constant behavior for elevation above 50°. The C/N_0 values for Galileo E5a exceed the values of the GPS L1 signals, but are lower than the values observed for GPS L5. The difference between the GPS and Galileo signals can be attributed to the different transmitted power as the receiver antenna pattern and the signal modulation are the same for both signals. Table 4.2 shows the values for the minimum and maximum received power on GPS and Galileo signals as specified in the ICDs [98, 99, 95]. These values refer to the received power levels and not directly to the C/N_0 values. However, lower received power level translate into lower C/N_0 values. From the specifications, it becomes clear that the power on the E1 signal is less than for L1 C/A signal which could explain the difference in the observed C/N_0. Furthermore, the maximum values specified for L5 are larger than the values specified for Galileo E5a which is again inline with the observations of the C/N_0 values.

Signal type	**Minimum Received Power [dBW]**	**Maximum Received Power [dBW]**	**Reference**
GPS L1 C/A	-158	-153.5	[98]
GPS L5	-160	-157	[98]
Galileo E1	-157	-150	[95]
Galileo E5a	-155	-152	[95]

Table 4.2: Minimum and maximum power levels for GPS and Galileo signals

A similar analysis of the C/N_0 values was presented in [85] using measurements

from DLR GBAS test bed over the month of August 2015 and the results are shown in Figure 4.7. During that period, only the 3 IOV Galileo satellites (PRN 11, 12, 19) and 10 GPS Block IIF were available. It is interesting to notice that lower C/N_0 values were observed for both GPS and Galileo satellites. For GPS, the values from 2018 increase of about 2 dB-Hz for both L1 and L5 signals. Both results from the two different years were derived only from the Block IIF satellites. Thus, this effect can be attributed to an increase in the transmitted power of the Block IIF satellites. The difference is larger for Galileo satellites and the values obtained from March 2018 are again above the values from 2015. For Galileo E1 signals the increase of the C/N_0 values observed in 2018 varies from 2 to 4 dB-Hz while for E5a signals an increase of up to 5 dB-Hz larger are observed. The results clearly suggest that an increase in the transmitted power occurred on the Galileo FOC satellites. For the further analysis, the results derived from March 2018 are used as they are considered representative for the current Galileo constellation.

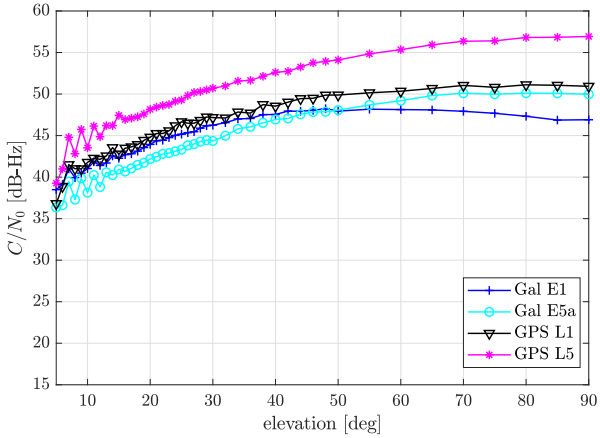


Figure 4.7: Mean C/N_0 from August 2015 for GPS L1 C/A signal (black curve with '$\triangledown$'), GPS L5 (magenta curve with '$*$'), Galileo E1(blue curve with '$+$') and Galileo E5a (light blue with '$\circ$')

The obtained C/N_0 values from 2018 and the different signal modulations impact the code noise error for each signal. This effect can be observed in Figure 4.8 where the standard deviation for the calculated noise error function of elevation bins for GPS L1, GPS L5, Galileo E1 and Galileo E5a are shown. The curves are derived for each elevation bin using the corresponding values from Figure 4.6 and the formulas described in Eq. (4.21), the power spectrum density from Eq. (4.22) and Eq. (4.23).

The noise standard deviation values for GPS L5 (magenta squares) and Galileo E5a (light blue circles) signals are close to each other as they have the same BPSK(10) modulation and the same chip rate. The slight decrease (from 40 mm for low elevations to 10mm for high elevations) in the GPS L5 curve is due to the higher C/N_0

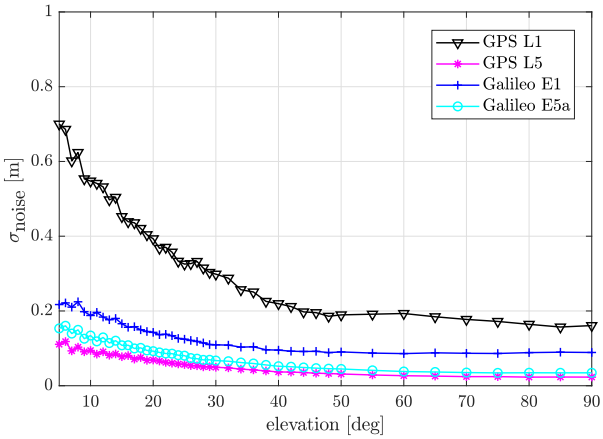


Figure 4.8: Standard deviation for theoretical noise for GPS L1 C/A signal (black curve with '$\triangledown$'), GPS L5 (magenta curve with '$*$'), Galileo E1(blue curve with '+') and Galileo E5a (light blue with '$\circ$')

values on GPS L5. The noise values for GPS L1 (black triangles) are about 3 times larger than those for Galileo E1 BOC(1,1) for elevations below 30°. For high elevations, the curves get closer to each other (with a ratio around 2.0 for elevation below 70° and 1.7 for elevation higher than 70°) due to the slight decrease of the C/N_0 on Galileo E1 signal. The lower noise on Galileo E1 signal (despite the lower C/N_0) can be attributed to the use of the BOC(1,1) modulation. The difference between the GPS L1 and GPS L5 is quite significant, the ratio between the values for the two curves increases from around 6 for elevation below 50° to above 7 for higher elevations. This increase can be explained by the increase in the C/N_0 values (which yields lower noise) on the GPS L5 signals, while the values for the GPS L1 stay rather constant. The difference between Galileo E1 and Galileo E5a noise error is not so larger, as the noise on the Galileo E1 BOC(1,1) modulated signals is lower than for the GPS L1 C/A signals. The ratio between the curves goes from 1.5 for elevations below 40° to 2.5 high elevations.

These results show the receiver thermal noise contribution to the overall performance. Now, the way the multipath affects the derived curves is discussed. It is expected that the difference between the signals shrinks as the multipath is the dominant source of error. This can be observed in Figure 4.9 where the standard deviations of the measured raw multipath and receiver noise for each elevation bin for GPS L1, GPS L5 and Galileo E1, E5a signals are shown. The difference between GPS L5 and Galileo E5a curves is almost negligible as the dominance of the multipath compensates the difference in the noise-only error. In the presence of multipath, Galileo E1 performance is closer to GPS L1 especially for low and high elevations (below 30° and above 70°). This can be explained by the fact that both signals are

highly affected by multipath. For medium elevations, the values for Galileo E1 are smaller compared with GPS L1, which is due to the better performance of the BOC modulation.

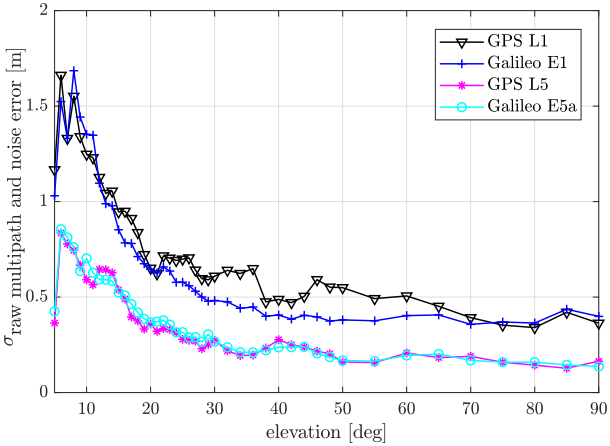


Figure 4.9: Standard deviation for raw multipath for GPS L1 C/A signal (black curve with '$\triangledown$'), GPS L5 (magenta curve with '$*$'), Galileo E1(blue curve with '+') and Galileo E5a (light blue with 'o')

These results are different from what was observed on the curves derived based on the noise-only, where the improvements of the BOC(1,1) modulation is more pronounced for all elevations. The BOC(1,1) component of the E1 signal brings a benefit for medium long range multipath, but for short range multipath the expected code error is similar with the one obtained from the BPSK(1) signal ([41], Chapter 15). This type of short range multipath is expected on the DLR test bed due to the installation of antenna on top of metallic shelter. Furthermore, the antenna gain pattern and the non-optimal installation of the ground station antennas introduces significant multipath i at low elevations. Thus also the difference between the GPS L1 - GPS L5 and Galileo E1 - Galileo E5a also shrinks due to the dominance of multipath over receiver noise on L5/E5a signals and the higher multipath on E1. However, the improved performance in terms of multipath for the BPSK (10) modulation used on the L5/E5a signals is significant and the curves are much lower than the L1/E1 ones. A comparison of the ratios between the curves obtained with the noise only and in the presence of multipath is shown in Table 4.3 for different signals combination.

Until now, the evaluation of the raw code noise and multipath has been presented. However, in GBAS carrier-smoothing is performed to minimize the effect of code noise and multipath. The value which describes the noise introduced by the ground station is represented by the $\sigma_{\text{pr_gnd}}$ and is computed based on the smoothed pseudoranges or B-values from the reference receivers as described in Section 4.2.2. In the following section, the evaluation of the $\sigma_{\text{pr_gnd}}$ using different signals and different smoothing constants is discussed.

Type/Ratio pairs	GPS L1 - Galileo E1	GPS L5 - Galileo E5a	GPS L1 - GPS L5	Galileo E1- Galileo E5a
noise only	1.7 - 3.2	0.6 - 0.7	5.4 - 7.2	0.7 - 2.6
multipath and noise	0.9 - 1.5	0.8 - 1.2	1.6 - 3.4	1.5 - 3

Table 4.3: Minimum and maximum ratios for different signals pairs

4.4.2 Results for derived $\sigma_{\mathbf{pr_gnd}}$ models

This section discusses the comparison of the $\sigma_{\text{pr_gnd}}$ curves for all the signals. The comparison is based on all the data collected over one month. As the Galileo constellation repeats every 10 days. While for the derivation of the $\sigma_{\text{pr_gnd}}$ in a certified station such a long period might not be desired and might introduce additional correlation, in this section it is considered to assess the performance of the Galileo satellites and to observe all the possible geometries. A discussion on the minimum period suggested for deriving the Galileo models is then separate discussed in Section 4.4.2.2.

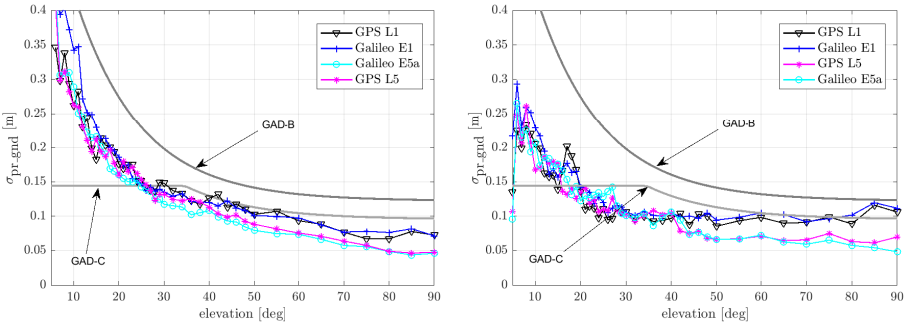
Note that, in this study $\sigma_{\text{pr_gnd}}$ contains only smoothed multipath and noise; no other contributions (e.g., inflation due to signal deformation, geometry screening, non-Gaussian behavior, or other error sources) are considered.

4.4.2.1 Comparison of the different signals

Using the relations derived in Section 4.2.2, the $\sigma_{\text{pr_gnd}}$ values are derived based on both methods, B-values and CMC method. For the B-values method, the $\sigma_{\text{pr_gnd}}$ curves for each reference receiver were computed based on the relation from Eq. (4.16), with $M = 3$. Only three of the receivers have been considered because the fourth did not log the data continuously during the entire period. The number of satellites, N refers to the number of satellites used to compute a pseudorange correction. For GPS L1, a value of 8 is suggested as an average for this number [32]. For the new signals, only 12 GPS satellites are broadcasting on L5 band and a total of 14 Galileo satellites were operational during the selected period. This means that the number considered for GPS L1 is too large to be applied for the new signals. One approach would be to consider this number varying with the elevation bins accounting for the different number of satellites at different elevations. From an integrity perspective it is safer to consider the most conservative value as this would inflate the final sigma an cover the worse case geometry. Analyzing the number of satellites simultaneously available and after the smoothing filter convergence, a values of $N = 4$ was established for both GPS Block IIF and Galileo satellites. It is expected that this number will increase with the addition of the new satellites, and value might be rather conservative. For this analysis an equal number was prefer for both constellation for not introducing additional differences between the different signals.

The values for each reference receiver based on the CMC method have been derived from the smooth dual frequency CMC as discussed in Section 4.2.2.2.

Figure 4.10 shows the derived $\sigma_{\text{pr_gnd}}$ curves from the two methods. The final curves were computed as a root mean square of the variances obtained from eah reference receiver. Figure 4.10a illustrates the $\sigma_{\text{pr_gnd}}$ values obtained from the B-values method for GPS L1 (black triangles), GPS L5 (magenta stars), Galileo E1 (dark blue crosses) and Galileo E5a (light blue circles). The curves are derived based on 100-seconds smoothed B-values. For reference, the Ground Accuracy Designator B (GAD-B) and Ground Accuracy Designator C (GAD-C) curves are shown as well which refer to the 100-seconds smoothed curves. As previously discussed in Chapter 2, the GAD-C curve represents the model for the typical GBAS ground station that uses special MLA antennas while the GAD-B model represents the level of performance that can be achieved with conventional choke ring antennas. The $\sigma_{\text{pr_gnd}}$ curve derived from DLR GBAS test bed for stays below the GAD-B curve and above the GAD-C model for low elevations which is well in line with the expected performance for the used hardware (choke ring antenna and a commercial receiver with a 0.1 chips correlator spacing).



(a) $\sigma_{\text{pr_gnd}}$ from B-values method for GPS L1, GPS L5, Galileo E1 and Galileo E5a

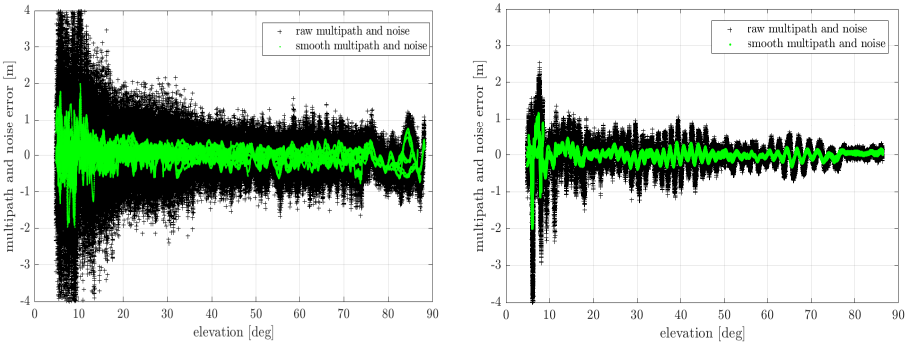
(b) $\sigma_{\text{pr_gnd}}$ from CMC method for GPS L1, GPS L5, Galileo E1 and Galileo E5a

Figure 4.10: $\sigma_{\text{pr_gnd}}$ results for 100 seconds smoothing time constant based on B-values (a) and CMC method (b)

Looking now at the difference between the $\sigma_{\text{pr_gnd}}$ curves derived for different signals in Figure 4.10a, we observe that they get closer to each other compared with the ones obtained from the raw (unsmoothed) errors. This is expected, as carrier smoothing attenuates noise and multipath error and is more effective on the "noisier" raw L1 and E1 measurements. The difference between GPS L1 to GPS L5 is much smaller and shows an increase for high elevations similar with the difference between Galileo E1 and Galileo E5a. It is interesting to note that, after 100 seconds of smoothing, the Galileo E1 curves is closer to the GPS L1. These effects can be explained by the location of the reference station antennas in a non-perfect environment. In particular, the locations of the antennas on the shelters create short-range multipath fading with amplitudes and frequencies depending on satellite elevation and azimuth.

An example of the multipath fading is shown in Figure 4.11a and Figure 4.11b, for

PRN 9 satellite on Galileo E1 and GPS L5, respectively. The raw and smoothed code multipath and noise on E1/L5 is plotted as a function of elevation. These results are processed based on the code-minus-carrier method using measurements from a single satellite over the full data period of one month. The repeatability of the ground track of the GPS satellites (over approximately every 24 hours) and the static position of the receivers lead to repeatability in the resulted multipath curve for each day. It is interesting to see that the smoothed curves (green) follow the pattern of the unsmoothed ones (black) perfectly but with a lower noise level. This effect is not removed by smoothing, as the correlation time of multipath errors is longer than the smoothing time constant. For Galileo satellite, the repeatability of the ground track occurs every 10-days, thus the oscillations do not repeat exactly every day as in the case of GPS, but they remain dominant after smoothing.



(a) Galileo E1 raw and smoothed multipath and noise error as a function of elevation for PRN 9

(b) GPS L5 raw and smoothed multipath and noise error as a function of elevation for PRN 27

Figure 4.11: Raw and smoothed multipath function of elevation for Galileo PRN 9 on E1 and GPS PRN 27 on L5

For the results obtained for the raw multipath and noise evaluation based on the code-minus-carrier method presented Figure 4.9, Galileo E1 signal showed slightly better performance than GPS L1 and the L5/E5a were much smaller compared with GPS L1 / Galileo E1 curves. Those curves were derived from a combination of the multipath and thermal noise. In Figure 4.8 it was shown that the expected noise on Galileo E5/GPS L5 signals is much lower compared with GPS L1/Galileo E1 signals. Also the BOC component of the E1 signal has a lower noise compared with GPS L1. However, after the carrier smoothing, the effect of the noise is removed and the multipath remain dominant in the smoothed pseudoranges. For multipath, the BPSK(10)modulation has an improved performance for multipath delays larger than 30 m (see Figure 4.12). The BOC(1,1) signal is expected to have improved performance on medium and long delay multipath. But for short delay multipath the performance of the BOC(1,1) modulation is the same with the BPSK(1) modulation.

This can be observed in Figure 4.12, where the multipath error envelope for

BPSK(1) modulation (solid lines), BPSK(10) modulation (dot lines), BOC(1,1) modulation (dashed curves) and also CBOC(6,1,1/11) are shown. The multipath envelopes were derived based on 0.1 chips correlator for the BPSK(1), BOC(1,1) and CBOC(6,1,1/11) modulations and 1 chip correlator space for the BPSK(10) modulation which is inline with the configuration of the ground reference receivers. The plots shows the pseudorange error that occurs when the multipath relative phase is 0 or π assuming an infinite bandwidth as described in Chapter 15 of [41].

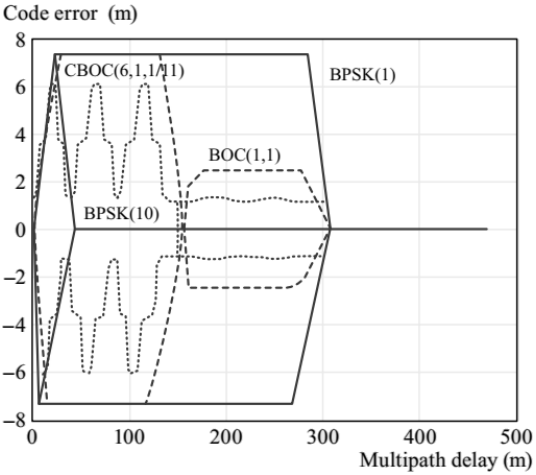


Figure 4.12: Multipath error envelope (taken from Chapter 15 of [41])

The BPSK(1) modulation bounds the envelopes of all the other modulations and leads as expected to the largest pseudorange errors for multipath delays up to 300 meters. It is interesting however to observe that while the CBOC modulation leads to smaller pseudorange errors for multipath longer than approximately 20 meters, the BOC(1,1) component has an improvement only for multipath delay longer than 150 meters. Furthermore, for very short delay multipath (below 10 meters) also the BPSK(10) follows the BPSK(1) envelope but rejects completely the multipath with delays larger than 30 m. When relating these results to the ones from the DLR's GBAS test bed, the small differences between the curves are explainable. This is because the type of multipath created by the installation on the metallic shelters is of short delay for which the improvement of the new signals is not very pronounced.

In previous analysis presented in [85], both Galileo curves derived for E1 and E5a were much lower compared with GPS L1 and GPS L5, respectively. The reason was that only 3 Galileo satellites were available during the period analyzed (August 2015) and thus the effects of the multipath fading were not so strong and were averaged out by the averaging of B-values to derive the $\sigma_{\mathrm{pr_gnd}}$ values. $\sigma_{\mathrm{pr_gnd}}$ is derived by sorting measured B-values from all azimuth into elevation bins. Furthermore, in the derivation of each B-value an average over all satellites (the clock adjustment process)

together with an average over all receivers is performed. If tThe multipath oscillations are very different for each of the satellites, they are averaged out during this process.

In a similar way with Figure 4.10a, Figure 4.10b presents the curves derived from the CMC method. The relation between the signals is somehow similar to the ones derived from the B-values with the following differences:

- for low elevations, the difference between the signals is much smaller and the derived curves are similar for all signals. This can be explained by the fact that the multipath oscillations previously discussed are more dominant in the CMC method because in this case no averaging among the receiver occur. The standard deviation for each reference receiver is only derived from the measurements from the corresponding receiver without the contribution from all the other receivers as it is the case in the computation of the B-values.
- the curves derived from this method look somehow smaller at low elevations compared to the curves derived from the B-values method. The reason for the lower values may also be attributed to the CMC processing. The estimation of the multipath from the dual-frequency code-minus-carrier method implies the removal of the mean over a full pass of the satellite. This removal can also remove part of the multipath and noise error. Furthermore, the usage of the measurements from a single reference receiver in the code-minus-carrier method might introduce higher correlation in the data; if the correlation is negative, the estimated variance is lower. Furthermore, effect can also be explained by the contribution of all the reference receivers to the computation of B-values. If one of the receiver has worse performance it will impact the obtained B-values from all the receiver. On the other side, in the CMC method, the worse performance of one receiver does not affect the results from the others and will be averaged out in the composite sigma.
- the values obtained at high elevations are larger than the values obtained from the B-values method, which might be attributed again to the averaging process that takes place in the computation of the B-values and the more dominant effect of the oscillations in the code-minus-carrier method.

A more detailed comparison of the two methods is provided in Section 4.4.5 where results obtained for each reference receiver are discussed.

4.4.2.2 Discussion for Galileo models

The results derived in the previous section have been based on the measurements collected over the month of March 2018. The entire set of data has been used in order to have sufficient samples to derive representative results and compare the performance of different signals.

The current ground multipath models for GPS L1 signals require an evaluation of the measurements over 24 hours. The reason for this is that the GPS constellation repeats almost every 24 hours (23 hours 56 minutes), meaning that the same satellites

would appear in almost the same location of the sky every day from a fixed location on Earth every day. Establishing the models based on data collected over more days is not desirable because of two main reasons: first, in a certified GBAS station the process of establishing the $\sigma_{\text{pr_gnd}}$ models should be rather short for not delaying the initialization and use of the station. Secondly, data gathered over many days will exhibit correlation due to the repeatability of the multipath errors [90].

For Galileo constellation, the repetition time is different. The orbit constellation selected for Galileo repeats every 10 days and the orbital revolution period is 14 hours and 7 minutes. During the 10 days, each satellite completes 17 complete revolutions. Figure 4.13 shows the track orbiting skyplot projection of one Galileo satellite (PRN 1) as seen from the reference receivers in DLR's GBAS test bed. Each color represents the track over a complete revolution of 14 hours and 7 minutes. It can be observed that for each of the tracks the track orbiting projection is different yielding very different geometries over the 10 days.

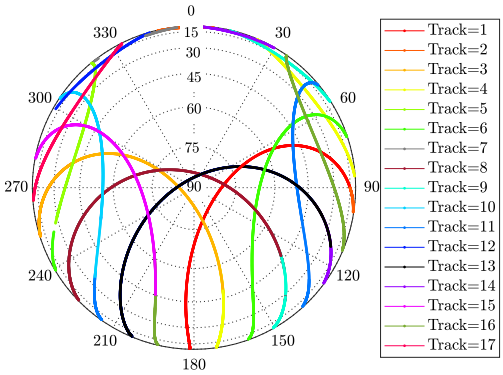


Figure 4.13: Track orbiting skyplot projection of Galileo PRN 1 satellite for 10 days. Each color refers to a complete orbit revolution of 14 hours and 7 minutes

Based on this, the establishment of the $\sigma_{\text{pr_gnd}}$ for Galileo signals should be done using measurements collected over minimum 10 days. In this way, all the geometries will be taken into account in the derived values. Note that, similar to the GPS case if longer period than the 10 days is considered additional correlation might be introduced in the data due to the repeatability of the ground tracks.

Another parameter that is different for the Galileo signals is the number of satellite used in the relation between the $\sigma_{\text{pr_gnd}}$ and σ_{B} (N in Eq. (4.14)). For GPS L1, a value of 8 is suggested as an average of the number of satellites used simultaneously in the GBAS ground processing. This value might however not be representative for the GPS L5 and Galileo satellites due to a lower number available. Based on the available satellites, a value of 4 has been used to derive the models for Galileo signals. For a

full constellation this value might be to conservative and the value of 8 suggested for GPS could be also representative for Galileo.

Summing up, the steps to derive the models for Galileo signals are as follows:

- recording of the B-values over 10 days from all reference receivers for each processing mode (e.g. single frequency E1, single frequency E5a, dual frequency E1/E5a Ifree combination). Simultaneously, satellite elevations for the used satellites should be collected,
- sorting the data from all satellites into elevation bins for each reference receiver. The same elevation bins as suggested for GPS can be selected (1° bin size for elevations below 30°, 2° for elevations between 30° and 50°, and 5° for elevations above 50°),
- computation of the mean and the variance for each elevation bin for each reference receiver and each processing mode independently,
- based on the variances of the B-values obtained in the previous step, the $\sigma_{\text{pr_gnd}}$ is computed for each reference receiver m and each processing mode using the relation described in Equation 4.16. The number of receivers will refer to the total number of reference receiver available during the 10 days and the number of satellites can be set to $N = 8$ when the entire constellation is available (Note again that in this thesis $N = 4$ is considered),
- application of the inflation factors for the different number of samples and for accounting for different effects such as correlation of the data, seasonal change. This step is a decision of the ground manufacturer,
- compute the broadcast $\sigma_{\text{pr_gnd}}$ as the root mean square of the individual variances for each receiver.

It is worth mentioning that the larger variation of the directions of arrival for the Galileo satellites yields to a stronger averaging of the multipath effects, especially of stationary multipath. This is different compared with the GPS satellites, for which the same errors are repeated every day.

4.4.3 Impact of different contributors

After showing the impact of 100 seconds on the residual multipath and noise, this section discusses the impact of different contributors such as the smoothing time constant and the correlator spacing in the reference receivers.

4.4.3.1 Smoothing time constant

The carrier smoothing is performed in GBAS to reduce the high frequency noise and multipath errors from the code measurements. In the current GBAS architecture, two smoothing time constants are used on both the ground and the airborne receivers, namely 100 and 30 seconds. In the proposed concept for a second frequency the 100 seconds smoothing time constant is used as baseline. In this study, the 30, 60 and

100 seconds smoothing time constant are considered for all signals to investigate the reaction of the multipath error from different signals to the carrier smoothing.

Figure 4.14 shows the resulting curves for GPS L5 in comparison to the ones for GPS L1 signals. The curves were computed using three smoothing time constants: 30 seconds, 60 seconds and 100 seconds. The GAD curves are excluded from this plot for simplicity. However, the GAD models refer to the 100 seconds smoothed residual error and it was shown previously that the curve derived for GPS L1 with 100 seconds of smoothing stays below the GAD-B curve. Looking at the different curves derived for the GPS L5 and GPS L1 signals it can be observed that a longer smoothing time brings along a slightly larger improvement for the L1 signals compared to the L5 signals. This mainly results from the larger amount of noise and multipath on the L1 signal before the smoothing (see Figure 4.4). The higher chipping rate and wider bandwidth of the L5 signal is more effective in rejecting long range multipath and also reduces the receiver thermal noise. The smoothing filter is effectively removing high frequency noise and fast changing multipath components. As the improvement on L5 for increasing smoothing time constants is very limited it can be concluded that a short smoothing time constant is sufficient to remove the noise contained in the measurements. Taking all these properties into account the remaining errors on the L5 signals thus mainly result from effects appearing as slowly varying short range multipath. As typically multipath for very high elevation satellites is not expected, other effects (such as antenna and receiver biases) may become the dominant contributors to the residual error. Such errors would, however, be specific to a certain installation and hardware setup.

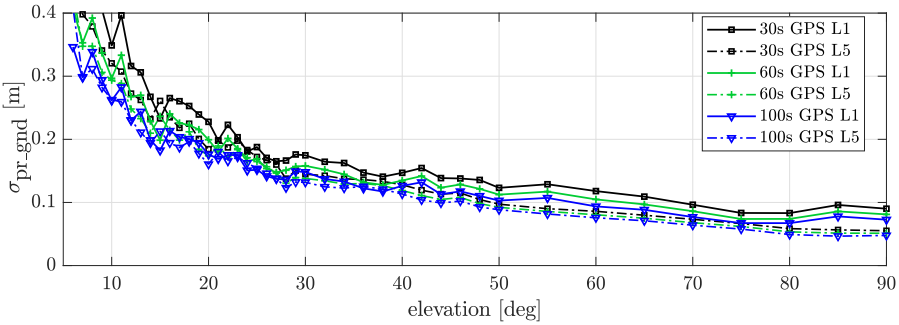


Figure 4.14: $\sigma_{\text{pr_gnd}}$ for GPS L5 signal for different smoothing time constants

The next two figures show the impact of the smoothing time constant on the Galileo signals E1 BOC(1,1) (Figure 4.15) and E5a (Figure 4.16). As reference the GPS L1 curve for 100 seconds is also shown.

Signals broadcast on GPS L1 and Galileo E1 have different modulations and different signal bandwidth. The BOC(1,1) component of the Galileo E1 signals results in a slightly better rejection of long range multipath compared to the BPSK(1) mod-

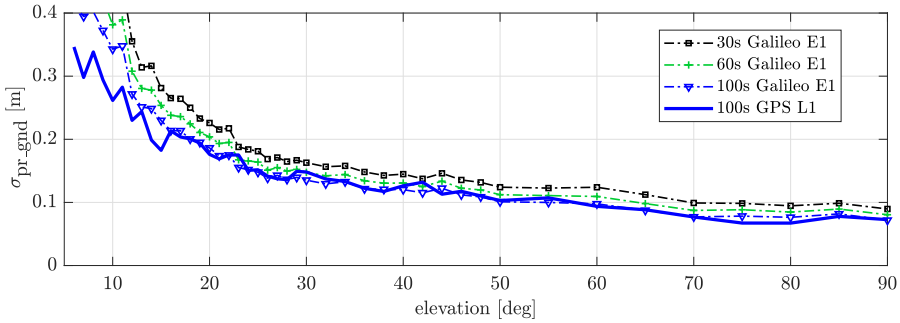


Figure 4.15: $\sigma_{\text{pr_gnd}}$ for Galileo E1 signal for different smoothing time constants

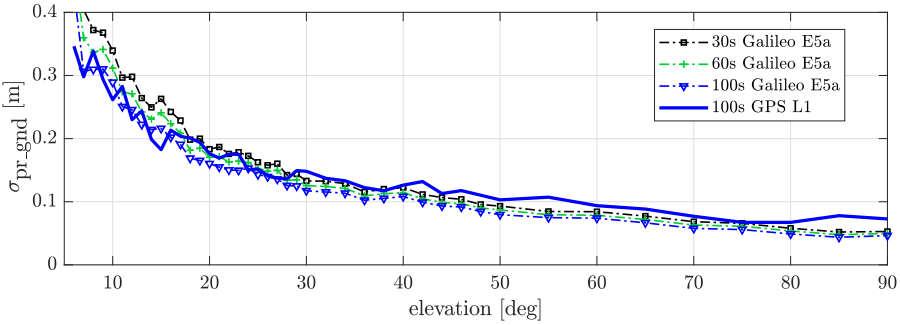


Figure 4.16: $\sigma_{\text{pr_gnd}}$ for Galileo E5a signal for different smoothing time constants

ulation used on the GPS L1 signals. However, in the DLR GBAS test station, the installation of the antennas on the shelters create multipath fading effects which remain dominant after the carrier smoothing. Looking at the difference between the curves computed with different smoothing time constants it is noted that the noise is still a relevant factor in the Galileo E1 signals as a reduction can be achieved by increasing the smoothing time. The increase is somehow smaller compared to the GPS L1 C/A case.

In the results discussed earlier in this section it was showed that the Galileo E5a has a lower residual error after 100 seconds smoothing which is comparable to the results of the GPS L5 signals. This is expected, as similar to GPS L5, the E5a signal has a wider bandwidth and a ten times higher chipping rate than the GPS L1 signal resulting in a better multipath rejection capabilities for long range multipath and lower residual noise. Thus, the Galileo E5a curves plotted in Figure 4.16 show a similar behavior to the GPS L5 curves in Figure 4.14. It can be observed again that the smoothing has almost no benefit for medium and high elevations but brings a slight improvement for low elevation satellites. Similar to the GPS L5 case, also for Galileo E5a the residual errors for high elevations may result from hardware effects

and may not be caused by multipath.

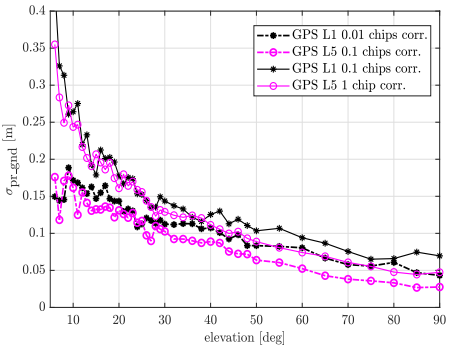
It can be concluded from these results that a shorter smoothing time constant for the Galileo signals (e.g., 60 seconds) is possible without losing much (if any) accuracy, as it generates approximately the same (for E1) or lower (for E5a) residual noise and multipath as a 100-second smoothing time constant on GPS L1. However, the addition of a new smoothing time constant for the Galileo signals might not be desired due to operational aspects and the restricted VDB capacity.

4.4.3.2 Correlator spacing

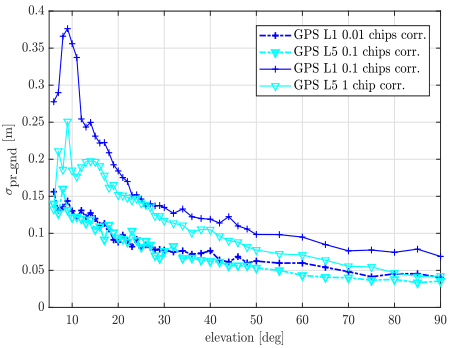
In addition to the environmental effects and antenna characteristics two other parameters that impact noise and multipath are the receiver bandwidth and correlator spacing. In order to show the impact of different correlators on $\sigma_{\text{pr_gnd}}$, measurements with two different correlator spacing values are compared. The previously described results (0.1 chip spacing for L1/E1 and 1 chip for L5/E5a) are compared with results derived using one month of measurements from December 2014 when the receivers were configured with a very narrow correlator of 0.01 chips for L1/E1 and 0.1 chips for L5/E5a [100]. During that period, seven GPS Block IIF (PRN 1, 6, 9, 24, 25, 27, and 30) and three Galileo IOV (PRN 11, 12, and 19) satellites were operational.

Figure 4.17 shows a comparison of the standard deviations of the smoothed-code multipath and noise for GPS and Galileo. In Figure 4.17a the GPS L1 and GPS L5 ($\sigma_{\text{pr_gnd}}$) curves for the two sets of data are shown. Note that in addition to the change in the correlator spacing, the number of satellite used during the different periods has changed. A smaller correlator spacing leads to a smaller multipath envelope and reduced noise and thus also lower $\sigma_{\text{pr_gnd}}$ curves. It can be noted that the effect is pronounced on both GPS L1, as well as the GPS L5 signals. The stronger elevation dependency for low elevation on the curves derived from March 2018 (wider corrrelator) might be attributed also to the change in the number of satellites. Figure 4.17b shows the same comparison for the Galileo E1 and E5a signals. In this case, the difference on the E1 signal is larger compared to the one on E5a. As already discussed, the addition of more satellites arriving from different directs has an impact in the $\sigma_{\text{pr_gnd}}$ values, especially on the E1 signal. It can also be observed that the shapes of the curves for all four signals are somehow similar, except the very low elevations. This suggests that, without any change of the ground-station hardware and the surrounding environment, the $\sigma_{\text{pr_gnd}}$ values will not change significantly.

One other interesting aspect worth discussing is the shape of the GPS and Galileo curves, especially for L5/E5a at high elevation. In Figure 4.17a, the rate of decrease with elevation of the GPS L5 signal is steeper, while for Galileo E5a above elevation of 60 degrees stays almost constant. This is highly correlated with the values of C/N_0 (see Figure 4.6). The C/N_0 for GPS L5 signals for higher elevations (above 70) increases more steeply than for Galileo E5a. The effect might be explained by the difference of the satellites' transmit antenna patterns and the slightly higher orbits of the Galileo satellites.



(a) $\sigma_{\text{pr_gnd}}$ for GPS L1(black curves) and GPS L5(magenta curves) for narrow correlator (dashed curves) and wide correlator (solid curves)



(b) $\sigma_{\text{pr_gnd}}$ for Galileo E1(blue curves) and Galileo E5a(magenta curves) for narrow correlator (dashed curves) and wide correlator (solid curves)

Figure 4.17: Impact of the correlator spacing on ground multipath and noise error

4.4.4 Dual frequency ionospheric free combination

As discussed in Chapter 3, one of the processing modes foreseen for DFDC GBAS is based on the ionospheric-free combination. An important advantage of lower multipath and noise on the L5/E5a measurements is to improve the Ifree position solution. In previous work in [79] it was shown that an increase in error by a factor of about 2.33 was observed for the Ifree standard deviation based on GPS L1 C/A code and L2 semi-codeless measurements. Considering the Ifree linear pseudorange combination from L1 (E1) and L5 (E5a) measurements and assuming that the errors on code and carrier phase measurements of both frequencies are statistically independent and uncorrelated (between frequencies), the standard deviation of Ifree error can be written as

$$\sigma_{\text{pr_gnd}_{\text{Ifree}}} = \sqrt{\left(\frac{f_{L_1}^2}{f_{L_1}^2 - f_{L_5}^2}\right)^2 \cdot \sigma^2_{\text{pr_gnd}_{L_1}} + \left(\frac{f_{L_5}^2}{f_{L_1}^2 - f_{L_5}^2}\right)^2 \cdot \sigma^2_{\text{pr_gnd}_{L_5}}}. \tag{4.24}$$

Under the assumption that $\sigma^2_{\text{pr_gnd}_1} = \sigma^2_{\text{pr_gnd}_5}$ (which is typically considered), the smoothed noise and multipath error on Ifree ($\sigma_{\text{pr_gnd}_{\text{Ifree}}}$) increases by a factor of 2.59 from single frequency L1 smoothed code error. However, from the evaluations presented previously, it can be concluded that there is a difference between $\sigma^2_{\text{pr_gnd}_1}$ and $\sigma^2_{\text{pr_gnd}_5}$, which means that this assumption is too conservative. Furthermore, if the L1/E1 and L5/E5a multipath and noise errors are statistically correlated, the assumption in deriving Eq. (4.24) is not valid and the standard deviation of the Ifree combination becomes

$$\sigma_{\text{pr_gnd}_{\text{Ifree}}} = \sqrt{\left(\frac{f_1^2}{f_1^2 - f_5^2}\right)^2 \cdot \sigma^2_{\text{pr_gnd}_1} + \left(\frac{f_5^2}{f_1^2 - f_5^2}\right)^2 \cdot \sigma^2_{\text{pr_gnd}_5} + 2 \cdot \frac{f_1^2}{f_1^2 - f_5^2} \cdot \frac{f_5^2}{f_1^2 - f_5^2} \cdot \text{Cov}(L1, L5)}. \tag{4.25}$$

If the multipath and noise errors between the two single frequencies are negative correlated, the values obtained by using Eq. 4.24 are overbounding the actual value. On the other side, positive correlation yields to increased standard deviation compared with the one derived based on independent samples.

Figure 4.18 shows the ratios between $\sigma_{\text{pr_gnd}_{\text{Ifree}}}$ for the GPS L1/L5 Ifree combination and $\sigma_{\text{pr_gnd}}$ for GPS L1, both based on 100-second smoothed code measurements. These results are based on the more-recent month measurements from March 2018. The value of $\sigma_{\text{pr_gnd}_{\text{Ifree}}}$ was computed for three cases: (1) assuming that GPS L1 and L5 multipath and noise errors are uncorrelated, and L1 and L5 error standard deviations after smoothing are equal; (2) assuming uncorrelated errors and using measurement-based sigmas (one month data set) for GPS L1 and GPS L5; and (3) computing the Ifree error standard deviation directly from one-month Ifree measurements (broadcast corrections and B-values). The assumption of the equality of $\sigma_{\text{pr_gnd}}$

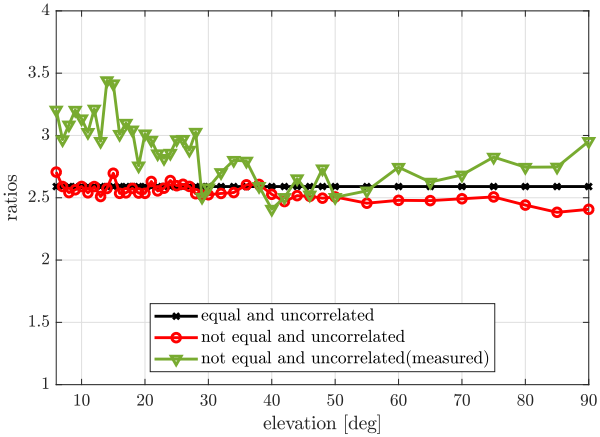


Figure 4.18: Ratio $\sigma_{\text{pr_gnd}_{\text{Ifree}}}$ GPS 100s smoothed- $\sigma_{\text{pr_gnd}_{L1}}$ GPS 100s smoothed function of elevation

on L1 and $\sigma_{\text{pr_gnd}}$ on L5 in case (1) (the black curve) is conservative compared with the curve derived based on the actual values of the single frequency $\sigma_{\text{pr_gnd}}$. It was shown in previous evaluations that the $\sigma_{\text{pr_gnd}}$ on L5 is lower than $\sigma_{\text{pr_gnd}}$ on L1 due to the better multipath rejection capability of L5 signals; thus the theoretical curve (red line) computed based on Eq. (4.24) (considering the real values for the single frequency standard deviations) is below the 2.59 ratio. Only at low elevations does this ratio (the red line) approach the value of 2.59, when the two standard deviations become almost equal.

However, it is important to observe the behavior of the measured ration. The measured ratio from case (3) (the green curve) exceeds the theoretical ratio computed based on the assumption of statistically independent samples from case (2) (the red

curve) and 2.59 bound. This can be explained by the fact that the multipath errors in the measurements are not independent, but instead have a significant degree of positive statistical correlation between frequencies. The correlation of multipath error between L1 and L5 varies with elevation and appears to be highest for low elevations. This likely depends on the repeatable multipath patterns in DLR installation. Figure 4.19 shows a scatter plot of the B-values for L1 versus B-values for L5. Both estimates are derived based on 100-seconds smoothed broadcast corrections and independent samples taken every 200 seconds were considered to generate the results. The B-values from the two frequencies show a positive correlation which confirm the results obtained in Figure 4.18. A similar pattern has been observed also for the Galileo

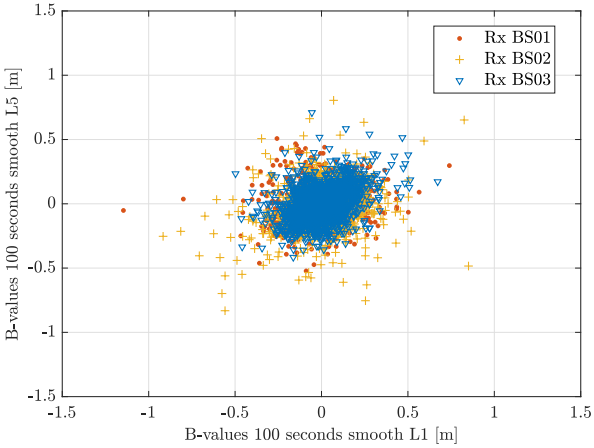


Figure 4.19: Correlation between the 100 seconds smoothed B-values on GPS L1 and GPS L5

signals and will thus not be shown further.

The results obtained in this section are important for the broadcast of the $\sigma_{\text{pr_gnd}_{\text{Ifree}}}$. The ground station broadcasts the single frequecy L1 and L5 pseudorange corrections and B-values and the Ifree combination is formed by the airborne receiver. It has been shown that if the pseudorange corrections are smoothed with the same smoothing time constant, the Ifree linear combination can be applied directly on the smooth single frequency pseudorange correction. However, this is not the case for the $\sigma_{\text{pr_gnd}_{\text{Ifree}}}$. If the ground broadcasts only the single frequency models without further information on the correlation of the L1 and L5 measurements errors, the value computed by the airborne receiver will be based on the relation from Eq. (4.24). From the results derived, it was shown that this value is not always a bound of the actual multipath and noise present in the Ifree pseudorange corrections. Thus, a DFDC GBAS ground station should broadcast a separate value for $\sigma_{\text{pr_gnd}_{\text{Ifree}}}$. Figure 4.20 shows the obtained curves for the Ifree combination for GPS (dark red curves) and Galileo (yellow curves) for 100 and 30 seconds smoothing time constants with solid and dashed lines respec-

tively. For this installation the models for the two constellations are very similar, but they might be different in a certified GBAS installations.

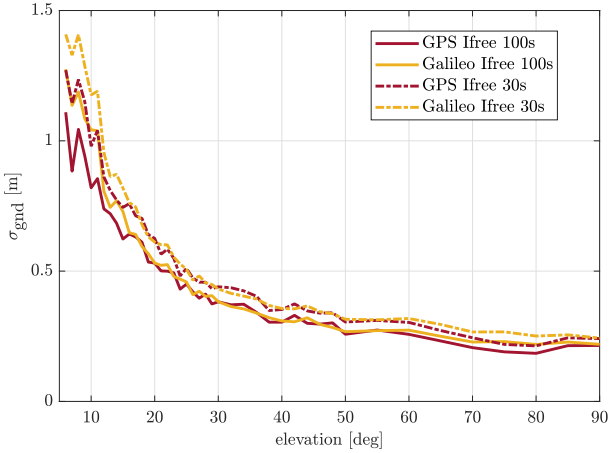


Figure 4.20: $\sigma_{\text{pr_gnd}_{\text{Ifree}}}$ for GPS L1/L5 and Galileo E1/E5a

4.4.5 Comparison of the B-values method and code-minus-carrier method

Section 4.2.2 presented the methodology to derive the $\sigma_{\text{pr_gnd}}$ values based on the two different methods: B-values technique and the code-minus-carrier technique. As previously discussed, both methods are proposed in the current standards. The B-value method is preffered as it is based directly on the broadcast pseudorange corrections and takes into account the ground system monitoring. However, until now a comparison of the two methods has not been performed. It is the intent of this section to compare in detail the results obtained from the two techniques and discuss the differences between them.

The analysis is performed for each of the reference receivers, in order to understand more in detail the differences between the methods. The comparison is performed only for GPS L1 for 24 hours. This is because additional correlation in the multipath errors might be introduced if measurements over longer period are considered. Furthermore, in addition to the measurements from DLR GBAS test bed, measurements over 24 hours from the certified GAST-C GBAS station in Malaga are used in this evaluation. The measurements from the certified GBAS station are available for 24 hours for GPS L1 C/A signal.

For DLR GBAS test bed, the results refer to measurements collected over 24 hours on 3$^{\text{rd}}$ of March 2018. For this chosen day, continuous measurements from all four reference receivers were available. The measurements from GBAS station in the Malaga data are available from 29$^{\text{th}}$ of March 2014. The multipath and noise estimation has been performed based the GPS L1 code measurements and dual frequency L1 and

L2 carrier phase measurements using the relation from Eq. (5.5). The carrier phase measurements on L2 frequency were chosen in this study because they are available for all GPS satellites broadcasting the L1 signal. This yields to additional data to perform the multipath error estimation. As the GBAS station in Malaga provides only measurements from GPS L1 signals, carrier phase measurements from a reference station closeby Malaga airport airport were used to estimate the ionospheric delay. More details will be given further in this section.

The raw multipath and noise estimated were smoothed by applying a smoothing filter with 100 seconds smoothing time constant (see Eq. (4.18)). The smoothed estimates were then sorted on elevation bins and the $\sigma_{\text{pr_gnd}}$ was computed for each reference receiver as described in Section 4.2.2.2. The curves based on the B-values method have been derived for each reference receiver from 100 seconds smoothed B-values using the relation from Eq. (4.16) with $M = 4$. For the number of satellites, an average of the number of available satellites $N = 8$ (which is suggested in standards for GPS L1) was used. In addition to the results based on smooth measurements, the curves based on the raw (unsmoothed) measurements were derived. The unsmooth measurements are used in order to remove the effect of the smoothing filter from the comparison of the two techniques.

Figure 4.21 shows the $\sigma_{\text{pr_gnd}}$ curves for DLR GBAS test bed derived from the B-values method (black curves) in comparison with the curves derived from CMC method (red curves) function of elevation for each of the reference receivers used in the processing. The solid lines represent the curves obtained using the raw (unsmoothed) measurements and the dashed lines represent the curves derived after applying a 100 seconds smoothing time constant. For the B-values method, the unsmoothed curves were obtained from (additional) generated pseudorange corrections and B-values from unsmoothed code measurements.

It can be observed that the differences between the two methods are not the same for each of the receivers. This can be explained by the fact the installation of each reference antenna and the surroundings are very different for each installation. Looking at the results, the values derived from the CMC method are somehow lower, especially after the 100 seconds smoothing. As previously discussed, this result might be attributed to the CMC methodology in which the mean over a continuous pass is removed to eliminate the carrier phase integer ambiguities. This removal could remove also multipath components.

Another major difference between the methods is that when deriving the results for one reference receiver, the CMC method uses only measurements from the corresponding reference receiver. The computation of the B-values, on the other hand, combines the measurements from all the receivers (see Eq. (4.3)). The assumption in the derivation of the $\sigma_{\text{pr_gnd}}$ based on B-vlues is that error variances from the reference receivers are almost equal. In case this assumption does not hold, the calculation of the B-values is affected. This can be observed for reference receiver BS03 in Figure 4.21 (graph left bottom). For low elevations (below 20°) the 100 seconds smoothed results derived from CMC estimates are rather constant (dashed red), but the re-

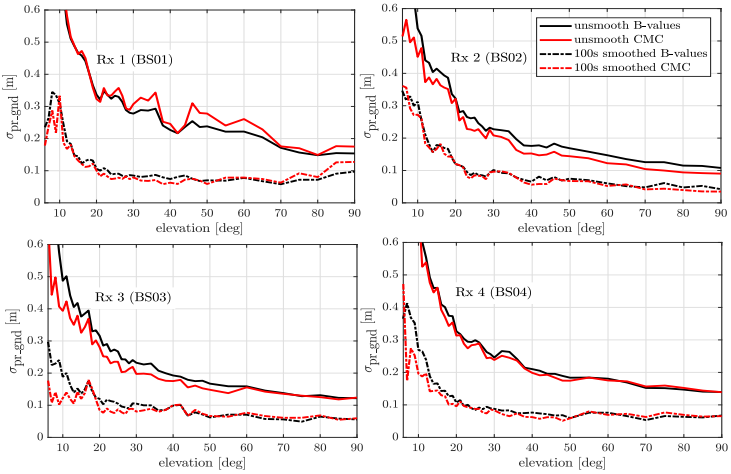


Figure 4.21: Comparison B-values - CMC method using measurements from DLR GBAS test bed

sults based on 100 seconds smoothed B-values increase significantly (dashed black curve). Analyzing the results after smoothing from the other three receivers, it can be noticed that all the curves increase significantly when using the B-values method. As all the other three receivers contribute to the computation of the B-values of the reference receiver BS03, this effect is propagated also to the estimates from the other receivers. The effect is not visible on the unsmoothed results, because the noise error and increases for low elevations (due to e.g the antenna gain pattern).

In addition to the equality of the error variance for the reference receivers, one requirement in a certified GBAS station is to minimize the multipath correlation for each reference receiver and between the receivers [34]. As discussed in previous sections, for the DLR installation, the locations of the antennas on the shelters create multipath fading with amplitudes and frequencies depending on the satellite's angle of arrival. These oscillations lead also to a long time correlation in the measurement errors. Figure 4.22 shows the autocorrelation values of the multipath and noise error for 600 seconds lag for all four receivers from the DLR GBAS test bed. The different colors of the lines represent the autocorrelation function for different satellites. It can be observed that the autocorrelation of the multipath is significant even after 100 seconds smoothing, especially for receiver BS01 and BS02. This multipath will remain dominant after the application of the 100-seconds smoothing filter.

In a certified GBAS station it is expected that the two methods provide similar results and the correlation of the multipath should be insignificant after 100 seconds. In order to validate these points, measurements from a certified GAST-C station from Malaga airport are used. The GBAS station consists of four reference receivers connected to BAE multipath limiting antennas [27]. As only single frequency mea-

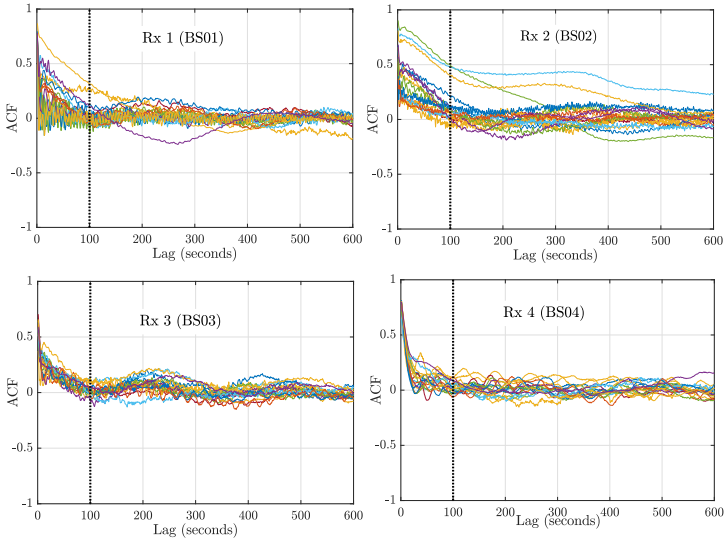


Figure 4.22: Multipath autocorrelation function for reference receivers of the DLR's GBAS test bed

surements from GPS L1 C/A signals were available from the GBAS station, dual-frequency carrier phase measurements from a reference station from the Instituto Geografico Nacional (IGN) network close by Malaga airport were used to estimate the ionospheric delay. The estimated ionospheric delay for each satellite (multiplied by 2) was subtracted from the single frequency CMC estimates of the GBAS station. Figure 4.23 shows in a similar manner as in Figure 4.21, the $\sigma_{\text{pr_gnd}}$ curves versus elevation derived from the CMC method and from the B-values method using unsmoothed and 100 seconds smoothed measurements. Both the unsmoothed and smoothed results look very similar and the differences are much smaller compared with the ones obtained from DLR GBAS test bed.

In Figure 4.24 the autocorrelation function of the multipath for 600 seconds for all four reference receivers is shown. In this case, there is no significant correlation after 100 seconds. However, receiver 4 (bottom right plot) shows a slightly different behavior. The autocorrelation function has larger values up to a lag of 100 seconds and decreases after, being characterized by sinusoidal oscillations (similar to the ones from DLR's measurements). This might be due to a different installation of the receiver. Compared to the results from DLR GBAS test bed however, the amplitudes are much lower and thus their impact is limited.

From this comparison, it can be concluded that the differences between the two methods are correlated with the installation of the reference antennas and the assumptions that are made in the derivation of the simplified relation between $\sigma_{\text{pr_gnd}}$ and σ_B (see Eq. (4.14)). The assumptions made in the derivation of the simplified

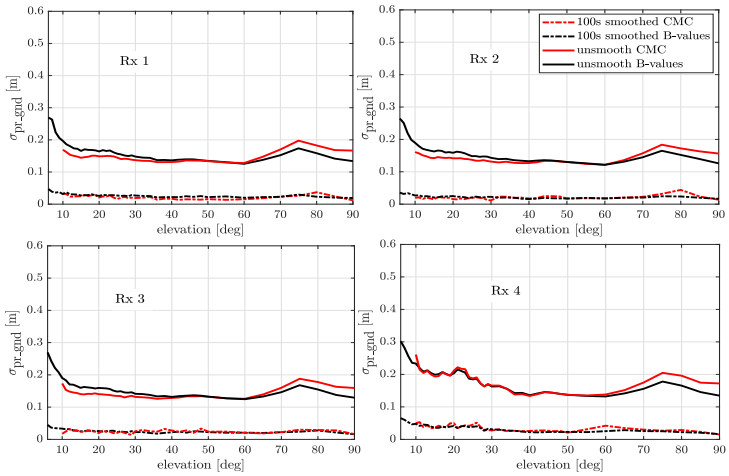


Figure 4.23: Comparison B-values - CMC method for using measurements from GBAS station in Malaga

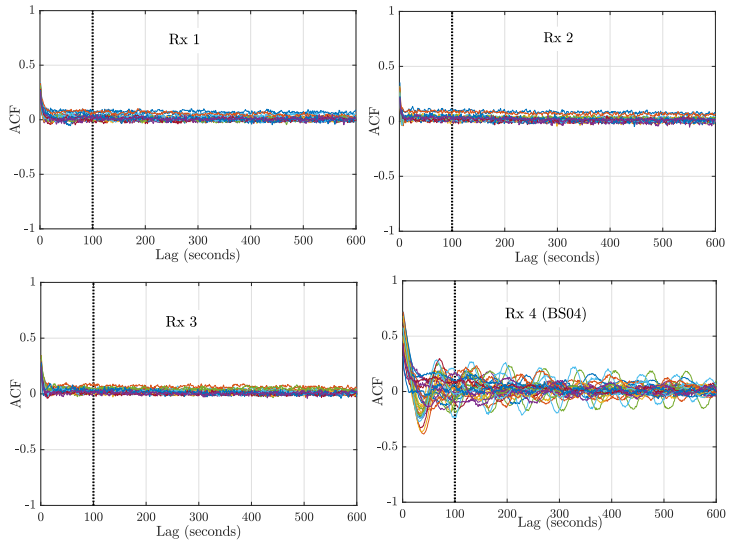


Figure 4.24: Multipath autocorrelation function for the measurements from the reference receivers of the GBAS station in Malaga

relation and their impact are as follows:

- The variance of the multipath and noise error for different satellites are equal. This assumption regards the use of the measurements from all satellites in

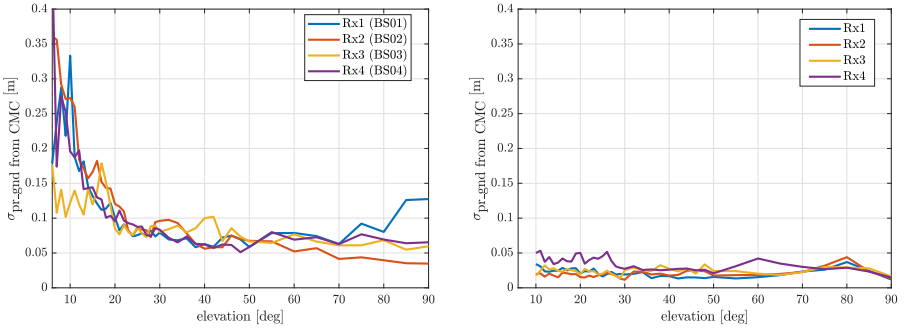
view to estimate the receiver clock bias in the calculation of the pseudorange corrections. In this step a weighted mean over all satellites is computed. If the weights considered are proportional with the elevation of the satellite (typically, the variance of the measurements errors is elevation dependent), the equality of the variances of the measurement errors from different satellites is reasonable,

- The multipath and noise errors from different receivers is uncorrelated (for the same and different satellites pares).
  The assumption that the measurements between different satellites and different receivers are uncorrelated is reasonable as different satellites arrive from different directions (elevation and azimuth) creating multipath errors with different characteristics. On the other hand, the multipath error of the same satellite might be correlated between the receivers due the fading effects created by the installation of the antennas on the shelters (see Figure 4.22). The amplitude of the oscillations depend on the height of the antennas. The errors would be perfectly correlated if the antennas are installed at exactly the same heights and the same location on the shelter. In DLR test bed, the antennas are located at slightly different heights which reduces the changes of having correlation between different receivers. Furthermore, the distance between the receivers is around 1 km which leads to the measurements being uncorrelated,

- The multipath and noise errors of two satellites from the same reference receiver are uncorrelated.
  The measurements errors from two satellites arriving from the same direction might be correlated due to the fading effects, but it is difficult to separate it from the correlation of any hardware or receiver biases. Furthermore, the correlation would be significant only for the satellites with exactly the same elevation and azimuth angle. Thus, the correlation between two the measurement errors of two different satellites tracked by the same receiver is considered negligible,

- Variances of the measurements errors of different receivers are equal.
  This is one of the main assumption in the derivation of the simplified relation between σ_B and $\sigma_{\text{pr_gnd}}$. As it was observed in the previous figures, this assumption does not entirely hold. A comparison of the $\sigma_{\text{pr_gnd}}$ derived for each reference receiver are shown in Figure 4.25 for Braunschweig (Figure 4.25a) and Malaga station (Figure 4.25b). The CMC method is chosen as the curves give an estimate of the errors for the receiver of interest only. For DLR GBAS test bed the differences between the receivers are quite significant, but it is interesting to notice that also for a certified station, the reference stations have different performance. An approach to account for this differences is discussed further in the next paragraphs.

The broadcast pseudorange corrections are computed by taking the default mean over all reference receivers. This step also assumes that the reference receiver have similar error variance. One approach to tackle this issue would be to apply a weighting for the reference receivers similar to the weighting of the measurements from different satellites (applied in the receiver clock removal step). This method can be applied as



(a) Reference receivers from DLR's GBAS Test Bed

(b) Reference receivers from Malaga GBAS station

Figure 4.25: 100 seconds smoothed $\sigma_{\text{pr_gnd}}$ obtained from CMC method

follows:

- computation of the $\sigma_{\text{pr_gnd}}$ for each reference receiver based on CMC method for L1 band, If large differences are observed, a weighting for each reference receiver can be applied
- the weighting factor can be computed based on the $\sigma_{\text{pr_gnd}}$ from each reference receiver as

$$w_m = \frac{\sigma_{\text{pr_gnd}_m}}{\sum_{m=1}^{M} \sigma_{\text{pr_gnd}_m}}, \tag{4.26}$$

- application of the weighting in the computation of the broadcast pseudorange corrections and in the B-values calculation as

$$PRC_{\text{TX}}^{n} = \sum_{m=1}^{M(n)} w_m \cdot {PRC_{\text{SCA}}}_m^n \tag{4.27}$$

$$B_m^n = w_m \cdot PRC_{\text{TX}}^{n} - \sum_{\substack{m'=1 \\ m' \neq m}}^{M} w_{m'} \cdot {PRC_{\text{SCA}}}_{m'}^{n}. \tag{4.28}$$

with w_m representing the weights of each reference receiver. Note that for DFDC GBAS system the same weighting should be applied for both single frequency corrections. This is especially important because the dual-frequency Ifree pseudorange corrections are computed by the airborne receiver and if different weights are used the combination introduces additional errors.

4.5 Publications

The work from this chapter was published in the Navigation Journal M.-S. Circiu, M. Meurer, M. Felux, D. Gerbeth, S. Thölert, M. Vergara, M. Sgammini, C. Enneking, S.

Pullen, and F. Antreich, "Evaluation of GPS L5 and Galileo E1 and E5a performance for future multifrequency and multiconstellation GBAS" ([85]).

Furthermore, the results have been presented at internal conferences and the various GBAS working groups such as Landing & Guided Take-Off Task Force (LATO) and International GBAS Working Group (IGWG) and Eurocae Working Group 28.

5 Airborne multipath models

5.1 Objectives and contributions

The previous chapter discussed the multipath and noise errors affecting the GBAS ground stations. These errors affect the measurements recorded by the ground receivers and need to be taken into account and bounded because they contribute to the calculation of the pseudorange corrections. However, in GBAS, the ground station uses antennas specifically designed and sited to eliminate most of the multipath effects. Thus, the code multipath errors are expected to be much lower compared to the airborne multipath. Airborne multipath errors may occur due to the airframe or due to ground reflections during landing, takeoff or taxiing on the runway. The airframe refers to the mechanical structure of an aircraft including the main components such as the fuselage, the wings, the tail and excluding its instrumentation. It represents a potentially large source of error driving the overall pseudorange residual uncertainty and thus, the protection levels which bound the residual position errors. These errors are especially dominant for dual-frequency users as the largest error source, the ionospheric error, is effectively removed.

Currently, the airborne multipath model specified in the single frequency standards ([18, 101]) is applicable only to the GPS L1 signals and was experimentally derived from flight test campaigns conducted by Boeing and Airbus. For the future navigation service for aviation models characterizing the single frequency Galileo E1, Galileo E5a and GPS L5 need to be developed.

This chapter develops and discusses the methodology to characterize the residual multipath and noise errors for the specific application of aeronautical navigation by combining the results of an extensive measurement campaign with a series of detailed studies on different factors of influence. Furthermore, models characterizing the multipath and noise errors in the ionospheric free pseudoranges are also needed and will be discussed in this work. Preliminary results derived from various flight tests will be shown and discussed.

The analysis and the results discussed in the previous chapter on the ground multipath errors focused on their application to GBAS. In contrast, the airborne multipath models are not only relevant for GBAS users, but also for all the other GNSS aviation applications such as SBAS, Advanced Receiver Autonomous Integrity Monitoring (ARAIM). This work contributed and was partially developed during the DUFMAN project funded by the European Commission. The scope of the project is to develop airborne multipath models for GPS L5 and Galileo E1 and E5a based on the one side on airborne measurements and on the other side, to perform a de-

tailed analysis of the factors of influence to the multipath error, such as airframe, antenna, receiver parameters. The author's contribution to the project focused on the derivation of the measurements-based models which is presented in this work. This includes the development of the methodology and implementation of the specific algorithms for estimating the multipath from measurements, the evaluation of flight data from different aircraft to derive the preliminary multipath models, the investigation of the several factors of influence such as the smoothing time constant, the receiver correlator spacing and the different airframes.

The first part of this chapter provides an overview of the airborne multipath errors in GBAS and the existing multipath models for the GPS L1 code measurements. The second part presents the methodology used to derive new dual-frequency dual-constellation multipath models. Based on the methodology, the last section shows the results obtained from different aircraft types and discusses the impact of different factors of influence to the multipath models such as the receiver parameters, the airframe and the smoothing time constant.

The main contributions to this chapter are as follows:

- development of an improved methodology for estimating the multipath error using measurements from flight trials,
- proposal of a decomposition of multipath errors and antenna-induced errors,
- first preliminary derivation of airborne multipath models for single frequency signals broadcast by GPS L5 and Galileo satellites and for dual-frequency combinations,
- investigation of the impact of the main factors of influence to the airborne multipath models including processing, smoothing time constant, receiver parameters and antenna.

5.2 Airborne multipath error

The airborne multipath error refers to the error introduced in the pseudorange measurements of the airborne receiver. These errors are specific to the airborne user and do not get canceled through the application of the differential corrections. The multipath at the airborne receiver can occur due to the reflections from the airframe or during landing and rollover due to reflections from the ground. Figure 5.1 shows a simplified example of a reflections of the GNSS signal due to the tail which translates into a time-delay of the waveform receiver by the antenna, and thus a pseudorange error. In reality, however the multipath error propagation is more complex and there are many additional sources of multipath on aircraft. A multipath error model needs to characterize all of the multipath contributions and to bound them [102].

As GBAS is primarily based on code measurements (with the carrier phase measurements being used in the smoothing process), the airborne multipath present in the pseudorange measurements has to be characterized. The airframe multipath errors can be determined either by making use of the GNSS observable or by means of

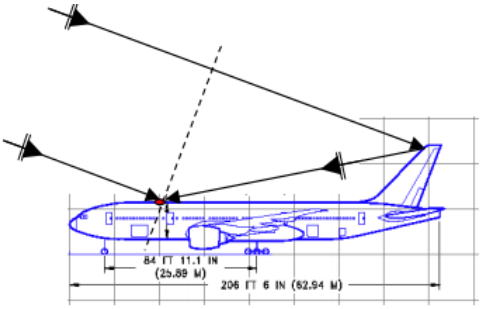


Figure 5.1: Example of airborne multipath (taken from [102])

electromagnetic simulations. This work will focus on the derivation of the multipath model from measurements.

5.3 State of the art: current airborne multipath models

The standards for GBAS ([18]) include an allocation for the multipath introduced by the airframe which is defined by a common error model. This model characterizes the errors introduced in the airborne pseudorange measurements by the airframe itself and from other components such as other antenna and from ground reflections. It is applied to the integrity bounds computed through the protection levels. Previous work in [103, 104, 105, 106] describe the assessments of the contribution of airborne multipath and the receiver thermal noise to the airborne accuracy allocation for GPS L1 C/A code.

The community agreed to develop and validate one standard model for the airborne multipath which is included in the $\sigma_{\text{pr_air}}$ term described previously in Section 2.5.2.2. The use of one standard model was preferred in order to avoid having different models and the associated difficulty in certification for each type of the aircraft. This approach was considered to be feasible because the "airframe multipath errors were predicted to be small based on theoretical knowledge of multipath effects on receiver tracking" [104]. Furthermore, it was considered that the movement of the aircraft would lead to a noise-like multipath error which is reduced by the carrier smoothing.

The multipath model included in the standards was initially proposed in [107] and [108] and is described in Eq.(2.32) and shown in Figure 2.8 (black curve). In addition to the multipath model, the standards include the two AAD performance for the receiver thermal noise (the red and green curve in Figure 2.8). The receiver thermal noise and the multipath noise are parameterized as zero-mean Gaussian overbounds and together they form an error distribution expressed as a function of the elevation angle of the satellite (see Eq.(2.31)). The elevation of the satellite refers to the elevation above horizon (in local level frame). The reason for defining these error bounds relative to the horizon is that most of the time, commercial aircraft are flying

straight and level and in this way the attitude of the airframe (as source of multipath reflections) does not need to be considered in the model making it easy to use.

The validation of this multipath model was done by several ICAO member states and organizations such as FAA, Boeing and Honeywell and Eurocae. In [104] the authors describe the work that was performed by FAA, Honeywell and Boeing to validate the initial model based on measurements collected over years during normal production flight testing from 6 different Boeing aircraft types. The outcome of the study was that the existing multipath model can be considered as an "adequate estimate of airframe multipath" for the different airframe types. However, the measurements used were collected from flight tests that were not explicitely designed to support the airframe multipath activity. Thus, it is believed that "limitations of the flight test instrumentation are likely to have caused errors from more sources than airborne multipath to be identified as multipath. Consequently the magnitude of the errors predicted by the model could have been artificially inflated" [109].

During 2^{nd} quarter of 2003 and 2^{nd} quarter of 2005, a joint dedicated research program was conducted by Boeing and FAA with the scope to re-evaluate the existing multipath model, to understand how new receiver requirements could impact the aiborne multipath model and finally to study if a separate multipath model needs to be defined for including the effect fo the ground multipath.

The airborne investigation program is described in [109] and included two main components, namely, the development of an electromagnetic model which is able to predict the effect of the airframe multipath as well as ground bounce multipath and the collection of GPS measurements on two commercial aircraft, used to validate the electromagnetic model.

The flight test campaign included hundred of flight hours flown on two Boeing 777-300ER airplanes to support the aircraft type certification and Boeing on 737-800NG airplane in support of development of a new autopilot. The measurements were collected during the entire duration of the flight and for all flight phases without adding any special condition or flight profiles [105, 106]. The main goal of the flight tests was to collect the measurements and to evaluate the multipath error experienced on the two aircraft. Onboard each aircraft, several GPS receivers were installed and connected to an active Novatel Model 512 L1/L2 antenna. Different configurations in terms of correlator type and correlation spacing values were selected for different receiver of the same type. Further information on the test equipment used in the flight tests are given in Table 1 and Figure 3 from [109]. The multipath errors were estimated by forming the difference between the code and carrier phase measurements with the ionospheric divergence removed using the dual-frequency carrier phase measurements. Based on these estimates, standard deviations were computed function of the elevation angle in order to derive a measurement-based model. The processing of the measurements and the derivation of the models are discussed in [105, 106, 109]. As the measurements contain both the influence of the multipath and the receiver thermal noise, a GNSS simulator was used to estimate and remove the receiver thermal noise.

In parallel with the measurements from the flights tests, an electromagnetic multipath model was developed which is described in [106, 109]. In this process, an electromagnetic computer model and algorithms developed by Boeing were used to derive the expected code error on the GPS L1 C/A signal induced by the multipath from airframe and ground bounce. The electromagnetic model was derived for both aircraft types and for different configuration of the receiver and the results were compared with the ones observed in flight tests.

The errors predicted by the electromagnetic simulations agree in general with the observation data within a few centimeters. The authors state that differences could be attributed to the residual errors that remain in the estimates of the code-minus carrier (e.g. carrier phase noise and multipath) [106].

The study conducted (based on flight analysis and electromagnetic modeling) indicated that the current multipath model is a "reasonable (if slightly conservative) representation of the airframe and ground bounce multipath" [106]. The authors also believe that the electromagnetic model are probably a more accurate estimation of the true code phase multipath and thus, it should be possible to consider a somewhat tighter multipath model. Thus, it was agreed that the model included in the standard can be seen as an upper bound on the expected multipath error and the receiver manufacturers could use other models if they are better (below the defined model).

However, as the new signals have new signal characteristics and modulation, it is necessary to investigate and if needed, to derive new airborne multipath models for dual-frequency dual-constellation aviation users. As motivated in the following subchapters, the existing methodology has to be extended and new appends have to be developed.

5.4 Overview of proposed methodology for new models

The derivation of the multipath models for new signals is done empirically based on GNSS measurements from extensive flight trials on different aircraft equipped with dual-frequency dual-constellation hardware. The error models need to bound the multipath and noise errors present on the code measurements, thus the observed multipath code error needs to be extracted from the available observations. The carrier phase measurements are as well affected by multipath, but such errors are considered to be negligible in this work because they are at least two orders of magnitude lower than the ones on the code measurements.

The multipath errors in the code measurements are estimated based on the well known code-minus-carrier method with ionospheric delay removal using dual-frequency carrier phase measurements (explained in Section 5.5). Several improvements are proposed in this work to the method used to derive the existing airborne multipath models. The multipath estimation process is not perfect as it is also affected by the ambiguities of the carrier phase measurements and antenna and receiver biases. Assuming no cycle slips have occurred in the carrier tracking loops, the

ambiguities are constant for each satellite pass which could be used to compensate their impact on code-minus-carrier measurements. The obtained results are passed through a smoothing filter similar to the carrier-smoothing performed in position solution. The multipath models are then derived by sorting the smoothed estimated multipath values in elevation bins. In this chapter different steps to refine the multipath estimation that could be used in deriving future airborne multipath models will be proposed. These steps include a new methodology to estimate the bias of the carrier phase ambiguities which is suitable for flight data. Furthermore, inflation for safely bound the risk in the tails and inflation for the limited number of samples will be discussed.

The process of the elimination of the ambiguities also removes any code biases such as the satellite and receiver instrumental delays on code and phase (which are assumed to be constant over a satellite pass). Additional errors introduced by the receiver antenna on the code (group delay variations) are also contained in the multipath estimation. Previous research in [110, 111] has shown that these errors are not necessarily constant but depend on the frequency and on the angle of arrival of the signal. These errors can be also very different for different antennas and will also vary with the installation of the antenna (e.g. on a metallic structure). Until now, these errors were considered together with the multipath and noise error and bounded through the multipath model. The existing model defined for GPS L1 is considered to bound both the multipath and antenna group delay variations for GPS L1 C/A code measurements. In [112], the authors show that the current receiver noise, multipath and group delay variation error models are considered an adequate bound for GPS L1 errors in the position domain due to the fact the modeled error bound are conservatively combined in the position domain assuming the worst case sign on every satellite simultaneously. However, the model was derived empirically by analysis of the results from flight tests conducted on different aircraft. In these tests, a specific antenna was used. This can not be generalized, because the obtained results are very dependent on the antenna used and the derived models would be either very conservative (in case a low performance antenna is used) or optimistic (in case a good performing antenna is used) and not sufficiently bounding the errors.

In [86], a first analysis of the noise and multipath performance of GPS L1 and the new signals broadcast by the Block IIF GPS satellites on L5 band and Galileo satellites on E1 and E5a bands was shown. The results were based on measurements collected during multiple flight trials executed on different types of aircraft, and using different antenna types and receiver parameters. The investigations showed that one of the main factors of influence to the multipath error is the airborne antenna [113]. Different performance levels can be obtained with different antennas and it was also showed that such influence could eventually produce results above the common overbound models. Figure 5.2 shows the standard deviations of the GPS L1 C/A code multipath and noise error (black curve) and GPS L5 code multipath and noise error (magenta curve) obtained from the measurements collected with a multiband antenna in comparison with the standard deviations of the GPS L1 C/A code multipath and noise error obtained from the measurements collected with the dual-band antenna

(green curve). It can be noticed that there is a large difference between the L1 results which can be attributed to the antenna (all other parameters being the same in the flight tests). More details of this effect are given in [113]. These initial results led to the conclusion that the antenna effect and the antenna-induced errors need to be properly taken into account especially for the dual-frequency applications for which the airborne multipath is a dominant source of error.

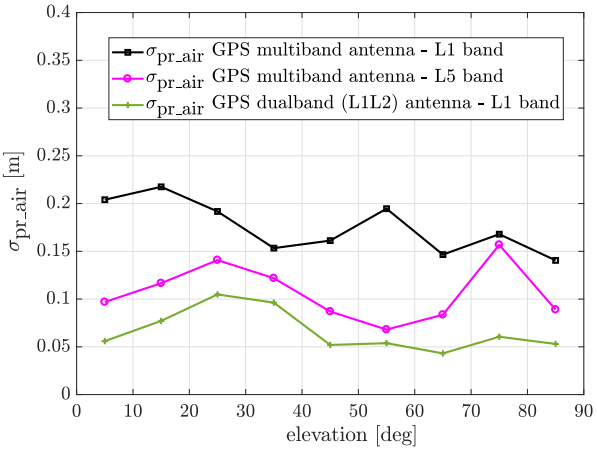


Figure 5.2: σ_{pr_air} curves function of elevation in the aircraft body frame for GPS L1 using a multiband antenna (black curve) and a dual-band L1-L2 antenna (green curves) and GPS L5 using the multiband antenna

The antenna related errors induced in the code measurements can be deterministically estimated by measuring the antenna phase patterns for each frequency in an anechoic chamber as described in [110]. In order to obtain an approximation of the installed performance of an antenna on the aircraft, the antenna is mounted on a rolled edges ground plane. This installation approximates the effect of the nearfield reflections due to installation on metallic platforms which modify the antenna radiation pattern [110]. The approach considered in this work includes a decomposition of the antenna-related error from the multipath errors using the deterministic code errors introduced by the receiver antenna.

For the derivation of the methodology and the evaluation of the airborne multipath error measurements from multiple flight tests using different aircraft types were collected. The DLR research aircraft were used in these flight tests. In addition, measurements from the first flight campaign that took place within DUFMAN project are considered for comparison. Dual frequency GPS L1 and GPS L5 as well as Galileo E1 and Galileo E5a measurements are recorded by the receiver onboard each aircraft. More information on the flight campaigns considered in this work and information on the hardware used are given in Section 5.8.

The next section presents the novel methodology used to estimate the multipath

errors from the measurements. A discussion on the antenna-induced error and the separation of these errors from the multipath estimates will be provided in Section 5.6.3.

5.5 Methodology for definition of multipath models from flight data

The multipath airborne models need to overbound the residual errors present in the code measurements after the carrier smoothing. Thus, the process of estimating the multipath should contain the same errors as in the smoothed measurements to the largest extent possible. As the multipath is typically dependent on the elevation of the satellite, models in the form of elevation function need to be defined to bound the errors in the code measurements. The models are obtained by performing the following steps:

- Assessment of the multipath error (representative for the code measurements used),
- Smoothing of the multipath and noise estimates using the code-carrier smoothing (Hatch filter) similar to the airborne processing,
- Computation of elevation angles,
- Generation of empirical statistics by sorting data into elevation bins and computation of a standard deviation overbounding the multipath and noise errors for each elevation bin.

Note that the current GPS L1 C/A code models include the contributions of thermal noise and multipath separately. In this work, the two errors are evaluated together as it is difficult to distinguish between the two components. However, the multipath is correlated in time and will remain predominant after smoothing, while the noise is uncorrelated and will be smoothed out almost completely. Each of these steps and their specific implementation is presented in the next sections.

5.5.1 Assessment of raw multipath and noise error

The process of estimating the multipath has to contain as close as possible only the error present in the code measurements. This thesis focuses on the estimation of the multipath for two cases: multipath and noise error present in the single-frequency code measurements (e.g. for L1/E1 or L5/E5a signals) and the estimation of the multipath and noise errors present in the dual-frequency ionospheric-free (Ifree) pseudoranges which are explained in the next subsections. First, the methodology to estimate the raw multipath and noise error in the single frequency and the Ifree combination is presented. These estimates are biased by the ambiguities of the carrier phase measurements. The methodology proposed to estimate the carrier phase ambiguities on measurements from flight trials is discussed after in this section.

5.5.1.1 Assessment of single frequency multipath and noise error

A commonly used way to estimate the residual multipath and noise errors is to look at the code minus carrier phase (CMC) measurements [114]. This approach assumes the carrier phase measurement to be ideal and unaffected by noise and multipath. While this is of course not entirely true, the carrier phase noise and carrier phase multipath errors are orders of magnitude smaller than the raw code multipath and noise errors. The equations of the code and carrier phase measurements for frequency i, receiver r and satellite s have been previously described in Chapter 2 and Chapter 4 and are recalled in Eq. (5.1) and (5.2) for the simplicity of understanding the derivation

$$\rho^s_{r,i} = R^s_r + c \cdot (\delta t_r - \delta t^s) + T^s_r + I^s_{r,i} + e^s_{r,i} + MP^s_{r,i} + \varepsilon^s_{r,i} + B^s_i + B_{r,i} + \xi_{r,i} + \xi^s_i, \tag{5.1}$$

$$\phi^s_{r,i} = R^s_r + c \cdot (\delta t_r - \delta t^s) + T^s_r - I^s_{r,i} + e^s_{r,i} + N^s_{r,i} \cdot \lambda_i + mp^s_{r,i} + \eta^s_{r,i} + \beta^s_i + \beta_{r,i} + \zeta_{r,i} + \zeta^s_i + wu_{\phi_i}{}^s \tag{5.2}$$

where R^s_r is the geometric range from the receiver r to the satellite s (in m), c the speed of light (in m/s), δt_r the receiver clock bias (in s), δt^s the satellite clock bias (in s), $I^s_{r,i}$ is the ionospheric delay for frequency i (in m), T^s_r is the tropospheric delay (in m), $N^s_{r,i}$ and λ_i the integer ambiguity (in cycles) and the corresponding wavelength of the frequency i. $MP^s_{r,i}$, $\varepsilon^s_{r,i}$ and $mp^s_{r,i}$, $\eta^s_{r,i}$ represent the multipath and thermal noise errors on the code and carrier phase measurements respectively (in m), the B^s_i, $B_{r,i}$ represent the satellite and receiver code-phase instrumental errors (in m) and β^s_i, $\beta_{r,i}$ represent the carrier-phase receiver and satellite instrumental errors (in m). The $\xi_{r,i}$ and ξ^s_i describe the errors introduced by the satellite and receiver antenna on code measurements on frequency i and the $\zeta_{r,i}$ and ζ^s_i describe the satellite and receiver antenna errors introduced on the carrier phase measurements on frequency i. The term $wu_{\phi_i}{}^s$ refers to the phase windup error that affects the carrier phase measurements and will be explained later in the section. The equations are slightly modified from the usual form to include the additional instrumental and antenna biases. Subtracting the code and the carrier-phase measurements leads to the code minus carrier (CMC) observable which by replacing the Eq. (5.1) and Eq. (5.2) becomes

$$\begin{aligned} CMC^s_{r,i} &= \rho^s_{r,i} - \phi^s_{r,i} = \\ &= 2 \cdot I^s_{r,i} + (MP^s_{r,i} + \varepsilon^s_{r,i} + B^s_i + B_{r,i} + \xi_{r,i} + \xi^s_i) - \\ &\quad -(N^s_{r,i} \cdot \lambda_i + mp^s_{r,i} + \eta^s_{r,i} + \beta^s_i + \beta_{r,i} + \zeta_{r,i} + \zeta^s_i + wu_{\phi_i}{}^s). \end{aligned} \tag{5.3}$$

The combination removes the clock errors, the tropospheric delay and the ephemeris error. However, it contains twice the ionospheric delay, the carrier phase ambiguity, the combined code multipath and noise, the combined phase multipath and noise and the code and carrier phase hardware delays (e.g. instrumental delays and antenna errors). The ionospheric delay is frequency dependent and the first-order relationship between the ionospheric delay experienced in the measurements (code and carrier phase) of two frequencies i and j is $I_j = f_i^2/f_j^2 \cdot I_j$. Thus, the ionospheric delay

between a satellite s and receiver r on frequency i can be estimated by combining the dual-frequency carrier phase measurements as follows:

$$I^s_{r,i} = \frac{f_j^2}{f_i^2 - f_j^2} \cdot (\phi^s_{r,i} - \phi^s_{r,j}) - \frac{f_j^2}{f_i^2 - f_j^2} \cdot (N^s_{r,i} \cdot \lambda_i - N^s_{r,j} \cdot \lambda_j) - \frac{f_j^2}{f_i^2 - f_j^2} \cdot (E_i - E_j) \tag{5.4}$$

where the terms E_i and E_j replace the additional errors affecting the carrier-phase measurements on frequency i and j such as the carrier-phase multipath and noise errors, carrier-phase instrumental errors, the satellite and receiver antenna errors and the phase windup errors on both frequencies (see Eq. (5.2)).

The higher orders of the ionospheric error are ignored, as usually they are very small. The carrier phase measurements are preferred for the estimation of the ionospheric delay because the noise and multipath variance is much lower compared with those on the code measurements. However, due to the unknown ambiguity on the carrier phase measurements, the ionospheric delay is affected by the linear combination of the integer ambiguities from the two measurements. The carrier phase ambiguities of both measurements and thus, also their linear combination, remain constant as long as a continuous tracking of the signal is ensured and will be removed in the final bias removal step as explained in Section 5.5.1.3.

By replacing the ionospheric delay with the relation from Eq. (5.4) and subtracting twice the result from the $CMC^s_{r,i,j}$ in Eq. (5.3), a biased estimate of the CMC with the ionospheric divergence removed is obtained. This observation is usually called CMC divergence-free (noted as $CMC_{\text{Dfree,bias}}$ in this chapter) and is expressed as

$$CMC_{\text{Dfree,bias}}{}^s_{r,i,j} = CMC^s_{r,i} - 2 \cdot I^s_{r,i} = \rho^s_{r,i} - \phi^s_{r,i} - 2 \cdot \frac{f_j^2}{f_i^2 - f_j^2} \cdot (\phi^s_{r,i} - \phi^s_{r,j}) \tag{5.5}$$

which can be written as

$$\begin{aligned} CMC_{\text{Dfree,bias}}{}^s_{r,i,j} = {} & \left(MP^s_{r,i} + \varepsilon^s_{r,i} + B^s_i + B_{r,i} + \xi_{r,i} + \xi^s_i\right) - \left(mp^s_{r,i} + \eta^s_{r,i} + \beta^s_i + \beta_{r,i} + \zeta_{r,i} + \zeta^s_i\right) - \\ & - 2 \cdot \frac{f_j^2}{f_i^2 - f_j^2} \cdot \left(mp^s_{r,i} + \eta^s_{r,i} + \beta^s_i + \beta_{r,i} + \zeta_{r,i} + \zeta^s_i - mp^s_{r,j} - \eta^s_{r,j} - \beta^s_j - \beta_{r,j} - \zeta_{r,j} - \zeta^s_j\right) - \\ & - N^s_{r,i} \cdot \lambda_i - 2 \cdot \frac{f_j^2}{f_i^2 - f_j^2} \cdot \left(N^s_{r,i} \cdot \lambda_i - N^s_{r,j} \cdot \lambda_j\right) \\ & - wu_{\phi_i}{}^s - 2 \cdot \frac{f_j^2}{f_i^2 - f_j^2} \cdot \left(wu_{\phi_i}{}^s - wu_{\phi_j}{}^s\right) \end{aligned} \tag{5.6}$$

The obtained $CMC_{\text{Dfree,bias}}{}^s_{r,i,j}$ contains the estimation of the single frequency code noise and multipath. The estimates are biased by the carrier phase ambiguities and hardware biases. When using measurements from flight data it becomes difficult to accurately estimate the carrier phase ambiguities due to the aircraft movement and more cycle slips (compared to the ground static scenarios) and loss-of-lock events through the ambiguities fixing algorithms (e.g. lambda method [115, 116]). Any

error in the calculation of the ambiguities would project wrongly into the multipath estimations. The typical approach is to consider that the carrier phase ambiguities are constant over a continuous pass of the satellite. The bias can then be removed as described in Section 5.5.1.3. The notation $CMC_{\mathrm{Dfree}}{}^{s}_{r,i,j}$ is used for the estimates obtained after the ambiguities removal. These values are used as estimates of the multipath and noise errors of the code measurements. The additional errors that affect this estimation are discussed further in Section 5.6.

5.5.1.2 Assessment of dual-frequency multipath and noise error

The availability of the second frequency enables the aviation user to form the Ifree combination and remove the dominant ionospheric error. In case the Ifree is chosen as a processing, the multipath error present in the Ifree smoothed pseudoranges needs to be assessed.

As previously shown in Chapter 3, the Ifree combination of the code and carrier phase measurements for L1/E1 and L5/E5a frequencies is formed as

$$\begin{aligned}
\phi_{\mathrm{Ifree}}{}^{s}_{r,\mathrm{L}_1,\mathrm{L}_5} &= \frac{f^2_{\mathrm{L}_1}}{f^2_{\mathrm{L}_1} - f^2_{\mathrm{L}_5}} \cdot \phi^{s}_{r,\mathrm{L}_1} - \frac{f^2_{\mathrm{L}_5}}{f^2_{\mathrm{L}_1} - f^2_{\mathrm{L}_5}} \cdot \phi^{s}_{r,\mathrm{L}_5}, \\
\rho_{\mathrm{Ifree}}{}^{s}_{r,\mathrm{L}_1,5} &= \frac{f^2_{\mathrm{L}_1}}{f^2_{\mathrm{L}_1} - f^2_{5}} \cdot \rho^{s}_{r,\mathrm{L}_1} - \frac{f^2_{\mathrm{L}_5}}{f^2_{\mathrm{L}_1} - f^2_{\mathrm{L}_5}} \cdot \rho^{s}_{r,\mathrm{L}_5}.
\end{aligned} \tag{5.7}$$

The multipath present in the ionospheric-free pseudoranges can be estimated by forming the ionospheric free combination on the single frequencies $CMC_{\mathrm{Dfree}}{}^{s}_{r,\mathrm{L}_1}$ and $CMC_{\mathrm{Dfree,bias}}{}^{s}_{r,\mathrm{L}_5}$ (the estimates before the carrier phase ambiguties removal, noted as $CMC_{\mathrm{Ifree,bias}}$)

$$CMC_{\mathrm{Ifree,bias}}{}^{s}_{r,\mathrm{L}_1,\mathrm{L}_5} = \frac{f^2_{\mathrm{L}_1}}{f^2_{\mathrm{L}_1} - f^2_{\mathrm{L}_5}} \cdot CMC_{\mathrm{Dfree,bias}}{}^{s}_{r,\mathrm{L}_1} - \frac{f^2_{\mathrm{L}_5}}{f^2_{\mathrm{L}_1} - f^2_{\mathrm{L}_5}} \cdot CMC_{\mathrm{Dfree,bias}}{}^{s}_{r,\mathrm{L}_5}. \tag{5.8}$$

Another way to obtain an estimate of the ionospheric free multipath and noise error is by subtracting the ionospheric free combined code and carrier phase measurements and the mathematical derivation is described in Appendix B. The multipath and noise estimates of the Ifree combination are affected by the combination of the single frequency ambiguities because both carrier phase measurements are used. Being a linear combination, the estimation of the carrier-phase ambiguities and their removal is similar as in the single frequency case and is explained in the next section.

5.5.1.3 Removal of carrier phase ambiguities

The carrier phase ambiguities are different for each satellite and frequency and change per satellite in case a cycle slip or loss of track occurs. This can happen due to banking during maneuvers or blockage of the signals by the parts of the airframe (e.g. the tail).

Thus, the input to the ambiguities removal algorithm is a continuous segment of the unsmoothed $CMC_{\text{Dfree,bias}}$ estimates for each satellite during which the receiver does not lose track of the signal and no cycle slips occur. An example of the separation of the $CMC_{\text{Dfree,bias}}$ in segments for one satellite (PRN 8 from a flight conducted on DLR's A320 aircraft on 12$^{\text{th}}$ May 2016 around Magdeburg-Cochstedt Airport) is given in Figure 5.3 where the red lines indicate the presence of a cycle slip or the loss of lock. Note that in this section the indexes for the $CMC_{\text{Dfree,bias}}$ and CMC_{Dfree} were removed for simplicity and they refer to the estimate of the single frequency multipath.

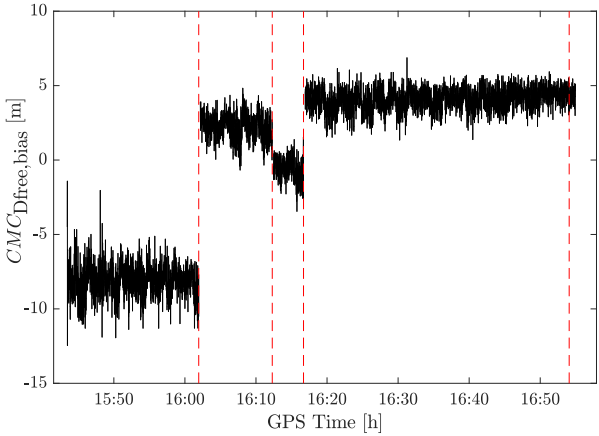


Figure 5.3: $CMC_{\text{Dfree,bias}}$ for L1 over time for GPS PRN 8

As previously mentioned, the use of carrier phase ambiguities fixing algorithms are not suitable for flight data because of the fast movement and the higher probability of cycle slips (due to e.g. loss-of-lock of the signals in maneuvering). Such algorithms would require a movement model and would need long continuous signal pass to provide a good estimate. Furthermore, the estimation process can introduce additional errors which would project in the multipath estimates. Thus the typical approach for estimating the ambiguities in aviation application is to compute the mean over a segment of continuous tracking of each satellite. This approach assumes that the multipath has a Gaussian distribution with zero mean. In a low multipath scenario this assumption holds and the average over the full segment represents a good estimation of the carrier phase ambiguities. An example of such a data set is shown in Figure 5.4 where one continuous segment of the $CMC_{\text{Dfree,bias}}$ for GPS L1 versus the elevation of the satellite is shown in the left plot (Figure 5.4a). Figure 5.4b shows the histogram of this data set in blue and the yellow line represents the estimated mean. The data was collected during a static ground scenario, in a low multipath environment (e.g. not much multipath was expected at medium to high elevations). In this example, it can be observed that the multipath and noise error has an expected trend and decreases with the increase of the satellite elevation. The

estimation of the carrier phase ambiguities of this segment can be done by calculating the mean, as in this case the mean of the noise and multipath errors can be assumed close to zero.

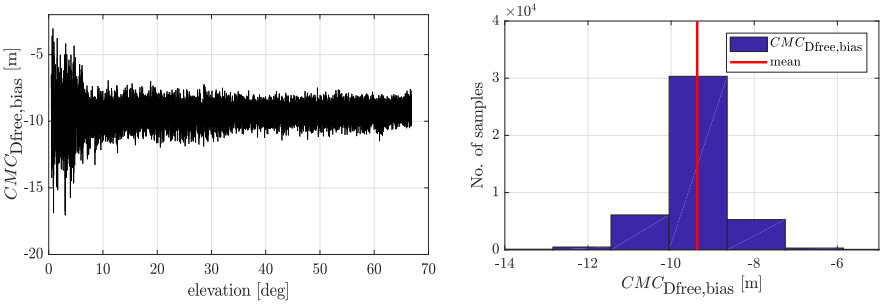


Figure 5.4: $CMC_{\text{Dfree,bias}}$ versus elevation (plot (a)) and histogram of the $CMC_{\text{Dfree,bias}}$ (plot (b)) on GPS L1 for one satellite (PRN 10) in a ground scenario with low multipath

However, the measurements from flight tests can show a different behavior. Figure 5.5a presents similar to Figure 5.4a, a continuous segment of the $CMC_{\text{Dfree,bias}}$ obtained from a flight test for one GPS satellite (PRN 6). The measurements were collected during a long-range flight test from Braunschweig to French Guyana which took place on 15$^{\text{th}}$ July 2017 on DLR's A320 aircraft. The left graph shows the behavior versus elevation (Figure 5.5a) and the histogram of the data with its mean is shown in the right plot (Figure 5.5b). The elevation of the satellite refers to the elevation with respect to the aircraft body frame. As the chosen flight contains long segments of straight level, the satellite difference of the satellite angles in body frame and the elevation above horizon is small most of the time. In this case it can be observed that the behavior of the multipath and noise error as a function of elevation is different than in the previously shown ground case. The decrease of the multipath and noise error with the increase of elevation does not happen and even measurements at higher elevations (between 60°-80°) are strongly affected by multipath. The large multipath errors can lead to wrong estimation of the carrier phase ambiguities as the mean over the continuous segment.

Another approach to remove the carrier phase ambiguities could to subtract the bias at the position in the dataset where the satellite elevation is the highest. This approach assumes that the multipath error is lower for high elevations and is again more suited for typical measurements from ground stations, where most of the multipath comes from low elevations (see Figure 4.5). This assumption does not hold always for the measurements from flight tests. The multipath error on the aircraft is mainly created by the airframe, and thus high elevation satellites might also be affected by the reflections from the airframe components as observed in the case from in Figure 5.5 (e.g. measurements from elevations above 60° show an increased multipath error).

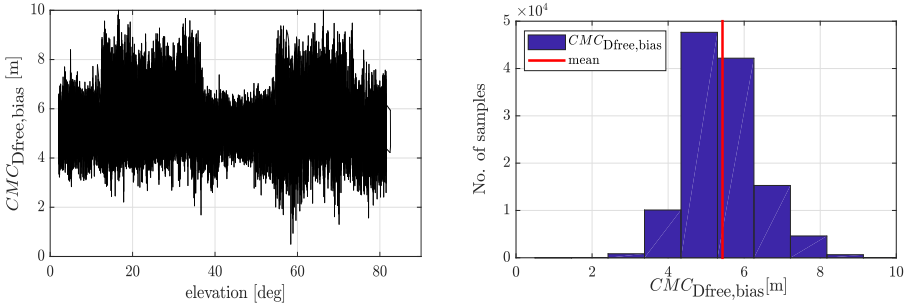


Figure 5.5: $CMC_{\mathrm{Dfree,bias}}$ versus elevation (plot (a)) and histogram of the $CMC_{\mathrm{Dfree,bias}}$ (plot (b)) on GPS L1 for one satellite (PRN 3) using measurements from flight tests

Thus, a new method is proposed. This method is intended to find portions from a continuous $CMC_{\mathrm{Dfree,bias}}$ segment, that are least affected by multipath and thus mainly contain receiver thermal noise. These clean portions of data are used to estimate the bias due to carrier phase ambiguities. The receiver thermal noise is zero mean Gaussian distributed and does not affect the estimation of the bias introduced by the carrier phase ambiguities and hardware errors.

The expected receiver thermal noise (in terms of standard deviation) can be computed based on a theoretical model as a function of $\mathrm{C/N_0}$ as explained in more detail below. If the measurements do not contain large multipath errors, the standard deviation estimated from $CMC_{\mathrm{Dfree,bias}}$ values will be close to the theoretical standard deviation of the receiver noise only. Thus, the estimated standard deviation from the measurements is compared with the theoretically derived values. If both values agree reasonably well, the specific portion of data will be used in the computation of the carrier phase ambiguities. Otherwise, a large difference would hint at data being affected by other errors which can affect the estimation of the carrier phase ambiguities. The input to the algorithm is a continuous segment of $CMC_{\mathrm{Dfree,bias}}$ estimates and the steps of this method in more detail are described in the following:

1. Each data set ($CMC_{\mathrm{Dfree,bias}}$ over one segment) is split into elevation bins (using the same binning used to compute the final models or fixed bins of e.g. 5°)

2. For each elevation bin, the standard deviation of the measurements inside the bin is computed (noted here $\sigma_{CMC_{\mathrm{Dfree,bias}}}$). This measured standard deviation is affected by the receiver thermal noise and multipath. The expected theoretical standard deviation due to the thermal noise (referred as σ_{n}) is computed using a theoretical reference model which was introduced in Chapter 4 in Eq (4.21)

and is recalled here

$$\sigma_{\mathrm{n}} = \sqrt{\frac{1}{T_c} \cdot \frac{B_L}{\mathrm{C/N_0}} \cdot \frac{\int_{-B_r}^{B_r} S(f) \cdot \sin^2(\pi f \Delta) df}{\left(\int_{-B_r}^{B_r} 2 \cdot \pi \cdot S(f) \cdot \sin(\pi f \Delta) df\right)^2} \cdot \left(1 + \frac{\int_{-B_r}^{B_r} S(f) \cdot \cos^2(\pi f \Delta) df}{\left(T_p \cdot \mathrm{C/N_0} \cdot \int_{-B_r}^{B_r} S(f) \cdot \cos(\pi f \Delta) df\right)^2}\right)}, \tag{4.21 revisited}$$

with B_L being the one sided bandwidth of the loop filter (3Hz in this case), B_r the two sided bandwidth of the receiver (23 MHz for Javad receiver), Δ the total early minus late correlator chip spacing (0.1 for L1/E1 and 1 chip for L5/E5a), T_c the code period, $\mathrm{C/N_0}$ the carrier to noise ratio and T_p the predetection integration time. The power spectrum density for the BPSK modulation used for GPS L1, GPS L5 and Galileo E5a signals is described in Eq (4.22). The Galileo E1 signal uses the CBOC modulation with a dominant BOC(1,1) modulation carrying 10/11 of the entire signal power. For aviation, only the BOC(1,1) component only is used, according to the current draft document of the RTCA/Eurocase dual frequency SBAS standard ([92]) and the power spectrum density the contribution of the BOC(1,1) component is described in Eq (4.23).

The theoretical standard deviation computed based on the above equation gives an estimate of the standard deviation of the $CMC_{\mathrm{Dfree,bias}}$ in the presence of the thermal noise, if no multipath would be present. However, the calculation of the standard deviation of the thermal noise depends not directly on the elevation, but it is a function of the $\mathrm{C/N_0}$ values. The observed $\mathrm{C/N_0}$ values at each epoch cannot be used directly as they are affected by multipath which can change the values. Furthermore, the $\mathrm{C/N_0}$ is a function of the satellite received power (and thus dependent on the elevation of the satellite above the horizon), but also of the gain pattern of the receiver antenna (and thus dependent on the angle of arrival in the aircraft's body frame). Thus, a model for the $\mathrm{C/N_0}$ as a function of elevation in local level frame is needed to estimate realistic values for the expected receiver thermal noise. The level flight portions are used because the satellite angle of arrival in level frame coincides with the body frame angle.

Figure 5.6 shows the dependency of the $\mathrm{C/N_0}$ values on the elevation for all signals GPS L1 in Figure 5.6a, GPS L5 in Figure 5.6b, Galileo E1 in Figure 5.6c and E5a in Figure 5.6d. The colors represent the number of samples (in logarithm scale) around that value and the black curve shows the median over elevation bins that is used as a model of $\mathrm{C/N_0}$ function of elevation.

3. Based on the standard deviation a one-sided hypothesis test with 5% false alarm is formed for each elevation bin following the two alternative hypothesis:

   - H_0: the data in the bin ($CMC_{\mathrm{Dfree,bias}}$) is free of multipath and the measurements are mainly affected by the receiver noise. If no large multipath is present in one elevation bin, it is expected that the standard deviation of the measured $CMC_{\mathrm{Dfree,bias}}$ is lower than upper confidence limit of the thermal noise only, σ_n. The upper confidence limit is computed based on the theory that any estimate of a standard deviation based on a finite num-

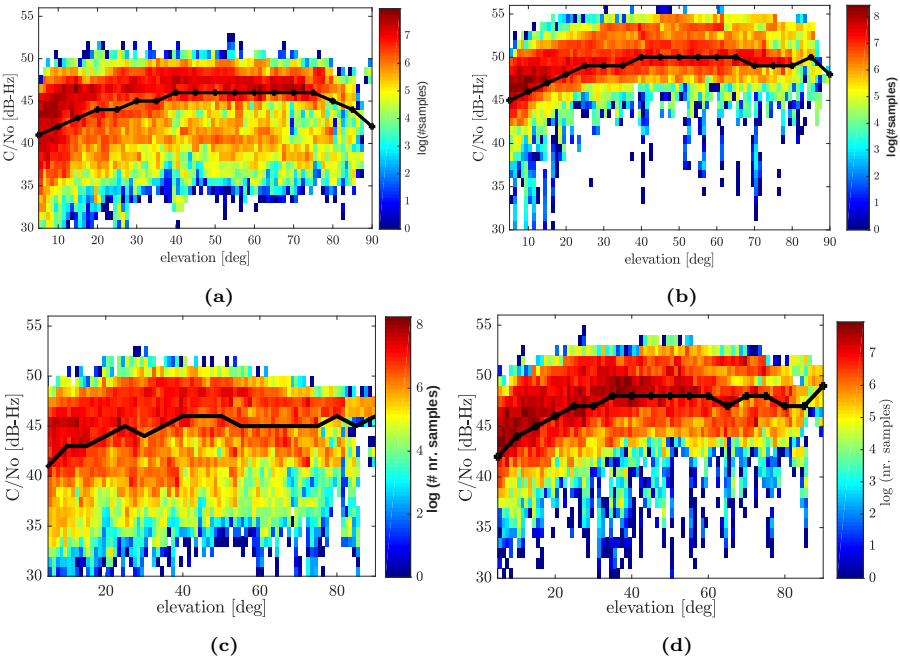


Figure 5.6: C/N_0 values from level segments of flights for GPS L1 (graph (a)), GPS L5 (graph (b)), Galileo E1 (graph (c)) and Galileo E5a (graph (d))

ber of samples from a population has a "Chi-squared" distribution with $N-1$ degrees of freedom. Assuming that σ_n is the estimated standard deviation, the upper confidence limit of the standard deviation is calculated as

$$bound_{up} = \sigma_n \cdot \sqrt{\frac{N-1}{A}}, \tag{5.9}$$

where A is the value for which ${\chi^2}_{N-1}$ has the probability $1-\alpha$ and N is the number of samples in the corresponding elevation bin. For this test, 95% upper bound is computed as it provides reasonably conservative bounds without inflating the expected standard deviation too large to allow high multipath to be accepted and without being too low to exclude all the measurements,

- H_1: the data contains multipath or other bias and should not be considered in the computation of carrier phase ambiguities.

The hypothesis H_0 is accepted if the standard deviation of the $CMC_{\mathrm{Dfree,bias}}$ ($\sigma_{CMC_{\mathrm{Dfree,bias}}}$) is below the upper bound of the defined confidence interval. If

the value of the $\sigma_{CMC_{\text{Dfree,bias}}}$ exceeded the limit defined by the null hypothesis, the hypothesis is rejected.

4. In the last step, the median over all the means of the accepted bins is computed as the estimation of the integer ambiguities. The median is chosen because it is a more robust estimator to the outliers. The outliers in this case refer to the situation when one of the elevation bins has a low standard deviation, but its mean deviates from the general mean due to e.g. an undetected cycle slip.

Figure 5.7 shows an example of this method applied to the data set (the continuous segment of the $CMC_{\text{Dfree,bias}}$) of Figure 5.5. The black curve represents the standard deviation due to noise only computed using Eq.(4.21) (theoretical σ_n) and the upper bound (upper confidence limit) of the standard deviation (described by Eq. (3) is represented with the green line. The variation of this upper bound among various elevation bins is driven by the number of samples. The blue curve (with 'o' markers) shows the standard deviation computed from the measurements.

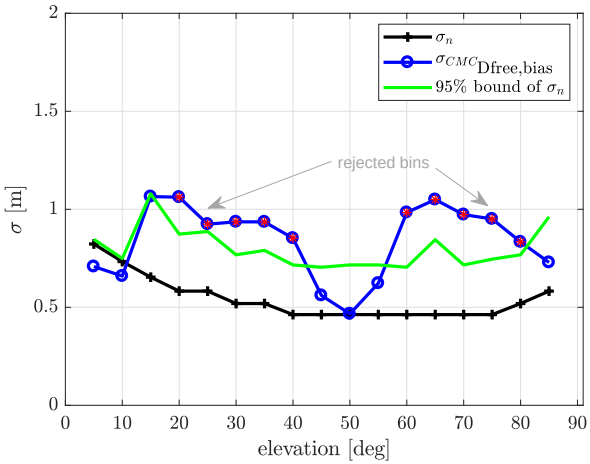


Figure 5.7: Improved method for bias removal. The plot shows the measured standard deviation of the $CMC_{\text{Dfree,bias}}$ (solid line with 'o' marker), the expected theoretical standard deviation (solid line with '+' marker) and the upper bound of the hypothesis test (dashed curves)

It can be observed that the portions that are affected by large multipath (between 20°-40°and 60°-80°) exceed the acceptable bounds (green line) and thus, are not considered in the calculation of the carrier phase ambiguities (the exclusion is shown with red dots in the '*' markers). The first two values of the standard deviation computed from the measurements are below the theoretical derived curve and are not excluded by the algorithm. This behavior can be explained by larger C/N_0 values experienced for those elevation angles compared with the median values that are used to compute the theoretical C/No model.

A comparison of the results obtained by the mean estimation and the improved method for the same data set (from Figure 4) is shown in Figure 5.8 for the two cases. The left plot represents the $CMC_{\text{Dfree,bias}}$ versus elevation and the right plot represents the histogram of the data together with the value estimated as carrier phase ambiguity from the two methods: mean over the full segment (red dashed line), improved method (green line).

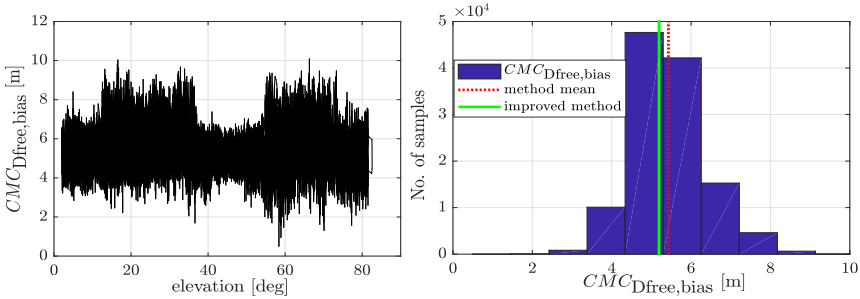


Figure 5.8: Comparison of different methods used for estimating the bias due to carrier phase ambiguities

The difference between the values estimated by the two methods on the same set of data is up to 24 cm which is significant in the multipath estimation context. If the entire data set is free of multipath, both methods should deliver very similar results. The improved method excludes portions of data from the given segment of $CMC_{\text{Dfree,bias}}$ values if the hypothesis of having multipath free measurements is not supported. This approach ensures that the determination of the carrier phase ambiguities is less affected by external effects. The consequence of excluding this data is that the estimate is based on the measurements less affected by other errors. The exclusion of the measurements yields to a larger uncertainty in the mean estimation, but the systematic error introduced in the estimation process of the carrier phase ambiguities is always expected to be lower. Furthermore, the improved method is suitable for all phases of flight, not only for level flight. If during a maneuver, the elevation of the satellite changes significantly, those periods might exceed the theoretical bounds due to the increase in noise. This would however not affect the final estimation.

The examples are shown for GPS L1 signal, but similar results have been obtained for all signals. The methodology can be applied also to the Ifree combination, where the theoretical noise corresponding to the combination is computed as

$$\sigma_{n,\text{Ifree}} = \sqrt{\frac{f_{\text{L}_1}^4 \cdot \sigma_{n,\text{L}_1}^2 + f_{\text{L}_5}^4 \cdot \sigma_{n,\text{L}_5}^2}{(f_{\text{L}_1}^2 - f_{\text{L}_5}^2)^2}}. \tag{5.10}$$

5.5.1.4 Cycle slip detections

In the estimation of the multipath and noise error the detection of the cycle slips play an important role. The receiver loss of lock leads to discontinuities in the carrier phase measurements that are seen as jumps of integer numbers of the frequency wavelength (cycle slips). Different algorithms for cycle slip detection are available in the literature based on single-frequency or dual-frequency and make use either of only carrier phase measurements or of both code and carrier phase measurements to detect jumps that occur due to cycle slips. Several algorithms that can be used as cycle slip detectors are presented in [117].

The airborne receiver performs a measurements quality monitor that detects large jumps in the code and carrier phase measurements as described in Section 2.7.7. This monitor is designed also for detection of cycle slips.

In addition to the exiting algorithm, two algorithms could be suitable to detect the cycle slips on both frequencies in the multipath estimation process: the detector based on code and carrier phase measurements that uses the Melbourbe-Wübbena combination and the detector that uses carrier phase geometry free combination. Both algorithms are described in Section 4.3.1 of [117]. The first algorithm provides a noisy estimate of the wide lane ambiguity by forming the difference between the wide-lane combination of the carrier phase measurements and narrow lane combination of the code measurements. This difference is used as input to the detector algorithm and the detection is based on the real time computation of the mean and sigma values of the observables. The mean and the standards deviation are computed at each epoch based on the previous measurements (from when a cycle slip was detected) and a cycle slip is declared when the difference between the predicted mean value over a predefined number of standard deviations (e.g 6). The second cycle slip detector is based on the carrier phase measurements only. The algorithm uses as input the geometry free combination of the carrier phase measurement which removes the geometry, the receiver and satellite clock errors and all non-dispersive effects in the signal. However, the combination is affected by the ionospheric effects. Thus, the detection is based on fitting a second degree polynomial to the observed carrier phase geometry free combination over a sliding window. The predicted value is compared with the measurements and a cycle slip is declared when the difference is above a defined threshold.

One of the disadvantages of the cycle slip detectors is that they can also trigger in case of sudden change in the multipath environment (e.g. sudden jumps during maneuvering). Thus, it is important that the algorithms used to detect the cycle slips in the multipath estimation process are the same as the ones used by the airborne receivers during operation. After discussion with relevant working groups and with avionics receiver manufacturer became clear that there is no requirement on the algorithms that should be used for the detection of the cycle slips and the avionics receivers do not use any complex cycle slip detectors. The detection of the cycle slips is mainly ensured (but not restricted to) through the MQM monitor and a limit on the C/N_0 values. The C/N_0 limits are set to 29 dB-Hz for L1/E1 and 27 dB-Hz for

L5/E5a signals. Signals with C/N_0 below these values are not used in the position solution. In this thesis a study on the impact of the different detectors on the multipath and noise error was performed using measurements from flight tests and the results are shown and discussed in Section 5.9.1.

5.5.2 Smoothing of the multipath and noise error

As already discussed, the standard way of using the GNSS measurements in aviation is to apply the code-carrier smoothing in order to reduce the high frequency noise and multipath from the code measurements. Therefore, the multipath error models have to represent the residual errors in the smooth code measurements.

The code-carrier smoothing uses the rate of the precise carrier phase measurements to propagate code measurements forward. The carrier smoothed code measurements at a epoch k are computed from the exponential weighted average of the CMC over the previous k epochs to which the current carrier phase measurements are added to reconstruct the geometry (see Appendix A). The smooth multipath at an epoch time k is obtained by applying the same smoothing filter to the raw multipath and noise estimates (after carrier ambiguities removal). One of the implementation of the smoothing filter presented in [101] and [18] is described as

$$\overline{CMC_{\mathrm{Dfree}}}(k) = \frac{\Delta T}{\tau} \cdot CMC_{\mathrm{Dfree}}(k) + (1 - \frac{\Delta T}{\tau}) \cdot \overline{CMC_{\mathrm{Dfree}}}(k-1), \tag{5.11}$$

with τ being the smoothing time constant and ΔT the measurements sampling interval (which has to be much smaller than τ). The indexes are again dropped for simplicity. The derivation of this equation is detailed in Appendix B. Using the derivation from the Appendix B and replacing $\frac{\Delta T}{\tau}$ with α, the smooth $\overline{CMC_{\mathrm{Dfree}}}$ at epoch time k can be written as function of the CMC_{Dfree} values from the previous k epochs as

$$\overline{CMC_{\mathrm{Dfree}}}(k) = (1-\alpha)^{k-1} \cdot [CMC_{\mathrm{Dfree}}(1)] + \alpha \cdot \sum_{n=2}^{k} (1-\alpha)^{k-n} \cdot [CMC_{\mathrm{Dfree}}(n)]. \tag{5.12}$$

In this work, only the errors in the filter steady state (after the smoothing filter converged) are characterized. It is assumed that the filter reaches the steady state after 3.6 times the smoothing time constant (e.g. 360 seconds for 100 seconds smoothing time as specified in the ED-114A document [32]). However, the receiver manufacturer can implement also a time variant version of this smoothing filter, in which case the measurements are used before the filter reaches steady state. The increase in the errors during the filter transient phase (from the filter initialization until the steady state) needs to be investigated and modeled in order to properly bound the errors, but this characterization is out of scope in this thesis.

The analysis of the multipath and noise errors will mainly based on the 100 and 30 seconds smoothing time constant which are used by the GBAS users. In addition,

the sensitivity of the airborne multipath and noise error to different smoothing time constants will be analyzed and discussed in Section 5.11.1.

5.5.3 Calculation of the elevation and azimuth angles

Unlike the atmospheric effects, the multipath is a local effect and the airborne multipath is highly dependent on the airframe. Thus, the errors depend on the elevation and azimuth of the satellite relative to the aircraft. In the flight data evaluations, roll, pitch and heading information from the basic aircraft instrumentation are used to translate the satellite coordinates into the aircraft body frame. The transformation from the coordinates in the ECEF to the coordinates in the body frame is performed as follows [117]:

- First, the ECEF coordinates $(x_{\mathrm{ECEF}}, y_{\mathrm{ECEF}}, z_{\mathrm{ECEF}})$ are transformed into local NED coordinates $(x_{\mathrm{NED}}, y_{\mathrm{NED}}, z_{\mathrm{NED}})$ using the relation

$$\begin{bmatrix} x_{\mathrm{NED}} \\ y_{\mathrm{NED}} \\ z_{\mathrm{NED}} \end{bmatrix} = \begin{bmatrix} -\sin lat \cdot \cos long & \sin lat \cdot \sin long & \cos lat \\ -\sin lat & \cos long & 0 \\ -\cos lat \cdot \cos long & -\cos lat \cdot \sin long & -\sin lat \end{bmatrix} \cdot \begin{bmatrix} x_{\mathrm{ECEF}} \\ y_{\mathrm{ECEF}} \\ z_{\mathrm{ECEF}} \end{bmatrix}, \tag{5.13}$$

  where *lat* and *long* represent the latitude and longitude of the aircraft in World Geodetic System 1984 (WGS84),

- The NED coordinates are then transformed into the body frame coordinates (noted as $x_{\mathrm{BF}}, y_{\mathrm{BF}}, z_{\mathrm{BF}}$) by performing first a rotation by the 3$^{\mathrm{rd}}$ axis by the heading angle, then rotation around the 2$^{\mathrm{nd}}$ axis for the pitch angle and finally by rotating the 1$^{\mathrm{st}}$ axis by the roll angle as

$$\begin{bmatrix} x_{\mathrm{BF}} \\ y_{\mathrm{BF}} \\ z_{\mathrm{BF}} \end{bmatrix} = \begin{bmatrix} \cos H & \sin H & 0 \\ -\sin H & \cos H & 0 \\ 0 & 0 & 1 \end{bmatrix} \cdot \begin{bmatrix} \cos P & 0 & \sin P \\ 0 & 1 & 0 \\ \sin P & 0 & \cos P \end{bmatrix} \cdot \begin{bmatrix} 1 & 0 & 0 \\ 0 & \cos R & \sin R \\ 0 & -\sin R & \cos R \end{bmatrix} \cdot \begin{bmatrix} x_{\mathrm{NED}} \\ y_{\mathrm{NED}} \\ z_{\mathrm{NED}} \end{bmatrix}, \tag{5.14}$$

  with H P R being the heading angle (from the true north), pitch angle and the roll angle. The body-fixed coordinate system refers to the nose right-wing down coordinate frame,

- Finally, the elevation and azimuth angle in the body frame $(\theta_{\mathrm{BF}}, \psi_{\mathrm{BF}})$ are obtained using the relation:

$$\begin{aligned} \theta_{\mathrm{BF}} &= \arctan\left(\frac{-z_{\mathrm{BF}}}{\sqrt{x_{\mathrm{BF}}^2 + y_{\mathrm{BF}}^2}}\right) \\ \psi_{\mathrm{BF}} &= \arctan\left(\frac{y_{\mathrm{BF}}}{x_{\mathrm{BF}}}\right), \end{aligned} \tag{5.15}$$

where 0° elevation angles denoted the horizon and the 90° the zenith. The azimuth angle is measured from 0° at the aircraft noise towards the right wing (which is 90°).

5.5.4 Generation of statistics

Finally the smooth estimates of the multipath and noise errors ($\overline{CMC_{\mathrm{Dfree}}}$) that will be used to build the airborne multipath models are grouped into elevation bins according to the elevation of the satellites (in aircraft body frame or in the local level frame). Section 5.10 provides a comparison of the models obtained in the two coordinate frames.

In this work, the models are proposed for the combination of the multipath and noise errors and are based on the smoothed code-minus-carrier data. While the multipath error is a function of the satellite angle of arrival in body frame, the receiver noise is a function of the C/N_0. The C/N_0 depends mainly on two parameters: first on the Equivalent Isotropic Radiated Power (EIRP) of the satellite which depends on the transmitted power and the satellite's angle above the horizon, and second on the gain pattern of the receiver antenna for which the angle of arrival in local body frame is relevant. Previous work presented a separation of the receiver noise error based on use of level flight data and a C/N_0 model as a function of the satellite elevation [105, 106]. In this work, the models refer to the standard deviation of the smoothed code-minus-carrier data containing multipath and noise combined.

However, the standard deviation only accounts for the core distribution of the errors. This approach might not be conservative enough if the actual error distribution has heavier tails than the Gaussian distribution used to describe the data.

Thus, in order to derive overbounding models, the tails of the distributions need to be taken into account. A Cumulative Distribution Function (CDF) overbounding is applied to inflate the final model. Furthermore, the multipath errors in one elevation bin may also have an azimuth dependency. This means that the multipath errors at a particular azimuth in the body frame may occur with higher probability than the tails of the bound for that elevation. This azimuth dependency can yield a non-zero mean for the distribution of the multipath error in an elevation bin. Such effects are also accommodated by the CDF overbounding method.

From a statistical point of view, the model should also account for the limited number of samples and the associated uncertainty in the estimated standard deviations of the errors in each elevation bin. The methodology to apply the two inflation steps is described in the next two sections and the obtained results are shown in Section 5.9.

5.5.4.1 Overbouding of the tails

Typically, the smooth multipath and noise error in each elevation bin is modeled as a Gaussian distribution with zero mean and the standard deviation derived as empirical

values from the measurements. This statement cannot always be assumed for the true error distribution. In order to avoid underestimating the probability of errors larger than predicted by the Gaussian model, an overbounding Gaussian distribution is used to model the data. The CDF overbounding is defined as

$$\begin{aligned} \Phi_{\text{overbound}}(x) &\geq \Phi(x) \text{ for all } x \leq x - \sigma_{\text{x}}, \\ \Phi_{\text{overbound}}(x) &\leq \Phi(x) \text{ for all } x \geq x - \sigma_{\text{x}}, \end{aligned} \tag{5.16}$$

with $\Phi(x) = \int_{-\infty}^{x} f(x)dx$ being the CDF of the random variable x and σ_{x} the standard deviation of the variable x (the Gaussian fit). As the integral of the probability density function is always 1 the overbounding condition is not fulfilled for all data points, but can be defined for examples to hold outside $\pm 1 \cdot \sigma_{\text{x}}$ (of the Gaussian fit).

5.5.4.2 Inflation for the number of samples

The values derived from the measurements are based on a limited number of samples and thus the measured standard deviation is not directly the true standard deviation of the data. In order to ensure statistical representation of the data, a further inflation factor needs to be applied to the values derived from the limited about of data. The inflation of the measurements-based standard deviations with respect to the true is determined based on the Chi-square distribution of the standard deviation as

$$inflation = \sqrt{\frac{N-1}{B}} \tag{5.17}$$

with N the number of effective independent samples used to derive the standard deviation in each elevation bin and B being the value for which the chi-square distribution χ^2_{N-1} has the probability 1-α (for 95% , α=0.05). The reason for choosing this formula is because the variance estimate from a finite number of samples is a random variable with a Chi-squared distribution with $N-1$ degrees of freedom. The 95% confidence bound is chosen in this work to be in line with the work of validating the existing airborne GPS L1 models as described in [104]. The 95% bound serves as a parameter that provides reasonably conservative bounds without inflating the model too far to impact the availability. It should be noted again at this point that the confidence bound only serves to address the statistical uncertainty resulting from the limited number of samples and does not address the required integrity risk. The integrity risk is ensured in the protection level calculation by multiplying the error bounds by the scalar k-factor (which is 5.81 for an integrity risk of $2{\cdot}10^{-7}$, see Chapter 2).

The driven factor in the derivation of the inflation factor is the number of independent samples, which depend on the correlation of the multipath errors and the choice of the bin sizes. In Section 5.9, results of the multipath autocorrelation function are shown and discussed, as well as the impact of choosing different elevation bin sizes.

5.6 Additional errors affecting the multipath estimation

The process of removing the carrier ambiguities eliminates also any code and carrier phase biases such as the instrumental errors that remain constant over the satellite pass. However, additional errors introduced by the receiver and satellite antenna are also contained in the multipath estimation. Table 5.1 summarizes these biases from both satellite and receiver side. The second column specifies symbol used in the equations. Most of the biases are almost constant per satellite, and thus will be removed in the carrier ambiguities removal process. The information of the time variability of the biases is shown in third and the fourth column of the table.

Bias type	**Symbol**	**Variation with time**	**Eliminated by ambiguities removal**
Code instrumental errors in the receiver	B_r	constant over time the same for all satellites	yes
Code instrumental errors in the satellite	B^s	constant over time for each satellite	yes
Phase instrumental errors in the receiver	β_r	constant over time the same for all satellites	yes
Phase instrumental errors in the satellite	β^s	constant over time for each satellite	yes
Code errors introduced by the receiver antenna	ξ_r	varies with the angle of arrival	yes
Code errors introduced by the satellite antenna	ξ^s	varies function of the nadir angle	no
Phase errors introduced by the receiver antenna	ζ_r	varies with the angle of arrival	no
Phase errors introduced by the satellite antenna	ζ^s	small variations function of the nadir angle	no
Phase windup errors	$wu_{\phi_{r,i}^s}$	varies with the angle of arrival	no

Table 5.1: Errors in multipath estimation

5.6.1 Errors not relevant for the multipath estimation

The satellite instrumental delay refers to the "delay between the signal radiated output of a specific SV (measured at the antenna phase center) and the output of that SV's on-board frequency source" (Paragraph 3.3.17 of IS-GPS 200 [98]). These delays

are different for each frequency, each signal and thus each satellite and the final error present in the user measurements depends on the parameters used in the user's receiver (e.g. correlator spacing and receiver bandwidth). However, previous studies in [118] have shown that these biases are almost constant for each satellite and thus, will not affect the multipath estimation being eliminated in the carrier-phase ambiguities removal process.

In addition to the instrumental delays, the anisotropy of the satellite antenna introduces group delays on the code measurements and phase center variation on the carrier-phase measurements. In the last years it has been shown that these errors are varying dependent of nadir angle [119]. However, these errors are much smaller compare with the multipath error and the errors introduced by the receiver antenna. Thus, in this work, the contribution of the errors introduced by the satellite antenna is not considered further as it is assumed that they are not dominant in the multipath estimation process.

The instrumental errors introduced by the user hardware processing chain (front-end, cables) are constant over time and are eliminated in the integer step removing the carrier-phase ambiguities. These errors are common to all satellites and will not affect the position solution because they will project into the receiver clock estimation.

5.6.2 Errors relevant for the multipath estimation

- *Errors due to the phase windup*

  The windup errors affect only the carrier phase measurements and it is due to the electromagnetic nature of the circularly polarized waves which are used in the GNSS signals. The effect of phase windup on the carrier phase measurements depends on the orientation of the antenna of the transmitter (the satellite) and the receiver (the user) and the direction of the line of sight [117]. For a static receiver, the windup occurs only due to the orbital motion of the satellite. However, in flight tests, the orientation between the satellite antenna and the airborne antenna changes very often. These errors will affect the multipath estimation and needs to be taken into account.

  In [120] a method to compute the phase correction due to the phase windup based on the aircraft attitude and the satellite attitude is shown. Another way to compute the error due to the phase wind-up is using the following relation [121]:

$$wu_{\phi}{}^{s}_{r,i} = \frac{\lambda_i^s}{2\pi} \cdot \psi^s \tag{5.18}$$

  with λ_i^s being the wavelength of the frequency i and ψ^s being the azimuth angle of the satellite s (in flight tests the azimuth angle refers to the angle in the aircraft body frame). Using attitude information data from flight tests, this correction can be computed and applied to the carrier phase measurements on both frequencies used in the multipath estimation.

- *Errors introduced by the receiver antenna*

  In addition to the instrumental errors, the receiver antenna introduces errors on both code and phase measurements. Unlike the errors introduced by the satellite antenna, these errors can be much larger and need to be considered. In [110] the authors have shown that the receiver antenna impacts the GNSS measurements by the differential group delay, the phase center variation, the gain and the cross-polarization isolation. The gain and the cross polarization isolation have a direct impact into the amount of multipath that is present in the GNSS measurements. The differential group delay is defined as "time-delay difference at each frequency component of the signal experiences while passing through the antenna" [110]. This parameter affects the code measurements and varies with the frequency as well as with the azimuth and elevation of the satellite.

  A detailed explanation of the derivation of the group delay variation and its relation with the antenna gain and phase pattern is given in [111] and [110]. The second effect, the phase center variation, has an impact on the carrier phase measurements by "erroneously adding a phase contribution (variable with satellite elevation and azimuth) not due to the actual distance from the satellite, but to the antenna characteristics" [110].

  While the errors introduced by the phase center variation are rather small and are only of interest for high precision application, the errors introduced on the code measurements can reach meter level. Thus, these errors will affect the multipath estimation and need to be taken into account. The remaining of the section describes in detail these errors and proposes a first concept to separate the antenna-induced errors from the multipaht and noise errors.

5.6.3 Code error introduced by the receiver antenna

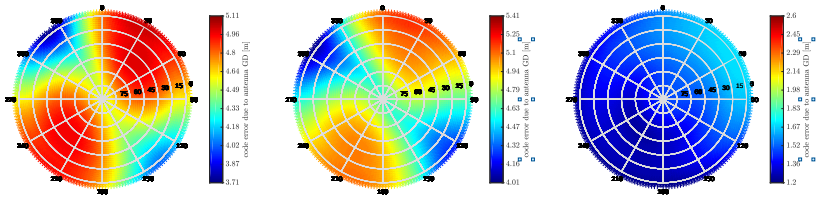
The differential group delay is directly impacted by the pattern uniformity of the antenna, meaning that if the pattern of the antenna is isotropic within the frequency band(s) of interest, the group delay will be equal for all elevation. In this case, the errors will project only into the receiver clock estimation.

As shown in [110], the antenna related errors ($\xi_{r,i}$) induced in the code measurements for a frequency i can be deterministically estimated by measuring the antenna phase patterns for each frequency in an anechoic chamber. The imperfections of the antenna response propagate through the receiver and result in code tracking biases, being dependent on the used signal and its modulation. Using a model of an ideal receiver described in [122] and the amplitude and phase response of the antenna versus frequency measured in the anechoic chamber, the errors biases introduced on the code measurements can be estimated. The biases are derived based on an ideal receiver for given parameters such as correlator spacing and bandwidth.

The methodology to estimate the ideal code errors introduced by the variations

of the antenna group delays is presented in detail in [110]. The paper includes the theoretical estimation of the code errors and an experimental validation of these ideal errors. The experimental validation was performed based on GNSS measurements collected in a low multipath environment in which the antenna induced error get dominant. The results show that the code errors estimated theoretically using the ideal receiver are very similar with what is observed in the actual measurements. Based on these findings, it can be assumed that the errors estimated based on the measurements from the anechoic chamber are representative and will be considered further in this work. The methodology of deriving the code errors due to the antenna group delays has been established by Dr. Stefano Caizzone and Mr. Christoph Enneking from the Institute of Communications and Navigation of DLR and is not an outcome of this thesis [111, 110]. This work studied the effect of these errors to the multipath and noise estimates.

As shown in [110], the variation of the antenna group delay with the angle of the arriving signal and the frequency is related with the homogenity of the gain and phase pattern: an homogenous antenna pattern results in very stable group delay for all satellites (and thus not affecting the position solution), while drops and changes in the gain pattern versus frequency and angle lead to large group delay variations which affect the position solution. On the flight tests performed on DLR's A320 aircraft an early version of a multiband antenna was used. This antenna exhibits large variation with the angle of arrival and frequency and, thus, large group delay variations. Figure 5.9 shows the code errors due to the absolute antenna group delays for GPS L1 C/A code with BPSK(1) modulation (graph 5.9a), for Galileo E1 (graph 5.9b) for the BOC(1,1) component of the modulation and for GPS L5/Galileo E5a with the BPSK(10) modulation (graph 5.9c) for all azimuth and elevation angles for the antenna mounted on the DLR's A320 from which most of the flight data is collected. The antenna measurements and the generation of the code errors through the ideal receiver have been performed by Dr. Stefano Caizzone and Mr. Christoph Enneking from the Navigation Department of the DLR's Institute of Communications and Navigation.



(a) **(b)** **(c)**

Figure 5.9: Code error due to the absolute antenna group delay for GPS L1 signal (a), Galileo E1 signal (b) and GPS L5/Galileo E5a signals (c)

The absolute group delay refers to the total amount of error introduced by the antenna comprising also the effect of the active components of the antenna which

are common to all satellites and will project into the receiver clock estimation if not corrected. Thus, the absolute ranges for the three signals are different and the starting value is different in the three graphs. However, the total variation (of 1.4 m) among the entire hemisphere is kept identical for all three cases. Looking at these figures, it can be concluded that the code errors due to the antenna group delay are different for each frequency and show large variations over the angle of arrival (in this case up to 1.4 m for L1 band and 0.5 m for L5 band). A significant spatial variation is observed on L1 and E1 signals, the variation on L5 signal is smaller but still relevant. For Galileo E5a signal, the results are the same as for L5, since both use a BPSK(10) modulation.

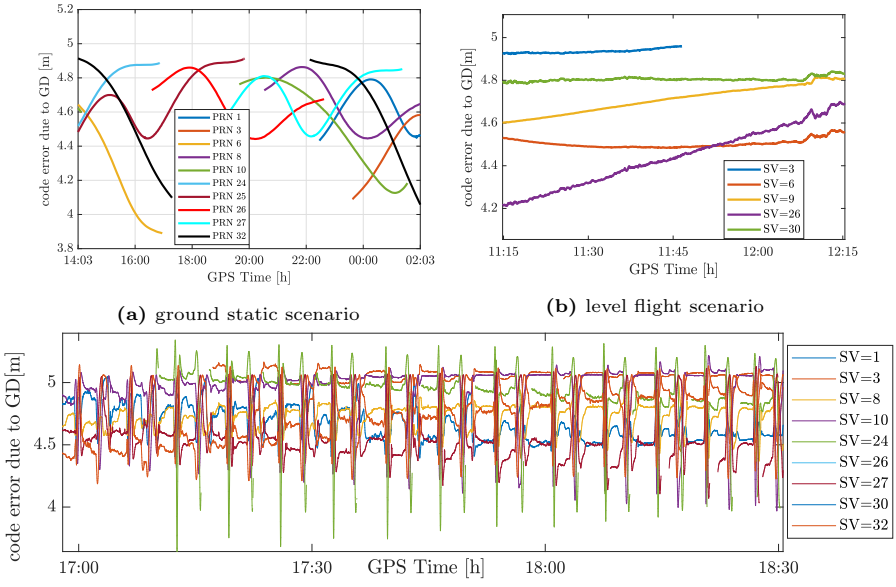
In order to understand how these errors behave and affect the user in real time, the code error error introduced by the antenna group delay variation was analyzed in three different scenarios. The results for GPS L1 in terms of code errors versus time are shown in Figure 5.10. The considered scenarios are:

- a ground static scenario in which the antenna was mounted in the field in the DLR campus in Oberpfaffenhofen for approximately 12h in Figure 5.10a,
- level flight segment of around 1 hour (during which no turn and no change of heading occurred) from a flight test shown in Figure 5.10b,
- segments with maneuvers from flight tests shown in Figure 5.10c.

For each scenario, the code errors showed in Figure 5.10 are computed from the actual geometry and taking the corresponding values derived for the L1 BPSK(1) signal for the specific angle (Figure 5.9a for the entire hemisphere). This means that the values are not based on GNSS measurements, but on the estimations computed using an ideal receiver (with the configuration of the bandwidth and correlator spacing matching the Javad receiver which recorded measurements on the aircraft) from the antenna frequency response. Note that during the flight tests the elevation and azimuth refer to the angles in aircraft body frame.

In the first static test (Figure 5.10a), it can be observed that the variation of the antenna errors introduced by the group delay is changing slowly only due to the movement of the satellites and look more bias like and are very different for each satellite. A similar behavior can be observed during a level flight (Figure 5.10b), during which the variation of the errors is again caused only by the movement of the satellite. However, this behavior changes completely during the maneuvers and the variation is much larger due to the fast change in the satellite angle with respect to the antenna. This can be observed in the third plot (Figure 5.10c) where the geometry from a flight with approximately 30 approaches around Braunschweig airport was considered. The bias-like behavior in the errors is only present over short time (e.g. 5-10 minutes) for the period of one maneuver.

These variations can lead to large position errors especially when considering the combination of both frequencies into an Ifree position solution, these errors become quite significant. In order to assess the actual position errors a study for the static scenario shown in Figure 5.10a was performed. At each epoch, using the actual



(a) ground static scenario

(b) level flight scenario

(c) flight with maneuvers

Figure 5.10: Estimated code error due to antenna group delay for different scenarios

geometry, the code errors were estimated from the results over the whole hemisphere presented in Figure 5.9. The process is the same as the one used to derive the results in the graphs of the Figure 5.10. The code errors for both frequencies L1/E1 and L5/E5a were calculated to derive the errors present in the Ifree combination. These code errors were then projected into the position solution. Figure 5.11 shows a plot of the 3D position errors for a dual-frequency GPS/Galileo solution introduced by the antenna biases only. Note that these errors are specific to the geometry observed from Oberpfaffenhofen during the chosen period (1h 40 minutes). The black curve shows the effect for single frequency L1 positioning, while the red curve shows the variations when forming the Ifree combination. The part common to all satellites from the absolute group delay project into the receiver clock estimation, but the variations in the position error is due to the variation of the antenna group delay.

According to the current MOPS for aviation based on GPS L1 only ([1]) [2]), the errors introduced by the antenna group delay were bounded together with the multipath errors. However, the previous results show that the behavior of these errors is quite different from the multipath errors which are considered to be zero mean and are characterized by a standard deviation value. These errors are more bias-like during a level flight segment showing a strong correlation over time. Faster variations occur during maneuvering due to the fast changing angle of arrival of the signal. Furthermore, the carrier-phase ambiguities removal will eliminate part of these

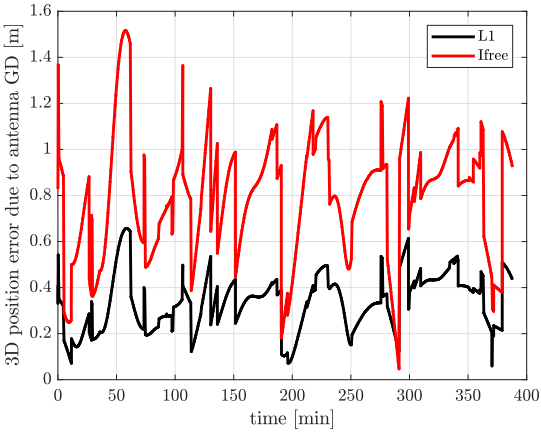


Figure 5.11: Position errors due to antenna biases for single frequency positioning (red curve) and dual frequency Ifree position solution (red curve)

errors. Consequently, it cannot be guaranteed that the bound is always conservative and covers all cases. The errors present at the user are very dependent on the flight type (e.g. level flight, maneuvers) and the bound should consider the worst case in order to ensure integrity. As a consequence, a separation of these errors from the multipath estimation is discussed. The methodology proposed for this separation is discussed in the next section.

This separation is especially important when analyzing the multipath errors from the DLR's A320 aircraft as this antenna is not designed according to the current dual frequency antenna standards which are described in DO-373 document [123]. The document specifies a limit in the the variation of the group delay to $\pm$ 1.5 ns which translates into a $\pm$ 45 cm code error for each frequency. Even in this case, when measurements from two frequencies are combined, the position errors can reach large values.

5.7 Separation of multipath error and antenna induced error

In order to ensure that the total error introduced by the antenna is eliminated from the multipath estimation, the calibration of the antenna induced errors needs to be applied before the carrier phase ambiguities removal (on the single frequency $CMC_{\mathrm{Dfree,bias}}$ estimates). This is necessary because otherwise the ambiguities removal would also remove parts of the antenna introduced errors. The absolute code errors introduced by the antenna are computed for each satellite taking the actual elevation and azimuth of the satellite and using the corresponding values from Figure 5.9 as explained in the previous section. For measurements from flight tests, it is important to mention that the elevation and the azimuth angles are computed with

respect to the body frame as the antenna induced error depend on the arrival angle of the satellite to the antenna.

Figure 5.12 shows the effect of the antenna calibration on the smooth multipath and noise error (CMC_{Dfree}) for GPS L1 for one satellite (left plot) together with the estimated code error group delay versus time (right plot). The black curve in the left plot shows the smooth error versus time before the calibration and the green curve represents the errors obtained after the antenna induced errors are removed. The calibration removes the drift from the multipath error and the resulting curve shows a much smoother behavior which is expected for the multipath error.

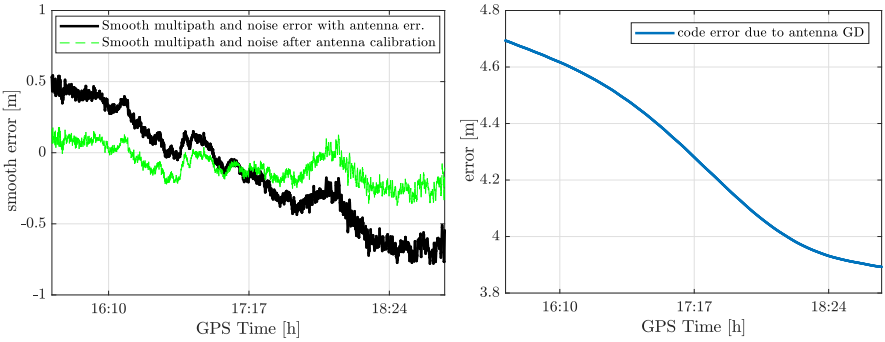


Figure 5.12: Calibration of antenna errors in a static ground scenario. The left plot shows the smooth multipath and noise on GPS L1 for one satellite before calibration (black solid curve) and after calibration (dashed green curve). The right plot shows the code error due to antenna group delay variation

In a similar manner, Figure 5.13 shows the effect of the calibration during flight tests. In this case, the antenna induced error (right plot) shows a larger variation due to the fast change in the angles of arrival in maneuvering. The calibration of the antenna errors reduces the variation of the smooth multipath error (green curve in the left plot) also in this case significantly.

These results show that by removing the code errors due to antenna group delay variations the trend of the antenna errors from the multipath estimation can be extracted. These errors constitute the near field errors due to the antenna pattern. The remaining errors are due to the reflections from the antenna far field, namely reflectors. The amount of multipath created by the far field reflectors and present in the code measurements is dependent on the specific antenna reject capabilities. In [124] the authors provide an analysis from the antenna point of view and discuss the parameters relevant for the multipath susceptibility of the antenna. Furthermore, the impact of different antenna on the final multipath curves will be discussed in Section 5.11.

It should be noted however, that when removing the errors introduced by the antenna group delay variations from the multipath error budget, they need to be

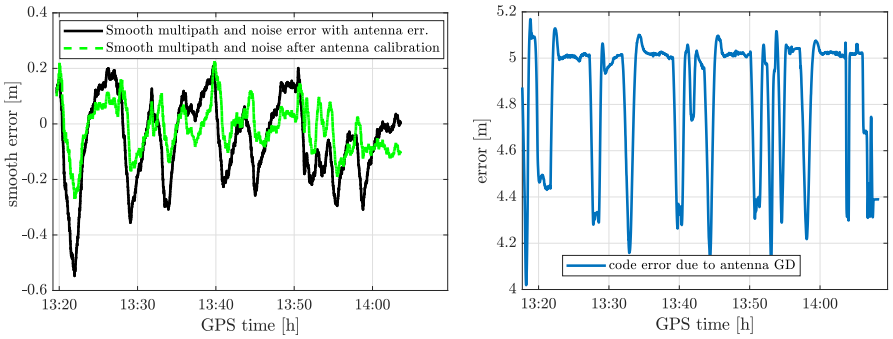


Figure 5.13: Calibration of antenna errors on measurements from flight. The left plot shows the smooth multipath and noise on GPS L1 for one satellite before calibration (black solid curve) and after calibration (dashed green curve). The right plot shows the code error due to antenna group delay variation

accounted for separately in the integrity concept. This analysis is out of the scope of this thesis and future work will investigate the bounding of the antenna induced errors.

5.8 Data collection for new models

For data collection, measurements from different aircraft types were used. Most of the data was collected on DLR's Airbus A320. Since 2015, a Javad Delta TRE3 receiver and a multiband antenna are permanently installed in this aircraft in order to collect as much multi-frequency multi-constellation data as possible. Dual constellation (GPS, Galileo), dual frequency (L1/E1 – L5/E5a) measurements were collected by the on board receiver at a rate of 20Hz. For most of the flights the configuration of the receiver was chosen according to the current plans for standardization (i.e. a 0.1 correlator chip spacing for L1/E1 and 1 chip for L5/E5a with a bandwidth of 23 MHz). During specific flights, the receiver parameters were changed in order to investigate the impact of the receiver parameters on the multipath error. An avionics multiband antenna was installed on the aircraft, not in its primary location, but further to the back. The antenna used is not compliant with the currently published MOPS for dual-frequency airborne antennas ([123]). It has a smaller axial ratio than the one required in the standards and the group delay variations exceed the given limits. Thus, the results obtained from this experimental setup are more conservative. Data from 78 flights conducted between November 2015 and July 2017 is available and a total of about 200 flight hours were evaluated to derive most of the results in this work. Figure 5.14 shows the ground tracks for all the flights. Most of the flights took place in Europe with the exception of one transatlantic flight from Braunschweig to French Guyana and back.

In February 2019, the first flight campaign within the DUFMAN project took

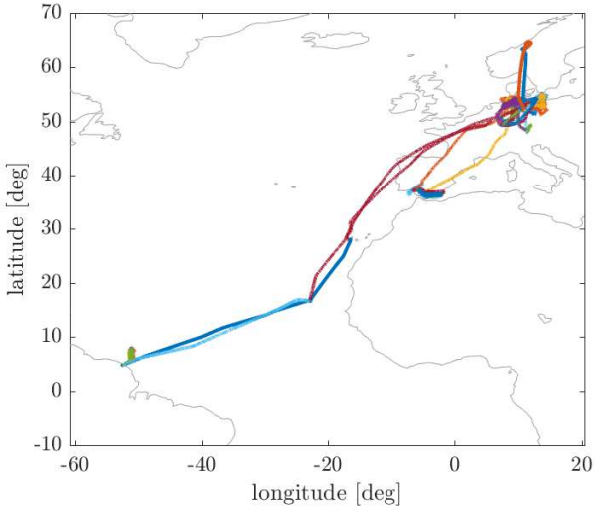


Figure 5.14: Ground tracks of the flights conducted on DLR's A320 during 2015-2018

place using the Airbus A321 aircraft. On this aircraft a multiband Javad AirAnt antenna was installed in one of the primary GNSS antenna locations (GPS2 in this case). Radio Frequency (RF) samples were collected by the onboard Syntony recorder. The RF samples were recorded during two flights with a total of around 5 hours. Figure 5.15 shows the ground track of the two flights: F0324 that took place on 14th of February 2019 and F0325 that took place on 15th of February 2019. The flights took place around Toulouse; the first flight was conducted south of Toulouse with one take-off and one landing while for the second flight five approaches around Toulouse airport were flown. Each of the approach ended with a landing and then taxiing back to the beginning of runway.

The RF-data was replayed in the laboratory through a Javad receiver similar to the one installed in the DLR's A320. The measurements from this flight are used for a first comparison of what is to be expected from a typical DFDC commercial installation. Furthermore, the Javad antenna that was installed on this aircraft has an improved performance compared with the antenna installed on the DLR's A320 and meets the requirements described in the DO-373 document. The performance of this antenna is discussed further in Section 5.8.1.

In order to investigate the impact of different airframes, measurements from the DLR's Dassault Falcon FA 20 aircraft are used. During July 2018, a number of flights were conducted on this aircraft, which is a business jet and significantly smaller than the Airbus aircraft. It has been modified for use in research by DLR and also contains additional antennas and provisions for the installation of measurement equipment on the fuselage. The aircraft has the horizontal stabilizer on the tail above the level of the GNSS antenna. The plane was equipped with a Javad Delta G3TH receiver with

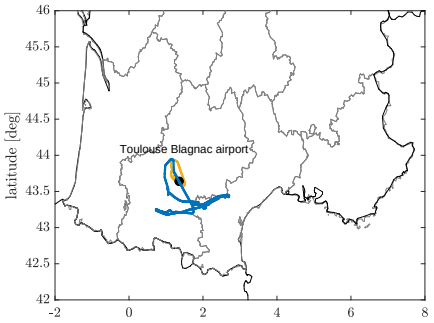


Figure 5.15: Ground tracks of the flights conducted on Airbus A321 within DUFMAN project

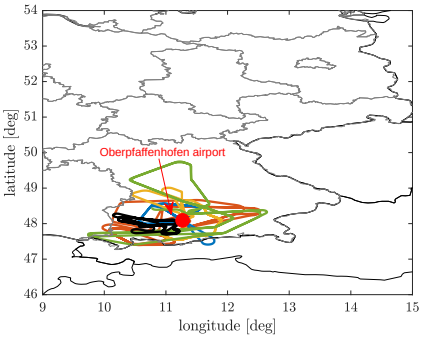


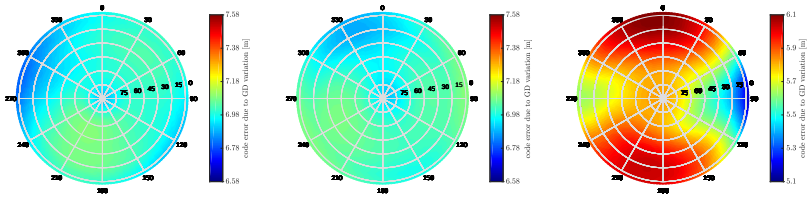
Figure 5.16: Ground tracks of the flights conducted on DLR's Dassault Falcon

the same functions and parameters as in the DLR's Airbus A320 and the same Javad AirAnt multiband antenna type that was used for the Airbus A321 tests. The receiver was configured with 23 MHz bandwidth and 0.1 chips correlator spacing for L1/E1 and 1 chip correlator spacing for L5/E5a band. Dual-frequency code and carrier-phase measurements on L1 (E1) and L5 (E5a) were recorded and post processed to assess the multipath error. The flights were conducted around Oberpfaffenhofen airport and Figure 5.16 shows the ground track of the flights.

5.8.1 Javad antenna measurements

The antenna installed on A321 and Dassault Falcon aircraft is a multiband Javad AirAnt antenna which was chosen because it meets the specification of the dual-frequency dual-constellation avionics antenna [123]. The antenna was measured in an anechoic chamber and the code tracking error introduced by the antenna group delay variations have been calculated and are shown in Figure 5.17. The antenna measurements and the estimation of the code tracking errors have been performed by Dr. Stefano Caizzone and Mr. Christoph Enneking and are used in this work for separation from the multipath errorsas previously discussed Section 5.6.3.

Again, the values refer to the absolute error without any normalization and thus they start at a different value for each frequency and modulation. The total variation is kept to 1m for all signals. It can be observed that compared with the Antcom antenna installed on DLR's A320, the variation of the code error introduced by the antenna group delay is smaller. The errors on L1/E1 bands show less variations compared with the error introduced on L5/E5a signal, which means that the antenna has an improved performance on L1 band. For the Antcom antenna, the performance on L1 band was much better compared to L5 band. The impact of these aspects on the multipath models is discussed further in Section 5.11.



(a) (b) (c)

Figure 5.17: Code error due to the absolute antenna group delay of the Javad AirAnt antenna for GPS L1 signal (a), Galileo E1 (b) and GPS L5/Galileo E5a (c)

5.9 Impact of the processing on the multipath and noise error models

The initial analysis of airborne multipath and noise is performed using the data collected from the DLR's Airbus A320 which is representative of a commercial airplane. The impact of different factors of influence such as airframe, receiver parameters and smoothing time constants are discussed as well. Before showing the obtained multipath models, the impact of several processing aspects on the final models are discussed in the next sections. These include:

- the choice of the cycle slips detectors used in the multipath estimating process,
- the removal of the code errors introduced by the receiver antenna group delay variation,
- the overbounding to safely bound the tails,
- the selection of elevation bins and the inflation for the number of independent samples.

5.9.1 Impact of cycle slip detectors

As previously discussed in Section 5.5.1.4, the choice of the cycle slip detectors has an impact on the multipath estimation process, because they lead to changes of the carrier phase ambiguities. The computation of the carrier phase ambiguities assumes that for a continuous segment of data, the value of the ambiguity is constant for each satellite.

Several cycle slip detectors can be used in the multipath estimation process and no standardized algorithm is defined. In order to investigate the impact of using different cycle slip detector on the final models, two limit cases are analyzed: (1) all the cycle slips detectors introduced previously in Section 5.5.1.4 were activated (including the C/N_0 limits, MQM, Melbourne-Wübbena (MW), the phase geometry-free detector) and (2) the cycle slip detectors were switched off and the C/N_0 limits were set to 0. The evaluation is performed using measurements from all the flights conducted on DLR's A320. The results are shown in Figure 5.18, where the standard deviations of the multipath and noise models for GPS L1 (top plot), GPS L5 (middle) plot and

GPS Ifree combination (bottom plot) are shown function of the elevation angle (in aircraft body frame) for the two limit cases: the solid line in each graph show the curves derived for the case (1) and the dashed lines represents the results obtained from the case (2) in which all detectors are switched off.

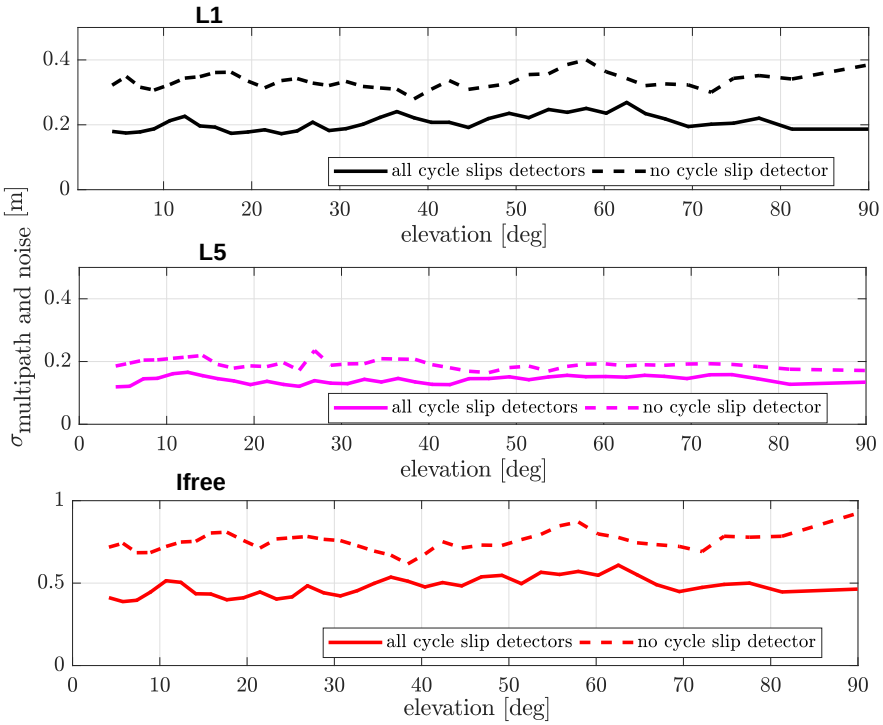


Figure 5.18: Standard deviation of the airborne multipath and noise error obtained when all cycle slip algorithm are enable (solid lines) and without any cycle slip detector (dashed lines) for GPS L1 (top plot), GPS L5 (middle plot) and Ifree combination (bottom plot)

It can be observed that the values increase when no cycle slips detectors are activated and there is a significant difference between the two derived curves for all three processing modes (single frequency L1, single frequency L5 and dual-frequency Ifree). On the single frequency L1 the difference is rather significant and varies between 10 and 20 cm. For the single frequency L5 the difference is smaller varying up to 10 cm for low elevations (below 45°) and around 4 cm for elevation above 50°. For the Ifree combination, the difference is more pronounced for all elevation angles and varies between 30 and 40 cm.

As these two cases can be considered as limit cases, the results obtained define the lower and respectively the upper limit of standard deviation that can be obtained

when different cycle slip detectors are used.

For the derivation of the final models, the cycle slips used in the multipath estimation should not exclude multipath components that will be present in the avionics receiver processing. Thus, based on the discussion from Section 5.5.1.4, in order to achieve results similar to a certified avionics receiver, only the MQM detectors (enabled for both L1/E1 and L5/E5a) is used in the derivation of the models and the C/N_0 limits are set to 27 dB-Hz for L5/E5a and 29 dB-Hz for L1/E1. The C/N_0 limit is especially important to have comparable results with an avionics receiver because the Javad receiver is able to track signals with very low C/N_0 (down to 10 dB-Hz).

5.9.2 Impact of removal of the antenna biases

Figure 5.19 and Figure 5.20 show the effect of the removal of the code errors introduced by the antenna group delay variations for GPS and Galileo, respectively. The plots show the standard deviations of the multipath and noise errors derived from measurements for L1/E1 frequency (in black lines for GPS L1 signal in Figure 5.19 and blue lines for Galileo E1 signal in Figure 5.20), for L5/E5a frequency (in green lines for GPS L5 signal and light blue line for Galileo E5a signal) and for the Ifree L1/E1-L5/E5a combination (in red lines for GPS and orange lines for Galileo). The solid lines represent the standard deviation of the multipath and noise error containing also the antenna introduced errors and the dashed lines show the curves after the code errors introduced by the antenna group delay variations are removed. The results are obtained based on measurements from all the flights conducted on the DLR's A320 aircraft.

It can be observed that the removal of the antenna errors has a stronger effect for low-medium elevations (up to 60°). This is because for low elevations the group delay variation is much larger (see Figure 5.9. The effect is more pronounced on L1/E1 band because the antenna performance on L5 is better and the group delay shows less variations. As previously discussed, these antenna-induced errors are more bias-like (and not noise-like as the multipath errors) and cannot be quantified only through the standard deviation. It is important mentioning again that if these errors are not separated, the final derived models might not bound completely the total error present in the pseudoranges due to the multipath estimation process when a part of these biases is removed. This separation is important especially for the results derived from measurements collected on DLR's A320 because the group delay variations exceed the limits specified in the standards for the dual-frequency dual-constellation antenna [123].

The results presented further in this chapter refer to the multipath and noise errors remaining after the removal of the code errors introduced by the antenna group delay variations (unless otherwise specified).

The above results refer to the estimated of the standard deviations. However, as discussed in the methodology section, the derivation of the multipath models is based on two inflation steps. First, a CDF overbounding is applied to account for the tails

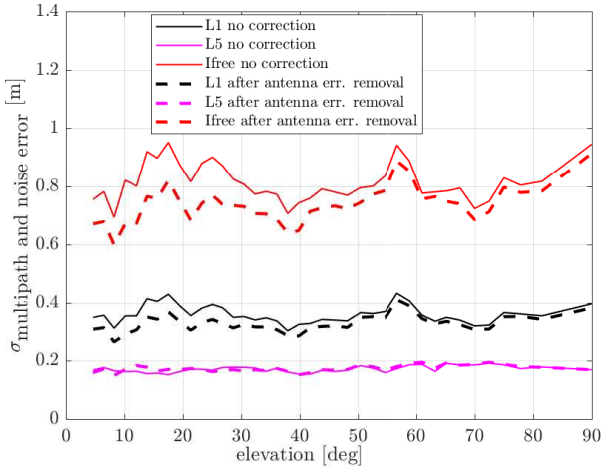


Figure 5.19: Standard deviation of the estimated 100 seconds smooth multipath and noise errors from measurements for GPS L1 (black curves), GPS L5 (magenta curves) and Ifree (red curves) before antenna errors removal (solid lines) and after removal of the code errors introduced by antenna group delay variation (dashed lines) function of elevation in aircraft body frame

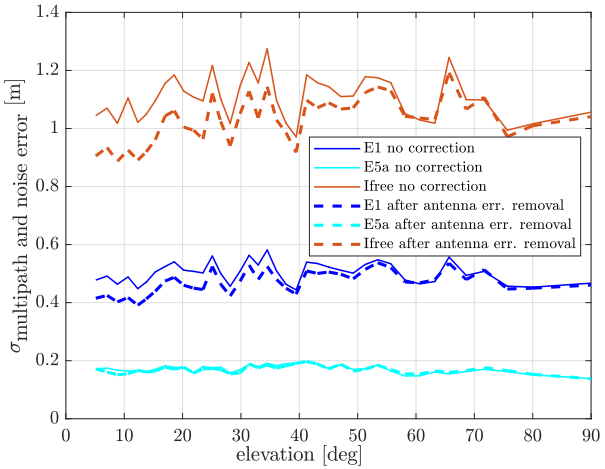


Figure 5.20: Standard deviation of the estimated 100 seconds smooth multipath and noise errors from measurements for Galileo E1 (blue curves), Galileo E5a (light blue curves) and Ifree (orange curves) before antenna errors removal (solid lines) and after removal of the code errors introduced by antenna group delay variation (dashed lines) function of elevation in aircraft body frame

of the distributions of the errors and second an inflation for the limited amount of samples is performed. The results obtained for each of this inflation are shown next.

5.9.3 Overbounding of the tails

The CDF overbounding method is applied to the estimated multipath and noise errors in each elevation bin. The inflation factor is computed as the minimum inflation that respects the condition described in Eq.(5.16). Figure 5.21 shows an example of the overbounding for one elevation bin (14-16° in this case) for Galileo E1 smooth multipath and noise error. The blue solid and dashed lines represent the CDF and 1-CDF of the smooth multipath and noise error measured in the specific elevation bin, the orange solid and dashed lines represents the CDF and 1-CDF of the Gaussian fit and the green solid and dashed lines represents the CDF and 1-CDF of the gausssian overbounding.

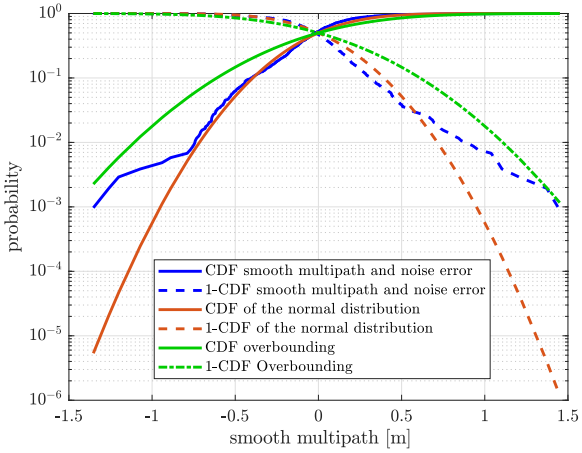


Figure 5.21: Example of overbounding for one elevation bin. The blue solid and dashed curve shows CDF and 1-CDF of the smooth multipath and noise error in the selected bin, the orange solid and dashed curves the CDF and 1-CDF of the Gaussian fit and the green solid and dashed curves the CDF and 1-CDF of the Gaussian overbound

Figure 5.22 and Figure 5.23 show the factor which needs to be applied to the standard deviation of the Gaussian fit in order to fulfill the overbounding condition for GPS and Galileo models, respectively. The inflation factors are derived based on the measurements from the DLR's A320. They vary roughly between values of around 1.2 and 2 for GPS and 1.17 and 1.9 for Galileo models, being therefore not negligible.

This overbounding is more conservative than using a fit, but ensures that the model conservatively bounds the observed multipath errors. It is important to note

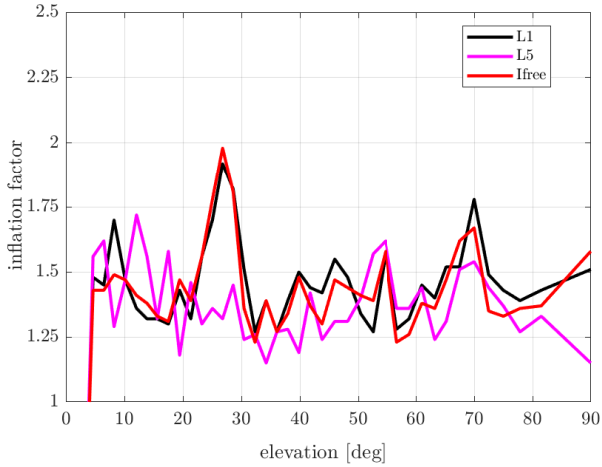


Figure 5.22: Inflation factor derived for all elevation bins to account for heavy tails for GPS L1 model (black curve), GPS L5 model (magenta curve) and Ifree model (magenta curve)

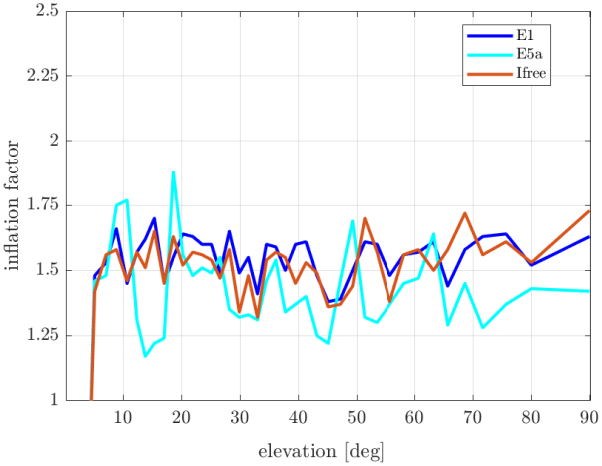


Figure 5.23: Inflation factor derived for all elevation bins to account for heavy tails for Galileo E1 model (blue curve), Galileo E5a model (light blue curve) and Galileo Ifree model (orange curve)

that when separating the measurements into elevation bins, the overbounding is applied over all azimuth angles from a specific elevation bin. This means that for a specific azimuth the bound may not provide the same bounding probability as another azimuth as multipath originates from certain parts of the aircraft (e.g. the

tail fin). However, in order to build multipath models, a significant number of samples is required in order to ensure that the elevation and azimuth variation are well represented in the data.

This overbounding is not sufficient to ensure bounding of position errors with the required integrity risk and is only applied in the derivation of the multipath error models. Meeting the integrity risk requirement is ensured in the protection level calculations where the error bounds are multiplied with the appropriate k-factor derived from the specified integrity risk for a given operation

For the final standardized multipath models, the level to which overbounding is performed may be subject to further research and discussion in the standardization activities.

5.9.4 Inflation for the limited number of samples

As previously discussed in Section 5.5.4, the models are finally inflated to account for the limited number of samples available from measurements. The inflation factor is computed using the relation from Eq. (5.17). The derivation of the number of the independent samples depends on the correlation of the multipath errors and the width of the elevation bins. Even if the antenna introduced errors are removed (which would create stronger correlation over time), the multipath error might still be correlated especially during level flights where the geometry of the satellite changes slowly and multipath effects are somewhat static.

As the multipath curves are derived based on the smoothed multipath and noise errors, the correlation of the errors after smoothing needs to be taken into account. Figure 5.24 shows the median of the autocorrelation function using measurements from all available flight tests on DLR A320 for the raw (unsmoothed) multipath and noise error (black curve) and for smoothed multipath using 100, 200, 300, 400, 500 and 600 seconds smoothing time constant.

A threshold of ± 0.2 is considered as the limit for weak correlation (typically considered in statistics). It can be observed that the raw multipath error does not show strong correlation even for lags below 50 seconds. However, the smoothed multipath error is highly correlated for lags lower than 300 seconds and for 100 seconds it reaches the 0.2 threshold only after 350 seconds. The longer smoothing introduces higher correlation in the measurements, and thus in the multipath and noise error (e.g. for 600 seconds smoothing the autocorrelation reaches values below 0.2 after 900 seconds).

Taking into account the autocorrelation of the multipath and noise error and selecting the independent sample yields to a reduction of the number of samples for each elevation bin. Figure 5.25 shows the convergence of the inflation factor function of the number of samples for a confidence level of 95% calculated based on the Chi-square probability density function defined in Eq.(5.17). From this figure, it can be

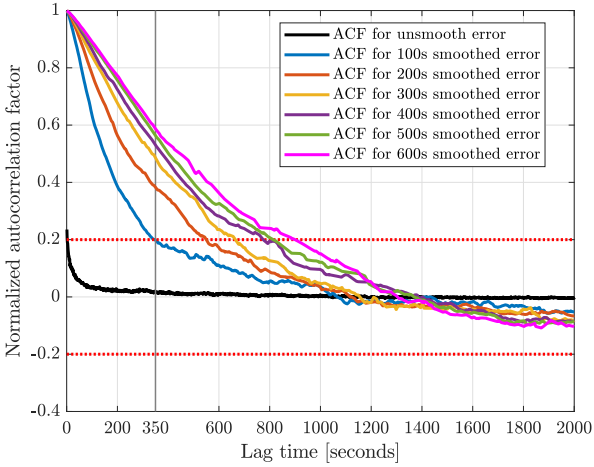


Figure 5.24: Median autocorrelation function of unsmoothed multipath error (black solid curve) and smoothed multipath error using folowwing smoothing time constants 100 seconds (blue curve), 200 seconds (dark red curve), 300 seconds (orange curve), 400 seconds (purple curve), 500 seconds (green curve) and 600 seconds (magenta curve)

observed that the inflation factor is significant for a low number of samples (below 300), but it decreases and stays rather constant above 300 samples.

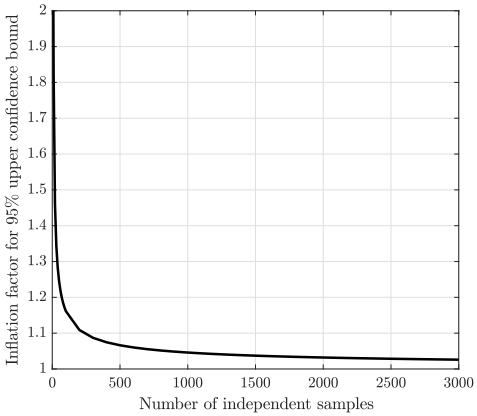


Figure 5.25: Inflation factor for 95% confidence limit function of number of samples

Another factor that drives the inflation for the number of samples is the size of the selected elevation bins. In the derivation of the ground multipath models (described in [32]), variable bin sizes are considered to account for the movement

of the satellite for different elevations (faster at high elevation and slower at higher elevations). Furthermore for a ground installation it is assumed that higher elevations have always lower errors. However, this is not always the case during flights tests in which the satellite directions might change fast due to maneuvers.

One approach to define the elevation bins is to consider fixed bins over all elevations. The resulting inflation factors together with the number of independent sample per elevation bins obtained for GPS satellites for 100 seconds smoothed multipath error for the case 2° and 5° are shown in Figure 5.26a for 2° binning and Figure 5.26b for 5° binning. The results are derived based on the measurements from DLR's A320 and the elevation refers to the elevation in the aircraft body frame. It can be observed that for both cases the inflation factors is rather constant for low-medium elevations. However, for high elevations (above 80°) the inflation factor increases significantly due to the less samples available (below 100) at high elevations. This increase could affect the final models and their elevation dependency. This is because it cannot be assumed that airborne multipath error is smaller for higher elevations, as the received multipath depends on the specific airframe geometry (e.g. the tail can create multipath on high elevation satellites).

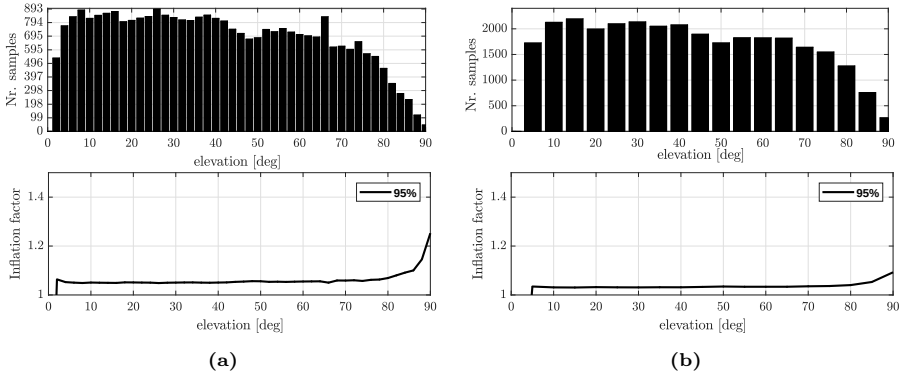


Figure 5.26: Number of samples per elevation bin (top plots) and resulting inflation factor to account for limited number of samples (bottom plot) for GPS for fixed 2 degrees elevation bins (a) and 5 degrees elevation bins (b)

A way to overcome the increase in the inflation factors is to define the elevation bins such that each bin contains the same number of samples. The number of bins can be selected such as the minimum number of samples per bin is at least 300, this being the value at which the inflation factor decreases significantly. An example of such binning is shown in Figure 5.27 showing the number of samples for each elevation bin and the derived inflation factor.

In this case, the inflation factor is constant for all elevation angles. The drawback of this approach is that the bins widths can get larger (e.g. the last bin at high elevation) and might introduce undesired average (for bins larger than 5°). Thus,

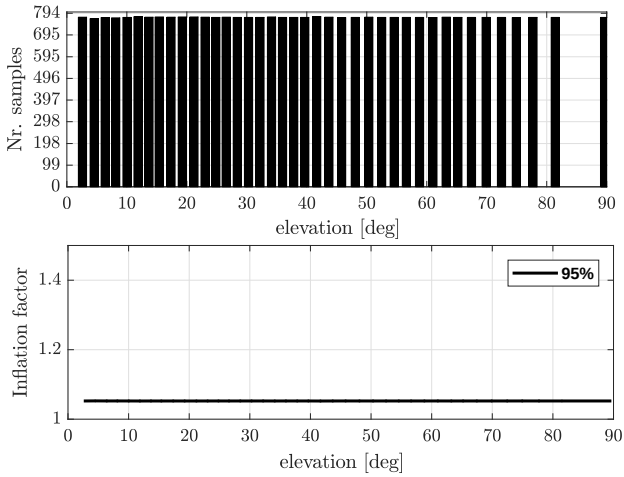


Figure 5.27: Number of samples per elevation bin (top plot) and resulting inflation factor to account for limited number of samples (bottom plot) for GPS for bins with equal number of samples

the decision of the elevation bins for the final model has to be made based on the specific data set and the trade-off between the increase in the inflation factor and the averaging. For the data sets from DLR's A320 the selection of the bins with equal number of samples will be used as the width of the bins is very similar across elevation except the bin from 80° to 90° where the averaging effect is considered negligible. Thus, this method will be used to derive further the multipath models.

5.10 Multipath error models for DLR's A320

Figure 5.28 and 5.29 show the multipath models obtained for DLR's A320 after carrying out the steps described previously for GPS and Galileo constellation respectively. The models are functions of the satellite elevation angle shown both in local body frame coordinate system and in local level frame. The plots show the obtained curves for the three models: L1/E1 (with black curves in Figure 5.28 for GPS L1 model and blue curves in Figure 5.29 for Galileo E1 model), L5/E5a (magenta curves for GPS L5 model in Figure 5.28 and light blue curve for E5a model in Figure 5.29) and for the L1/E1-L5/E5a Ifree combination (with red curves in Figure 5.28 for GPS and dark orange in Figure 5.29 for Galileo). The solid lines refer to the models obtained based on the elevation of the satellites in body frame and the dashed lines represent the models obtained when the elevation of the satellite above horizon is used (local level frame). To derive the curves, the elevation bins were selected such that the bins have almost equal number of samples and the inflation factor from Figure 5.27 has been applied for GPS signals.

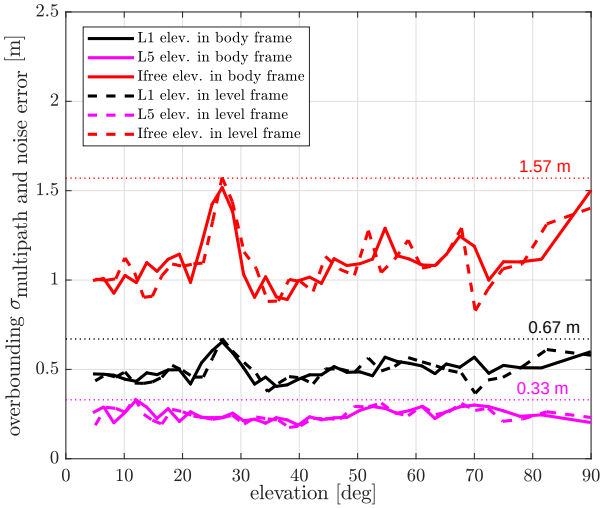


Figure 5.28: Overbounding models of the estimated 100 seconds smoothed multipath and noise errors from measurements for GPS L1 (black curves), GPS L5 (magenta curves) and Ifree (red curves) function of elevation in the aircraft body frame (solid lines) and in local level (dashed lines)

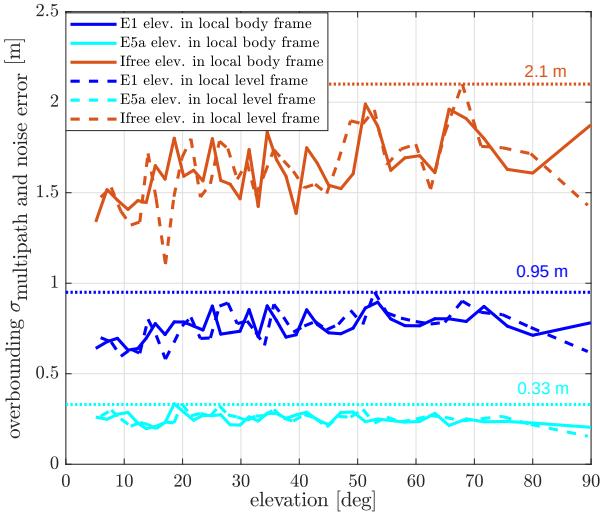


Figure 5.29: Overbounding models of the estimated 100 seconds smoothed multipath and noise errors from measurements for Galileo E1 (blue curves), Galileo E5a (light blue curve) and Ifree (dark orange curves) function of elevation in aircraft body frame (solid lines) and in local level frame (dashed lines)

For both constellations it can be observed that the differences when considering the two coordinate frames to compute the satellite elevation angles are very small. This effect can be attributed to the smoothing filter with a time constant that is relatively long compared to typical aircraft maneuvers. The results suggest that the multipath error models can be defined in the local level frame. This statement needs to be verified with measurements from different airframes and from the primary location of the GNSS antenna before standardizing the models. However, the information of the satellite angle of arrival in a body frame coordinate system is needed and important to be considered for the antenna-induced errors. A separate analysis on how to account for these errors without requiring aircraft attitude information to derive the necessary error bounds for the pseudorange measurements has to be performed. However, this investigation is out of scope of this thesis and will be considered in future.

Another aspect to notice is that the curves do not show much dependency on the elevation and thus the models can be considered as constant values over elevation shown in dot lines in the figures. The constant values is chosen conservatively as the maximum over all the values versus elevation. This effect might be due to specific DLR's A320 installation for which increased multipath is expected for all elevations from different azimuth angles. When the measurements are combined into elevation bins, the multipath spreads over all bins. In addition, the antenna has a poor multipath rejection capability meaning that it will not mitigate the multipath errors from any direction.

Comparing the values obtained for GPS and Galileo, the values are slightly different. For L5/E5a, the obtained curves are quite comparable which is expected as the signal modulation and the frequency are identical for both signals. For L1/E1, the values obtained for Galileo E1 are somehow larger than the ones obtained for GPS L1. The reasons might be attributed to the fact that the flight data dates back to 2015 and it cannot be excluded that variations in the signal quality and signal power level may be reflected in the data (see Figure 4.7). Furthermore, as previously stated in Chapter 4, the improved performance of the BOC(1,1) component of the CBOC modulation in multipath rejection is effective on long range multipath (above 150 m), while on the aircraft shorter range multipath is characteristic (see Figure 4.12). For short range multipath, the performance of BOC(1,1) modulation is very similar with the one on BPSK(1) modulation.

The absolute values obtained for the multipath models are not to be considered final values as they are derived based on an experimental installation on a single aircraft type. The antenna used in the data collection is non-compliant with dual-frequency antenna MOPS which leads to worse results than what is expected from a MOPS compliant antenna. Even if the code errors induced by the antenna group delay variations were removed, the antenna multipath rejection capability plays an important role in how much multipath is received. As the antenna used has a small axial ratio, this effect is reflected in the measurements and the obtained results. Furthermore, the antenna was not installed in its primary location, but in an experimental location

further to the back of the aircraft. In this location, the antenna is closer to other reflectors and thus the amount of multipath that is received is higher. Finally, the receiver used was a commercial receiver designed for geodetic applications. While the correlator spacing and the bandwidth were modified to values representative of an avionics receiver there may be differences in the implementation.

For DFDC GBAS, depending on the final processing mode, airborne multipath models based on 30 seconds smoothing time constant might be needed as well. Figure 5.30 and Figure 5.31 show the derived models for 30 seconds smoothing time constant for GPS and Galileo. The curves were derived and are shown in the same manner as for the 100 seconds smoothing time constant.

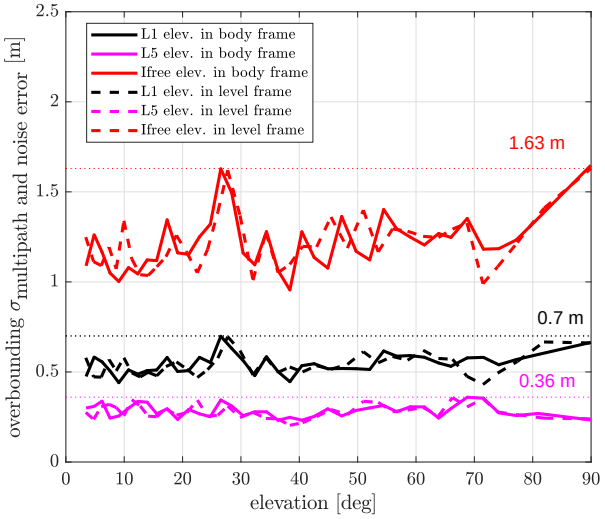


Figure 5.30: Overbounding models of the estimated 30 seconds smoothed multipath and noise errors from measurements for GPS L1 (black curves), GPS L5 (magenta curves) and Ifree (red curves) function of elevation in the aircraft body frame (solid lines) and in local level frame (dashed lines)

The shorter smoothing time constant yields to an increased multipath and noise error. For this case, the increase in the maximum value on L1/E1 is around 2-3 cm, 3 cm for L5 signal and 15 cm for E5a signal. The larger increase in the E5a signal is driven by a jump at 19° which might be due to an undetected cycle slip. For the Ifree combination, the increase reaches 6 cm for GPS and 15 cm for Galileo. Similar to the models derived based on 100 second smoothing time, the 30 seconds smoothed multipath models do not show an elevation dependency. Furthermore, the difference between the two coordinate systems stay very small.

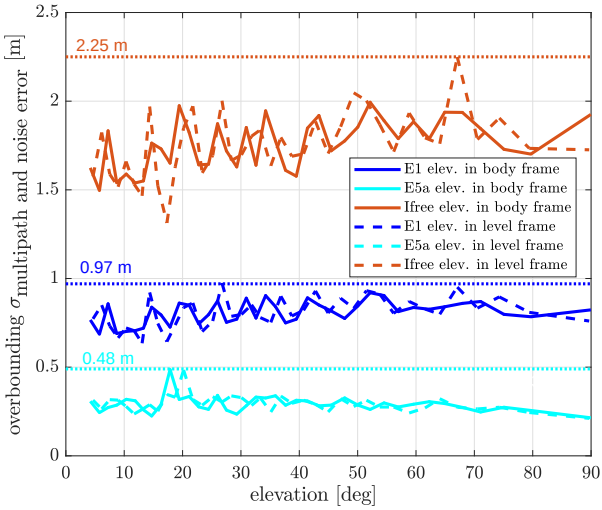


Figure 5.31: Overbounding models of the estimated 30 seconds smoothed multipath and noise errors from measurements for Galileo E1 (blue curves), Galileo E5a (light blue curve) and Ifree (dark orange curves) function of elevation in aircraft body frame (solid lines) and in local level frame (dashed lines)

5.11 Factors of influence on the airborne multipath models

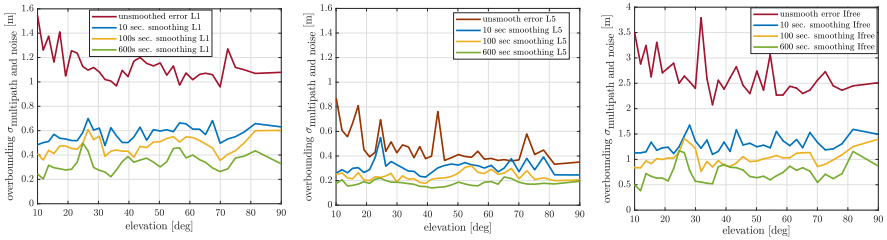
The main factors of influence that can have an impact on the multipath error present in the pseudorange measurements includes mainly the airframe, receiver parameters and smoothing time constants. The effect of each of this factor of influence is shown and discussed in the next sections.

5.11.1 Impact of the smoothing time constant

After showing the models derived for 100 and 30 seconds smoothing time constant, this section discusses possible consequences on the smoothing time constant required for the new signals. In the previous chapter, based on measurements from ground stations, it was observed that the new signals broadcast on GPS L1 and Galileo E5a band are less sensitive to the smoothing time constant. For GPS L5 and E5a, there is already almost no additional error reduction for smoothing longer than 30 seconds. In the same manner, an evaluation of the different smoothing times on airborne noise and multipath is shown here using the same measurements from the flights conducted on DLR's A320.

Figure 5.32 shows the overbounding models function of elevation for GPS L1, GPS L5 and Ifree combination for smoothing time constant of 10, 100 and 600 seconds. In addition, the overbounding models of the unsmoothed multipath and noise error is also shown. The unsmoothed models are needed because the avionics receiver might

use the raw GNSS measurements in the integration with the inertial system.

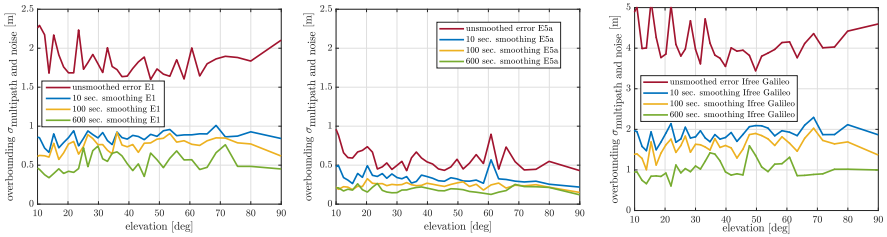


(a) GPS L1 **(b)** GPS L5 **(c)** GPS Ifree combination

Figure 5.32: Overbounding airborne multipath results for GPS L1 (a), GPS L5 (b) and the Ifree combination (c) for different smoothing time constants. The red lines represent the models obtained from unsmoothed measurements, the blue lines the models for 10 seconds smoothing, the dark yellow the 100 seconds smoothing and the green curves the 600 seconds smoothing.

The results show that the difference between the curve derived based on unsmoothed multipath and noise error for GPS L1 and GPS L5 is quite significant. This has also been observed on the measurements from the ground stations and it is due to the larger noise on the L1 signal (using a BPSK(1) modulation) compared to the L5 signal which has an increased chipping rate. Most of this noise is reduced by the smoothing filter even using 10 seconds smoothing time constant. The curves based on 10 seconds smoothing time decrease significantly for L1, while for L5 the difference is much smaller. The impact of the longer smoothing time (600 seconds) on the L5 signals is significantly lower compared to the L1 signal. This effect was expected, since the properties of the new signals show better performance in terms of multipath rejection. Thus, with lower multipath in the signals to begin with, the benefit of extended smoothing is not as large as with the L1 signals. On the Ifree combination, the longer smoothing time constant does bring a significant benefit, with a decrease of about 60 cm from 100 seconds to 600 seconds.

In Figure 5.33, the same analysis is shown for Galileo E1, Galileo E5a and Ifree combination. A similar effect of smoothing filter duration is seen on E1 and E5a signals as for L1 and L5 signals. On the E1 signal, the decrease in the residual error with the increase of the smoothing time constant is more pronounced. The 10 seconds smoothing time constant reduces already most of the uncorrelated noise and multipath, thus the difference to 100 seconds smoothing time constant is rather small. The use of 600 seconds smoothing time constant reduces the curves by 30 cm. This is because a long smoothing time constant would reduce also correlated multipath error if the correlation time is lower than the smoothing time constant (in DLR's A320 the median autocorrelation is around 350 seconds).



(a) Galileo E1 **(b)** Galileo E5a **(c)** Galileo Ifree combination

Figure 5.33: Overbounding models for Galileo E1 (a), Galileo E5a (b) and the Ifree combination (c) for different smoothing time constants. The red lines represent the models obtained from unsmoothed measurements, the blue lines the models for 10 seconds smoothing, the dark yellow the 100 seconds smoothing and the green curves the 600 seconds smoothing.

5.11.2 Impact of different antennas and different airframe

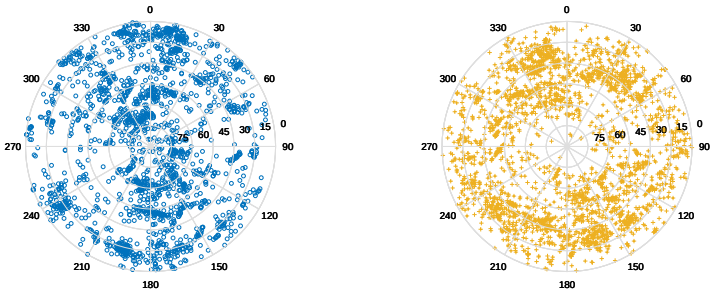
An important factor of influence to the airborne multipath is the shape of the antenna and the airframe itself and the location of the GNSS antenna with respect to its reflecting surfaces. In order to evaluate the impact of different aircraft types and antenna types and locations, measurements from A321 collected within DUFMAN project flight campaign [1] and DLR's Dassault Falcon aircraft will be used.

As described in Section 5.8, on both of these aircraft the Javad AirAnt antenna has been installed [125]. For both aircraft types, the measurements were collected with the same receiver: the RF-data collected on A321 was replayed through a Javad receiver with the same configuration as the one used on DLR's A320, and for Dassault Falcon the receiver was installed in the aircraft and collected the GNSS measurements. The data available from these flight tests is limited, but it is used for a first indication of the residual errors on different aircraft and using different antennas. Figure 5.34 and Figure 5.35 show the skyplot (with the elevation and azimuth of the satellite in aircraft body frame) of the GPS (Figures (a)) and Galileo (Figures (b)) satellites tracked during all the flight tests on A321 and Falcon, respectively.

Based on the measurements from each aircraft, the multipath and noise curves were derived following the steps described previously. The inflation due to the limited number of samples was not performed because the number of samples available is too small and the distribution of the samples across the elevations to uneven in order to obtain meaningful results.

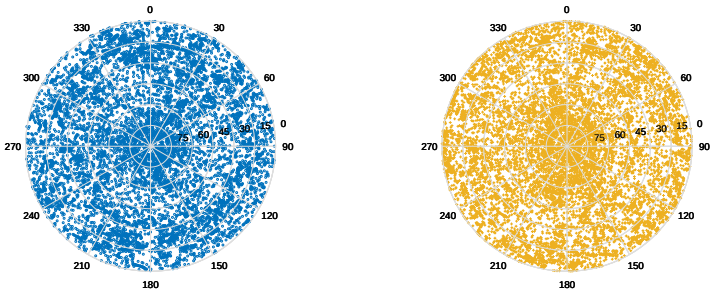
Figure 5.36 shows the obtained multipath curves for GPS (Figure (a)) and Galileo signals function of elevation in aircraft body frame. The results refer to the 100

[1] The flight campaigns were carried out in the frame of the project DUFMAN funded by the European Commission (DG-GROW / JRC) and the author would like to thank European Commission for the approval of using the data. Opinions expressed herein are those of the author and do not represent the contracting authorities' official position.



(a) GPS **(b)** Galileo

Figure 5.34: Skyplot of the GPS and Galileo satellites tracked during the two flight tests conducted on Airbus A321 in aircraft body frame

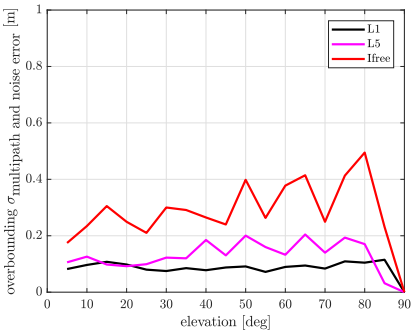


(a) GPS **(b)** Galileo

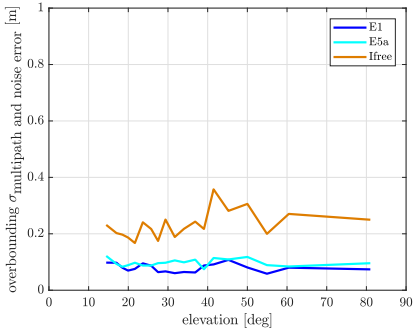
Figure 5.35: Skyplot of the GPS and Galileo satellites tracked during the flight tests conducted on Dassault Falcon aircraft in aircraft body frame

seconds smoothed multipath and noise error, after the removal of the antenna-induced errors was performed based on the code errors shown in Figure 5.17.

The results obtained from this aircraft show much lower residual noise and multipath errors than the results obtained from DLR's Airbus A320 experimental installation shown in Figure 5.28 and 5.29. This can be explained by two factors: (1) the experimental antenna installed on DLR's A320 has a bad performance in terms of multipath rejection capability and group delay variations and (2) the experimental antenna on DLR's A320 is installed further to the back on the fuselage and is therefore subject to more multipath from the airframe. Furthermore, the aircraft is equipped with several other antennas and installations on the fuselage in the vicinity of the experimental GNSS antenna creating again more multipath than a standard installation would experience. The combination of all these effects yields larger multipath errors compared to the one expected from the Airbus A321 installation.



(a) GPS L1 (black curve), GPS L5 (magenta curve), GPS Ifree combination (red curve)



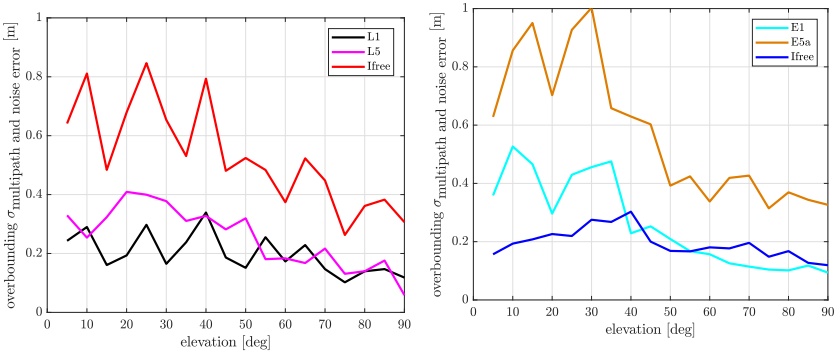
(b) Galileo E1 (dark blue curve), Galileo E5a (light blue curve), Galileo Ifree combination (red curve)

Figure 5.36: Overbounding airborne multipath models for 100 seconds smoothed multipath and noise obtained from the measurements on A321 for GPS and Galileo signals

It is interesting to notice that these results show a different behavior for L1/E1 and L5/E5a. Until now, the L5/E5a signal showed an improved performance and lower residual and noise error. Comparing the results obtained for different signal from measurements collected on A321 aircraft after smoothing, it can be observed that the performance on both signals is quite similar with slightly better results for L1/E1, contrary to the observations that were previously made on data from DLR's experimental installation. This behavior can be attributed to the antenna performance that is worse on L5/E5a compared to L1/E1. Similar to the curves from A320, the models do not show an elevation dependency.

A similar effect of the slightly better results on L5/E5a can be observed on the models derived from the measurements on Falcon shown in Figure 5.37 for both GPS and Galileo constellations. The models were derived in the same manner as for the A321, with the removal of antenna errors and without the inflation for the number of samples. It can be observed that also in this case the models for L5/E5a are somewhat larger than the L1/E1 ones. The difference is more pronounced for Galileo signals, especially at lower elevations. These results confirm that the effect can be attributed to the antenna. On Falcon the same Javad antenna as the one installed on the A321 was used. The antenna shows better performance in terms of group delay variation and better multipath rejection capability for L1/E1 than for L5/E5a.

Compared to the results of the A321, the results obtained from Falcon are larger and show a slight elevation dependency for both constellations. This dependency can be attributed to the geometry of the aircraft and has not been observed on the larger aircraft (A320, A321). The increase of the multipath errors and the elevation dependency is larger on the L1/E1 signal compared to the L5/E5a. This can be explained by the better multipath rejection capability of the L5/E5a BPSK(10) modulation.



(a) GPS L1 (black curve), GPS L5 (magenta curve), GPS Ifree combination (red curve)

(b) Galileo E1 (dark blue curve), Galileo E5a (light blue curve), Galileo Ifree combination (red curve)

Figure 5.37: Overbounding airborne multipath models for the 100 seconds smoothed multipath and noise obtained from the measurements on Falcon aircraft for GPS and Galileo signals

The difference between the GPS and the Galileo models is an effect of the limited amount of data and the different satellite geometry (the number of samples on Galileo is almost two times larger than for GPS).

5.11.3 Impact of correlator spacing

Another factor of influence to the multipath and noise errors is the configuration of the receiver, more specifically the choice of the correlator spacing and bandwidth. The single frequency airborne specifications for GBAS (from DO-253D document, [18]) define allowed regions for combination of receiver bandwidth and early-minus-late correlator spacing as shown in Figure 5.38.

Previous work of the author presented in [86] and [113] investigated the impact of the correlator spacing on the multipath and noise models. The analysis was performed using measurements from the receiver installed in the DLR's Airbus A320 with two different correlator spacing values. The Javad receiver has a bandwidth of 23 MHz and the correlator spacing was modified to 0.1 chips for L1/E1 and 1 chip for L5/E5a for most of the flight tests. However, measurements with default correlator of the receiver set to 0.01 chips for L1/E1 and 0.1 chips for L5/E5a were collected during initial flight tests. Even if the narrow correlator is outside the specified design space, it was used as a relevant value for narrow correlator receivers. The comparison results obtained during that study are shown in Figure 5.39 (Figure 5.39a for GPS and Figure 5.39b for Galileo). The figures show the standard deviation of the multipath and noise errors and were derived based on the methodology described in [86, 113] without any further modifications.

The results derived for GPS show a noticeable difference for both signals when

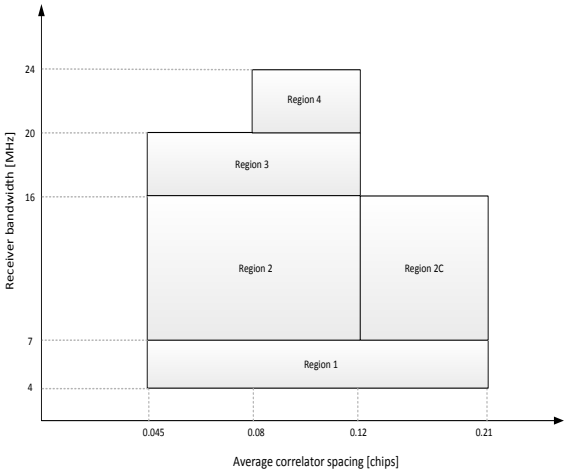
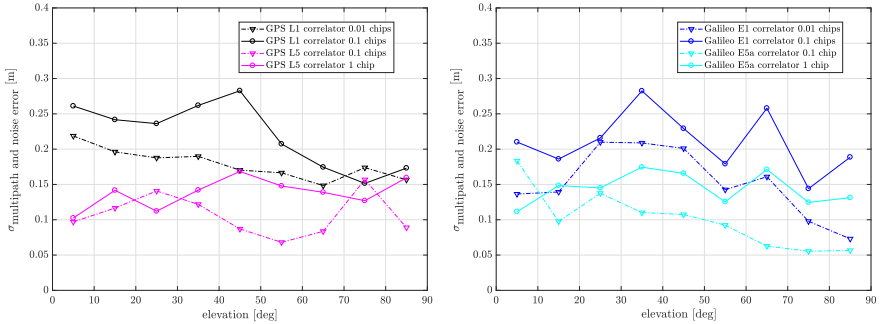


Figure 5.38: Allowed E-L Discriminator Tracking of GPS satellites as specified in [18]



(a) GPS L1 (black curves) and GPS L5 (magenta curves)

(b) Galileo E1 (blue curves) and Galileo E5a (light blue curves)

Figure 5.39: Standard deviation for the noise and multipath error obtained from DLR's A320 aircraft with 0.01 chips correlator for L1 / 0.1 for L5 (dashed lines in both graphs) and 0.1 chips correlator spacing for L1 / 1 chip correlator spacing for L5 (solid lines)

different correlator spacings are used. The difference is more pronounced for GPS L1 signal, especially for elevations below 60°. A similar outcome can be observed on the Galileo signals, for which the narrow correlator results also in smaller variance of the multipath and noise errors.

The main drawback of this study is that the results were obtained from different

flight tests during which different satellite geometries were available. Thus, the results might not reflect directly only the impact of the correlator spacing, but also the impact of different multipath errors experienced in the different flight tests. Furthermore, for DFDC avionics application, the receiver design space has been restricted as shown in Figure 5.40. The receiver bandwidth can take values between 12 and 24 MHz and the correlator spacing varies from 0.08 chips to 0.12 chips for L1 and 0.8 chips (0.9 in [92]) to 1.2 chips (1.1 chips in [92]) for L5/E5a according to [126].

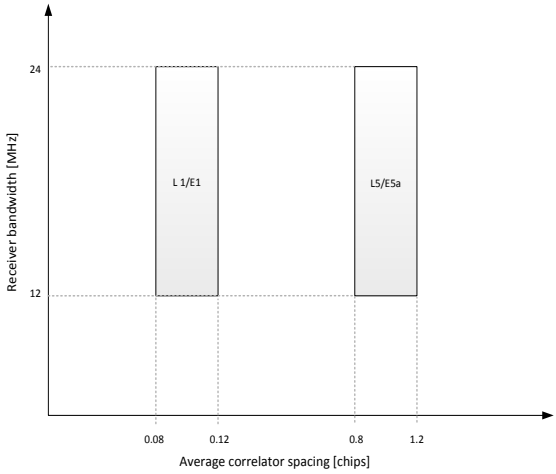


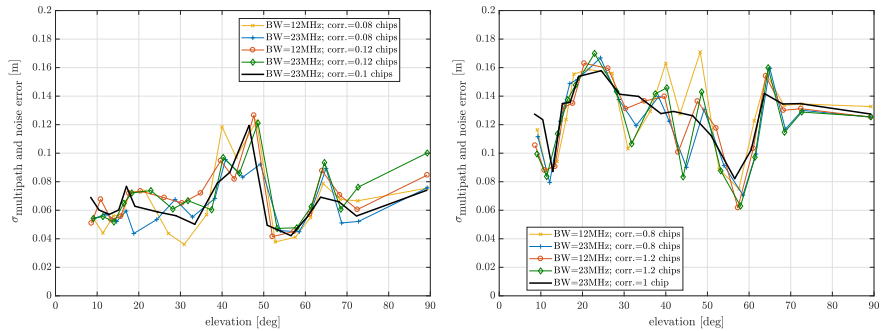
Figure 5.40: DFDC airborne receiver design characteristics as specified in [92]

The impact of the correlator spacing has, thus been reassessed in a systematic self consistent way based on the new design and using measurements collected within DUFMAN project. The study was performed using RF-data collected during the first flight test on Airbus A321. The RF samples were replayed through the Javad receiver using four different combinations of the bandwidth-correlator spacing such as

1. 12 MHz bandwidth with 0.08 chips correlator spacing for L1/E1 and 0.8 chips correlator for L5/E5a,
2. 12 MHz bandwidth with 0.12 chips correlator spacing for L1/E1 and 1.2 chips correlator spacing for L5/E5a,
3. 23 MHz bandwidth with 0.08 chips correlator spacing for L1/E1 and 0.8 chips correlator for L5/E5a
4. 23 MHz bandwidth with 0.12 chips correlator spacing for L1/E1 and 1.2 chips correlator spacing for L5/E5a

The four values represent the corners of the design space and thus represent the maximum variation that is to be expected from any other combination.

The use of the RF samples for this investigation is very important because it allows the isolation of other errors and assessment of only the receiver parameters without the impact of the geometry. Figure 5.41 shows the comparison of the standard deviation of the 100 seconds smoothed multipath and noise errors function of elevation for the four combinations of receiver bandwidth-correlator spacing for L1 signal (left plot) and for L5 signal as follows: the yellow curve with '*' represents the curve derived based on 12 MHz - 0.08 chips for L1/0.8 chips for L5), the blue curve with '+' represents the curve derived based on 23 MHz - 0.08 chips for L1/0.8 chips for L5), the orange curve with 'o' represents the curve derived based on 12 MHz - 0.12 chips for L1 / 1.2 chips for L5), the green curve with diamond markers represents the curve derived based on 23 MHz - 0.12 chips for L1/1.2 chips for L5. In addition, the results previously presented based on 23 MHz and 0.1 chips correlator for L1/1 chip correlator for L5 is plotted.



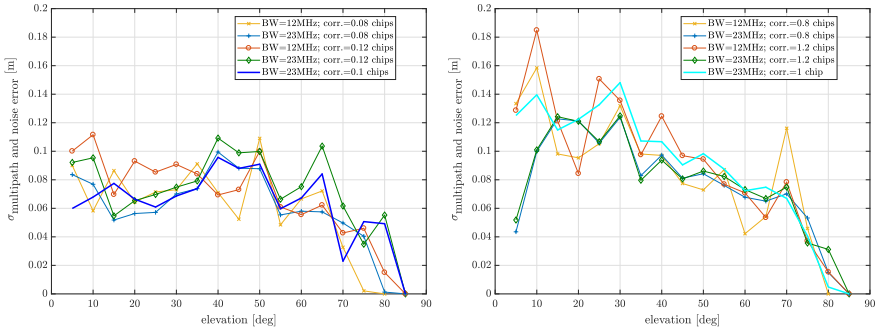
(a) GPS L1 **(b)** GPS L5

Figure 5.41: Standard deviation of noise and multipath error function of elevation for GPS signals for different bandwidth-correlator spacings combinations: 12 MHz bandwidth - 0.08/0.8 chips correlator for L1/L5; 12 MHz - 0.12/1.2 chips correlator for L1/L5; 23 MHz bandwidth - 0.08/0.8 chips correlator for L1/L5; 23 MHz - 0.12/1.2 chips correlator for L1/L5

It can be observed that the differences between the results obtained with different configuration for both L1 and L5 signals are small and reach a maximum of about 4 cm. For L5 signal, the largest values are obtained with the narrow bandwidth and narrow correlator, while for L1 it seems that the larger bandwidth and larger correlator spacing lead to a slight increase in the multipath and noise errors.

A similar behavior can be observed for Galileo signals in Figure 5.42. The left plots show the standard deviations of the 100 seconds smoothed errors derived for E1 signals and in the right plot the results for the E5a signal. The colors represent the same configurations as in the GPS case. The differences between the different configurations are again very small, within few centimeters for both signals.

The conclusion from these results is that one multipath model (at least for 100 seconds smoothing time constant) would be sufficient to cover the entire design space



(a) Galileo E1 **(b)** Galileo E5a

Figure 5.42: Standard deviation of noise and multipath error function of elevation for Galileo signals for different bandwidth-correlator spacings combinations: 12 MHz bandwidth - 0.08/0.8 chips correlator for E1/E5a; 12 MHz - 0.12/1.2 chips correlator for E1/E5a; 23 MHz bandwidth - 0.08/0.8 chips correlator for E1/E5a; 23 MHz - 0.12/1.2 chips correlator for E1/E5a

and no additional inflation would be need to cover different receiver specifications.

5.12 Initial multipath models derived within DUFMAN

Based on the first set of measurements collected during DUFMAN flight campaign, initial airborne multipath models have been proposed and presented during ICAO Navigation System Panel (NSP) meeting [127].

As the amount of data was still limited, the impact of the overbounding for the non-Gaussian data in the elevation bins, different examples of the models have been derived, bounding only the root mean square (RMS) of the sample data or bounding the overbounded results accounting for non-Gaussian distribution of the multipath error. Details of the assumptions made and the different derived models are given in [127].

Figure 5.43 shows the upper bounds of the 100 seconds multipath models for the GPS L1/Galileo E1 signal with black line, for L5/E5a signals with green line and for Ifree combination in red line. Even if the modulation on GPS L1 and Galileo E1 are different, one single model has been suggested because similar performance has been observed for the two signals. It can be observed that the proposed model is less conservative for low elevations than the existing GPS L1 model. For L5/E5a signal, the suggested model shows lower values than the proposed GPS L1/Galileo E1 model due to the improved performance of the signal. For the Ifree combination one constant model over elevation has been proposed for both GPS and Galileo signals. This is because no elevation dependency has been observed in the derived results.

The models have been derived following the same methodology described in this

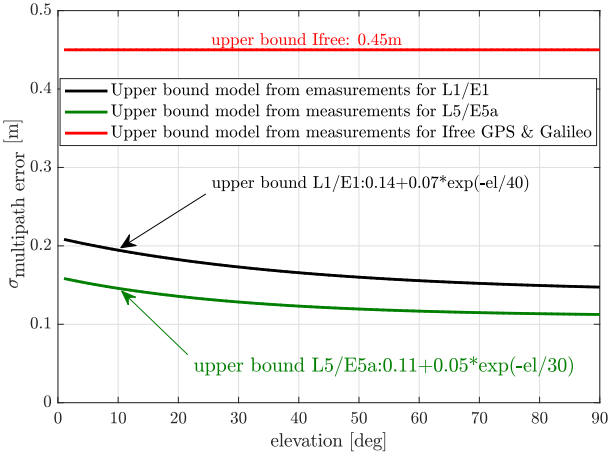


Figure 5.43: Proposed models within DUFMAN project for L1/E1 signals (black line), L5/E5a signals (green curve) and Ifree combination for GPS and Galileo for 100 seconds smoothing time constants

thesis included the removal of the antenna induced errors. The only difference is that the receiver noise contribution was removed from the measurements, conservatively assuming $\sigma_n = 0.02$m for all signals.

Comparing the models with the ones derived from the DLR's A320 two main observations can be made: the results are much lower and the difference between the L1/E1 and L5/E5a curves are not very large. This outcome can be explained by the improved performance of the antenna used in DUFMAN flight tests and installation in the primary position of the GPS antenna, further away from the reflectors.

While the models are not final yet, they will be used in this thesis for initial performance studies of the different processing modes in Chapter 7.

5.13 Publications

The work included in this chapter has been published in several conference and journal papers as follows:

- Paper presented during International Technical Meeting of The Satellite Division of the Institute of Navigation (ION GNSS+ 2015): M.-S. Circiu, M. Felux, B. Belabbas, M. Meurer, J. Lee, M. Kim, and S. Pullen, "Evaluation of GPS L5, Galileo E1 and Galileo E5a Performance in Flight Trials for Multi Frequency Multi Constellation GBAS" [86],
- Paper presented at the International Symposium on Certification of GNSS System & Services (CERGAL): M.-S. Circiu, M. Rippl, M. Felux, S. Caizzone, C.

Enneking, B. Belabbas, and M. Meurer, "Development of Airborne Performance Models for new GNSS Signals" [113],

- Paper presented during International Technical Meeting of The Satellite Division of the Institute of Navigation (ION GNSS+ 2018): M.-S. Circiu, S. Caizzone, M. Felux, C. Enneking, M. Meurer, "Improved Airborne Multipath Modelling" [128],
- Article in Navigation Journal: M.-S. Circiu, S. Caizzone, M. Felux, C. Enneking, M. Rippl, M. Meurer "Development of the dual-frequency dual-constellation airborne multipath models" (in press in the Navigation Journal). This paper has been published based on the content of this chapter.

Furthermore, the work has been presented during standardization group meetings such as ICAO NSP, RTCA and Eurocae WG-62:

- Information paper for the NSP meeting in May 2015 (WGW): Simona Circiu, Michael Felux, Boubeker Belabbas, Michael Meurer (presented By Stefan Naerlich and Eric Chatre): "Airborne performance evaluation of Galileo signals",
- Information paper for NSP meeting in November 2016 (NSP/1-IP/12): M.-S. Circiu, M. Rippl, M. Felux, S. Caizzone, C. Enneking, B. Belabbas, M. Meurer (presented By Stefan Naerlich): "Development of airborne performance models for new GNSS signals",
- Presentation at Eurocae WG-62 meeting in December 2016: M.-S. Circiu, M. Felux, S. Caizzone, C. Enneking, M. Rippl, B. Belabbas, M. Meurer, "Development of airborne performance models for new signals",
- Information paper during NSP meeting in November 2018: S. Circiu, M. Felux, S. Caizzone, C. Enneking, F. Fohlmeister, M., "Development of airborne multipath models for dual frequency and multi constellation applications",
- Presentation at Eurocae WG-62 2018 which included an overview of the DUFMAN project and initial results which are reffered to also in this work.

6 Satellite code biases in DFDC GBAS

6.1 Objectives and contributions

Another source of error in the GNSS measurements are the satellites signal deformations. The signal deformations are caused by the frequency response variations and the delay differences in the analog or digital parts of the signal generation processing chain and of the satellite antenna yielding to non-ideal CDMA pulse shapes. They introduce pseudorange biases that are dependent on the satellite, modulation and receiver hardware. These biases are referred in this thesis as satellite code biases.

GBAS is based on pseudorange measurements and the accuracy of the position is improved by the use of the pseudorange corrections broadcast by the ground station. The ground reference receivers and the airborne receiver could use different code tracking and different receiver parameters (e.g. correlator spacing and bandwidth). Thus, the code biases introduced by the satellite signal deformation might disagree. This leads to a differential satellite code bias between the ground system and the airborne receiver that will affect the position solution.

In the single-frequency case, the differential satellite code biases could be neglected because they are dominated by the larger ionospheric error. However, in the dual-frequency case, with the ionospheric error eliminated, they become relevant and need to be taken into account. Furthermore, the dual-frequency linear combinations are affected by the combination of the biases from the two frequencies.

The goal of this chapter is to investigate and assess the impact of the differential satellite code biases on the DFDC GBAS user. The first section provides an overview of the satellite code biases and the existing metrics that are currently being used to quantify them. The existing parameters are not applicable to GBAS because they do not take into account the local configurations of the receivers. Thus, this thesis uses the estimates of the satellite code biases from high gain antenna measurements. The methodology uses a joint estimation of analog and digital distortions and takes into account the receiver configuration allowing the calculation of the differential satellite code biases for different receiver configurations. The code tracking error biases and variances are derived based on receiver models described in the work presented in [118]. An overview of the methodology and the metrics used to analyze the differential satellite code biases are discussed in Section 6.3.

Using the DFDC receiver design space described in Section 6.4, a first assessment of the magnitude of the differential satellite code biases is shown in Section 6.5. Finally, first concepts to account for these errors in the integrity concept is discussed

in Section 6.6.

The main contributions in this chapter are:

- first analysis of the impact of the differential satellite code biases on the GBAS user taking into account different receiver configurations in terms of correlator spacing and bandwidth. This analysis is done based on measurements of the satellite code biases from the high gain antenna,
- proposal of different concepts for integrating the differential biases in the integrity concept.

6.2 Overview of the satellite-induced code biases

The satellite biases represent a systematic difference between the actual measurement and an idealized, bias-free observation, caused by hardware related delays as well as frequency response variations. The biases may be caused by "digital delays in the signal generator or receiver but also group delays in the analog part of the signal chain. Other than digital delays, that may be uniquely attributed to either the transmitter or the receiver and add up in the total bias, the same is not necessarily true for biases related to the analogue part of the signal chain. Since timing measurements inside a receiver are based on sensing the chips of the modulated ranging code with a specific correlator architecture, the pseudorange measurements depend on the actual chip shape as seen by the receiver. This, in turn, is determined by the frequency characteristics of the entire signal chain including filters and antennas onboard the satellites as well as antennas and filters on the receiving end." [129]. More details on the origin of the biases and how they affect the signal are given in [118] and [130].

Currently, these biases are mitigated by the use of external information. On one side, the control segment of the satellite navigation systems broadcast corrections for these biases within the navigation message. These parameters are treated as satellite clock corrections. This is because for each navigation system the estimation of the orbits and clocks are performed using the Ifree combination of code measurements from two frequencies (in order to remove the ionospheric errors).

For GPS, the Ifree combination of the P(Y) signals on L1 and L2 is used to compute the satellites clock and "single-frequency user and the dual-frequency L1 and L5 and L2 and L5 users must apply additional terms to the SV clock corrections equations". Thus, each GPS satellite broadcasts a parameter, referred as Time Group Delay parameter (noted as T_{gd}) which represents a scaled version of the satellite differential L1/L2 P(Y) code bias [129]. In addition, the newer GPS satellite generation provide additional correction terms, referred as Inter-Signal Corrections (ISCs) to account for the effect of inter-signal biases between L1 P(Y) and L2 P(Y), L1 P(Y) and L5 I5, and between L1 P(Y) and L5 Q5, respectively. By applying these corrections, the user can use the broadcast satellite correction consistently with single-frequency or other dual-frequency combinations. The application of the corrections is described in the Section 30.3.3.3.1.1 of the GPS ICD (GPS-IS-200K, [98]) for L1 C/A and

L2 and in the Section 20.3.3.3.1.2.1 of the GPS L5 ICD (GPS-IS-705F, [99]) for L5 signals.

In the case of Galileo, the clocks are estimated using the Ifree combination of the E1-E5a or E1-E5b signals. The users are provided with correction terms that represent scaled versions of the differential biases between the different signals. The corrections terms are referred as Broadcast Group Delays (BGDs). Each satellite provides the BGDs parameters for the E1-E5a combination and E1-E5b combination and they need to be applied by the single-frequency users. These terms are similar to the GPS T_{gd} and no additional ISCs are broadcast. This because the BGDs terms are available for the different combination of signals, allowing the calculation of the independent biases for the different signals. The application of the BGDs corrections is described in Section 5.1.5 of the Galileo ICD ([95]).

These values are based on measurements made during the satellite manufacturing and can be subsequently updated to reflect the actual on-orbit group delay differential [99].

In addition to the parameters broadcast by the navigation system, precise estimates of these values are also available from different analysis centers of the IGS for offline processing. These estimates are referred as Differential Code Biases (DCBs) and are currently estimated for almost all available satellite. The DCBs are derived from a global multi-GNSS network of receivers. In [131] and [132] the authors describe the methodology employed to determine these parameters. In the estimation process, the absolute biases are not available, only the differential biases between different signals. The typical notation used for a differential code bias for satellite s between frequency i and j is $\mathrm{DCB}^{s}_{i,j}$. In the estimation process, a separation between the satellite specific biases and the station specific biases is not clearly employed.

Even if the parameters broadcast in the navigation message are treated as satellite clock offsets, they are equivalent with the precise estimated DCBs. In [129], the authors provide an overview of the differential satellite code biases and describe the relation between the different available parameters. The relation between the T_{gd} parameters broadcast by GPS and the DCBs values estimated by IGS is described in [129] as

$$c \cdot T_{\mathrm{gd}} = -\frac{f_{\mathrm{L2}}^2}{f_{\mathrm{L1}}^2 - f_{\mathrm{L2}}^2} \cdot \mathrm{DCB}^{s}_{i,j} \tag{6.1}$$

As introduced before, the satellite code biases are induced by hardware delays in the digital and analog processing chain and are specific for each satellite signal. They are function of the receiver parameters such as correlator spacing and bandwidth. For GPS, the values of the correlator spacing and bandwidth to which the broadcast parameters (T_{gd} and ISCs) apply are clearly specified in the ICD document ([98] Section 30.3.3.3.1): "The broadcast group delay differential correction terms apply to the pseudorange measurements produced by an ideal correlation receiver with

a bandwidth of 20.46 MHz centered at the reference waveform nominal frequency whose phase is linear over that bandwidth using an exact replica of the reference waveform in an early-late discriminator having a correlator spacing of 97.75 nanoseconds. The group delay differential correction terms may not apply to pseudorange measurements produced by different methods due to potential distortion of the transmitted waveform". For Galileo, however no clear design space is provided in the ICD document. Thus, they do not take into account the actual configuration of the user receiver. Several studies have already shown that different receiver correlator spacing and bandwidth yield different code biases [97, 118, 130, 133].

This is especially an issue for GBAS, since the ground equipment and the airborne receiver can be different. In this case, the biases are not removed through differential corrections. Furthermore the biases are different for different satellites and different constellations, as analog and digital distortions for different payloads and between frequencies are non-identical. Therefore, they are not absorbed into the clock offset estimate generated in the position solution estimation. For GBAS, the use of the broadcast parameters in the navigation message is not relevant, because the ground reference receivers and airborne receiver would use the same correction parameters which will cancel out through the application of corrections. While the DCBs terms are derived for different receiver types with different configurations [133], not all combinations are taken into account to be applicable to GBAS.

In this work a different approach to investigate the effect of the satellite cpde biases in GBAS is taken. The estimates of the satellite code biases are based on measurements from a 30 m dish antenna available at DLR. An overview of the methodology and the metrics used are described in the next section.

6.3 Considerations and metrics used for the satellite code biases

The satellite code biases are derived based on measurements from the 30 m high gain antenna located at DLR's ground station in Weilheim, Germany. The signal processing and analysis based on the dish antenna has been established since 2005 at the Institute of Communications and Navigation in DLR and is routinely used for monitoring and performance analysis of the GNSS signals [134, 135]. The antenna has a beam width less than 0.5° and it thus allow the signals to be tracked with much higher gain than the normal GNSS antennas. Furthermore, the measurements are not affected by ground multipath errors.

The measurements from the high-gain antenna are used to derive estimates of the nominal distortions of the available satellites using a joint estimation of analog and digital distortions. The characterization of the nominal signal distortion and the models derived for them are described in detail in [118]. Based on these estimates of the analog and digital distortion, code tracking errors are derived using ideal receiver models as described in [118, 136].

The advantage of this approach is that it provides an estimate of satellite specific

biases (since the receiver is considered ideal and does not introduce additional errors) and it allows to generate the satellite code biases for different receiver configuration in terms of bandwidth and correlator spacing. Furthermore, it allows more flexibility in the investigation of the biases for different combinations and different configurations. The absolute code biases for each signal can be computed if accurate estimates of the satellite clocks are available as otherwise the signal deformations can not be isolated from the clock offsets. This synchronization is not needed when the differential biases between different receiver configurations or different signals are computed.

The measurements with the high-gain antenna, the methodology and the derivation of the absolute satellite code biases are performed by Mr. Steffen Thölert and are not an output of this work [137]. The analysis in this thesis uses these estimated as input and investigates the impact of the satellite code biases in GBAS without focusing on the methodology used to derive them.

Based on the absolute satellite code biases, the differential biases between different satellite signals (DCBs-like terms) can be computed and the values obtained should be comparable with the ones computed by IGS. However, the bias estimates derived using the high gain antenna measurements refer to the error introduced only by the satellites, while the broadcast parameters and the available DCBs estimates might contain also contributions of the receiver error. Future work will investigate and compare the differences on the estimated obtained from different methods.

As the derived biases are not directly equivalent with the existing values, the notations used in this chapter are as follows:

- $\mathrm{scb}^{s}_{rx,i}$ - refers to the absolute satellite code (pseudorange) bias for the satellite s on the frequency i using the receiver configuration rx (where the configuration refers to the correlator spacing and receiver bandwidth). This parameter can be related to the existing DCBs by

$$\mathrm{DCB}^{s}_{rx,i,j} = \mathrm{scb}^{s}_{rx,i} - \mathrm{scb}^{s}_{rx,j}, \tag{6.2}$$

  where $\mathrm{DCB}^{s}_{rx,i,j}$ represents the precise estimate of the DCBs for the satellite s between the signals on frequency i and j. Note that the scb term contains both the satellite instrumental errors and the code errors due to the satellite antenna which have been discussed in the previous chapters (e.g. B^{n}_{i} and ξ^{n}_{i} in Eq.2.1)

- $\Delta\mathrm{scb}^{s}_{(rx_1-rx_2),i}$ - refers to the differential satellite code (pseudorange) bias for the satellite s on the frequency i between the receiver configuration rx_1 and receiver configuration rx_2. The receiver configurations refer again to the correlator spacing and receiver bandwidth. This term is computed by subtracting the absolute biases obtained from the two configurations as

$$\Delta\mathrm{scb}^{s}_{(rx_1-rx_2),i} = \mathrm{scb}^{s}_{rx_1,i} - \mathrm{scb}^{s}_{rx_2,i}, \tag{6.3}$$

For DFDC GBAS, one of the possible processing modes is the Ifree mode. The Ifree pseudorange measurements are affected by a combination of the biases from

both frequencies used. Often in literature this term is referred as Inter-frequency bias (IFB) (Section 4.1.1 in [117]). In this chapter, the following two terms will be used to refer to the satellite biases present in the Ifree pseudoranges.

- $\mathrm{scb}^{s}_{rx,\mathrm{Ifree}_{i,j}}$ - represents the satellite code bias for satellite s and receiver configuration rx present in the Ifree combination of the pseudoranges of the frequencies i and j. As the ionospheric combination is a linear combination, this term can be computed from the single-frequency biases as

$$\mathrm{scb}^{s}_{rx,\mathrm{Ifree}_{i,j}} = \frac{f_i^2}{f_i^2 - f_j^2} \cdot \mathrm{scb}^{s}_{rx,i} - \frac{f_j^2}{f_i^2 - f_j^2} \cdot \mathrm{scb}^{s}_{rx,j} \tag{6.4}$$

- $\Delta\mathrm{scb}^{s}_{(rx_1-rx_2),\mathrm{Ifree}_{i,j}}$ - represents the differential satellite code bias for satellite s betwen the receiver configuration rx_1 and rx_2 present in the Ifree combination of the code measurements from frequencies i and j. This term can be computed from the single-frequency differential biases as:

$$\Delta\mathrm{scb}^{s}_{rx_1-rx_2,\mathrm{Ifree}_{i,j}} = \frac{f_i^2}{f_i^2 - f_j^2} \cdot \Delta\mathrm{scb}^{s}_{rx_1-rx_2,i} - \frac{f_j^2}{f_i^2 - f_j^2} \cdot \Delta\mathrm{scb}^{s}_{rx_1-rx_2,j} \tag{6.5}$$

The GBAS user is affected by the differential satellite code bias between the airborne receiver and the ground reference receivers. For simplicity, the GBAS differential bias is noted as $\Delta\mathrm{scb}^{s}_{\mathrm{GBAS}} = \mathrm{scb}^{s}_{\mathrm{gnd}} - \mathrm{scb}^{s}_{\mathrm{air}}$.

6.4 Receiver design space considered

This section provides an overview of the design space considered for the GBAS ground reference receivers and the airborne receiver.

In the current standards for GBAS two types of correlator are proposed to be used, the early-minus-late and double-delta correlators [18]. In this work the analysis is restricted to the first type, the early-minus-late correlator for both, the ground reference receiver and the airborne receiver. For the early-minus-late spacing and the bandwidth, the current standards allow a variety of receiver architectures. As introduced in Chapter 5, the airborne standards for GPS L1 (DO-253D [18]) define four regions for the airborne receivers for the correlator spacing and bandwidth values (illustrated in Figure 5.38). For the dual-frequency GBAS no final definition is made on the airborne design space. However, the current version of the SBAS DFDC standards specified in the ED-259 document ([92]) define restricted regions for L1/E1 and L5/E5a the receiver design space in terms of correlator spacing and bandwidth as shown in Figure 5.40. As the configuration of the avionics receiver does not change for different applications, the same design space is used for the GBAS avionics receiver in this work.

For the ground reference receiver, the design space is not clearly defined or restricted to specific values. Based on discussions with the GBAS ground manufacturers, a value of 0.1 chip for correlator spacing and 16 MHz for bandwidth are currently used in the single-frequency receivers (values also suggested in the existing standards for the single-frequency ground stations [32]). This value is used as reference for the initial studies. For the values for the L5 band, it is assumed that the bandwidth is the same and the correlator spacing is 10 times higher than the ones on the L1 band (in chips). Table 6.1 summarizes the regions that are considered in this work and the corresponding values for the correlator spacing and bandwidth for the airborne receiver and the GBAS ground receivers. This setup will be used in the evaluations presented in next section.

		Airborne receiver		**Ground ref. receivers**	
Region	**Parameter**	**L1(E1)**	**L5(E5a)**	**L1(E1)**	**L5(E5a)**
Single freq. region 1	Correlator spacing [chips]	0.045-0.21	-	0.1	-
	Bandwidth [MHz]	4-7	-	16	-
Single freq. region 2	Correlator spacing [chips]	0.045-0.21	-	0.1	-
	Bandwidth [MHz]	7-16	-	16	-
Single freq. region 3	Correlator spacing [chips]	0.045-0.12	-	0.1	-
	Bandwidth [MHz]	16-20	-	16	-
Single freq. region 4	Correlator spacing [chips]	0.08-0.12	-	0.1	-
	Bandwidth [MHz]	20-24	-	16	-
Dual freq. region	Correlator spacing [chips]	0.08-0.1	0.8-1	0.1	1
	Bandwidth [MHz]	12-24	12-24	16	16

Table 6.1: Design spaces considered for correlator-spacing and bandwidth for airborne receiver and ground reference receiver

6.5 Initial results for the differential satellite code biases

After introducing the satellite code biases and the receiver design space, this section shows exemplary results of the differential satellite code biases for three GPS Block IIF satellites. The differential biases are computed based on the fixed configuration for the ground receiver (16 MHz bandwidth and 0.1 correlator spacing for L1 and 1 chip correlator spacing for L5) for the different regions introduced in the previous section for the airborne receiver design space.

Figure 6.1 shows the obtained differential satellite code biases for the three GPS satellite (PRN 9, 24 and 27) for the four defined regions for the receiver design space in the current single-frequency standards. From these results, it can be observed that the differential code biases can take negative or positive values for the different configuration of the airborne receiver. For two of the satellites, the error varies between -10 cm to 10 cm (PRN 9 and 27). For PRN 24, which is one of the first launched Block IIF satellite, the differential errors reach values of 60 cm. As already mentioned in the previous sections, the biases are dependent on the satellite hardware and thus are different for each satellite.

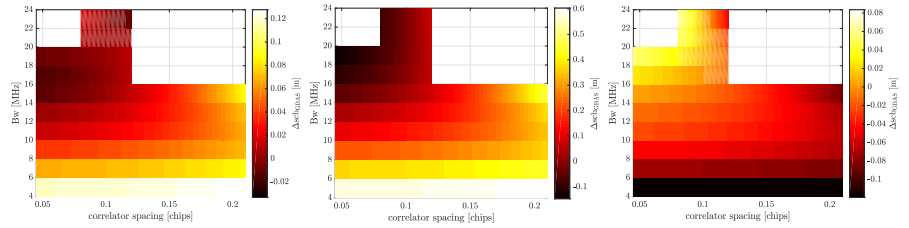
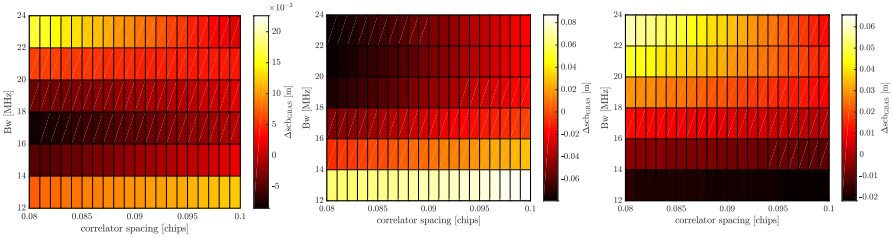


Figure 6.1: Differential code bias using a ground receiver with the configuration of 0.1 chips for L1 and 16 MHz bandwidth and the airborne receiver taking the values from the dingle frequency design space for GPS PRN 9 (a),GPS PRN 24 (b) and GPS PRN 27 (c)

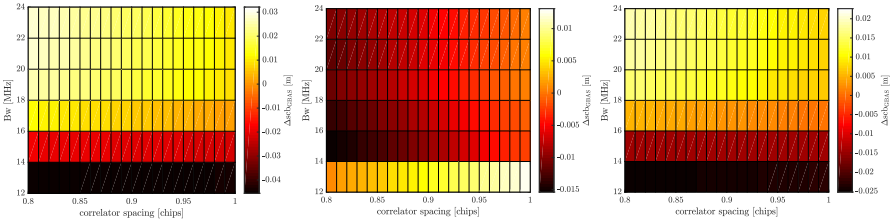
In a future DFDC GBAS, however, the design space for the airborne receiver is narrower compared to the single-frequency one (see Table 6.1 for dual-frequency region). In a similar manner with the figure above, Figure 6.2 and 6.3 present the differential satellite code biases obtained for the DFDC design space chosen for the avionics receiver for the L1 and L5 signal, respectively. In this case, the differential errors for L1 signal are in the order of centimeters, varying from a minimum of -6 cm to a maximum of 8 cm for PRN 24. For L5, the errors look somewhat smaller, and they vary from -4 cm to 3 cm. It is also interesting to notice that for the L5 signal, a different satellite (PRN 9) shows the largest differential code errors.

Figure 6.4 shows the differential satellite code bias obtained for dual-frequency design space for the Ifree combination. As already mentioned, in the Ifree case it is assumed that the receiver has the same bandwidth for both frequency bands and the correlator spacing on L5 (in chips) is 10 times larger than the correlator spacing on



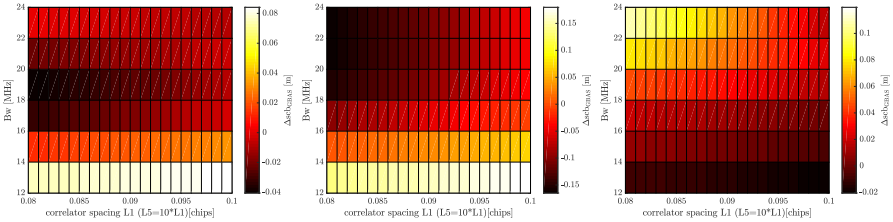
(a) PRN 9 **(b)** PRN 24 **(c)** PRN27

Figure 6.2: Differential satellite code bias on L1 using a ground receiver with the configuration of 0.1 chips and 16 MHz bandwidth and the airborne receiver taking the values from the dual-frequency design space for GPS PRN 9 (a),GPS PRN 24 (b) and GPS PRN 27 (c)



(a) PRN 9 **(b)** PRN 24 **(c)** PRN 27

Figure 6.3: Differential satellite code bias on L5 using a ground receiver with the configuration of 1 chips for L5 and 16 MHz bandwidth and the airborne receiver taking the values from the dual-frequency design space for GPS PRN 9 (a),GPS PRN 24 (b) and GPS PRN 27 (c)



(a) PRN 9 **(b)** PRN 24 **(c)** PRN 27

Figure 6.4: Differential satellite code bias for the Ifree combination using a ground receiver with the configuration of 0.1 chips for L1 and 1 chips for L5 and 16 MHz bandwidth and the airborne receiver taking the values from the dual-frequency design space for GPS PRN 9 (a),GPS PRN 24 (b) and GPS PRN 27 (c). The x-axis refers to the correlator spacing values for L1 with L5 being 10 times larger (in chips)

L1 (in chips). This configuration is used by most of the hardware receiver. The Ifree biases are a combination of the biases from the two frequency bands, and thus, the total code errors get larger with values ranging from -15 cm to 15 cm.

These initial results suggest that the differential satellite code biases affecting the DFDC GBAS user are not negligible and need to be taken into account. This is especially important for the dual-frequency Ifree solution for which the single-frequency biases are combined. Even in the single-frequency case the errors in each satellite project can project into decimeters error in the position solution [137]. In single-frequency, these biases are dominated by the large ionospheric error, thus they could be ignored. However, for dual-frequency applications for which the dominant ionospheric error is removed, the satellite code biases become relevant. Several methods to account for these biases in GBAS concept are proposed in the following sections.

6.6 Inclusion of satellite-biases in GBAS

This section discusses different concepts that are proposed for the inclusion of the satellite code biases in the GBAS implementation and integrity concept. The first concept discussed in the next section proposes the removal of the satellite code biases from the ground and airborne measurements. A residual uncertainty associated with this process of bias removal is then included in the protection level for integrity assessments.

While this technique can provide lower errors, it might not be practically applicable. Thus, a new method that relies on the derivation of the maximum range error induced by the satellite biases is presented in Section 6.6.2.

6.6.1 Method 1: Calibration for the satellite code biases in ground and airborne system

A first method of accounting for the satellite biases was proposed in [85]. This method suggests the correction of the absolute biases from the code measurements of the ground reference receiver and the airborne receiver for each frequency. Using the measurements and the methods described in [118, 136], the absolute code biases resulting from the nominal distortions can be derived for each signal up to a residual uncertainty. This residual uncertainty is given by the accuracy of the measurements and of the models applied in the estimation process. This uncertainty can be assessed in detail starting from the derivation of measurements noise up the estimated biases as described in [85].

The estimation of the absolute biases for each frequency needs however an accurate estimate of the satellite clock. Without this information it is not possible to distinguish between the satellite clock error and the satellite signal deformation (which yields the satellite code biases). Assuming that the absolute biases and the uncertainty of the estimation are available, the proposed concept of the biases removal and residual bias incorporation described in [85] is composed of the following steps:

1. Estimation of the absolute biases for each satellite and frequency for the design space defined in the previous section($\text{scb}^{s}_{rx_m,i,j}$, with rx_m representing the configuration of the receiver in terms of correlator spacing and bandwidth). A table containing these biases as a function of the receiver parameters can be made available to the ground and airborne systems. A process of guaranteeing the use of the same set of biases on the ground and in the airborne receivers (e.g. inclusion in the regular navigation data base update cycle and a consistency check between air and ground subsystems) would have to be developed and established,

2. Independent removal of code biases resulting from nominal signal deformations from ground and airborne measurements. As both ground station and avionics receiver know the details of the receivers used for processing, these biases can be estimated independently. If the biases for each frequency are corrected, the biases from the Ifree measurements are also removed,

3. Characterization of the residual uncertainty associated with each of the bias removals. As described in [85], this residual uncertainty can characterized and overbounded by a Gaussian distribution. First, the residual uncertainty associated with the bias resulting from nominal signal deformation on each frequency is characterized. The Ifree bias uncertainty is computed from the combination of the two uncertainties. After the bias removal process, the residual uncertainties should be included in $\sigma_{\text{pr_gnd}}$ (for the ground) and $\sigma_{\text{pr_air}}$ (for the airborne).

While this method would remove the impact of the satellite biases from the code measurements and would yield lower position errors, the process implies that each time a new satellite is launched its performance would have to be measured and this information updated in the ground and airborne equipment. This solution might not be practical, especially for the airborne equipment. Thus, different methods to integrate these biases in the integrity concept are proposed in the next section.

6.6.2 Method 2: Derivation of the maximum range error

If the satellite code biases can not be calibrated, different solution to account for the biases is to assess the maximum differential range error than can be obtained and integrated in the integrity concept.

This approach relies on the ground system to provide the differential satellite code bias information to the GBAS user. Knowing the configuration of the ground reference receiver and the airborne receiver design space, the ground system can compute the maximum differential code error that could occur for the entire airborne receiver design space.

As discussed in Chapter 3, using the existing VDB message format it will not be possible to broadcast additional values for each satellite. A solution to overcome this limitation is to broadcast the maximum differential code satellite bias over all satellites from each constellation. This approach is conservative and assumes that

each satellite within the constellation is affected by this maximum range error, but requires less broadcast parameters.

The process of deriving the broadcast parameters for the satellite code biases and their inclusion in the protection level is described as follows:

1. Estimation of the satellite code biases for each satellite and each frequency for the ground configuration and airborne design space.

   Note that as the differential satellite code biases are used, no accurate estimation of the satellite clock or synchronization between frequencies is needed (which was the case for the first method),

2. Computation of the differential satellite code biases for the entire airborne design space using known ground configuration.

   This step is performed for each satellite usable for which measurements are available. The outputs of this step will be similar to the results shown in the previous section, namely the differential satellite code biases for each satellite s, frequency i and for each receiver configuration within the airborne design space (rx), noted as $\Delta\text{scb}_{\text{GBAS}}{}^{s}_{rx,i}$,

3. Computation of a maximum range error for each satellite.

   Because the differential code biases can have different signs, the maximum values are calculated on the absolute values of the differential biases. The maximum GBAS differential satellite code bias for satellite s and frequency i, $\Delta\text{scb}_{\text{GBAS}}{}^{s}_{\text{max},i}$, is computed over the entire airborne receiver design space

$$\Delta\text{scb}_{\text{GBAS}}{}^{s}_{\text{max},i} = \max\Big(\underbrace{\left|\Delta\text{scb}_{\text{GBAS}}{}^{s}_{rx,i}\right|}_{rx\in\text{Config}_{\text{airborne design}}} \Big), \tag{6.6}$$

4. Computation of broadcast parameter as the maximum differential code bias over all satellites from one constellation.
   When performing the airborne position solution in the airborne receiver, the common part of the biases does not affect the position estimate, but projects into the receiver clock. Thus, before broadcasting the maximum differential bias, the ground system needs to take this into account. Because the ground station does not have any knowledge on the actual set of satellites used by the airborne receiver, it needs to consider all subsets that could reasonably be used by the airborne receiver. A common approach is to consider that up to two satellites per constellation for which corrections are provided are not used in the airborne position solution. Thus, the mean removal process has to be performed over all these subsets to determine the maximum differential errors that will be broadcast. The maximum derived value that is broadcast for each constellaton c and frequency i is noted as $\Delta\text{scb}_{\text{GBAS,brdg}_{c,i}}$.

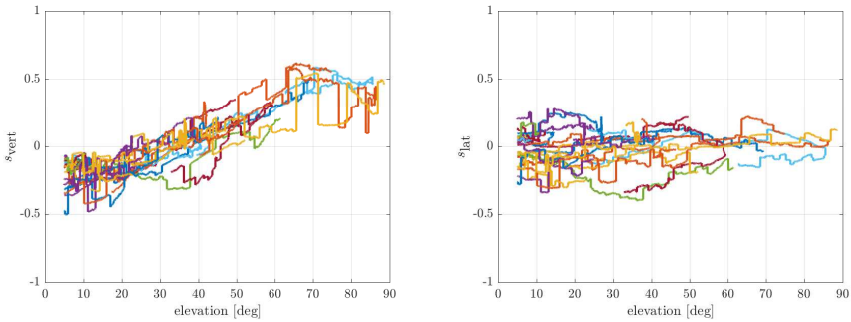
5. Integration of the error in the protection levels
   With the information of the maximum differential range errors broadcast by

the ground system, the airborne receiver can account for them in the protection levels. A range bias projects into the position solutions with the weight of the $\boldsymbol{S}$-matrix terms. Thus, the additional term to account for the satellite code biases in the protection levels can be described as:

$$\begin{cases} \Delta VPL_{\mathrm{H_0}} = \sum_{c\in\text{Constellations}} \sum_{s=1}^{N} |s_{\text{apr_vert}_i^s}| \cdot \left|\Delta \text{scb}_{\text{GBAS,brdg}_{c,i}}\right| \\ \Delta LPL_{\mathrm{H_0}} = \sum_{c\in\text{Constellations}} \sum_{s=1}^{N} |s_{\text{apr_lat}_i^s}| \cdot \left|\Delta \text{scb}_{\text{GBAS,brdg}_{c,i}}\right| \end{cases} \tag{6.7}$$

Note that the absolute values of the $\boldsymbol{S}$-matrix terms are considered.

The method described above is, however, conservative and assumes the maximum absolute bias on each satellite. As shown in Figures 6.1 to 6.4 the biases can have positive and negative values. Furthermore, the s_{ii} terms can also be positive and negative. Figure 6.5 illustrates the derived $s_{\text{apr_vert}}$ values and $s_{\text{apr_lat}}$ values during one flight test for complete GPS-Galileo constellation simulated. It can be observed, that especially for the $s_{\text{apr_vert}}$ values there is a clear trend: the low elevation satellites have negative values while the high elevation satellites have positive values. For the lateral case, however, no clear dependency on the satellite elevation is observed.



(a) $s_{\text{apr_vert}}$ values function of satellite elevation **(b)** $s_{\text{apr_lat}}$ values function of satellite elevation

Figure 6.5: $s_{\text{apr_vert}}$ values (a) and $s_{\text{apr_lat}}$ values obtained during a flight tests for dual-constellation GPS Galileo solution

Thus, a less conservative assumption for the vertical domain would be to take the sign of the bias and the $s_{\text{apr_vert}}$-values into account.

For the vertical position error, the worst case would then be that all biases with one sign are projected into the position solution with $s_{\text{apr_vert}}$-values with the same sign among them (positive or negative). In order for the airborne receiver to be able to compute this new term taking the sign into account, the ground system needs to broadcast a minimum and a maximum of the differential satellite code biases. The maximum and the minimum values are computed as explained in Steps 3 and 4 above with the maximum being computed over all positive values (referred as $\Delta \text{scb}_{\text{GBAS,brdg,max}_{c,i}}$) and the minimum bias (referred as $\Delta \text{scb}_{\text{GBAS,brdg,min}_{c,i}}$) over

all negative values for each constellation. Thus, the additional term to the vertical protection levels that takes the sign into account can be described as

$$\Delta VPL_{\mathrm{H_0}} = \sum_{c\in\text{Constellations}} \max\Bigg(\sum_{\substack{s_1=1 \\ s_{\text{apr_vert}}<0}}^{N_1} {s_{\text{apr_vert}}}_i^{s_1} \cdot \Delta\text{scb}_{\text{GBAS,brdg,min}_i} + \sum_{\substack{s_2=1 \\ s_{\text{apr_vert}}>=0}}^{N_2} {s_{\text{apr_vert}}}_i^{s_2} \cdot \Delta\text{scb}_{\text{GBAS,brdg,max}_{c,i}}; \left| \sum_{\substack{s_1=1 \\ s_{\text{apr_vert}}<0}}^{N_1} {s_{\text{apr_vert}}}_i^{s_1} \cdot \Delta\text{scb}_{\text{GBAS,brdg,max}_{c,i}} + \sum_{\substack{s_2=1 \\ s_{\text{apr_vert}}>=0}}^{N_2} {s_{\text{apr_vert}}}_i^{s_2} \cdot \Delta\text{scb}_{\text{GBAS,brdg,min}_{c,i}} \right| \Bigg) \tag{6.8}$$

For the lateral position errors, assessing the worst case scenario when the signs are taken into account is not straight forward. This because the lateral position error is computed as the root sum square of the east and north error. However, it can be assumed that the difference between the values obtained from the worst case and the values obtained when the signs are taken into account is rather small. This because the lateral position errors are typically smaller than the vertical ones and the $s_{\text{apr_lat}}$ values do not show a strong variation in the sign.

6.6.2.1 Initial evaluation

The differential satellite code biases from the three satellites discussed in Section 6.5 are used for an initial assessment of the values that need to be added to the protection levels to account for these biases.

The $s_{\text{apr_vert}}$-values and the $s_{\text{apr_lat}}$ values were computed based on the trajectory from a flight test conducted around Braunschweig airport. For this evaluation, complete dual-frequency GPS and Galileo constellation with 32 and 27 satellite, respectively were simulated. For both constellations, the maximum and the minimum values derived from the three satellites are calculated. While this assumption might not be valid to cover the worst case from both constellations, it gives a first idea of the magnitude of the error term that is to be added to account for the differential satellite code biases.

Figure 6.6 shows the additional term for the vertical protection levels ($\Delta VPL_{\mathrm{H_0}}$)for the dual constellation L1/E1 processing (black lines), dual constellation L5/E5a processing (green lines) and for the Ifree L1/E1-L5/E5a processing (red lines) over the period of the flight test. The solid line represent the worst case scenario when the maximum of the absolute values is taken and the dashed lines show the obtained values when the signs are taken into account (Eq. (6.8)).

The smallest values are obtained for the L5/E5a solution for which the $\Delta VPL_{\mathrm{H_0}}$ stays around 5cm. For this case also the difference between the two approaches is rather small. This is because the differential code biases and, thus, their variation are much smaller for the three considered satellites. For the L1/E1 case the values of the $\Delta VPL_{\mathrm{H_0}}$ increase to values between 10-15 cm and the difference between the

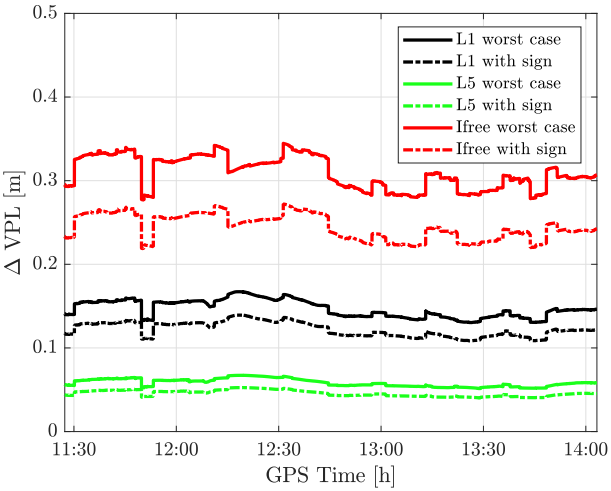


Figure 6.6: Simulated ΔVPL_{H_0} term (to be added to the nominal VPL_{H_0}) for L1/E1, L5/E5a and Ifree solutions. The solid lines represent the worst case and the dashed lines the case when the sign is taken into account

two methods is more pronounced reaching a maximum of 5 cm. The large differential biases on the Ifree combination yield also to large values to be added to the protection levels. The values vary between 25 - 35 cm and the difference between the two approaches is around 10 cm.

In the lateral case, shown in Figure 6.7, the values to be added to the protection levels (ΔLPL_{H_0}) are much smaller than the ones for the vertical case for all three solutions and they reach a maximum of 10 cm for the L1/E1 solution and 20 cm for the Ifree solution.

Even if the method of broadcasting the maximum value over all satellites is conservative, the initial results show that the total error to be added to the protection levels is below 40 cm. For a complete dual constellation scenario there is sufficient margin between the protection levels and the minimum alert limits and thus, these values should not impact the availability of the system.

6.6.2.2 Further improvements of the proposed method

The method described above proposes the broadcast of a maximum and a minimum differential bias calculated over all satellites. While the initial results derived show that the additional terms to be added to the protection levels are rather small, they might increase when analyzing the biases from all satellites. Furthermore, the method requires the ground system to compute a maximum value over all subsets of N to $N-2$ satellites (with N being the number of satellites in view at the ground station) to derive the worst case from all the satellite geometries the airborne receiver might

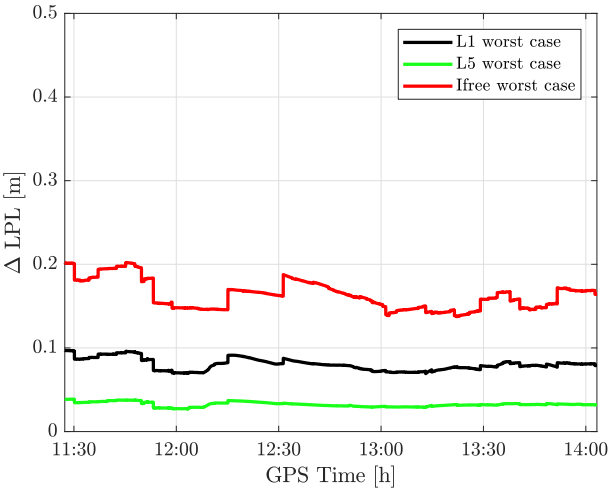


Figure 6.7: Simulated $\Delta LPL_{\mathrm{H_0}}$ term (to be added to the nominal $LPL_{\mathrm{H_0}}$) for L1/E1, L5/E5a and Ifree solutions

use.

An improvement to the suggested proposal is to broadcast individual values for each satellite. In this way, the airborne receiver can remove the mean over the actual set of satellites that is being used. The calculation of the additional term for the protection levels is done in a similar manner as described in Eq.(6.7) by replacing the maximum value (over all satellites) with the individual values per satellite. As shown in the result above, the lowest vertical errors are achieved when the sign of the biases and the $s_{\mathrm{apr_vert}}$-values are taken into account. This requires that the ground system broadcasts the maximum and the minimum differential satellite code bias for each satellite for which corrections are available.

This approach would yield lower protection levels, but will require more space in the VDB message. To decide the final broadcast parameters, further trade off studies of the performance improvement versus the VDB space required are needed.

7 Assessment of different processing modes

The previous chapters discussed the changes to the residual error when using the E1/E5a signals from the Galileo satellites and GPS L5 satellites. The goal of this chapter is to assess the nominal performance of the different candidate processing modes for DFDC GBAS.

Based on the derived ground and airborne multipath models in Chapter 4 and Chapter 5, the nominal performance of the different processing modes for a DFDC GBAS is evaluated. This study contributes to the effort of defining a DFDC GBAS concept. The selected processing modes considered for analysis are based on the discussion from Chapter 3 and include:

- single-frequency dual-constellation L1/E1 mode based on 100 seconds smoothing,
- single-frequency dual-constellation L1/E1 mode based on 30 seconds smoothing,
- single-frequency dual-constellation L5/E5a mode based on 100 seconds smoothing,
- single-frequency dual-constellation L5/E5a mode based on 30 seconds smoothing,
- dual-frequency dual-constellation Ifree mode based on 100 seconds smoothing, and
- dual-frequency dual-constellation Ifree mode based on 30 seconds smoothed.

The discussions in Chapter 3 indicated that the 100 seconds smoothing time is preferred for the L5/E5a processing modes for enabling the airborne receiver to form the 100 seconds smoothed Ifree solution. However, in this study the 30 seconds smoothing time is considered as well to assess the performance of the processing modes based on the shorter smoothing times constant. The evaluations are based on measurements collected during one flight trial that was conducted on 2nd February 2018 on DLR's A320 aircraft. The flight lasted for 2.5 hours. A total of 5 approaches with subsequent go-around to runway 08 of the airport of Braunschweig and one final landing were conducted. The ground track of the flight is shown in Figure 7.1 where the color represents the aircraft altitude above ground.

7.1 Evaluation of position errors in flight test

The performance evaluation starts with the analysis of the actual navigation error for the L1/E1 dual-constellation based on 100 seconds smoothing time constant,

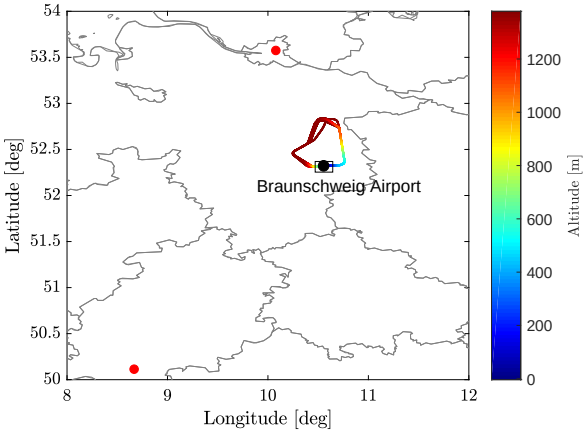


Figure 7.1: Ground track of the flight considered in evaluations

L1/E1 dual-constellation based on 30 seconds smoothing time constant, L5/E5a dual-constellation based on 100 and 30 seconds smoothing time constants, and the Ifree dual-constellation based on 100 and 30 seconds smoothing time constant solutions. The computation of the navigation position error was performed using as reference a post-processed dual-frequency carrier phase position solution obtained from Novatel's GrafNav software in a combined forward-backward smoothing mode.

Figure 7.2 shows a comparison of the north-east errors for all processing modes. The largest error occur on the Ifree solution when using both 100 and 30 smoothing time constants. This behavior is expected due to the larger noise and multipath on the measurements. The difference in the position errors between the two smoothing time constants is noticeable, which can be explained by the reduction of the dominant time-wise uncorrelated multipath and noise errors with the increase of the smoothing time constant. For the L1/E1 position solutions, the errors get smaller. Also in this case, the errors computed based on the 100 seconds smoothing time constant are smaller compared to the 30 seconds smoothed ones. However, the difference between the two smoothing time constant is smaller than in the Ifree case. The smallest position errors are achieved with the L5/E5a solution for which also the difference between the two smoothing time constant is very small. This can be attributed to the lower noise and multipath errors in the raw measurements on which the effect of a longer smoothing time constant is not pronounced.

A similar behavior with the east-north errors can be observed in the vertical errors shown in Figure 7.3. The Ifree vertical errors go up to 5 m for 30 seconds smoothing time constant and 3 m for 100 seconds smoothing time constant, the L1/E1 errors reach up to 2 m while the L5/E5a errors stay below 1 m during all times. The difference between the errors based on the two smoothing time constants is also in

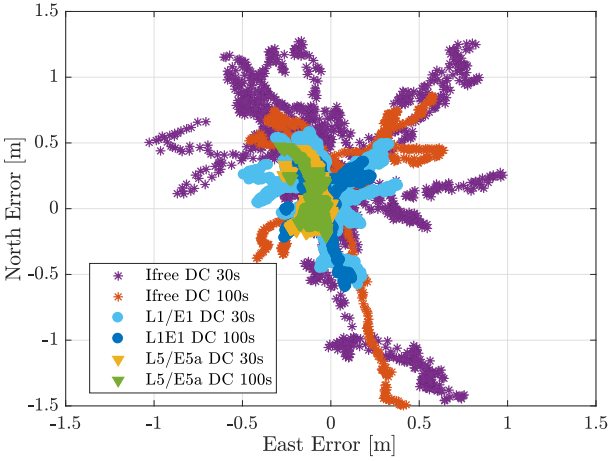


Figure 7.2: East-north errors for GPS/Galileo 30 seconds, Ifree GPS/Galileo 100 seconds, L1/E1 GPS/Galileo 30 seconds, L1/E1 GPS/Galileo 100 seconds, L5/E5a GPS/Galileo 30 seconds, L5/E5a GPS/Galileo 100 seconds

this case more pronounced in the Ifree and L1/E1 errors but very small for the L5/E5a solutions.

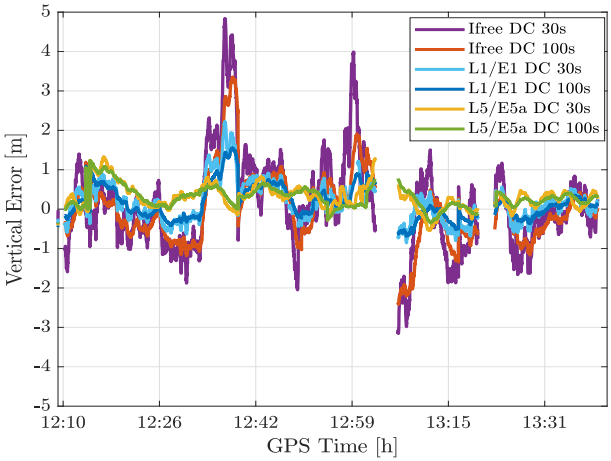


Figure 7.3: Vertical error versus time for Ifree GPS/Galileo 30 seconds, Ifree GPS/Galileo 100 seconds, L1/E1 GPS/Galileo 30 seconds, L1/E1 GPS/Galileo 100 seconds, L5/E5a GPS/Galileo 30 seconds, L5/E5a GPS/Galileo 100 seconds

For all the processing modes, only the GPS Block IIF and the available Galileo satellites were used. During the flights tests, several maneuvers with steep turns were performed, leading to a quite frequent loss of lock of several satellite signals. Figure 7.4

shows the number of usable dual-frequency GPS Block IIF and Galileo satellites. It can be observed that the number of used satellites (in all position solutions) is around 6-8 and thus, the position errors derived might be somehow worse than what is to be expected from two complete constellations. However, they give a good indication of the performance of the different processing modes and can be considered to be a conservative assessment of the performance of a future operational DFDC GBAS. Around 13:00h a complete loss of the navigation solution occurred yielding to a re-initialization of all the smoothing filter and therefore the number of satellites used goes to 0 for a short period.

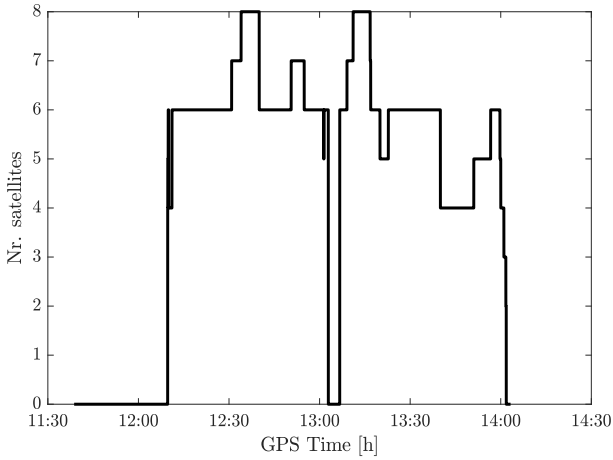


Figure 7.4: Total number of GPS Block IIF and Galileo satellites used in GBAS position error evaluation

7.2 Assessment of nominal protection levels

After discussing the navigation errors, this section shows the protection level performance under the nominal case (H_0) for the same processing modes. As explained in Chapter 2, the protection levels are conservative bounds of the actual errors. Only the vertical protection levels will be used to assess the performance of different processing modes because the vertical requirements are more stringent: the vertical errors are typically larger than the lateral ones in GNSS while the vertical alert limits are smaller (10 km close to the GBAS reference point) at the same time. The protection levels for the different processing modes are calculated as described in Eq.(2.20) with the changes in the error models for each processing modes discussed in Section 3.6.3.

The protection levels are affected by two factors: geometry and the residual error bounds. As mentioned above, the number of satellites usable during the flight tests was rather low and not representative for the geometry that is to be expected from a future complete dual-constellation scenario. This would yield to large unrealistic

protection levels. Thus, for the calculation of the protection levels, complete dual-frequency GPS and Galileo constellation with 32 and 27 satellites, respectively are simulated. The position of the aircraft and the speed are used from the actual flight data. With two complete constellation, the number of satellites available are around 20 when an elevation mask of 5° is chosen. A detailed study of the impact of the geometry on the protection levels is provided in [84], considering different assumptions and different satellite elevations masks. One important aspect to note is that the protection levels derived from the simulated full constellations are not expected to bound the above derived position errors due to an improved geometry.

A second contributor to the protection levels is the residual error bound. Section 3.6.3 presented in detail the changes that have to be considered for the error bounds for each processing mode. The following errors models will be considered in the evaluations presented next:

- Models for ground multipath and receiver noise ($\sigma_{\text{pr_gnd}}$)
  The measurements-based models derived in Chapter 4 are used for $\sigma_{\text{pr_gnd}}$ in the evaluation. For single-frequency dual-constellation L1/E1 and L5/E5a processing modes, the curves shown in Figures 4.14 to Figure 4.16 derived for 100 and 30 seconds smoothing times constant will be considered.

  In Chapter 4, ground multipath models for the dual-frequency Ifree combination 100 seconds and 30 seconds smoothing time constants were derived as well using measurements from the DLR GBAS test bed. The derived models for GPS and Galileo are shown in Figure 4.20 and are used for $\sigma_{\text{pr_gnd}}$ in the Ifree processing modes,

- Models for the airborne multipath and residual noise ($\sigma_{\text{pr_air}}$)
  For the airborne multipath, the models developed in Chapter 5 are used in the simulations. First, an evaluation based on the models derived from DLR's Airbus A320 (referred as Advanced Techonology Research Aircraft (ATRA)) is shown. Figure 5.28 and 5.29 show the multipath error models derived for single-frequency L1/E1 and L5/E5a processing modes and for the dual-frequency Ifree based on 100 seconds smoothing time constant for GPS and Galileo, respectively. The error models based on 30 seconds smoothing times constant for all processing modes for GPS and Galileo are shown in Figure 5.30 and Figure 5.31, respectively.

  As already discussed in Chapter 5, the airborne multipath models derived from the DLR experimental installation are expected to be conservative due the antenna used and its installation. This was also confirmed by the initial results derived from the measurements collected within DUFMAN project using representative DFDC hardware (see Section 5.12). In order to assess the impact of the different airborne multipath models, an evaluation of the vertical protection levels using the DUFMAN models is performed. This comparison is restricted to 100 seconds smoothing time constant. Note again that, as discussed in Chapter 5, the models derived from both ATRA and within DUFMAN project do

not contain the effect of the antenna-induced errors due to the group delay variations. Further work will investigate how to account for these errors in the integrity budget and they are not considered in this thesis. One of the differences between the models derived from ATRA and the ones derived within DUFMAN is that in the models derived within DUFMAN the receiver noise was removed from the final curves. A value of 0.2 m was assumed for the standard deviation of the receiver noise. This value is used in the simulations together with the DUFMAN multipath models to compute the $\sigma_{\text{pr_air}}$ as described in Eq.(2.31).

- Model for the residual ionospheric error
  As the ionospheric error is frequency dependent, the model of the residual ionospheric error will be different for each processing mode. The changes that need to be done are discussed in Section 3.6.3.2. In order to assess the impact of the different ionospheric threat models (represented by σ_{vig}), the threat model for CONUS ($\sigma_{\text{vig}} = 4$mm/km) and for Germany ($\sigma_{\text{vig}} = 2.07$mm/km) will be considered.

- Model for tropospheric residual error
  As discussed in Section 3.6.3.1, the tropospheric residual error does not change between the different processing modes and the models described in Eq. (2.33) are used for all solutions.

- Satellite code biases
  In this experimental flight test, the same type of receiver with the same configuration was used for the ground reference receivers and on the aircraft. Thus, the satellite code biases cancel out and no additional term is considered.

Figure 7.5 shows the vertical protection levels during the flight test for all processing modes: the L1/E1 based on 100 seconds smoothing time constant with dark blue curve, L1/E1 based on 30 seconds smoothing time constant with light blue curve, L5/E5a based on 100 seconds smoothing time constant with green line, L5/E5a using 30 seconds smoothing with yellow line, Ifree 100 seconds smoothing with red line and Ifree using 30 seconds smoothing with purple line. The gray dashed line shows the distance-dependent vertical alert limit which decreases from 43.35 m to a value of 10 m on the final approach segment close to the runway threshold. The protection levels were computed using the ATRA airborne multipath models and the CONUS σ_{vig} of 4 mm/km. Note that the L1/E1 protection levels based on 30 seconds smoothing are computed based on 100 seconds smoothing time constant (as in the GAST-D case). As already mentioned in Chapter 2, in GAST-D, the bounding is done based on the parameters for 100 seconds smoothing time constant and the difference between the 30 seconds and 100 seconds smoothing time constants is accounted in the D_{v} terms for the vertical error. The D_{v} term depends on the residual airborne noise and multipath. Thus, in order to account for it, for the 30 seconds protection levels for all the processing modes, the $\sigma_{\text{pr_air}}$ parameters derived based on the 30 seconds smoothing time constant were used.

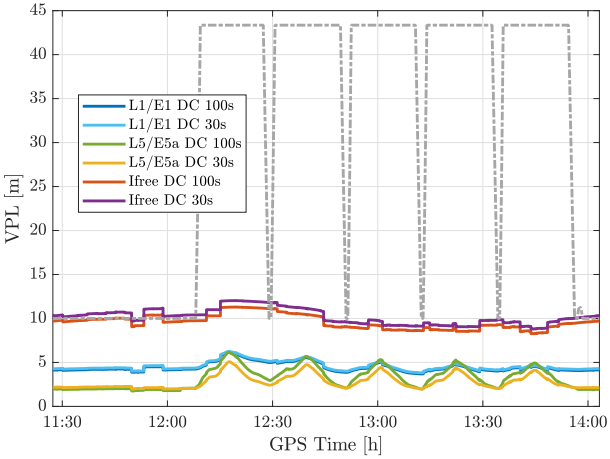


Figure 7.5: VPL versus time for L1/E1 dual-constellation 100 seconds smoothing (dark blue curve) and 30 seconds smoothing (light blue curve), L5/E5a dual-constellation 100 seconds smoothing (green curve) and 30 seconds smoothing (yellow curve) and Ifree 100 seconds smoothing (red curve) and 30 seconds smoothing (purple curve)

Looking at the VPL curves in Figure 7.5, different behavior over time can be observed. For some periods, the behavior is also somewhat different than the one observed in the evaluation of the position errors.

When the aircraft is close to the runway and the VAL value is 10 m, the Ifree VPL values are very close to the limit, exceeding it at some points (especially the protection levels based 30 seconds smoothing). During these periods, the L5/E5a values are lower than the L1/E1 ones for both smoothing time constants. However, when the aircraft flies far away from the ground reference station (and the VAL values increase), the VPL values for both L5/E5a and L1/E1 start increasing. The increase on the L5/E5a VPLs is much steeper, and it reaches (slightly exceeding) the L1/E1 VPLs. The increase in the single-frequency protection levels is due to the increase of the σ_{iono} that gets larger with the distance and the aircraft speed (see Eq.(2.35)). Due to the larger ionospheric error on L5/E5a band and therefore the inflated σ_{iono} (by a factor of 1.8 compared to L1/E1), the vertical protection levels for the single-frequency dual-constellation L5/E5a solution increase much faster than the single-frequency L1/E1 ones. This is visible in the slope of the curves at around 12:15, 12:45, 13, 13:15, 13:45. During this flight, the aircraft flew several approaches around Braunschweig airport and these times correspond to the periods when the aircraft is further away than 50 km from the reference station and flies with a speed above 100 m/s. The distance to the GBAS reference point and the aircraft speed are shown in Figure 7.6. The difference between the L5/E5a based on 30 seconds and 100 seconds smoothing time constant comes for the $2 \cdot \tau \cdot v_{\text{air}}$ term added to the σ_{iono} values (see Eq.(2.35)) with τ being the smoothing time constant. The speed

dependence yields to a faster increase of the solution based on a larger smoothing time constant. In L1/E1 case, the GAST-C and GAST-D concept was used and the σ_{iono} is computed for both cases for $\tau = 100$ seconds. Thus, the difference between the solution computed with the two smoothing time constant is much lower.

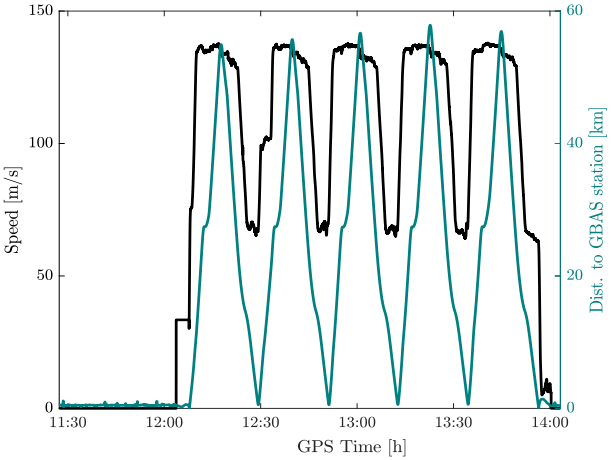


Figure 7.6: Aircraft speed and distance to the GBAS reference station during the flight used in evaluation

In order to better illustrate the distance dependency of the protection levels, Figure 7.7 shows the simulated vertical protection levels as a function of the distance to the GBAS reference point. The same vertical protection levels as the ones discussed above are shown, but for only one approach and the maximum distance was set to 43 km which covers the limit of the GBAS service volume. Here it can be observed that the Ifree position solutions do not show any distance dependency. The two jumps appear due to a change in the satellites geometry. For the single-frequency solutions the distance dependency is more pronounced for L5/E5a than the L1/E1 solution. Even if the increase with the distance is faster for the L5/E5a processing modes, it still provides the best performance and the vertical protection levels get as large as the L1/E1 ones only at distances above 35 km. At distances close to the GBAS reference point, the $\sigma_{\text{pr_gnd}}$ and $\sigma_{\text{pr_air}}$ dominate the protection levels, while with the increase of the distance the contribution of the σ_{iono} becomes more dominant. For this scenario, the airborne multipath models derived for the DLR' A320 aircraft were used. The L5/E5a models derived for this aircraft are much lower compared with the L1/E1 ones. The effect is mainly attributed to the improved multipath rejection capabilities of the BPSK(10) modulation and also to the antenna used which has improved performance for L5/E5a band. Therefore, the improved results of the L5/E5a protection levels compared to L1/E1 for all distances can be explained by the fact that the lower airborne multipath models compensate for the effect of the σ_{iono}.

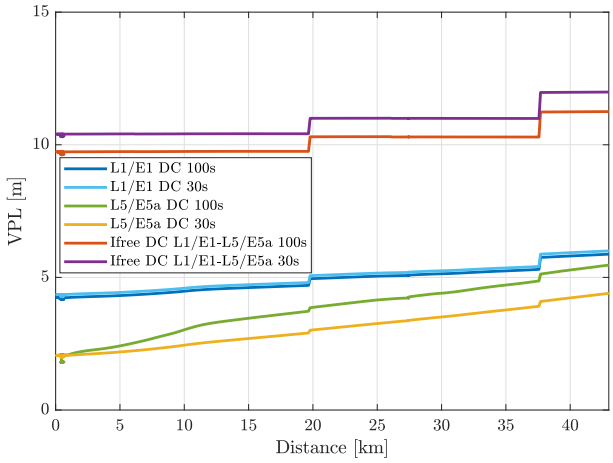


Figure 7.7: VPL versus distance for L1/E1 dual-constellation 100 seconds smoothing (dark blue curve) and 30 seconds smoothing (light blue curve), L5/E5a dual-constellation 100 seconds smoothing (green curve) and 30 seconds smoothing (yellow curve) and Ifree 100 seconds smoothing (red curve) and 30 seconds smoothing (purple curve) using DLR's airborne multipath models and CONUS ionosphere threat model (σ_{vig})

Figure 7.8 shows the same vertical protection levels for the case when the Germany iono threat model is used, for which $\sigma_{\text{vig}} = 2.07$ mm/km. In this scenario, the improvement of the L5/E5a processing mode is even more visible and the difference to the L1/E1 stays up to 1 m even for distances above 30 km. It is interesting to notice that the change of the σ_{vig} to 2.07 mm/km has the largest effect on the L5/E5a 100 seconds and in this scenario the difference between the two L5/E5a solutions (based on the two smoothing time constants) is very low.

Figure 7.9 shows the impact of different airborne multipath models. The results presented until now where based on the airborne multipath models derived from the experimental installation on DLR's A320 aircraft. However, as already mentioned these models are considered conservative. Thus, in order to assess a less conservative future dual-frequency dual-constellation performance, the initial airborne multipath models derived within DUFMAN project are used. These models show a slight improvement for the L5/E5a band compared to L1/E1, but the difference is much smaller than in the case of DLR's A320 aircraft. For this analysis, only the processing modes based on 100 smoothing time constant are considered. The figure shows the vertical protection levels for 100 seconds smoothing derived with the DLR's airborne multipath models (referred as ATRA models) are shown with solid lines in comparison with the protection levels computed using the DUFMAN airborne multipath models shown in dashed lines. The protection levels are computed for L1/E1 100 seconds smoothing time constant (blue curves), L5/E5a 100 seconds smoothing time constant (green curves) and Ifree based on 100 seconds smoothing time constant (red curves).

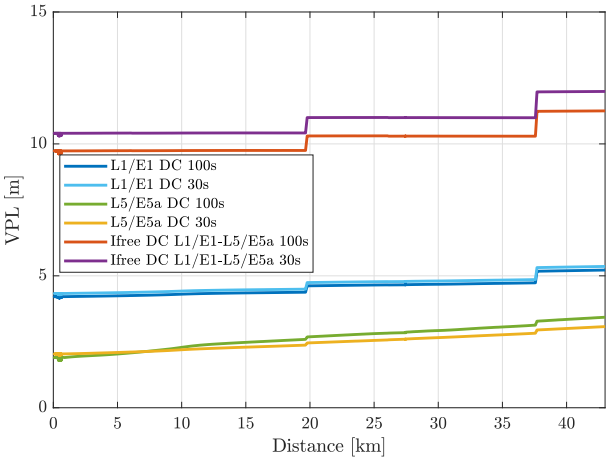


Figure 7.8: VPL versus distance for L1/E1 dual-constellation 100 seconds smoothing (dark blue curve) and 30 seconds smoothing (light blue curve), L5/E5a dual-constellation 100 seconds smoothing (green curve) and 30 seconds smoothing (yellow curve) and Ifree 100 seconds smoothing (red curve) and 30 seconds smoothing (purple curve) using DLR airborne multipath models and Germany ionosphere threat model (σ_{vig})

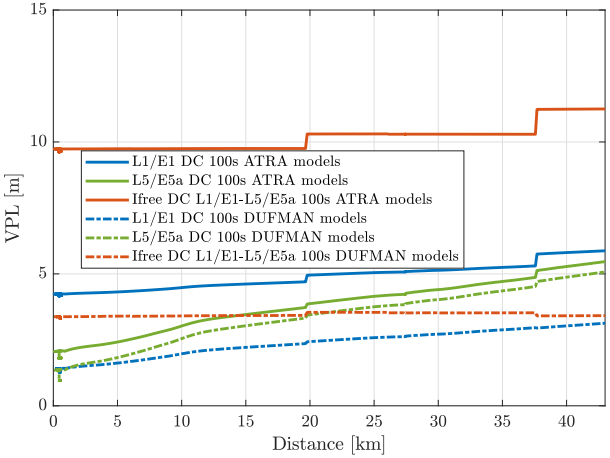


Figure 7.9: VPL versus distance for L1/E1 dual-constellation 100 seconds smoothing (dark blue curve), L5/E5a dual-constellation 100 seconds smoothing (green curve) and Ifree 100 seconds smoothing (red curve) using ATRA and DUFMAN airborne multipath models and CONUS ionosphere threat model (σ_{vig})

The much lower airborne multipath models developed within DUFMAN (especially for L1/E1) have a strong impact on the performance of the L1/E1 and the Ifree processing mode. In this case, the Ifree vertical protection levels are in the range of 3 m, while the L1/E1 protection levels vary from 1 m at short distances to around 3 m for distances above 35 km. For L5/E5a the values are not very different because the difference in the airborne multipath models is rather small. However, looking at the comparison between the three processing modes derived with the DUFMAN models (the dashed green, dashed blue and dashed red lines), it can be observed that their performance is completely different than the one observed in the previous results. Similar to the scenarios discussed above, the Ifree solution does not show a distance dependency, but the single-frequency increase with the distance. The dependency on the distance is more pronounced for the L5/E5a processing mode. For this scenario, the best results are achieved by the dual-constellation L1/E1 processing mode. The dual-constellation L5/E5a processing mode shows similar performance to the L1/E1 one only at very short distances to the GBAS reference point (below 3 km) and it increases with increasing distance quite strongly exceeding even the Ifree protection levels at a distance around 20 km. This change of performance can be explained by the fact that in this scenario, the difference between the airborne multipath models is not very large, and thus the effect of the ionospheric residual become dominant.

Finally, Figure 7.10 shows the results for the two airborne multipath models when considering the Germany ionospheric model. It can be observed that when using a lower σ_{vig} of 2.07 mm/km, the L5/E5a achieves the best results for distances up to 6-7 km, where typically the aircraft would touch down. Furthermore, the increase of the single-frequency protection levels is much smaller and it does not exceed the Ifree protection levels.

7.3 Discussion

This chapter provided an evaluation of the different processing modes enabled by the use of a second frequency and second constellation. The choice of a processing scheme for the future DFDC GBAS depends on many parameters.

The study focused on the evaluation of the nominal vertical protection levels. The nominal protection levels are influenced by the satellite geometry and the expected residual errors on the corrected pseudorange measurements. The single-frequency processing modes are characterized by lower residual errors for the ground and airborne multipath ($\sigma_{\text{pr_gnd}}$ and $\sigma_{\text{pr_air}}$), but have to account for the decorrelation of the ionospheric error with distance. At shorter distances, typically, the largest contributors to the residual errors to the GBAS reference point are the $\sigma_{\text{pr_gnd}}$ and $\sigma_{\text{pr_air}}$. At larger distances, however, the ionospheric error residual gets dominant in the nominal protection levels due to the increase of the ionospheric residual with distance and aircraft speed. On the L5/E5a frequency the ionospheric delay for a given ionospheric state is 1.8 times larger than the delay on L1. This leads to a more pronounced dependency of the L5/E5a protection levels with distance compared to the L1/E1

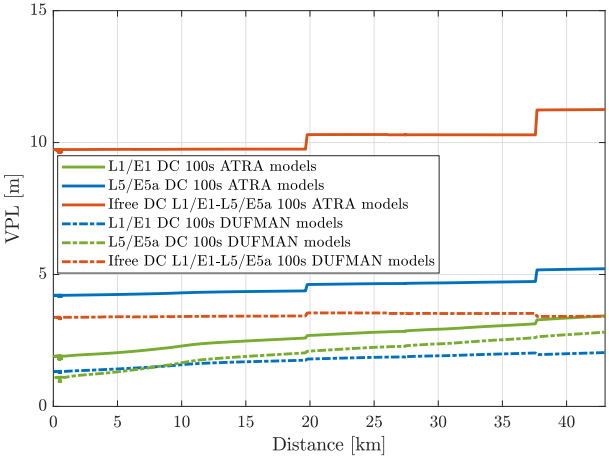


Figure 7.10: VPL versus distance for L1/E1 dual-constellation 100 seconds smoothing (dark blue curve), L5/E5a dual-constellation 100 seconds smoothing (green curve) and Ifree 100 seconds smoothing (red curve) using ATRA and DUFMAN airborne multipath models and Germany ionospheric threat model (σ_{vig})

protection levels. The results showed that when there is a large difference between the airborne multipath models of the L1/E1 signals and L5/E5a signals (as in the case of the curves derived from DLR's A320), this difference compensates for the increase in the ionospheric error. In this case, L5/E5a processing mode provides the best results regardless of the distances to the GBAS reference point.

However, when the airborne and ground multipath errors are similar for both frequencies L1/E1 and L5/E5a the dual-constellation L5/E5a mode provides best results for very short distances to the GBAS reference point and the L1/E1 performance is better long larger distances (above 3-5 km).

While the single-frequency protection levels show the increase with distance, in the Ifree modes the protection levels (black and red curves) stay rather constant due to the lack of σ_{iono}. This behavior might be of interest for the extension of the GBAS service volume which is currently set to 43 km. However, at larger distances the ephemeris protection level might become dominant which were not considered in this work. This matter needs further investigations. Although the Ifree modes show a constant behavior over distance, for distances close to the GBAS, the Ifree protection levels are large due to the increase on the noise and multipath. This might lead to system unavailability as the protection levels would exceed the alert limits that get tighter when the aircraft is approaching the runway threshold.

8 Conclusion

8.1 Summary and main contributions

The work in this thesis focused on providing a contribution to the development of a future DFDC GBAS. This included the investigation and discussion of the relevant contributors to the error budget. In the following, each chapter with the main contributions is summarized.

Chapter 2 provided a detailed review of the current single-frequency GBAS architecture and integrity concept. The aim of the chapter is to set the framework and identify the aspects needed in the development of the DFDC GBAS.

Chapter 3 discusses different aspects and the modifications needed in the integrity concept when evolving from a single-frequency single constellation to a future DFDC GBAS. The use of a second frequency and second constellation enables many different processing modes. The proposal in this thesis for building the DFDC GBAS is based on upgrading the existing GBAS, but maintaining the main characteristics (e.g. upgrading to DFDC receivers, but maintaining the VDB link). This concept is also adopted and investigated in the SESAR project [82]. This approach, however, adds navigational and practical constrains such as backwards compatibility to the existing GAST-C and GAST-D systems and is driven by the limited remaining VDB capacity. Taking into account all the constraints, the most promising processing modes are discussed with their advantages and disadvantages. The proposed processing modes are used as baseline in the next chapters. The contribution in this chapter is the identification of the integrity aspects that need to be taken into account when using different processing modes.

Chapter 4 focused on the analysis of the multipath error introduced in the ground stations. The analysis is carried out using measurements from DLR GBAS test bed. The study focused on the analysis of the Galileo satellites as they have different signal modulations and different constellation repeatability time. This and the following chapter are the main focus of the thesis and contain most of the contributions. For this chapter, these are:

- The first contribution in this chapter is an assessment of the multipath error in the GBAS ground station for the new signals broadcast by the GPS satellites on the L5 band and by the Galileo satellites on E1 and E5a bands. Before smoothing, the signals broadcast on GPS L5 and Galileo E5a show improved performance and much lower raw multipath and noise error compared to the GPS L1 ones. The Galileo E1, signal shows only slight improvements (in com-

parison with GPS L1) in terms of raw multipath and noise. After 100 seconds smoothing, the difference between the signals shrinks. For GPS L5 and Galileo E5a the results are very similar with L1/E1 curves for low satellite elevations and show slight improvement only for satellite elevations above 40°. The 100 seconds smoothed multipath curves for Galileo E1 signal look very similar to the ones derived from the GPS L1 measurements. This result is believed to be specific to the DLR installation, where short multipath reflections are creating by the installation of the antennas on metallic shelter. For short range multipath, the expected code errors from the BOC(1,1) modulation used on the Galileo E1 signal and from the BPSK(10) modulation used for GPS L5 and Galileo E5a signals are expected to be the same with the code errors on GPS L1 BPSK(1) modulation.

- The second contributions is the investigation of the applicability of the existing method used to derive $\sigma_{\text{pr_gnd}}$ to the Galileo constellation. For GPS L1 the $\sigma_{\text{pr_gnd}}$ values are computed based on 24h of measurements because the constellation ground track repeats almost every sideral day. However, the Galileo constellation ground tracks repeat only every 10 days. Thus, in the analysis performed in this work it is suggested to increase the period used for derivation of $\sigma_{\text{pr_gnd}}$ for Galileo satellites to 10 days in order to observe all combinations of elevation-azimuth for each satellite.

- The third contribution is the comparison of two different methods used to derive the ground multipath models and analysis of the possible difference. The results show that the two methods lead to different results in case the ussualy followed assumptions made in the derivation of the $\sigma_{\text{pr_gnd}}$ from the standard deviation of the B-values are not valid. One important assumption is the equality of the variances of the measurement errors from different receivers which is not always satisfied. In this case, a weighting of the reference receivers is proposed and discussed.

- The fourth contribution is the investigation of the different effects having an impact on the multipath error models such as the smoothing time constant and the receiver parameters. In addition to the curves derived for a smoothing time constant of 100 seconds, an evaluation of the $\sigma_{\text{pr_gnd}}$ curves for different smoothing time constants is presented. It was found that the new signals are less sensitive to the choice of the carrier smoothing time constant than the GPS L1 signal. For Galileo E1, a smoothing time constant longer than 60 seconds does not provide a significant improvement on the residual error, while for GPS L5 and E5a, there is already almost no additional error reduction for smoothing time constants longer than 30 seconds. This improvement can bring a benefit and may allow the use of less specialized antennas (e.g. choke ring antennas) instead of the special multipath limiting antennas currently used. Measurements collected with two different receiver configurations in terms of correlator spacing are compared. The receiver parameters have an impact on the multipath and noise errors and a significant difference is observed between the errors derived

from a narrow correlator (0.015chips for L1/E1 and 0.15 chips for L5/E5a) and a wide correlator (0.1 for L1/E1, 1 chip for L5/E5a). This result should be considered in the definition of future receiver standards.

- The fifth contribution is the development of the dual-frequency ground multipath models that differ from combining the single-frequency models mentioned earlier. The results show that the Ifree $\sigma_{\text{pr_gnd}}$ curve derived based on measurements is not always lower than the theoretical curve computed from the assumption that the multipath and noise errors are uncorrelated between frequencies. This is the case when the multipath and noise error on both frequencies are positively correlated. Thus, values derived from Ifree measurements have to be broadcast to the airborne receiver in order to ensure integrity.

Chapter 5 presents the development of the single and dual-frequency airborne multipath models for the new signals broadcast by the GPS Bock IIF satellite on L5 band and by the Galileo satellites on E1 and E5a band. This work was presented at numerous standardization group meetings and contributed to the DUFMAN project, that aims at developing and standardizing airborne multipath models. The main contributions in this chapter are:

- The first contribution in this chapter is the suggestion of an improved methodology to derive the airborne mutipath models. The code-minus-carrier measurements used as proxy for multipath estimation are affected by the carrier phase ambiguities. The approach currently used to estimate the carrier phase ambiguities is to compute the mean over a continuous segment of the satellite or to use the bias at the highest satellite elevation as the bias approximation. It was shown that these methods are not always suitable. As first adaption of the multipath estimation process, a new method for estimating the carrier phase ambiguities is proposed. It is able to exclude the data highly affected by multipath that would lead to a less accurate bias estimation. The second change is separating the antenna induced errors due to group delay variation from the multipath error. The results show that the code errors introduced by the antenna group delay variations have a different signature compared with the multipath error and should not be bounded by a standard deviation only. The errors introduced by the antenna group delay variation can be deterministically computed using the antenna gain and phase patterns from measurements in an anechoic chamber. These deterministic values are used to calibrate the multipath estimates. Next, a CDF overbounding of the estimated standard deviation is proposed in order to account for the non-Gaussian distribution of the multipath. Finally, an inflation for the limited number of samples is suggested. These steps are especially important for dual-frequency aviation users, where the airframe multipath becomes a dominant source of error.

- The next contribution is the derivation of the preliminary multipath models for GPS L5 and Galileo E1 and E5a using measurements from flight tests conducted on DLR's A320 aircraft. The initial models developed from an experimental installation on the A320 aircraft are more conservative than the current existing

models. The main reason for this is the use of the experimental antenna which was not compliant with the current MOPS requirements. Even if the antenna-induced error are calibrated, the antenna multipath rejection capability still affects the amount of multipath that is present in the measurements. Furthermore, the antenna was installed in a non-optimal location on the fuselage. Compared to the existing models, the two inflation steps discussed above were applied.

- The third contribution is the investigation of different contributors to the airborne multipath models including the smoothing time constant, the antenna, the airframe and the receiver parameters.

  As observed on the ground measurements, the impact of the smoothing time constant is lower for GPS L5/Galileo E5a compared to GPS L1. However, the effectiveness of the smoothing filter is more pronounced on airborne measurements when compared to those from the ground, as airborne measurements are characterized by higher uncorrelated noise and slightly-correlated multipath.

  For the investigation of the impact of the antenna and the airframe on the airborne multipath error, measurements collected from the first flight campaign in the DUFMAN project are used. The flights were conducted on an Airbus A321. The results derived from these measurements show much lower multipath and noise error in comparison to the ones derived from the DLR experimental installation on the Airbus A320. Furthermore, the difference between L1/E1 and L5/E5a curves is very small and the L5/E5a signals do not show significantly improved performance. This outcome can be attributed to the antenna used. The performance of the antenna installed on commercial aircraft within the DUFMAN project meets the requirements defined in the antenna MOPS, but performs better on L1/E1 band than on the L5/E5a band. The better antenna performance on the L1/E1 compensates for the worse multipath rejection capability of the modulations used on this band.

Chapter 6 discusses the effect of the satellite code biases on DFDC GBAS. The satellite code biases differ between satellites and depend on the satellite signal and receiver hardware (correlator spacing and bandwidth). They can be calculated based on measurements from a high gain antenna. Initial estimates of the biases were used to study the effect on the GBAS user. The main contributions in this chapter are:

- The first contribution is an analysis of the impact of the differential satellite code biases on a GBAS user. Based on a fixed ground receiver configuration, the differential satellite code biases considering different design space for the airborne receiver were calculated. The results show that the differential code biases vary from few centimeters to decimeters. The values get even larger in the Ifree case due to the combination of the biases from the two frequencies. The outcome of this study is that the differential satellite code biases are not negligible in the GBAS context and need to be taken into account for an integrity concept.

- The second contribution is a proposal of their inclusion in the GBAS integrity concept. Different methods for the inclusion of the biases are proposed which differ in the type of information that is broadcast by the ground subsystem. The first solution proposes the calibration of the biases in the ground and airborne measurements and integration of a residual uncertainty in the $\sigma_{\text{pr_air}}$ and $\sigma_{\text{pr_gnd}}$ terms. A second method proposes the broadcast of the bias information from the ground system. Based on its known configuration, the ground system can compute a maximum differential bias over the design space used by the airborne receiver. Depending on the available VDB space, different values for each satellite or the worst case biases can be broadcast. Having this information, the airborne receiver computes the additional term bounding these errors.

Chapter 7 assesses the performance of different processing modes for future DFDC based on measurements from flight trials and the error models derived in this thesis. The work contributes to the trade-off studies needed for the selection of an optimal processing mode for future DFDC GBAS. The definition of a best processing mode, however, depends on many different parameters. The single-frequency processing modes have to account for the decorrelation of the ionospheric error (introduced by the single-frequency smoothing filter) with the aircraft speed and distance from the GBAS reference point. The Ifree processing modes removes the effect of the ionospheric error, but shows increased multipath and noise error due to the combination of the two code measurements. Thus, the single-frequency protection levels have much lower values when the aircraft is close to the GBAS reference point but increase with distance. The increase is much faster for the L5/E5a due to the larger ionospheric error (1.8 times larger).

The single-frequency modes are beneficial for short distances, where the improved performance is required (having lower error limits). For the L5/E5a processing mode, its improved performance due to lower multipath and noise could be used for the aircraft taxiing. The L1/E1 seems to be the most promising solution to cover the GBAS service volume. In the studies, the same ionospheric residual modeling with the existing single-frequency mode was used. However, the second frequency could be used for the monitoring which has the potential to decrease the ionospheric residual bound. Finally, the Ifree processing mode could be relevant for large distances, especially for extending the current service volume to distances larger than 43 km.

8.2 Recommendation and further research

DFDC GBAS is currently in an early phase of development. Thus, there is still a need and potential for further research and refinement of the concepts. Based on the findings in this thesis, further studies on the following topics are suggested:

- As discussed in Chapter 3, one of the main constraints in the development of a future DFDC GBAS is the limited capacity of the VDB link. This capacity limits the choices for the possible processing modes and potentials for efficient design of a new service type. In this work, the concept and the processing modes

selected were based on the idea that the same VDB as the current one is used. If in future a different approach is considered that does not have such stringent limitations in terms of capacity as today's VDB, different parameters could be broadcast enabling the use of other processing modes. It is therefore suggested to further study the feasibility of using new data transmission schemes with the VDB technology or move to a different broadcast technology. The introduction of the new ground-air digital communication standard L-band Digital Aeronautical Communications System (LDACS) [138] is a promising starting point to this development.

- In Chapter 4, the derivation of the multipath errors on the ground reference receivers was carried out based on the experimental GBAS test bed. The multipath error is, however, dependent on the receiver antenna and the installation. In order to quantify the improvements of the new signals broadcast on GPS L5 and Galileo E1 and E5a in a certified GBAS station, measurements from an actual installation with multipath limiting antenna set up according to the siting requirements should be analyzed. Furthermore, the evaluations should also be extended to the additional Galileo satellites and the newly launched GPS Block III satellites.

- In Chapter 5 the development of the initial airborne multipath models was discussed. Before proposing final models, more investigations should be carried out. First, the validation of the initially developed models with more data collected on different aircraft types is recommended. This ensures that a representative model for a variety of different airframes is developed and the obtained results are statistically relevant.

  The results, furthermore, show that the performance of the antenna has a significant impact on the obtained results. The study in this work is based on measurements collected with two different antennas. The first antenna has a very good performance on the L5/E5a band, while the L1/E1 the performance was not meeting the requirements of the current DFDC antenna MOPS. The second antenna is reasonably well performing at L1/E1 band and can be considered as minimum compliant to the MOPS regarding group delay variation and multipath susceptibility in the L5/E5a band (for certain elevation angles the requirements are slightly exceeded). Thus, the final models should also be based on a minimum compliant antenna on L1/E1 in order to ensure that all MOPS compliant installations meet the expected performance.

  In the development of the airborne multipath models, the errors introduced by the antenna group delay variation were separated using antenna gain and phase measurements from an anechoic chamber. The results showed that these have a different signature compared with the multipath error and should not be bounded by a standard deviation only. Future work should investigate the optimal method for a separate bounding of these errors and the impact on performance in terms of availability of protection levels.

- For the inclusion of the satellite code biases, an initial evaluation has been made. Further work needs to validate these initial results when measurements from all available GPS Block IIF and Galileo satellites are available. Furthermore, based on the results from all the satellites, a final decision on the broadcast parameters needs to be taken (e.g. if one parameter per constellation is sufficient).
- The evaluations in Chapter 7 provided a first assessment of the different processing modes. Based on the final decision, further trade-off studies need to be performed taking into account complexity issues, availability considerations and ongoing standardization decisions.
- Finally, the thesis discussed relevant integrity aspects needed for DFDC GBAS error models. The analysis of nominal errors contributions were the focus of this investigation. However, in order to finalize the integrity concept also all non-nominal error contributions (i.e. non nominal ionospheric errors, RFI and other threats) need to be addressed in detail and further research should investigate the required monitoring scheme in the ground station and airborne system in order for the integrity concept to be complete and address all potential threats to a future DFDC GBAS.

A Smoothing Filter

A.1 Single frequency smoothed pseudoranges

The carrier smoothing uses the rate of the precise carrier phase measurements to propagate code measurements forward and the smooth pseudoranges at epoch k is described as

$$\overline{\rho}^s_{r,i}(k) = \frac{\Delta T}{\tau} \cdot \rho^s_{r,i}(k) + (1 - \frac{\Delta T}{\tau}) \cdot \left[\overline{\rho}^s_{r,i}(k-1) + \phi^s_{r,i}(k) - \phi^s_{r,i}(k-1)\right], \quad \text{(A.1)}$$

with τ and ΔT being the smoothing time constant and the measurements sampling interval. All the terms refer to the measurements on frequency i between the receiver r and satellite s. The indexes for the receiver and satellite have been omitted for the sake of brevity. Using the notation $\alpha = \frac{\Delta T}{\tau}$ and rearranging the terms the equation can be written

$$\overline{\rho}^s_{r,i}(k) = \phi^s_{r,i}(k) + \underbrace{\alpha \cdot \left(\rho^s_{r,i}(k) - \phi^s_{r,i}(k)\right) + (1-\alpha) \cdot \left(\overline{\rho}^s_{r,i}(k-1) - \phi^s_{r,i}(k-1)\right)}_{\text{A}}. \quad \text{(A.2)}$$

Looking at this equation, it can be observed that the smooth pseudorange at epoch k are formed by the EWMA of the previous k epochs of the $CMC^s_{r,i}$ time series to which $\phi^s_{r,i}(k)$ is added to reconstruct the geometry information. The exponentially weighted moving average acts as a low pass filter removing the high frequency components of the noise and multipath. For a time series $y(t)$, the exponential weighted moving average $s(t)$ with $\begin{cases} s(1) = y(1) \\ s(t) = \alpha \cdot y(t) + (1-\alpha) \cdot s(t-1) \end{cases}$ can be written as a weighted sum as

$$s(t) = (1-\alpha)^{t-1} \cdot y(1) + \alpha \cdot \sum_{n=2}^{t} (1-\alpha)^{t-n} \cdot y(n). \quad \text{(A.3)}$$

Using this equation in Eq. A.2 and setting $\overline{\rho}^s_{r,i}(1) = \rho^s_{r,i}(1)$, the smooth pseudorange at epoch time k can be written as a weighted sum as

$$\overline{\rho}^s_{r,i}(k) = \phi^s_{r,i}(k) + (1-\alpha)^{k-1} \cdot \left(\rho^s_{r,i}(1) - \phi^s_{r,i}(1)\right) + \alpha \cdot \sum_{n=2}^{k} (1-\alpha)^{k-n} \cdot \left(\rho^s_{r,i}(n) - \phi^s_{r,i}(n)\right). \quad \text{(A.4)}$$

Expanding the terms for the code and phase measurements using Eq.2.1 and 2.2, the smooth pseudorange becomes

$$
\begin{aligned}
&\overline{\rho}^s_{r,i}(k) = \\
&R^s_r(k) + c\cdot(\delta t_r(k) - \delta t^s(k)) + T^s_r(k) - I^s_{r,i}(k) + mp^s_{r,i}(k) + \eta^s_{r,i}(k) + \beta^s_i(k) + \beta_{r,i}(k) + \zeta_{r,i}(k) + \zeta^s_i(k) + N^s_{r,i}(k)\cdot\lambda_i(k) + \\
&+ (1-\alpha)^{k-1}\cdot\big[2\cdot I^s_{r,i}(1) + MP^s_{r,i}(1) + \varepsilon^s_{r,i}(1) + B^s_i(1) + B_{r,i}(1) + \xi_{r,i}(1) + \xi^s_i(1) - \\
&- mp^s_{r,i}(1) + \eta^s_{r,i}(1) + \beta^s_i(1) + \beta_{r,i}(1) + \zeta_{r,i}(1) + \zeta^s_i(1) + N^s_{r,i}(1)\cdot\lambda_i(1)\big] + \\
&+ \alpha\cdot\sum_{n=2}^{k}(1-\alpha)^{k-n}\cdot\big[2\cdot I^s_{r,i}(n) + MP^s_{r,i}(n) + \varepsilon^s_{r,i}(n) + B^s_i(n) + B_{r,i}(n) + \xi_{r,i}(n) + \xi^s_i(n)\big] - \\
&\alpha\cdot\sum_{n=2}^{k}(1-\alpha)^{k-n}\cdot\big[-mp^s_{r,i}(n) + \eta^s_{r,i}(n) + \beta^s_i(n) + \beta_{r,i}(n) + \zeta_{r,i}(n) + \zeta^s_i(n) + N^s_{r,i}(n)\cdot\lambda_i(n)\big].
\end{aligned}
\tag{A.5}
$$

A.2 Ifree smoothed pseudoranges

Recalling Eq. 3.8, the smooth Ifree pseudoranges for frequencies i and j described as

$$
\overline{\rho_{\text{Ifree}}}^s_{r,i,j}(k) = \frac{\Delta T}{\tau}\cdot{\rho_{\text{Ifree}}}^s_{r,i}(k) + (1-\frac{\Delta T}{\tau})\cdot\big[\overline{\rho_{\text{Ifree}}}^s_{r,i,j}(k-1) + {\phi_{\text{Ifree}}}^s_{r,i,j}(k) - {\phi_{\text{Ifree}}}^s_{r,i,j}(k-1)\big]. \tag{A.6}
$$

Using the notation $CMC_{\text{Ifree}} = \rho_{\text{Ifree}} - \phi_{\text{Ifree}}$ and based on the derivation presented in the previous section of this Appendix, the $\overline{\rho_{\text{Ifree}}}^s_{r,i,j}(k)$ can be written as a sum of the Ifree combination of the carrier phases at epoch k and the weighted sum of the CMC_{Ifree} as

$$
\overline{\rho_{\text{Ifree}}}^s_{r,i,j}(k) = {\phi_{\text{Ifree}}}^s_{r,i,j}(k) + (1-\alpha)^{k-1}\cdot\big({\rho_{\text{Ifree}}}^s_{r,i,j}(1) - {\phi_{\text{Ifree}}}^s_{r,i,j}(1)\big) + \alpha\cdot\sum_{n=2}^{k}(1-\alpha)^{k-n}\cdot\big({\rho_{\text{Ifree}}}^s_{r,i,j}(n) - {\phi_{\text{Ifree}}}^s_{r,i,j}(n)\big). \tag{A.7}
$$

Replacing ${\phi_{\text{Ifree}}}^s_{r,i,j}$ and ${\rho_{\text{Ifree}}}^s_{r,i,j}$ with Eq. 3.6 and 3.7, the equation can be written as

$$
\begin{aligned}
\overline{\rho_{\text{Ifree}}}^s_{r,i,j}(k) = &\frac{f_i^2}{f_i^2-f_j^2}\cdot\phi^s_{r,i}(k) - \frac{f_j^2}{f_i^2-f_j^2}\cdot\phi^s_{r,j}(k) + \\
&+ (1-\alpha)^{k-1}\cdot\left(\frac{f_i^2}{f_i^2-f_j^2}\cdot\rho^s_{r,i}(1) - \frac{f_j^2}{f_i^2-f_j^2}\cdot\rho^s_{r,j}(1) - \frac{f_i^2}{f_i^2-f_j^2}\cdot\phi^s_{r,i}(1) + \frac{f_j^2}{f_i^2-f_j^2}\cdot\phi^s_{r,j}(1)\right) + \\
&+ \alpha\cdot\sum_{n=2}^{k}(1-\alpha)^{k-n}\cdot\left(\frac{f_i^2}{f_i^2-f_j^2}\cdot\rho^s_{r,i}(n) - \frac{f_j^2}{f_i^2-f_j^2}\cdot\rho^s_{r,j}(n) - \frac{f_i^2}{f_i^2-f_j^2}\cdot\phi^s_{r,i}(n) + \frac{f_j^2}{f_i^2-f_j^2}\cdot\phi^s_{r,j}(n)\right).
\end{aligned}
\tag{A.8}
$$

Rearranging the terms and multiplying the parenthesis the above equation be-

comes:

$$
\begin{aligned}
\overline{\rho_{\mathrm{Ifree}}}^{s}_{r,i,j}(k) =& \frac{f_i^2}{f_i^2 - f_j^2} \cdot \phi^s_{r,i}(k) + \frac{f_i^2}{f_i^2 - f_j^2} \cdot (1-\alpha)^{k-1} \cdot \left(\rho^s_{r,i}(1) - \cdot\phi^s_{r,i}(1)\right) + \frac{f_i^2}{f_i^2 - f_j^2} \cdot \alpha \cdot \sum_{n=2}^{k} (1-\alpha)^{k-n} \cdot \left(\cdot\rho^s_{r,i}(n) - \phi^s_{r,i}(n)\right) - \\
&- \frac{f_j^2}{f_i^2 - f_j^2} \cdot \phi^s_{r,j}(k) - \frac{f_j^2}{f_i^2 - f_j^2} \cdot (1-\alpha)^{k-1} \cdot \left(\rho^s_{r,j}(1) - \cdot\phi^s_{r,j}(1)\right) - \frac{f_j^2}{f_i^2 - f_j^2} \cdot \alpha \cdot \sum_{n=2}^{k} (1-\alpha)^{k-n} \cdot \left(\cdot\rho^s_{r,j}(n) - \phi^s_{r,j}(n)\right) \\
=& \frac{f_i^2}{f_i^2 - f_j^2} \cdot \underbrace{\left[\phi^s_{r,i}(k) + (1-\alpha)^{k-1} \cdot \left(\rho^s_{r,i}(1) - \cdot\phi^s_{r,i}(1)\right) + \alpha \cdot \sum_{n=2}^{k} (1-\alpha)^{k-n} \cdot \left(\cdot\rho^s_{r,i}(n) - \phi^s_{r,i}(n)\right)\right]}_{\overline{\rho}^s_{r,i}(k)} - \\
&- \frac{f_j^2}{f_i^2 - f_j^2} \cdot \underbrace{\left[\phi^s_{r,j}(k) + (1-\alpha)^{k-1} \cdot \left(\rho^s_{r,j}(1) - \cdot\phi^s_{r,j}(1)\right) + \alpha \cdot \sum_{n=2}^{k} (1-\alpha)^{k-n} \cdot \left(\cdot\rho^s_{r,j}(n) - \phi^s_{r,j}(n)\right)\right]}_{\overline{\rho}^s_{r,j}(k)} \\
=& \frac{f_i^2}{f_i^2 - f_j^2} \cdot \overline{\rho}^s_{r,i}(k) - \frac{f_j^2}{f_i^2 - f_j^2} \cdot \overline{\rho}^s_{r,j}(k).
\end{aligned}
\tag{A.9}
$$

The obtained results means that the Ifree smooth pseudorange can be obtained also by forming the Ifree combination on the smooth single frequency psedoranges under the condition that the same smoothing time constant is applied for both frequencies and the filters run time are equal (e.g. they reset at the same time).

B Smooth Multipath Derivation

B.1 Single frequency

The smooth multipath represents the error on the smooth pseudoranges, thus the derivation starts from the equation of the smooth pseudorange. In Appendix A it was shown that the smooth pseudorangefor a satellite s, receiver r and frequency i at epoch k can be write as a sum of the carrier phase measurement at epoch k ($\phi^s_{r,i}(k)$)and the EWMA of the previous k epoch of the $CMC^s_{r,i}$ (see Eq. A.2 - A.4)

Subtracting the current carrier-phase measurements ($\phi^s_{r,i}(k)$) from Eq.A.4, yields an estimate of the smooth ($\overline{CMC}^s_{r,i}$)

$$\overline{CMC}^s_{r,i}(k) = \overline{\rho}^s_{r,i}(k) - \phi^s_{r,i}(k) = (1-\alpha)^{k-1} \cdot \left[\rho^s_{r,i}(1) - \phi^s_{r,i}(1)\right] + \alpha \cdot \sum_{n=2}^{k} (1-\alpha)^{k-n} \cdot \left[\rho^s_{r,i}(n) - \phi^s_{r,i}(n)\right]. \tag{B.1}$$

As the raw code-minus-carrier (Eq. 5.3), the smooth estimate of the code minus carrier contains twice the smooth ionospheric error. The ionospheric delay is not constant over time, thus the smoothing filter (EWMA) will introduce an additional delay. The total ionospheric error present in the smooth ($\overline{CMC}^s_{r,i}$) at epoch k can be expressed as

$$\overline{I}^s_{r,i}(k) = 2 \cdot \left[(1-\alpha)^{k-1} \cdot I^s_{r,i}(1) + \alpha \cdot \sum_{n=2}^{k} (1-\alpha)^{k-n} \cdot I^s_{r,i}(n)\right]. \tag{B.2}$$

The delay introduced by the smoothing filter can be obtained by applying the same exponentially weighted moving average on the raw error as:

$$\begin{aligned} \overline{I}^s_{r,i}(k) &= \alpha \cdot I^s_{r,i}(k) + (1-\alpha) \cdot \overline{I}^s_{r,i}(k-1) = \\ &= (1-\alpha)^{k-1} \cdot I^s_{r,i}(1) + \alpha \cdot \sum_{n=2}^{k} (1-\alpha)^{k-n} \cdot I^s_{r,i}(n), \end{aligned} \tag{B.3}$$

where $\overline{I}^s_{r,i}(1) = I^s_{r,i}(1)$ and the raw ionospheric delay $I^s_{r,i}(k)$ can be determined using Eq.5.4. Replacing the terms, the smooth ionospheric delay at epoch k becomes

$$\overline{I}^s_{r,i}(k) = \frac{f_j^2}{f_i^2 - f_j^2} \cdot (1-\alpha)^{k-1} \cdot \left[\phi^s_{r,i}(1) - \phi^s_{r,j}(1)\right] + \frac{f_j^2}{f_i^2 - f_j^2} \cdot \alpha \cdot \sum_{n=2}^{k} (1-\alpha)^{k-n} \left[\phi^s_{r,i}(n) - \phi^s_{r,j}(n)\right]. \tag{B.4}$$

Substituting this equation and subtracting twice the smooth ionospheric delay in B.1 estimate of the smooth code minus carrier divergence free ($\overline{CMC_{\text{Dfree,bias}}}^{s}_{r,i,j}(k)$) (see Eq. 5.5) is obtained. This estimate can be rewritten as

$$\begin{aligned}
\overline{CMC_{\text{Dfree,bias}}}^{s}_{r,i,j}(k) &= \overline{CMC}^{s}_{r,i}(k) - 2\cdot \overline{I}^{s}_{r,i}(k) = \\
&= (1-\alpha)^{k-1}\cdot\left[\rho^{s}_{r,i}(1) - \phi^{s}_{r,i}(1) - 2\cdot\frac{f_j^2}{f_i^2-f_j^2}\cdot\left(\rho^{s}_{r,i}(1) - \phi^{s}_{r,i}(1)\right)\right] + \\
&+ \alpha\cdot\sum_{n=2}^{k}(1-\alpha)^{k-n}\cdot\left[\rho^{s}_{r,i}(n) - \phi^{s}_{r,i}(n) - 2\cdot\frac{f_j^2}{f_i^2-f_j^2}\cdot\left(\rho^{s}_{r,i}(n) - \phi^{s}_{r,i}(n)\right)\right] = \\
&= (1-\alpha)^{k-1}\left[CMC_{\text{Dfree,bias}}{}^{s}_{r,i,j}(1)\right] + \alpha\cdot\sum_{n=2}^{k}(1-\alpha)^{k-n}\cdot\left[CMC_{\text{Dfree,bias}}{}^{s}_{r,i,j}(n)\right].
\end{aligned} \tag{B.5}$$

The quantity on the left side is actually the EWMA of the $CMC_{\text{Dfree,bias}}{}^{s}_{r,i}(k)$, meaning that the smooth multipath and noise error can be obtained by applying directly the smoothing filter to the raw $CMC_{\text{Dfree,bias}}{}^{s}_{r,i}$.

B.2 Dual frequency Ifree multipath estimation

In order to show the derivation of the Ifree multipath estimation, the Ifree combination for the code and carrier phase measurements is re-written

$$\phi_{\text{Ifree}}{}^{s}_{r,i,j} = \frac{f_i^2}{f_i^2-f_j^2}\cdot\phi^{s}_{r,i} - \frac{f_j^2}{f_i^2-f_j^2}\cdot\phi^{s}_{r,j}, \tag{B.6}$$

$$\rho_{\text{Ifree}}{}^{s}_{r,i,j} = \frac{f_i^2}{f_i^2-f_j^2}\cdot\rho^{s}_{r,i} - \frac{f_j^2}{f_i^2-f_j^2}\cdot\rho^{s}_{r,j}. \tag{B.7}$$

The multipath and noise error on the Ifree code measurements combination of frequencies i and j for a receiver r, and a satellite s can be estimated from the single frequency estimates of code-minus-carrier divergence free $CMC_{\text{Dfree,bias}}{}^{s}_{r,i,j}$ and $CMC_{\text{Dfree,bias}}{}^{s}_{r,j}$

$$CMC_{\text{Ifree,bias}}{}^{s}_{r,i,j} = \frac{f_i^2}{f_i^2-f_j^2}\cdot CMC_{\text{Dfree,bias}}{}^{s}_{r,i} - \frac{f_j^2}{f_i^2-f_j^2}\cdot CMC_{\text{Dfree,bias}}{}^{s}_{r,j}. \tag{B.8}$$

Replacing $CMC_{\text{Dfree,bias}}{}^{s}_{r,i}$ and $CMC_{\text{Dfree,bias}}{}^{s}_{r,j}$ with the Eq. 5.5, the estimated $CMC_{\text{Ifree,bias}}{}^{s}_{r}$ becomes:

$$\begin{aligned}
CMC_{\text{Ifree,bias}}{}^{s}_{r,i,j} &= \frac{f_i^2}{f_i^2-f_j^2}\cdot\left[\rho^{s}_{r,i} - \phi^{s}_{r,i} - \frac{f_j^2}{f_i^2-f_j^2}\cdot\left(\phi^{s}_{r,i} - \phi^{s}_{r,j}\right)\right] - \\
&- \frac{f_j^2}{f_i^2-f_j^2}\cdot\left[\rho^{s}_{r,j} - \phi^{s}_{r,j} - \frac{f_i^2}{f_j^2-f_i^2}\cdot\left(\phi^{s}_{r,j} - \phi^{s}_{r,i}\right)\right] \\
&= \rho_{\text{Ifree}}{}^{s}_{r,i,j} - \phi_{\text{Ifree}}{}^{s}_{r,i,j}.
\end{aligned} \tag{B.9}$$

As the smoothing is a linear equation, the smooth Ifree multipath and noise error can be derived by forming the Ifree combination on the smooth single frequency code-minus-carrier divergence free estimates ($\overline{CMC_{\mathrm{Dfree,bias}}}^{s}_{r,i,j}$ and $\overline{CMC_{\mathrm{Dfree,bias}}}^{s}_{r,j,i}$) or by differenciating the Ifree carrier phase measurements from the Ifree smooth code measurements.

Bibliography

[1] S. Pullen and P. Enge, "An overview of GBAS integrity monitoring with a focus on ionospheric spatial anomalies," *Indian Journal of Radion & Space Physics (94.20. Vv; 94.20 B6)*, vol. 36, pp. 249–260, 2007.

[2] J. Lee, M. Yoon, S. Pullen, J. Gillespie, N. Mather, R. Cole, J. Rodriguez de Souza, P. Doherty, and R. Pradipta, "Preliminary Results from Ionospheric Threat Model Development to Support GBAS Operations in the Brazilian Region," in *Proceedings of the 28th International Technical Meeting of the Satellite Division of the Institute of Navigation (ION GNSS+15)*, Jan. 2015.

[3] T. Fujiwara and T. Tsujii, "GBAS availability assessment and modeling of ionospheric scintillation effects," *Navigation*, vol. 63, no. 4, pp. 405–413, Dec. 2016.

[4] European Commision, Directorate-General for Research and Innovation, Directorate General for Mobility and Transport , "Flightpath 2050 Europe's Vision for Aviation," 2011.

[5] Bundesministerium für Wirtschaft und Energie, "Die Luftfahrtstrategie der Bundesregierung," 2014. [Online]. Available: https://www.bmwi.de/Redaktion/DE/Publikationen/Technologie/luftfahrtstrategie-der-bundesregierung.html

[6] United States Federal Aviation Administration, "FAA Aeropace Forecast," 2019. [Online]. Available: https://www.faa.gov/data_research/aviation/aerospace_forecasts/

[7] Eurocontrol, "Eurocontrol Seven-Year Forecast, Flight Movements and Service Units 2019-2025," 2019. [Online]. Available: https://www.eurocontrol.int/publication/seven-year-forecast-flight-movements-and-service-units-february-2019

[8] International Air Transport Association. (2019) Air traffic frequency. [Online]. Available: https://www.iata.org/publications/store/Pages/20-year-passenger-forecast.aspx

[9] European Comission. (2017) Airport capacity and quality. [Online]. Available: https://ec.europa.eu/transport/modes/air/airports/airport_capacity_and_quality_en

[10] Eurocontrol, "European aviation in 2040. Challenges of Growth. Network Congestion," 2018.

[11] European Union, Eurocontrol. Sesar website. [Online]. Available: https://www.sesarju.eu/

[12] United States Federal Aviation Administration. NextGen Program. [Online]. Available: https://www.faa.gov/nextgen/

[13] International Civil Aviation Organization, "International Standards and Recommended Practices (SARPs). Annex 10 to the Convention of International Civil Aviation. Volume I -Radio Navigation Aids," Tech. Rep., Jul. 2018.

[14] United States Federal Aviation Administration. WAAS Quick Facts Sheet. [Online]. Available: https://www.faa.gov/about/office_org/headquarters_offices/ato/service_units/techops/navservices/gnss/library/factsheets/media/WAAS_QFSheet.pdf

[15] European Global Navigation Satellite Systems Agency. EGNOS LPV 200 Enables Safer Aircraft Landings. [Online]. Available: https://www.gsa.europa.eu/news/egnos-lpv-200-enables-safer-aircraft-landings

[16] Unites States Federal Aviation Administration. GBAS-Quick Facts. [Online]. Available: https://www.faa.gov/about/office_org/headquarters_offices/ato/service_units/techops/navservices/gnss/library/factsheets/media/GBAS_QFactSheet.pdf

[17] [Online]. Available: flygls.net

[18] Radio Technical Commission for Aeronautics, "DO-253D, Minimum Operational Performance Standards for GPS Local Area Augmentation System Airborne Equipment," Tech. Rep., 2017.

[19] United States Federal Aviation Administration. Satellite Navigation — Ground Based Augmentation System (GBAS). [Online]. Available: https://www.faa.gov/about/office_org/headquarters_offices/ato/service_units/techops/navservices/gnss/laas/

[20] M. Yoon, D. Kim, J. Lee, S. Rungruengwajiake, and S. Pullen, "Assessment of Equatorial Plasma Bubble Impacts on Ground-Based Augmentation Systems in the Brazilian Region," *Proceedings of the 2016 International Technical Meeting of The Institute of Navigation*, pp. 368–379, Jan. 2016.

[21] C. Mayer, B. Belabbas, N. Jakowski, M. Meurer, and W. Dunkel, "Ionosphere Threat Space Model Assessment for GBAS," in *Proceedings of the 22nd International Technical Meeting of the Satellite Division of The Institute of Navigation (ION GNSS 2009)*, Sep. 2009, pp. 1091–1099.

[22] J. Lee, M. Luo, S. Pullen, Y. S. Park, P. Enge, and M. Brenner, "Position-Domain Geometry Screening to Maximize LAAS Availability in the Presence of Ionosphere Anomalies," in *Proceedings of the 19th International Technical Meeting of the Satellite Division of The Institute of Navigation (ION GNSS 2006)*, Sep. 2006, pp. 393–408.

[23] M. Yoon, D. Kim, S. Pullen, and J. Lee, "Assessment and mitigation of equatorial plasma bubble impacts on category I GBAS operations in the Brazilian region," *Navigation*, vol. 66, no. 3, pp. 643–659, Aug. 2019.

[24] S. Pullen, R. Cassell, B. Johnson, M. Brenner, D. Weed, L. Cypriano, M. Topland, T. Stakkeland, B. Pervan, M. Harris, S. Saito, J. Lee, B. Clark, S. Beauchamp, and J. Dennis, "Impact of Ionospheric Anomalies on GBAS GAST D Service and Validation of Relevant ICAO SARPs Requirements," in *Proceedings of the 30th International Technical Meeting of the Satellite Division of The Institute of Navigation (ION GNSS+ 2017)*, Sep. 2017, pp. 2085–2105.

[25] K. C. Yeh and C.-H. Liu, "Radio wave scintillations in the ionosphere," *Proceedings of the IEEE*, vol. 70, no. 4, pp. 324–360, 1982.

[26] S. Skone, M. Feng, F. Ghafoori, and R. Tiwari, "Investigation of Scintillation Characteristics for High Latitude Phenomena," in *Proceedings of the 21st International Technical Meeting of the Satellite Division of The Institute of Navigation (ION GNSS 2008)*, Sep., pp. 2425–2433.

[27] A. R. Lopez, "LAAS/GBAS Ground Reference Antenna With Enhanced Mitigation of Ground Multipath," in *Proceedings of the 2008 National Technical Meeting of The Institute of Navigation*, Sep. 2008.

[28] M. Felux, T. Dautermann, and H. Becker, "GBAS Landing System - Precision Approach Guidance after ILS," *Aircraft Engineering and Aerospace Technology*, vol. 85/5, pp. 382–388, 2013.

[29] R. Cassell, B. Clark, and M. Harris, "Working paper WP 19 - Dmax and GBAS Approach Service Volume," NSP-CSG Meeting, Tech. Rep., Nov. 2016.

[30] Airbus, "Getting to Grips with Category II and III Operations," Tech. Rep., 2001.

[31] Radio Technical Commission for Aeronautics, "DO-246E, GNSS-Based Precision Approach Local Area Augmentation System Signal-in-Space Interface Control Document," Tech. Rep., 2017.

[32] Eurocae, *ED-114A, Minimum Operational Performance Specification for Global Navigation Satellite Ground Based Augmentation System Ground Equipment to Support Category I Operations*, Eurocae Std. ED-114A, Mar. 2013.

[33] United States Federal Aviation Administration, "Category I Local Area Augmenation System Ground Facility - NON-FED Specification," Tech. Rep. FAA-E-AJW44-2937A, 2005.

[34] ——, "Siting Order for Ground Based Augmentation System," Tech. Rep. Order 6884.1, Dec. 2010.

[35] Radio Technical Commission for Aeronautics, "DO-301, Minimum Operational Perforamnce Standards (MOPS) for GNSS Airborne Active Antenna Equipment for the L1 frequency band," Tech. Rep., 2016.

[36] R. Hatch, "The Synergism of GPS Code and Carrier Measurements," vol. 2, 1982, pp. 1213–1231.

[37] P. Misra and P. Enge, *Global Positioning System, Signals, Measurements and Performance*, second edition ed. Ganga-Jamuna Press, 2006.

[38] International Civil Aviation Organization, "International Standards and Recommended Practices (SARPs). Annex 10 to the Convention of International Civil Aviation. Volume I -Radio Navigation Aids," Tech. Rep., May 2010.

[39] J. Rife, S. Pullen, P. Enge, and B. Pervan, "Paired overbounding for nonideal LAAS and WAAS error distributions," *IEEE Transactions on Aerospace and Electronic Systems*, vol. 42, no. 4, pp. 1386–1395, Oct. 2006.

[40] B. Pervan and E. Sayim, "Sigma inflation for the local area augmentation of GPS," *IEEE Transactions on Aerospace and Electronic Systems*, vol. 37, no. 4, pp. 1301–1311, Oct. 2001.

[41] P. J. G. Teunissen and O. Montenbruck, *Springer Handbook of Global Navigation Satellite Systems*. Springer, 2017.

[42] G. A. McGraw, T. Murphy, M. Brenner, S. Pullen, and A. J. V. Dierendonck, "Development of the LAAS Accuracy Models," in *Proceedings of the 13th International Technical Meeting of the Satellite Division of The Institute of Navigation (ION GPS 2000)*, Sep. 2000, pp. 1212–1223.

[43] F. van Graas and Z. Zhen, "Tropospheric Delay Threats for the Ground Based Augmentation System," in *Proceedings of the 2011 International Technical Meeting of The Institute of Navigation*, Sep. 2011.

[44] S. Datta-Barua, T. Walter, S. Pullen, M. Luo, J. Blanch, and P. Enge, "Using WAAS Ionospheric Data to Estimate LAAS Short Baseline Gradients," in *Proceedings of the 2002 National Technical Meeting of The Institute of Navigation*, Jan. 2002, pp. 523–530.

[45] J. Lee, S. Pullen, S. Datta-Barua, and P. Enge, "Assessment of Ionosphere Spatial Decorrelation for Global Positioning System-Based Aircraft Landing Systems," *Journal of Aircraft*, vol. 44, no. 5, pp. 1662–1669, Sep. 2007.

[46] J. Lee, S. Pullen, G. Xie, and P. Enge, "LAAS Sigma-Mean Monitor Analysis and Failure-Test Verification," in *Proceedings of the 57th Annual Meeting of The Institute of Navigation (2001)*, Jun. 2001, pp. 694–704.

[47] J. Lee, S. Pullen, and E. Per, "Sigma Overbounding using a Position Domain Method for the Local Area Augmentaion of GPS," *IEEE Transactions on Aerospace and Electronic Systems*, vol. 45, no. 4, pp. 1262–1274, Oct. 2009.

[48] D. V. Simili and B. Pervan, "Code-Carrier Divergence Monitoring for the GPS Local Area Augmentation System," in *Proceedings of the Position, Location, And Navigation Symposium 2006*, Apr. 2006, pp. 483–493.

[49] M. Stakkeland, Y. L. Andalsvik, and K. S. Jacobsen, "Estimating Satellite Excessive Acceleration in the Presence of Phase Scintillations," in *Proceedings of the 27th International Technical Meeting of The Satellite Division of the Institute of Navigation (ION GNSS+ 2014)*, Sep. 2014, pp. 3532–3541.

[50] S. Pullen, G. Gao, C. Tedeschi, and Wartburton, "The Impact of Uninformed RF Interference on GBAS and Potential Mitigations," in *Proceedings of the 2012 International Technical Meeting of the Institute of Navigation*, Jan. 2012.

[51] M. Felux, T. Dautermann, and B. Belabbas, "Towards Full GAST-D Capability - Flight testing DLR's Experimental GBAS Station," in *Proceedings of the 2012 International Technical Meeting of the Institute of Navigation*, Jan. 2012, pp. 1648–1654.

[52] S. Datta-Barua, T. Walter, S. Pullen, M. Luo, J. Blanch, and P. Enge, "Using WAAS Ionospheric Data to Estimate LAAS Short Baseline Gradients," in *Proceedings of the 2002 National Technical Meeting of The Institute of Navigation*, Jan. 20002.

[53] S. Pullen, Y. S. Park, and P. Enge, "Impact and mitigation of ionospheric anomalies on ground-based augmentation of GNSS," *Radio Science*, vol. 44, 2009.

[54] S. Datta-Barua, J. Lee, S. Pullen, M. Luo, A. Ene, D. Qiu, G. Zhang, and P. Enge, "Ionospheric Threat Parameterization for Local Area Global-Positioning-System-Based Aircraft Landing Systems," *Journal of Aircraft*, vol. 47, no. 4, pp. 1141–1151, 2010.

[55] M. Kim, Y. Choi, H.-S. Jun, and J. Lee, "GBAS ionospheric threat model assessment for category I operation in the Korean region," *GPS Solutions*, no. doi:10.1007/s10291-014-0404-6, Sep. 2014.

[56] C. A. Shively and R. Niles, "Safety Concepts for Mitigation of Ionospheric Anomaly Erros in GBAS," in *Proceedings of the 2008 National Technical Meeting of The Institute of Navigation*, Sep. 2008, pp. 361–381.

[57] J. Lee, J. Seo, Y. S. Park, S. Pullen, and P. Enge, "Ionospheric threat mitigation by geometry screening in Ground-Based Augmentation Systems," *Journal of Aircraft*, vol. 48, no. 4, pp. 1422–1433, 2011.

[58] J. Seo, J. Lee, S. Pullen, P. Enge, and S. Close, "Targeted parameter inflation within ground-based augmentation systems to minimize anomalous ionospheric impact," *Journal of aircraft*, vol. 49, no. 2, pp. 587–599, 2012.

[59] S. Ramakrishnan, J. Lee, S. Pullen, and P. Enge, "Targeted ephemeris decorrelation parameter inflation for improved LAAS availability during severe ionosphere anomalies," in *Proceedings of the 2008 National Technical Meeting of The Institute of Navigation (ION GNSS 2008)*, Sep. 2008, pp. 28–30.

[60] J. Huang and F. van Graas, "Characterization of Tropospheric Spatial Decorrelation Errors Over a 5-km Baseline," *Navigation*, vol. 55, pp. 39–53, 2008.

[61] J. Burns, B. Clark, R. Cassell, C. Shively, T. Murphy, and M. Harris, "Conceptual Framework for the Proposal for GBAS to Support CAT III Operations," ICAO Navigation Systems Panel, Tech. Rep., 2009.

[62] EASA, "Certification Specifications for All-Weather Operations (CS-AWO)," EASA, Oct. 2003.

[63] U.S. Department of Transportation Federal Aviation Administration, *Criteria for approval of Category III weather minima for takeoff, landing, and rollout*, US Department of Transportation Std. AC 120-28D, Jul. 1999.

[64] M. Felux, J. Lee, and F. Holzapfel, "Total system performance in gbas-based landings," in *Proceedings of the ION 2015 Pacific PNT Meeting*, Apr. 2015.

[65] T. Murphy, L. Anderson, M. Harris, and N. H. Tang, "CAT III Simulated Landing Performance for GLS and ILS Systems," in *Proceedings of the 14th International Technical Meeting of the Satellite Division of The Institute of Navigation (ION GPS 2001)*, Sep. 2001, pp. 1679–1688.

[66] Boeing, "Volume IV: Determining the Vertical Alert Limit Requirements for a Level of GBAS Service that is Appropriate to Support CAT II/III Operations," Boeing, Tech. Rep., 2005.

[67] ——, "Volume I: GBAS CAT II Requirements Development Research Program Overview and Summary of Results," Boeing, Tech. Rep. Vol I, Oct. 2005.

[68] B. Clark and B. DeCleene, "Alert Limits: Do we Need Them for CAT III?" in *Proceedings of the 19th International Technical Meeting of the Satellite Division of The Institute of Navigation (ION GNSS 2006)*, Sep. 2006, pp. 3070–3081.

[69] R. Cassel, "WP17 - Background on mitigation of GAST-D anomalous ionospheric conditions," 2014.

[70] S. Khanafseh, P. Pullen, and J. Warburton, "Carrier Phase Ionospheric Gradient Ground Monitor for GBAS with Experimental Validation," *Navigation*, vol. 59, no. 1, pp. 51–60, Mar. 2012.

[71] J. McDonald, D. Weed, and B. Johnson, "WP16 - Observed Nominal Atmospheric Behavior Using Honeywell's GAST D Ionosphere Gradient Monitor," ICAO NSP WGW, Tech. Rep., 2014.

[72] M. Stakkeland, M. Topland, and IGM ad-hoc group, "IP5 - GAST D Iono Mitigation Using Approach 1 (Detect and React to Troposphere Noise)," ICAO NSP, Tech. Rep., 2015.

[73] B. Johnson, "WP2 - IGM Requirement Validation Overview," ICAO NSP JGW, Tech. Rep., 2016.

[74] B. Johnson and J. McDonald, "WP13 - Proposed Modification for GAST D Anomalous Ionosphere Gradient Requirements," ICAO NSP WG1&2, Tech. Rep., 2014.

[75] Radio Technical Commission for Aeronautics, "DO-253C, Minimum Operational Performance Standards for GPS Local Area Augmentation System Airborne Equipment," Tech. Rep., 2008.

[76] F. Salabert and CONOPS AD-Hoc drafting group, "Flimsy 30 - Next Generation GNSS CONOPS," ICAO NSPl, Tech. Rep., 2016.

[77] P. Y. Hwang, G. A. McGraw, and J. R. Bader, "Enhanced Differential GPS Carrier-Smoothed Code Processing Using Dual-Frequency Measurements," *Navigation*, vol. 46, no. 2, pp. 127–137, 1999.

[78] H. Konno, S. Pullen, J. Rife, and P. Enge, "Evaluation of two types of dual-frequency differential GPS techniques under anomalous ionosphere conditions," in *Proceedings of ION National Technical Meeting 2006.* Citeseer, Jan. 2006, pp. 18–20.

[79] M.-S. Circiu, M. Felux, P. Remi, B. Belabbas, and S. Pullen, "Evaluation of Dual Frequency GBAS Performance using Flight Data," in *Proceedings of the 2014 International Technical Meeting of The Institute of Navigation*, Jan. 2014, pp. 645–656.

[80] M. Felux, M.-S. Circiu, J. Lee, and F. Holzapfel, "Ionospheric Gradient Threat Mitigation in Future Dual Frequency GBAS," *International Journal of Aerospace Engineering*, vol. 2017, pp. 1–10, 2017.

[81] M. Stanisak, A. Lipp, and T. Feuerle, "Possible VDB formatting for multi-constellation multi-frequency GBAS services," in *Proceedings of the 28th International Technical Meeting of the Satellite Division of the Institute of Navigation (ION GNSS+15)*, Sep. 2015, pp. 1507–1518.

[82] P. Durba, "WP27 - High level concept and modes for DFMC GBAS," ICAO NSP - Joint Working Groups, Tech. Rep., 2018.

[83] M.-S. Circiu, M. Felux, D. Gerbeth, M. Caamano, and M. Meurer, "Assessment of Different Dual-frequency Dual-constellation GBAS Processing Modes Based on Flight Trials," in *Proceedings of the 29th International Technical Meeting of The Satellite Division of the Institute of Navigation (ION GNSS+ 2016)*, Nov. 2016.

[84] M.-S. Gerbeth, D.and Circiu, M. Caamano, and M. Felux, "Nominal Performance of Future Dual Frequency Dual Constellation GBAS," *International Journal of Aerospace Engineering*, vol. 2016, pp. 1–20, 2016.

[85] M.-S. Circiu, M. Meurer, M. Felux, D. Gerbeth, S. Thölert, M. Vergara, M. Sgammini, C. Enneking, S. Pullen, and F. Antreich, "Evaluation of gps l5 and galileo e1 and e5a performance for future multifrequency and multiconstellation gbas," *Navigation*, vol. 64, no. 1, pp. 149–163, Mar. 2017.

[86] M.-S. Circiu, M. Felux, B. Belabbas, M. Meurer, J. Lee, M. Kim, and S. Pullen, "Evaluation of GPS L5, Galileo E1 and Galileo E5a Performance in Flight Trials for Multi Frequency Multi Constellation GBAS," in *Proceedings of the*

28th International Technical Meeting of The Satellite Division of the Institute of Navigation (ION GNSS+ 2015), Sep. 2015, pp. 897–906.

[87] A. Guilbert, "Non-Nominal Troposphere Reassessment for Meeting CAT II/III with MC/MF GBAS," in *Proceedings of the 28th International Technical Meeting of The Satellite Division of the Institute of Navigation (ION GNSS+ 2015)*, Sep. 2015, pp. 1526–1537.

[88] B. Pervan and T. Sayim, "Issues and Results Concerning the LAAS $\sigma_{pr,gnd}$ Overbound," in *IEEE Position Location and Navigation Symposium (PLANS) 2000*, Mar. 2000.

[89] B. Pervan, S. Pullen, and I. Sayim, "Sigma estimation, inflation, and monitoring in the LAAS ground system," in *Proceedings of the 13th International Technical Meeting of the Satellite Division of the Institute of Navigation*, Sep. 2000.

[90] I. Sayim and B. Pervan, "Experimental and Theoretical Results on the LAAS Sigma Overbound," in *Proceedings of the 15th International Technical Meeting of the Satellite Division of the Institute of Navigation (ION GPS-2002)*, Sep. 2002.

[91] ——, "LAAS Ranging Error Overbound for Non-Zero Mean and Non-Gaussian Error Distributions," in *Proceedings of the 59th Annual Meeting of the Institute of Navigation*, Jun. 2003.

[92] Eurocae, " ED259-Minimum Operational Performance Standard for Galileo/Global Positioning System/Satellite-Based Augmentation System Airborne Equipment," Tech. Rep., 2018.

[93] NATMIG, Thales, DFS, AENA, DSNA, "Project Number 15.03.06. D04. Ground Architecture and Airport Installation," Sesar Joint Undertaking, Tech. Rep., 2013. [Online]. Available: https://www.sesarju.eu/sites/default/files/solutions/5_Precision_approaches_GBAS_CAT_II_III_L1_TS_ground.pdf

[94] US Government. Official U.S. government information about the Global Positioning System (GPS) and related topics. [Online]. Available: http://www.gps.gov/systems/gps/modernization/civilsignals/

[95] European Union, "European galileo open service signal in space interface control document, issue 1.3," European Union, Tech. Rep., 2016.

[96] M. Vergara, F. Antreich, and A. Hornbostel, "Multipath Effects on a GNSS Receiver Tracking Performance," in *Wave Propagation and Scattering in Communications, Microwave Remote Sensing and Navigation*, Nov. 2009.

[97] M. Vergara, F. Antreich, and M. Meurer, "Effect of Multipath on Code-Tracking Error Jitter of a Delay Locked Loop," in *Fourth European Workshop on GNSS signals and signal processing*, Dec. 2009.

[98] Global Positioning Sytems Directorate, Systems Enigneering and Integration,

"Interface Specifications, Navstar GPS Space Segment / Navigation User Segment Interfaces (IS-GPS-200 Revision K)," Tech. Rep., 2019.

[99] ——, "Interface Specifications, Navstar GPS Space Segment / Segment L5 Interfaces (IS-GPS-705 Revision F)," Tech. Rep., 2019.

[100] M.-S. Circiu, M. Felux, S. Thölert, F. Antreich, M. Vergara, M. Sgammini, C. Enneking, and S. Pullen, "Evaluation of GPS L5 and Galileo E1 and E5a Performance for Future Multi Frequency and Multi Constellation GBAS," in *Proceedings of the 2015 International Technical Meeting of The Institute of Navigation*, Jan. 2015, pp. 374–382.

[101] Radio Technical Commission for Aeronautics, SC-159, "DO-229E - Minimum Operational Performance Standards for Global Positioning System/Satellite-Based Augmentation System Airborne Equipment," Tech. Rep., 2016.

[102] Boeing, "Volume II: Electromagnetic Modeling of Airframe and Ground Bounce Multipath," Boeing, Tech. Rep. Vol I, Oct. 2005.

[103] T. Murphy, R. Snow, and M. Braasch, "GPS Multipath on Large Commercial Air Transport Airframes," *Navigation*, vol. 43, no. 4, pp. 397–406.

[104] J. Booth, T. Murphy, B. Clark, and F. Liu, "Validation of the Airframe Multipath Error Allocation for Local Area Differential GPS," in *Proceedings of the IAIN World Congress and the 56th Annual Meeting of The Institute of Navigation (2000)*, 2000, pp. 689–698.

[105] T. Murphy, M. Harris, P. Geren, T. Pankaskie, B. Clark, J. Burns, and T. Urda, "Results from the Program for the Investigation of Airborne Multipath Errors," in *Proceedings of the 2005 National Technical Meeting of The Institute of Navigation*, Sep. 2005, pp. 2670–2687.

[106] T. Murphy, M. Harris, P. Geren, T. Pankaskie, B. Clark, and J. Burns, "More Results From the Investigation of Airborne Multipath Errors," in *Proceedings of the 18th International Technical Meeting of the Satellite Division of The Institute of Navigation*, Jan. 2005, pp. 153–169 – 2687.

[107] T. Murphy and J. Booth, "WP43 - GBAS SARPs Review and Validation of Airborne Multipath Requirements," ICAO, GNSSP WG B, Tech. Rep., 1999.

[108] ——, "GBAS SARPs Review and Validation of Airborne Multipath Requirements, (Sections B3.6.5.4.1 and B3.6.8.2.1)," ICAO, GNSSP WG B, Tech. Rep., 2000.

[109] T. Murphy, R. Friedman, J. Booth, P. Geren, N. Molloy, B. Clark, and J. Burns, "Program for the Investigation of Airborne Multipath Errors," in *Proceedings of the 2004 National Technical Meeting of The Institute of Navigation*, 2005, pp. 781–792.

[110] S. Caizzone, M.-S. Circiu, W. Elmarissi, C. Enneking, M. Felux, and K. Yinusa, "Antenna influence on Global Navigation Satellite

System pseudorange performance for future aeronautics multifrequency standardization," *Navigation*, vol. 66, no. 1, pp. 99–116. [Online]. Available: https://onlinelibrary.wiley.com/doi/abs/10.1002/navi.281

[111] ——, "Effect of Antenna Pattern Uniformity on the Pseudorange Tracking Error," in *Proceedings of the 30th International Technical Meeting of The Satellite Division of the Institute of Navigation (ION GNSS+ 2017)*, Sep. 2017, pp. 3460–3470.

[112] M. Harris, M. Miltner, T. Murphy, A. Raghuvanshi, and F. van Graas, "Bounding GPS L1 Antenna Group Delay Variation for GNSS Landing System Integrity," in *Proceedings of the 2017 International Technical Meeting of The Institute of Navigation (ITM)*, Jan. 2017, pp. 591–605.

[113] M.-S. Circiu, M. Rippl, M. Felux, S. Caizzone, C. Enneking, B. Belabbas, and M. Meurer, "Development of Airborne Performance Models for new GNSS Signals," in *International Symposium on Certification of GNSS Systems & Services (CERGAL)*, 2017.

[114] P. Misra and P. Enge, *Global Positioning System. Signal, Measurements, and Performance*, 2006.

[115] P. Teunissen, P. De Jonge, and J. Tiberius, "Performance of the LAMBDA Method for Fast GPS Ambiguity Resolution," *Navigation*, vol. 44, no. 3, pp. 373–383, sep 1997.

[116] P. Teunissen, "GPS Carrier Phase Ambiguity Fixing Concepts," in *GPS for Geodesy*. Springer Berlin Heidelberg, 1998, pp. 319–388.

[117] J. S. Subirana, J. M. J. Zornoza, M. Hernández-Pajares, E. S. Agency, and K. Fletcher, *GNSS Data Processing*, ser. ESA TM. ESA Communications, 2013, no. Bd. 1. [Online]. Available: https://books.google.de/books?id=RO8xngEACAAJ

[118] S. Thoelert, M. Vergara, M. Sgammini, C. Enneking, F. Antreich, M. Meurer, D. Brocard, and C. Rodriguez, "Characterization of Nominal Signal Distortions and Impact on Receiver Performance for GPS (IIF) L1/L5 and Galileo (IOV) E1 /E5a Signals," in *Proceedings of the 27th International Technical Meeting of The Satellite Division of the Institute of Navigation (ION GNSS+ 2014)*, Jan. 2014, pp. 3113–3128.

[119] L. Wanninger, H. Sumaya, and S. Beer, "Group delay variations of GPS transmitting and receiving antennas," *Journal of Geodesy*, vol. 91, no. 9, pp. 1099–1116, Sep. 2017.

[120] J. Wu, S. Wu, G. Hajj, W. I. Bertiger, and S. Lichten, "Effects of antenna orientation on GPS carrier phase," *Manuscripta Geodetica*, vol. 18, pp. 91–98, Feb. 1993.

[121] Boeing, "Volume III: Multipath Flight Test Program & Results," Boeing, Tech. Rep. Vol I, Oct. 2005.

[122] M. Vergara, F. Antreich, C. Enneking, M. Sgammini, and G. Seco-Granados, "A model for assessing the impact of linear and nonlinear distortions on a GNSS receiver," *GPS Solutions*, vol. 24, no. 1, p. 5, Nov 2019. [Online]. Available: https://doi.org/10.1007/s10291-019-0917-0

[123] Radio Technical Commission for Aeronautics, SC-159, "DO-373, MOPS for GNSS active antenna in the L1/E1 and L5/E5A bands," Tech. Rep., 2018.

[124] S. Caizzone, M.-S. Circiu, W. Elmarissi, C. Enneking, M. Felux, and K. Yinusa, "Multipath rejection capability analysis of GNSS antennas," in *Proceedings of the 31st International Technical Meeting of The Satellite Division of the Institute of Navigation (ION GNSS2018)*. Institute of Navigation, Oct. 2018.

[125] Javad. Javad AirAnt antenna datasheet. [Online]. Available: https://www.javad.com/jgnss/products/antennas/AirAnt_spec.html

[126] M. Mabilleau, "JWG/3-IP35, Galileo Evil Wave Form Model Methodology," ICAO NSP - Joint Working Groups, Tech. Rep., 2018.

[127] M.-S. Circiu, S. Caizzone, M. Felux, C. Enneking, F. Fohlmeister, M. Rippl, and M. Sgammini, "NSP JWG/WP35 - Initial DFMC airborne multipath models from DUFMAN project," Tech. Rep., 2019.

[128] M.-S. Circiu, S. Caizzone, M. Felux, C. Enneking, and M. Meurer, "Improved Airborne Multipath Modelling," in *Proceedings of the 31st International Technical Meeting of The Satellite Division of the Institute of Navigation (ION GNSS+ 2018)*. Institute of Navigation, Oct. 2018.

[129] O. Montenbruck and A. Hauschild, "Code Biases in Multi-GNSS Point Positioning," in *Proceedings of the 2013 International Technical Meeting of The Institute of Navigation*, Jan. 2013, pp. 616–628.

[130] A. Hauschild and O. Montenbruck, "A study on the dependency of GNSS pseudorange biases on correlator spacing," *GPS Solutions*, vol. 20, no. 2, pp. 159–171, Nov. 2014.

[131] O. Montenbruck, A. Hauschild, and P. Steigenberger, "Differential Code Bias Estimation using Multi-GNSS Observations and Global Ionosphere Maps," *Navigation*, vol. 61, no. 3, pp. 191–201, Sep. 2014.

[132] N. Wang, Y. Yuan, Z. Li, O. Montenbruck, and B. Tan, "Determination of differential code biases with multi-GNSS observations," *Journal of Geodesy*, vol. 90, no. 3, pp. 209–228, Nov. 2015.

[133] A. Hauschild and O. Montenbruck, "The Effect of Correlator and Front-End Design on GNSS Pseudorange Biases for Geodetic Receivers," *Navigation*, vol. 63, no. 4, pp. 443–453, Dec. 2016.

[134] S. Thoelert, S. Erker, and M. Meurer, "GNSS Signal Verification with a High Gain Antenna-Calibration Strategies and High Quality Signal Assessment," in

Proceedings of the 2009 International Technical Meeting of The Institute of Navigation, Jan. 2009, pp. 289–300.

[135] S. Thoelert, J. Furthner, and M. Meurer, "GNSS Survey - Signal Quality Assessment of the Latest GNSS Satellites," in *Proceedings of the 2013 International Technical Meeting of The Institute of Navigation*, Jan. 2013, pp. 608–615.

[136] M. Vergara, M. Sgammini, S. Thoelert, C. Enneking, Y. Zhu, and F. Antreich, "Tracking Error Modeling in Presence of Satellite Imperfections," *Navigation*, vol. 63, no. 1, pp. 3–13, Mar. 2016.

[137] S. Thoelert, M.-S. Circiu, and M. Meurer, "Impact of Satellite Biases on the Position in Differential MFMC Applications," in *Proceedings of the 2020 International Technical Meeting of The Institute of Navigation.* Institute of Navigation, feb 2020.

[138] Deutsches Zentrum für Luft- und Raumfahrt (DLR) Institut für Kommunikation und Navigation. LDACS Website. [Online]. Available: https://www.ldacs.com/